Single and Two-Phase Hydrodynamics in Confined Vortex Technology

Een- en Tweefasehydrodynamica in Begrensde Vortex Technologie

Kaustav Niyogi

Promotoren: prof. dr. Geraldine J. Heynderickx en prof. dr. ir. Guy B. Marin
Proefschrift ingediend tot het behalen van de graad van
Doctor in de Ingenieurswetenschappen: Chemische Technologie

Vakgroep Chemische Proceskunde en Technische Chemie
Voorzitter: prof. dr. ir. Guy B. Marin
Faculteit Ingenieurswetenschappen en Architectuur
Academiejaar 2016 – 2017

UNIVERSITEIT
GENT

Promotoren:

Prof. dr. ir. Guy B. Marin
Laboratorium voor Chemische Technologie
Vakgroep Chemische Proceskunde en Technische Chemie
Universiteit Gent

Prof. dr. ir. Geraldine J. Heynderickx
Laboratorium voor Chemische Technologie
Vakgroep Chemische Proceskunde en Technische Chemie
Universiteit Gent

Decaan: Prof. dr. ir. Rik Van de Walle

Rector: Prof. dr. Anne De Paepe

The authors acknowledge financial support from the “Long Term Structural *Methusalem* Funding by the Flemish Government” and from the European Research Council under the European Union's Seventh Framework Program FP7/2007-2013 ERC grant agreement n° 290793.

EXAMENCOMMISSIE

Leescommissie
Prof. dr. ir. Vivek V. Ranade
School of Chemistry and Chemical Engineering
Queen's University Belfast, Northern Ireland, UK

Prof. dr. ir. Juray De Wilde
Divisie Materiaal- en Processkunde (IMAP)
Université catholique de Louvain
Louvain-la-Neuve

Prof. dr. ir. Frederik Ronsse
Department of Biosystems Engineering
Faculty of Bioscience Engineering
Universiteit Gent

Prof. dr. ir. Kevin Van Geem
Vakgroep Chemische Proceskunde en Chemische Technologie
Faculteit Ingenieurswetenschappen en Architectuur
Universiteit Gent

Andere leden
Prof. Prof. Patrick De Baets [voorzitter]
Secretariat of the Board of Governors
Department of Electrical energy, systems and automation
Universiteit Gent

Prof. dr. ir. Guy B. Marin [promotor]
Laboratorium voor Chemische Technologie
Vakgroep Chemische Proceskunde en Technische Chemie
Universiteit Gent

Prof. dr. ir. Geraldine J. Heynderickx [promotor]
Vakgroep Chemische Proceskunde en Chemische Technologie
Faculteit Ingenieurswetenschappen en Architectuur
Universiteit Gent

Dr. Maria Del Mar Torregrosa [secretary]
Laboratorium voor Chemische Technologie
Vakgroep Chemische Proceskunde en Technische Chemie
Universiteit Gent

Acknowledgements

------------------------------------ *To be filled in for final thesis hardcopy* --------------------------------------

Contents

Samenvatting

Procesintensifiëring is een recent aandachtspunt in de chemische en energie-industrie met het oog op de bouw van meer energie-efficiënte, compacte eenheden met een grote doorvoer.

Dergelijke eenheden verhogen niet alleen de doorvoer en opbrengsten, maar verlagen de ‘carbon foot print’ van een bedrijf en reduceren de investeringskosten door verschillende productiestappen in één eenheid te combineren. Gebruik maken van een centrifugaalveld in een (reactor)geometrie wordt gezien als een mogelijk methode voor procesintensifiëring. Wanneer een cylindrische geometrie mechanisch geroteerd wordt, vormt zich een centrifugaalveld. Een meer recente technologie realiseert het centrifugaalveld in een niet-bewegende eenheid door een fluïdum langs inlaten, tangentieel geplaatst op de omtrek van een cilindrische geometrie, te injecteren. Een roterende stroming van het fluïdum is het gevolg. De hydrodynamica in een dergelijke eenheid, vortex eenheid genoemd, wordt bestudeerd in dit werk. In een vortex eenheid, een platte schijfvormige geometrie, is de verhouding van hoogte tot diameter beduidend kleiner dan 1. De afstand tussen bovenste en onderste wand van de schijf is klein, met als gevolg de vorming van complexe secundaire stromingspatronen. Deze liggen mee aan de basis van het potentieel van een vortex eenheid voor procesintensifiëring.

Een experimentele studie van de hydrodynamica in een vortex eenheid vraagt een weloverwogen keuze van de meetapparatuur. Intrusieve technieken zullen het stromingsveld in de experimentele eenheid verstoren. Niet-intrusieve technieken, zoals stereoscopische Particle Image Velocimetry kennen dan weer beperkingen doordat ze visuele toegankelijkheid vragen.

Een betrouwbare numerieke studie van een vortex eenheid zou toelaten veel bijkomende informatie over de hydrodynamica in vortex eenheden te verzamelen. In dit werk wordt voor de numerieke studie gebruik gemaakt van het commerciële software pakket FLUENT®. Het laat toe een volledig kader voor een numerieke studie van vortex eenheden uit te werken.

In dit werk worden zowel één-fase als meer-fase stromingen in een vortex eenheid bestudeerd. De vortex eenheid met enkel gasstroming wordt Gas Vortex Eenheid (GVU) genoemd. Bij de numerieke studie van de GVU wordt de turbulente stroming berekend met het Reynolds Stress turbulentiemodel

met het oog op het correct modelleren van de secundaire stromingspatronen in een GVU. Bij de injectie van gas door de tangentieel geplaatste inlaten, vormt zich een wervelend stromingspatroon in de vortex eenheid. De tangentiële snelheid van het gas in de eenheid neemt toe met afnemende straal tot het gas de centrale uitlaat bereikt. In de dwarsdoorsnede van die uitlaat vermindert de werveling van de stroming door het ontstaan van grote axiale snelheidsgradiënten. Het resultaat is een geleidelijke afname van de tangentiële gassnelheid tot die 0 wordt op de centrale as. Naarmate de wervelende stroming dichter bij de uitlaat komt doorheen de afnemend circumferentiële oppervlakte van de cilindrische eenheid, is de verwachting dat de radiale gassnelheid afneemt met afnemende straal. Simulatie van de vortex unit leert echter dat opvallende secundaire stromingspatronen ontstaan in radiale richting. Deze secundaire stromingen worden veroorzaakt door de vorming van '*near-wall jets*' tegen de bovenste en onderste wand van de eenheid. In de bulkstroming van de vortex eenheid wordt de radiaal-inwaarts gerichte drukgradiënt in evenwicht gehouden door de radiaal-uitwaarts gerichte centrifugaal kracht op een gaselement. Echter, in de gaslagen bij de bovenste en onderste wand van de eenheid wordt dit evenwicht verstoord. De tangentiële snelheid van het gas wordt 0 als gevolg van de 'no-slip' randvoorwaarde bij de wanden, opgelegd in de numerieke studie. Deze verstoring van het evenwicht 'duwt' het gas radiaal-uitwaarts. Dit resulteert in de vorming van '*near-wall jets*' bij de wanden van de GVU. De jetstroming blijft bewegen over de onderste en bovenste wand, een gevolg van de hoge turbulentie in de bulkstroming van de vortex eenheid. De jets bewegen van de circumferentiële wand naar de centrale gasuitlaat, worden eerste sterker maar zwakken dan geleidelijk af. De lange axiale uitlaatpijp voor het gas en de '*near-wall jets*' resulteren in twee secundaire stromingspatronen in de GVU. Terwijl het gas door de uitlaatpijp wervelt, verliezen de wervels in kracht door wrijving met de wand van de uitlaatpijp. Hierdoor ontstaat een inverse drukgradiënt in de uitlaatpijp. Gas wordt uit de omgeving in de eenheid gezogen. Hierdoor ontstaat een lange *zone met terugstroom* in het centrum van de uitlaatpijp. Ook in de vortex eenheid zelf vormt zich een secundair stromingspatroon. De jets sleuren gas mee dat via de tangentiële inlaten naar de vortex eenheid gevoed wordt. Met toenemende werveling in de stroming, zal het gas dat meegesleurd wordt door de jets uiteindelijk groter worden dan de instroom. Gas uit de bulk van de vortex eenheid zelf wordt nu meegesleurd om de jet te voeden. De zone met recirculatie van gas, opgebouwd uit twee vortices, roterend in tegengestelde zin, wordt de *zone met tegenstroom* genoemd. Zowel de *zone met terugstroom* als de *zone met tegenstroom* maken de stromingspatronen in een GVU zeer complex. Zo ontstaan in de GVU meerdere stagnatiepunten voor stroming in een globaal snelle stroming. Goede menging in een GVU kan dus verwacht worden. De GVU is dan ook beloftevol als alternatieve kamer voor, bijvoorbeeld, verbrandingsprocessen.

Wanneer vaste deeltje gevoed worden in een vortex eenheid veranderen de stromingspatronen sterk. De wervelende gasstroming verdwijnt nagenoeg volledig doordat een groot deel van het tangentiële momentum van het instromende gas overgaat op de deeltjes. De deeltjes roteren in de vortex eenheid. Door de hoge dichtheid van het vaste materiaal is de centrifugaalkracht van de deeltjes hoog. De deeltjes worden naar de circumferentiële wand van de vortex eenheid meegenomen, waar ze een dichtgepakt roterend wervelbed vormen. In deze vortex eenheid, Gas Vast Vortex Eenheid (GSVU) genoemd, vormt zich een centrifugaal-gefluïdiseerd bed. Met toenemende gasstroom neemt ook de overdracht van momentum toe. De hogere snelheid van de deeltjes maakt ket centrifugaalveld sterker. Dit is in schril contrast met de conventioneel-gefluïdiseerde bedden in het zwaartekrachtveld, waar de zwaartekracht constant blijft bij wijzigende werkingsvoorwaarden of geometrie. Bijkomend kan de instroom van gas en dus de sterkte van het centrifugaal veld toenemen, terwijl er toch geen deeltjes meegesleurd worden uit de vortex eenheid. De GSVU is bovendien niet onderhevig aan mechanische slijtage en wordt zo een waardevol alternatief voor de roterende geometrieën gebruikt in de industrie.

In dit werk worden CFD berekeningen van de GSVU gepresenteerd, uitgevoerd met een Euleriaans-Euleriaans model waarbij de beide fazen als inter-penetrerende continue fazen berekend worden. De Euleriaanse berekeningen laten niet toe de beweging van groepen deeltjes of individuele deeltjes te analyseren maar geven toch excellente kwalitatieve resultaten tegen een relatief lage rekenkost. Dat laatste wordt gestaafd door vergelijking met een brede set aan beschikbare experimentele gegevens.

De toevoeging van deeltjes aan de vortex eenheid resulteert in een sterke afname van de drukval over de GSVU in vergelijking met de GVU. Dit laatste is gevoelsmatig onverwacht, zeker in vergelijking met de conventieel-gefluïdiseerde wervelbedtechnologieën. De toevoeging van deeltjes breekt de wervelende aard van de gasstroming in dergelijke mate dat de *zone met terugstroom* in de uitlaatlijn van het gas opvallend smaller wordt. De ring in de uitlaatlijn waardoor het gas ontsnapt naar de omgeving wordt breder waardoor de gassnelheid in de uitlaatlijn afneemt. De berekeningen leren ook dat het bed dichtgepakt is, met fracties aan vast materiaal die de waarden voor een (nagenoeg) volledig gepakt bed benaderen. Simulaties en experimenten worden onder semi-batch voorwaarden uitgevoerd. De slipsnelheid tussen beide fazen is hoog, waardoor vlotte massa- en warmteoverdracht zeer waarschijnlijk zijn. Ook dit laatste maakt de GSVU een waardevol alternatief voor procesintensifiëring.

Het bed dat in de vortex eenheid gevormd wordt, blijft zeer stabiel bij toenemend gasdoorvoer. Simulaties worden uitgevoerd voor deeltjes van verschillende materialen en met verschillende diameters om het hydrodynamisch gedrag van de GSVU grondig te analyseren en begrijpen. Een GSVU wervelbed roteert sneller wanneer de deeltjes lichter zijn. Voor een gegeven gasdoorvoer vermindert de centrifugaalkracht op een lichter deeltje minder dan de meesleuringskracht, waardoor het bed minder sterk naar de wand geduwd wordt. De weerstand tegen de roterende beweging van de lichtere deeltjes veroorzaakt door wrijving van de deeltjes met de wand vermindert, waardoor de deeltjessnelheid toeneemt. Maar, daar de gasdoorvoer constant gehouden wordt voor simulaties met lichtere en zwaardere deeltjes, zullen de hogere snelheden van lichte deeltjes de slipsnelheid tussen beide fazen doen afnemen. Dit beperkt dan weer procesintensifiëring door afname van massa- en warmte-overdracht eenbed van lichtere eeltjes. Een afname van de diameter van de deeltjes resulteert mogelijk ook in een wijziging van het regime van fluïdisatie van dichtgepakt bed naar bubbelbed. De verhouding van meesleurings- tot centrifugaal kracht wijzigt voor kleinere deeltjes, met de vorming van gasbellen in het bed tot gevolg. Toename van het gasdebiet in een gefluïdiseerd wervelbed in het zwaartekrachtveld leidt uiteindelijk tot meesleuring van de deeltjes. In de vortex eenheid daarentegen zal het wervelbed dichter gepakt worden naarmate de gasdoorvoer toeneemt. Deze overwegingen suggereren dat stromingsregime mappen voor een vortex eenheid zullen verschillen van de mappen in het zwaartekrachtveld.

Er kan besloten worden dat de voornaamste voordeel van een vortex eenheid het feit is dat processen met zowel één-fase als meer-fase fluïdisatie kunnen intensifiëren. Procesintensifiëring in een vortex eenheid omvat een toename van de doorvoer, een afname van de het reactorvolume, de vorming van een stabiel wervelbed zonder meesleuring van deeltjes en, tenslotte, een toename van massa- en warmte-overdracht door een toename van de slipsnelheid tussen de verschillende fazen.

Summary

Process intensification is a recent focal point for chemicals and energy industry in order to build more energy-efficient and more compact processes. A process intensified technology may signicantly increase the product yield, improve the company's carbon footprint or may reduce equipment costs by combining separate operations in one device. In this context, harnessing the centrifugal force in a reactor geometry can be considered one of the main process intensification methodologies. The centrifugal force can be generated by rotating the reactor vessel. However, a more novel technique can be to azimuthally inject a gas from slots along the circumferential wall of a stationary disc-shaped geometry thereby creating a swirling flow inside the unit. This unit, referred to as the Vortex Unit is the main topic of interest in the presented work. One of the most interesting features of the vortex unit is that the aspect ratio of the geometry is less than 1, giving it a thin disc-like shape. The proximity of the walls in the geometry may generate certain complex secondary flow features which are crucial for understanding the potential of the vortex unit as a process intensification device.

One of the challenges that the vortex unit presents is its susceptibility to experimental intrusive measurement techniques. Measurement through a non-intrusive technique such as the Particle Image Velocimetry can also be limited in scope due to visibility issues as will be discussed in the following text. Hence, a proper numerical investigation of the vortex unit can prove highly beneficial in discerning its internal hydrodynamics. The presented work uses the commercial finite-volume package FLUENT® for building a numerical framework which can be used for investigating the vortex unit flow.

The thesis can broadly be divided in two sections. In the first section, a single-phase gas flow is studied in the vortex unit, regarded in this case as the Gas Vortex Unit (GVU). The simulations for the single-phase GVU are carried out using the Reynolds Stress Modeling approach for turbulence modeling and hence can accurately capture the secondary flows arising in the geometry.

When the gas is introduced from the injection slots in the device, a swirling flow structure is established in the unit. The azimuthal velocity of the gas increases with decreasing radius, until the gas

reaches the central unidirectional exhaust. Inside the exhaust region, due to large axial velocity gradients, the swirling tendency of the gas reduces resulting in a gradual decrease in the azimuthal velocity, until it becomes zero at the axis of the unit. As the swirling flow approaches the central exhaust through diminishing surface area, the radial velocity of the gas is also expected to increase with decreasing radius. However, the simulations show interesting secondary flows appearing in the unit with respect to the radial through flow in the unit, as a consequence of the proximity of the end-walls of the unit.

In the bulk flow of the unit, the radially inward pressure gradient is balanced by the outward centrifugal force acting on the gas elements. In the boundary layers close to the end-walls of the unit, this balance between the two forces break as the azimuthal velocity of the gas drops to zero because of no-slip boundary condition. The unbalanced radial pressure gradient “pushes” the gas radially outwards near the walls resulting in the formation of the *near-wall jets* in the GVU. The jets remain confined to the close proximity of the end-walls, due to the high Reynolds number of the flow. The jets initially gain strength as they proceed inside the unit from the circumferential wall but gradually lose strength as they gradually approach the central exhaust.

The presence of the axially elongated exhaust and the near-wall jets generate two secondary flows in the GVU. As the gas leaving the unit, swirls through the central exhaust line, wall friction results in a decay in its swirl strength. This generates a reverse pressure gradient in the exhaust line, causing ambient gas to be sucked into the unit from the exhaust outlet. This results in the formation od an extended *backflow* region along the exhaust of the unit. Inside the main disc-part of the unit, the near-wall jets entrain the inflowing gas flowing through the bulk of the GVU. At high degree of swirl in the unit, the jet entrainment flow rate may exceed the incoming gas flow rate, resulting in a second recirculation region inside the disc part of the unit. This recirculation region, formed of two counter-rotating vortices is referred to as the *counterflow*. Both the backflow and the counterflow complicate the flow topology of single phase flow in the GVU. The flow topology is found to be highly sensitive to the degree of swirl in the unit, compared to the Reynolds number of the flow. The range of gas flow rates suitable for the industrial GVU application is so high that the flow becomes independent of the

Reynolds number. The presence of the counterflow and backflow in the GVU results in multiple stagnation points in a high velocity flow, thereby suggesting the possibility of significantly enhancing the mixing capability in such a device. This intense mixing potential in the GVU can be used for process intensification of processes such as combustion.

When solid particles are introduced in the vortex unit, the flow topology changes significantly. The swirling structure of the gas is significantly reduced as most of the injected gas azimuthal momentum is transferred to the solids which start rotating in the geometry. As the centrifugal force of the solids are high due to their higher density the solids are pushed radially outwards near the circumferential wall of the unit where they form a dense rotating solids bed. The vortex unit, referred to as the Gas Solid Vortex Unit for particulate flow, now acts as a *centrifugal fluidized bed.* With increasing gas flow rate the amount of azimuthal momentum transferred to the solids also increases, thereby increasing the centrifugal force acting on them. This sets the contrast of the GSVU with the conventional gravitational fluidized bed , where the force of gravity is constant and cannot be manipulated through geometry design. One of the major advantages of such a technology is that the gas flow rates used for fluidization can be increased to significantly higher values as compared to the gravitational beds, where particle elutriation would have resulted. Also, absence of any mechanically moving parts makes the GSVU a worthy contender with respect to the industrial rotating packed beds which include mechanically rotated geometries prone to mechanical abrasion. The two-phase GSVU simulations are carried out using an Eulerian-Eulerian framework, by which the gas and the solids are treated as interpenetrating continua. The Eulerian simulations though unable to resolve the flow characteristics of particle groups or individual particles, provides an excellent qualitative description of the entire bed dynamics at relatively lower computational costs.

The inclusion of particles in the GSVU significantly reduces the pressure drop over the unit in comparison to the single-phase flow. This pressure drop behavior is highly interesting as it is counter-intuitive when compared to the traditional fluidization technologies. The inclusion of solids breaks the swirl structure in the GSVU flow such that the backflow region generated in gas-only flow diminishes resulting in more surface area for the gas to leave the unit. The simulations show that the rotating solids bed in the GSVU is dense in nature with solids fractions reaching as high as that of packed beds. Moreover, as the solids are retained in the unit, the high radial gas flow velocity through the bed provides a significantly high slip velocity between the two phases. The high slip velocity may in turn result in higher heat and mass transfer between the two phases, thus highlighting for the first time the process intensification capacity of the GSVU.

The solids bed formed in the vortex unit is found to be highly stable with respect to increased gas flow rates. Different density solids and varying diameter particles are considered in the simulations next to understand the GSVU bed behavior for different materials. The GSVU solids bed is found to rotate faster for lighter solids material. The lighter solids are pressed less strongly to the circumferential wall while rotating and hence the friction opposition to rotation is reduced increasing their velocities. However, as the gas flow rate is kept the same, higher velocities in the case of lighter solids indicates a reduction in slip velocity and a reduction in the process intensification capacity. Reducing the size of the particles may result in a shift in the fluidization regime from dense to bubbling behavior. The local drag to centrifugal force balance is disturbed when particle size is reduced causing the formation of the bubbles in the solids bed. Increasing the gas flow rate in the gravitational bubbling fluidized bed causes particle elutriation. However, in the GSVU, increasing the gas flow rate increases the centrifugal force on the particles causing the bed to revert back to its dense form. This last result highlights the significant difference between the two fluidization technologies and the need to generate alternate flow regime maps for the vortex unit fluidization. It is thus concluded that one of the main benefits of the vortex unit is its potential to intensify both single phase and fluidization processes. Process Intensification through the use of the vortex unit technology takes place though a reduction in the reactor volume or via increased heat and mass transfer rates.

List of symbols

A_P	cross-sectional area of a particle (m^2)
D_E	GVU exhaust diameter downstream (m)
D_{Ew}	GVU exhaust diameter at the front wall (m)
D_R	GVU circumferential wall diameter (m)
d_p	particle diameter (m)
e	dissipation rate of turbulent kinetic energy [GSVU] (m^2/s^3)
e_{ss}	restitution coefficient
F_c	cumulative centrifugal force over bed (N)
F_d	cumulative radial drag force over bed (N)
f	cyclostrophic ratio function
G_M	gas flow rate (Nm^3/s)
g	acceleration due to gravity (m/s^2)
L	GSVU length (m)
I_O	slot width (m)
k	turbulent kinetic energy (m^2/s^2)
Ma	Mach number
P	gas pressure (Pa)
P_{gauge}	static gauge pressure (Pa)
P_{scaled}	scaled gauge gas pressure
ΔP_{bed}	bed pressure drop (Pa)
Q	cumulative normalized gas flow rate
r	radial position (m)
$r_{normalized}$	normalized radial position
Re	Reynolds number
S	swirl ratio

S_{in}	injection swirl ratio
U	mean gas velocity (m/s)
U_{slip}	slip velocity (m/s)
$U_{,slot}$	mean slot injection velocity (m/s)
$U_{r,\ normalized}$	normalized mean radial gas velocity
$U_{\theta,\ scaled}$	scaled mean azimuthal gas velocity
u'	fluctuating gas velocity component (m/s)
$\overline{u_i' u_j'}$	Reynolds stress (N/m^2)
V_P	volume of a particle (m^3)
V_T	total volume of particles (m^3)
z	axial position (m)

Greek symbols (for single phase GVU flow)

γ	injection slot angle (deg)
δ	boundary layer thickness (m)
ε	dissipation rate of turbulent kinetic energy [GVU] (m^2/s^3)
μ	gas viscosity (Pa s)
ρ	gas density (kg/m^3)
ω	angular velocity (rad/s)
θ	angular coordinate (rad)
τ	wall shear stress (N/m^2)

Greek symbols (for two phase GSVU flow)

β	gas-solid drag coefficient (kg/m^3 s)
δ	angle of internal friction (deg)
ε	volume fraction
$\varepsilon_{s,max}$	maximum packing limit solids volume fraction

γ	dissipation of granular temperature due to collisions (kg/m s^3)
λ_s	solids bulk viscosity (Pa s)
μ	granular viscosity (Pa s)
μ_{col}	solid phase collisional viscosity (Pa s)
μ_{fr}	solid phase frictional viscosity (Pa s)
μ_{kin}	solid phase kinetic viscosity (Pa s)
φ	specularity coefficient
Θ	granular temperature (J/kg)
ρ	phase density (kg/m^3)
θ	angular coordinate (rad)
τ	wall shear stress (N/m^2)

Subscripts

g	gas phase
s	solid phase
t	turbulent
col	collisional
fr	frictional
kin	kinetic
c	circumferential wall
e	end-wall

Glossary

Axial velocity: particle or gas velocity in the axial direction, z, defined as $u_z = \frac{dz}{dt}$.

Azimuthal velocity: particle or gas velocity in the azimuthal direction, θ, defined as $u_\theta = \frac{d\theta}{dt}$.

Radial velocity: particle or gas velocity in the radial direction, r, defined as $u_r = \frac{dr}{dt}$.

Near-wall jets: radial velocity peaks originated in the boundary layer region close to the end-walls of the GVU, resulting from the imbalance between the outward centrifugal force and the inward pressure gradient on gas elements.

Backflow: secondary axially directed recirculation region created in the gas exhaust line, near the axis of the GVU formed due to the adverse pressure gradient due to swirl decay in the exhaust line.

Counterflow: secondary radially directed recirculation region created in the disc part of the GVU, generated as a result of the entrainment of the bulk gas by the near-wall jets.

Cyclostrophic balance: balance between the radial pressure gradient and the centrifugal force per unit volume for incompressible swirling gas flow in the GVU, formed due to the radial gas velocity component being significantly smaller than the azimuthal gas velocity component, simplifying the radial momentum balance to $\frac{\partial P}{\partial r} = \frac{\rho_g u_{g,\theta}^2}{r}$.

Channeling: flow behavior of the rotating solids bed in the GSVU characterized by axial non-uniformity, where gas and particles form two separate axial layers and gas bypasses the solids.

Freeboard: volume of the disc part of the GSVU between the central gas exhaust and the edge of the solids bed, with a significantly reduced solids fraction.

Particle entrainment: flow pattern observed in the horizontal-axis of the GSVU where the radially inward drag force exerted by the gas on the particles overcomes the centrifugal force acting radially outwards, causing the particles to leave the unit with the gas through the central exhaust.

Stable bed: rotating fluidized bed in semi-batch operation with neither slugging nor channeling nor particle fall-out nor particle entrainment. The inner edge of the bed is clearly defined.

Solids capacity: bed mass of the GSVU.

Swirling flow: flow with spiraling pattern and a high azimuthal to radial velocity ratio.

Superficial gas velocity: theoretical gas velocity when the total circumferential area of the GSVU is considered for the gas flow; if G_M is the total gas mass flow rate through the GSVU, the superficial gas velocity at the radial position r is defined as $u_{g,superficial} = G_M/2\pi rL$, being L the length of the GSVU.

Chapter 1

Introduction

1.1 Introduction

An increasing global energy demand and a continuous rise in the atmospheric CO_2 levels due to burning of fossil fuels have brought the sustainability of the present energy production processes for the chemical industry under the limelight[1]. According to the International Energy Association projections, the world energy needs will increase by more than 30% by 2040, as compared to 2016[2]. However, the primary and conventional sources of energy production in the form of fossil fuels are not equally distributed across nations. This may result in an energy import cost escalation in several countries and may negatively affect its Gross Domestic Product (GDP). For instance, Europe currently imports nearly 50% of its oil and gas, which may escalate to 55% by 2035[3]. Moreover, the continued dependence on fossil fuels for energy and power generation results in higher carbon emissions, causing the global temperatures to rise. A severe global warming is already showing its havoc impact by amplifying resource scarcity and causing severe natural disasters in several parts of the world[4]. The year 2015 was officially declared by NASA as the hottest year since recorded times and the trend continues in 2016[5].

A major part of this energy demand comes from the chemicals manufacturing industry[6]. In 2011, the world chemicals turnover was valued at 2744 billion Euro[7]. The European Union contributes 20% to these global sales. In the United States alone, almost 14,000 manufacturers in the chemical industry transform raw materials into more than 70,000 different compounds for every-day use. The daily manufacturing of such amount of chemical products requires a huge amount of energy. Figure 1.1 highlights the remarkable contribution of the present day chemical industry in consuming fossil fuels such as petroleum and natural gas. Innovations in the chemical production sector are required to develop novel, carbon-neutral, energy conservative state-of-the-art technologies, which should help lower the industrial carbon footprint. Process Intensification (PI), targeted towards applications in the chemical industry, plays a significant role in this aspect.

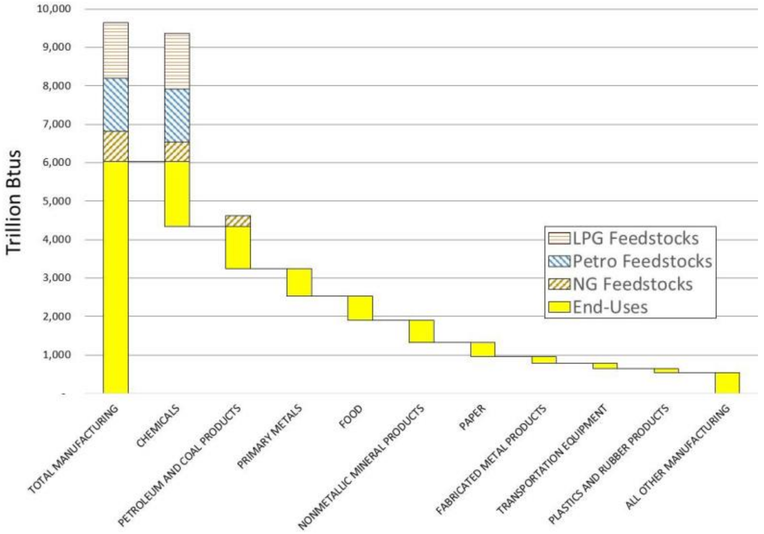

Fig. 1.1. Feedstock consumption by the Top 10 energy consuming manufacturing sectors, adopted from “US Department of Energy Process Intensification Report”, 2007.

PI involves combining different unit operations such as reaction and separation into a single equipment resulting in a more efficient, cleaner, and economical manufacturing process[6]. In the chemical industry, PI can aim at significantly enhancing the mixing process, which would result in better mass and heat transfer, reaction kinetics and yields. These improvements may help to achieve an overall decrease in the number of equipment or process complexity, thereby reducing the operational cost and risk in chemical manufacturing facilities. Ramshaw[8], one of the initial pioneers of technology, defines PI as a decrease in the size of a chemical plant without compromising on the product output. Stankiewicz[9] later extended the definition to include any chemical process improvement which results in a significant reduction of the size of reactors, increases in energy efficiency and/or production capacity, or in a remarkable reduction of waste production[9]. Gerven and Stankiewicz[10] provide the following four basic guiding principles for PI:

- Maximizing the effectiveness of intra-molecular and inter-molecular events (example: dynamically changing conditions to attain kinetic regimes with higher conversion and selectivity)
- Providing all molecules the same process experience (example: plug flow reactor with uniform, gradient-less heating)
- Optimizing the driving forces at all scales and maximizing the specific surface areas to which they apply (example: increase transfer surface area through micro-channel designs)
- Maximize synergistic effects from partial processes (example: affecting reaction equilibrium by removing products where and when they are formed)

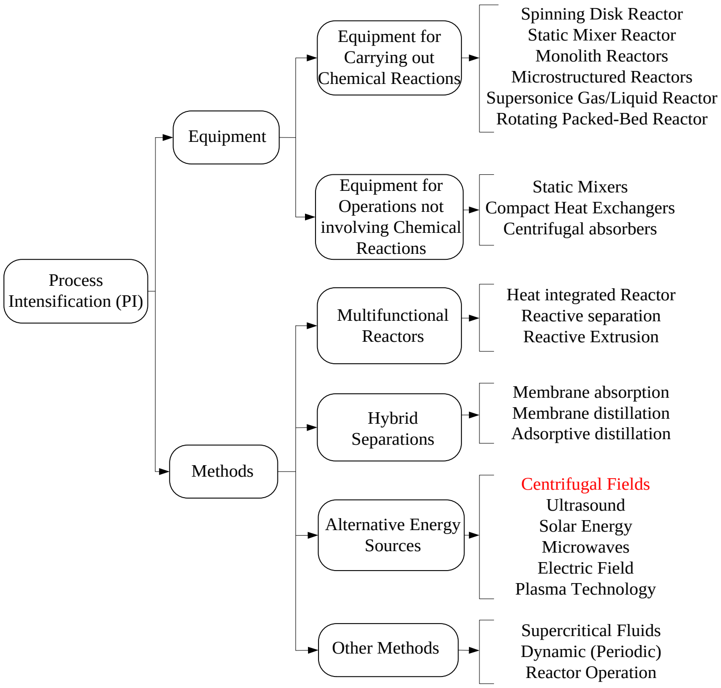

Fig. 1.2. Process Intensification options, adopted from “European Roadmap for Process Intensification”, 2007.

Based on these guidelines, various pathways for achieving PI in industry have been chalked out in the European Roadmap for PI, 2007 as shown in Figure 1.2[11]. The focus of the work presented in this thesis is to investigate the feasibility of using *centrifugal fields* for PI of chemicals manufacturing processes.

The use of centrifugal force in chemical reactor design for PI has been well documented in literature[12,13]. The purpose of adding a centrifugal force to a reactor geometry and its constituents is mainly to improve multiphase mixing and increase the mass and heat transfer efficiency. The centrifugal force can reach much higher values than its gravitational counterpart and can be fine-tuned according to the specific industrial requirements. This helps high throughput applications and multi-component mixing. Additionally, the secondary flows generated in such highly swirling flows result in a high turbulence thus achieving a more rigorous heat and mass transfer in the device. As a result, the conversion and yields of certain favorable products can be significantly increased by suppressing phenomena such as the formation of dead-zones and hot-spots[14]. A centrifugal force can be induced in a number of ways: using different types of stirrers[15,16], by rotating the overall reactor geometry along a central axis[17,18] or by employing a fluid to establish a swirling flow in a stationary geometry[19-21]. The present work focuses on the last mentioned technology, where a swirling fluid flow field is established in a *stationary* disc-shaped (unit length-to-diameter aspect ratio < 1) Vortex Unit by injecting a gas through azimuthally inclined periodic slots placed along the circumferential wall of the disc. The operating principle of single phase and multiphase Vortex Units is briefly discussed next.

1.2 Gas/Gas-Solid Vortex Unit – Operating Principle

A Vortex Unit comprises of a disc-shaped stationary geometry confined on opposite sides by two flat end-walls, as shown in Figure 1.3. The axis of the vessel can be oriented either horizontally or vertically. A series of multiple equidistant vanes are located along the entire circumferential wall of the unit (Figure 1(a)). The narrow rectangular gap in between two consecutive vanes forms an injection slot, through which the gas is sent into the geometry in an azimuthally inclined manner. This high-speed angular injection of the gas generates a swirling vortex flow structure in the unit, while the gas elements gradually proceed radially inwards towards the central, axially-aligned gas exhaust located on one of the end-walls of the unit. Thus the flow in the Vortex Unit predominantly resembles the *annular vortex-sink* type of flow[22].

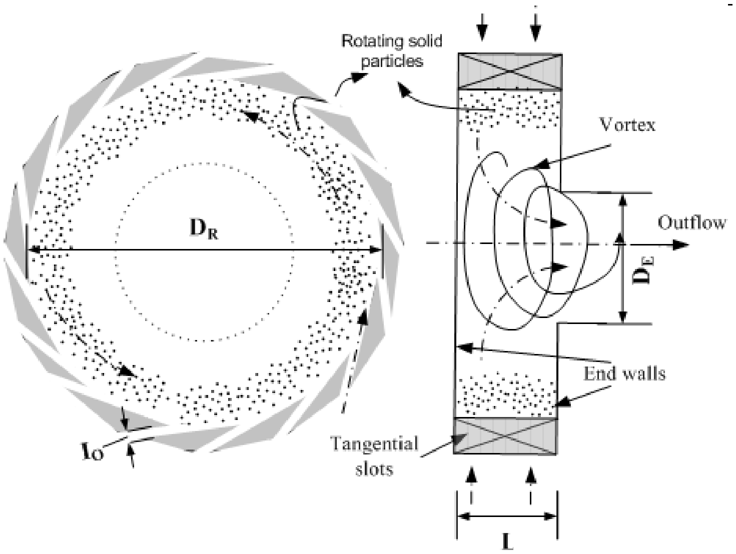

(a) (b)

Fig. 1.3. Schematic view of a Gas-Solid Vortex Unit (GSVU) with multiple injection slots and a horizontal axis of rotation. D_R = diameter of the chamber, L = length of the unit, D_E = axial discharge diameter, I_O = width of the gap between two consecutive vanes, constituting the injection slot thickness; (a) front view and (b) side view.

Solids can be introduced in the unit through the injection slots along with the gas feeding. If the particle size becomes larger than the slot thickness, a separate solids inlet, placed in one of the end-walls of the unit, may be used. As soon as the particles enter the geometry, the swirling gas imparts an azimuthal momentum to the particles. The solids start to rotate and the centrifugal force generated pushes them closer to the circumferential wall, resulting in the formation of a dense rotating annular solids bed. Depending on the solids feeding mechanism, the GSVU can be operated in a continuous mode with solids removal, or in a semi-batch mode, in which the solids feeding stops when a given mass of solids is fed to the unit. In theory, an individual particle will be *retained* in the vessel, whenever the centrifugal force, F_C, acting on it, is equal or higher than the radial drag force, F_D. A higher drag force will result in particles entrainment via the central exhaust of the unit. The mathematical representation of the force balance on a single particle is given by:

$$F_C = F_D \tag{1.2}$$

$$\frac{\left(\frac{U_S^2}{D_R}\right)\rho_p\left(\pi d_p^3\right)}{3} = \frac{C_d\left(\pi d_p^2\right)}{4} U_g^2 \rho_g \tag{1.3}$$

where,

Us = Azimuthal velocity of particle, m/s

D_R = Diameter of the path of the rotating particle, m

d_p = Particle diameter, m

ρ_p , ρ_g = Density of solid and gas, respectively, kg/m^3

U_g = Radial velocity of the gas around a particle, m/s

C_d = Drag coefficient, -

The GSVU is thus a *rotational analogue* of the gravitational gas-solid fluidized bed. In a gravitational fluidized bed, the particles are suspended by a balance between the gravitational force, acting downwards and the upward drag force, exerted by the gas flowing past the particles.

The force of gravity cannot be manipulated by altering the operating conditions of the fluidized bed, such as, eg, the gas flow rate. However, since increasing the gas flow to a GSVU increases the azimuthal momentum input and thus the azimuthal momentum transferred to the solids as well, the centrifugal force can be tuned. Moreover, as the centrifugal force considerably exceeds the gravitational force, higher gas velocities can be achieved in the GSVU than in a gravitational fluidized bed, for similar particle dimensions. Furthermore, the slip velocity (~1-10 m/s) in a GSVU, is high as compared to gravitational fluidized beds (Ashcraft et al., 2012). The same remark can be made for the solids volume fraction (~0.3-0.6) (Kovacevic et al., 2014). As a result, compared to gravitational fluidized beds, the GSVU offers advantages such as high gas throughput and a uniform, dense solids bed, which is useful for better gas-solid contacting and more efficient heat and mass transfer[23]. The latter enables the overall geometry to be more compact and results in intensification of the fluidization process at particle scale as well as reactor scale. The application of these unique characteristics enables the GSVU to qualify as a PI technology in petrochemical and cleanchem applications[21].

1.3 Literature review

A Vortex Unit can be used both in single phase and multiphase modes of operation. As it will be seen in subsequent sections, the hydrodynamics for the two modes significantly differ from each other. The presence of solids disrupts the swirl structure of the gas and important secondary flow features of single phase flow are lost. Hence, in order to elaborate on the cold flow literature on the Vortex Unit, it naturally follows to present a separate literature review for the Gas Vortex Unit (GVU) and the Gas Solid Vortex Unit (GSVU).

1.3.1 GVU hydrodynamics

Unconfined vortex flow phenomena have traditionally been studied in literature to understand the working principle behind natural events such as formation of tornadoes[24]. In the past fifty years, research interest on *confined* vortex flows has gained limelight. The presence of walls bounding a vortex flow in a confined space can severely alter the vortex hydrodynamics through the formation of secondary flows and consequently, the turbulence and mixing patterns[25,26]. The secondary flow features can be manipulated into a wide spectrum of applications such as vortex amplifiers[27], stable flame generation[28], vortex diodes[29] and nuclear rocket propulsion[30]. Taylor[31] first demonstrated that confining swirling flows by end-walls can result in secondary flows in the geometry due to boundary layer formation. Under given operating conditions, a major section of the gas throughput in the unit is limited to the boundary layers close to the unit end-walls. Under these conditions, the presence of high velocity gradients close to the end-walls induces high shear in the boundary layers and may significantly enhance processes such as liquid atomization[31]. Rietema and Krajenbrink[32] mathematically investigated the confined vortex hydrodynamics in geometries with a length to diameter ratio lower than 1. They demonstrated that the swirling flow inside the unit geometry resembles a free-swirl structure, that is, the azimuthal gas velocity increases with decreasing radius. However the hyperbolic radial profile of the azimuthal velocity, found in free-swirl flow, is lost due to end-wall friction. The authors also demonstrated that a complete azimuthal flow symmetry can be achieved by increasing the number of equidistant gas injection slots along the circumferential wall of the unit. The initial application of the free-swirl flow structure in a gas Vortex Unit dates back to the 1960s when the National Aeronautics and Space Administration (NASA) applied the design in a nuclear rocket propulsion mechanism[33]. It was postulated that, if a mixture of light and heavy gasses is sent through a Vortex Unit, where the heavy gas contains the dispersed nuclear fission material and the lighter gas acts as a propellant, the outward centrifugal force, developed in such a device, will retain the heavier fissioning material within the unit. The lighter propellant gas, driven by a radially-inward pressure gradient, will diffuse towards the central exhaust, carrying off the enormous fission reaction heat produced. This heat can then be converted into pressure energy in the exhaust, providing the thrust necessary for rocket propulsion. Thus a GVU can be used to significantly increase the propulsion efficiency of rockets. Another important application of the gas Vortex Unit was postulated almost parallelly, in the later part of the 1950s, for magneto-hydrodynamic power generation[34,35]. The primary idea was that it would help in efficient heat removal from nuclear reactors. The thermal energy of the nuclear reaction is to be converted to kinetic energy of a flowing gas. In the next step the kinetic energy of the gas can be converted to electrical energy by bringing it into contact with a rotating ionic liquid in a vortex chamber. The intense mixing of the two phases and the high throughput of the device make the energy conversion process significantly more efficient. Subsequent studies were carried out focusing on the operating conditions and geometric parameters on which the secondary flows in the Vortex Unit depend. Through an analytical investigation, it was found that the mass flow through the end–wall boundary layers can be appreciably high for both compressible and incompressible flows[36]. The analytical models which were formulated to describe the GVU flow needed experimental validation. Through a comprehensive series of Laser Doppler Anemometry (LDA) and pitot tube measurements of the velocity distribution in a confined Vortex Unit, Savino and Keshok experimentally confirmed the presence of secondary flows[30]. However, the effect of gas flow rate and geometrical parameters on the boundary layer flow was not investigated. Later studies revealed that the aspect ratio of the unit (length-to-diameter ratio of the unit) has a strong influence on the secondary flows[37]. The overall effect of the end-walls, being restricted mostly in the span of the boundary layers, tends to decrease with increasing aspect ratio of the geometry. The secondary flows in the GVU indicate the presence of high-shear regions, and hence may affect the flow turbulence. Experimental studies confirmed this conjecture by showing that the secondary flows in the bulk and the near-wall boundary layers in the Vortex Unit are indeed highly turbulent in nature[34]. It was shown that the turbulence level resulting from a multi-point fluid injection over the circumferential wall was significantly greater than for a single-point injection. The higher level of turbulence was attributed to the thinner boundary layers close to the end-walls of the unit, resulting in regions of intense shear in the near-wall flow. Several mathematical formulations of the near-wall flow, secondary flows and turbulence followed in an attempt to capture the complete hydrodynamics of the GVU. A momentum integral analysis for the swirling flow in the GVU was carried out to decipher the interaction between the potential flow in the bulk of the GVU and the turbulent boundary layer. A shear law which bears resemblance with the Prandtl boundary layer theory over a flat plate was developed, with a correction factor accounting for swirling flow[38]. In another study, the fluid velocities in the boundary layers were expressed in terms of a power series, where the coefficients were determined by the wall and injection boundary conditions[39]. This helped to mathematically obtain an expression for the quantity of fluid flowing though the boundary layers or retained in the secondary flow structures in the Vortex Unit.

A further elaborate mathematical analysis was carried out using dimensionless swirl and discharge coefficients to characterize the secondary flow and boundary layers in the GVU[40]. Hashimoto and

Matsuya[41] continued the experimental study on the GVU and demonstrated the efficiency of the unit in separating gas-liquid mixtures. The authors demonstrated the capability of gas-liquid segregation in the GVU since the liquid having higher centrifugal force acting on it, can be separated from the gas phase and can be collected from the circumferential wall while the gas flows out through the central exhaust. Claypole and Syred[42] experimentally demonstrated that secondary flows, such as a counter vortex formed near the central exhaust of the GVU, can be used to produce highly stable flames for natural gas combustion. The authors found that a recirculation region developed near the exhaust of the unit when a high degree of swirl was introduced in the flow through the unit. The recirculation brought the burnt gases back into the center of the reaction region, resulting in an increased combustion efficiency. Later research empirically determined the size of this recirculation region as a function of the ratio of the unit-to-exhaust diameter and found it to be independent of the gas flow rate but dependent on the degree of swirl in the geometry[43]. The near-wall boundary layer flow in the GVU also found an interesting application when it was demonstrated that these near-wall boundary regions of high shear, high velocity flow can be efficiently used for effective heat transfer from the walls of the unit to the gas[26]. The main throughput in the GVU takes place near the end-walls of the unit. In order to understand the working mechanism of this hydrodynamic phenomenon, LDA measurements in the bulk flow region of the unit between the two end-walls were carried out[44]. A significant recirculation zone was observed in the core of the main unit. This zone causes the gas to flow in the radially outward direction in the core, causing the entering gas to split in two streams flowing close to the end-walls. However, no physical reasoning explaining the presence of this counterflow region was provided. The work also highlighted the difference in accuracy in the experimental measurements in the bulk flow and close to the end-walls of the unit. The near-wall velocity measurements significantly differed from previous analytical results. Intrusive measurement techniques such as pneumatic probes were shown to disturb the local flow and to decrease experimental accuracy[45].

Hence, all the experimental techniques mentioned above suffer from measurement limitations wither due to influencing local flow or due to the geometrical constrains of the unit. The near-wall boundary layers are so thin at the operating Reynolds numbers (Re), that measurement techniques such as LDA and Particle Image Velocimetry (PIV) suffer from near-wall reflections and are not capable of capturing the phenomena. Hence, the need for sophisticated computational fluid mechanics tools in discerning the GVU hydrodynamics became clear around the early 2000s[45,46]. Initially, simple two-parameter Reynolds averaged turbulence models such as the k-ε family of models were used to capture the turbulence and secondary flows in the GVU, as these models were computationally less demanding[45]. However, the presence of a high degree of stress anisotropy in the GVU flow due to strong streamline curvature necessitated the implementation of the more sophisticated Reynolds Stress Model (RSM)[25,29,47]. Though RSM is computationally more demanding and uses approximately 50%-60% more CPU time and 15%-20% more memory when compared to the two-parameter k-ε model, it was found to yield significantly better results than both the k-ε and Re Normalization Group (RNG) k-ε models when compared with LDA data. Recent research of GVU flow has also implemented more detailed turbulence modeling such as Large Eddy Simulation (LES)[48]. However, the computational cost for LES when compared to RANS models is very high. To perform a more accurate LES, a finer mesh should be used in the wall-dominated GVU flow. LES usually works to determine hydrodynamics when the flow is governed by large turbulent vortices, which can be captured by a comparatively coarser mesh. However, since the near-wall boundary layers are important for GVU flow, LES will require a much finer mesh for accurate flow predictions in the near-wall regions and will significantly blow up the computational demand[46]. Keeping this point under consideration the RANS modeling approach is adopted in the present work.

1.3.2 GSVU Hydrodynamics

Suspending a rotating bed of solids in a cylindrical unit by means of an azimuthal injection of gas was initially proposed as early as the 1960's by Kerrebrock and Meghblean[33]. Since then, research activities have been carried out by different research groups, testing the concept of rotating solids bed to enhance multiphase heat and mass transfer for a wide range of applications, such as colloid core nuclear rocket propulsion[49], coal combustion[50], vortex scrubber for removal of flue gases[51], distillation[18], fine particle coating[52], biomass pyrolysis[53]. However, in spite of their distinct features and advantages, gas-solid vortex type devices are relatively unknown in chemical process industry. The lack of a well-developed and already established theory describing the hydrodynamics, as well as a poor analysis of operational challenges for vortex devices, such as creating a stable flow field of the secondary phase and overall scale-up/down of a unit, have caused this reluctance in industrial adoption of the technology. Hence, the focus of the present work is to explore various flow characteristics of a Gas-Solid Vortex Unit (GSVU). But, prior to a main literature review, a short discussion on a reactor largely comparable to the GSVU, that is the Rotating Fluidized Bed (RFB) reactor, is given. As the RFB reactors have been more implemented in the chemical industry, well-established theories can be found in literature.

The concept of an RFB was proposed more than 30 years ago[54]. RFB operates by the same principle as the GSVU, i.e. using a centrifugal force to retain particles in a cylindrical unit. However, the centrifugal field is established by mechanically rotating the unit using a motor attached to it. The particles in the RFB are set in a rotating motion, generating the necessary centrifugal force to push the particle layers radially outwards[55]. The particle bed acquires an azimuthal velocity, which is assumed to be equal to that of the rotor and can thus be controlled arbitrarily. The fluidizing gas is introduced radially through the porous surface of the unit’s circumferential wall. Increasing the gas flow rate increases the fluidizing gas superficial velocity, resulting in the transformation of the packed rotating solid bed into a radially fluidized solid bed. In principle, the balance of the radially outward oriented centrifugal force exerted on the particles and the radially inward oriented drag force exerted by the fluidizing gas, results in fluidization. As soon as the centrifugal force exerted on the solid bed is higher than the radial drag force, the rotating solid bed becomes packed. The described phenomena are analogous to those in gravitational fluidized beds, wherein, at a given superficial velocity, the entire solid bed in a packed state, suddenly becomes fluidized. The advantage of the RFB over its gravitational counterpart is that the centrifugal force, determined by the particles’ azimuthal velocity, and the drag force, exerted on the particles and determined by the gas-solid radial slip velocity, can be controlled independently in RFBs. Initial studies on the RFB technology studied both packed and fluidized beds in a rotating vessel separately[20]. In the experiments, Geldart-B and Geldart-D particles were observed to give bubbling fluidization in a centrifugal field[20]. The first efforts to theoretically describe and validate the RFB mode of operation were performed during the first half of the 1980s[56,57]. Based on the experimental results on minimal fluidization conditions and on pressure drop over the bed, a model for the incipient fluidization was proposed. Both experimental results and simulated values showed that the pressure drop over the bed increases with increasing superficial velocity of the fluid. At a critical fluidization velocity, the pressure drop across the bed reaches its maximum and then decreases when the superficial fluid velocity further increases above that critical value. Chen[55] proposed a fundamental theory based on a local momentum balance, resulting in the concept of layer-by-layer fluidization. Fluidization of rotating beds is initiated when centrifugal and drag force are balanced. Given that these forces are a function of the radial coordinate, they cannot balance each other at all radial positions for a given gas flow rate. Hence, fluidization of rotating beds will take place layer-by-layer starting from the edge of the bed and moving towards the circumferential wall of the reactor chamber. The gas velocity at which fluidization at the inner layer of the bed is initiated is called minimum fluidization velocity, while the gas velocity for which the whole of the bed is fluidized is referred to as critical fluidization velocity. Contrary to previous literature[57], several researchers, using the model proposed by Chen, showed that beyond the critical fluidization velocity, the pressure drop over the bed remains constant when further increasing the fluid flow[58,59]. When the bed is fully fluidized, bubbling behavior was reported and it was shown that particles can behave differently in the gravitational and in a centrifugal field[60]. Particles observed to behave like Geldart-A particles in the gravitational field can shift to Geldart-B particle behavior in a centrifugal field. Correspondingly, Geldart-C particles shift to Geldart-A particle behavior. Geldart-B particle behavior was studied experimentally and computationally and it was concluded that the solids bed loses its dense homogenous form and bubbling takes place in the bed[61]. Moreover, it was reported that fluidization regimes in RFBs change from a fixed bed to a partially fluidized bed and to a partially bubbling bed with increasing gas flow rate. When the gas flow rate keeps being increased the bubble distribution in the bed is observed to become uniform. Finally turbulent fluidization is reached. Even though the fluidization behavior of RFBs is quite extensively studied, particle velocities have not been reported, as particles are supposed to rotate with the same velocity as the motor-driven rotating vessel.

Although RFBs offer high possibilities for PI, their applications are limited to small-scale set-ups [62,63]. RFBs are not very attractive for use on industrial scale, because a rotating vessel with its moving parts suffers from severe limitations caused by vibrational and other mechanical issues[64]. In contrast to RFBs, in Gas Solid Vortex Units (GSVU) the centrifugal force is established in a static vessel by tangentially introducing the fluid through the cylindrical circumferential wall of the unit. Momentum transfer from the fluid to the particles makes the latter rotate. The fluid leaves the reactor through a central exhaust. Most of the advantages of RFBs over gravitational beds remain valid in the GSVUs. Additionally, there is no rotor and hence no mechanically moving parts, which makes the GSVU a lucrative option for PI in fluidization technology[21,49,65,66]. These advantages have made GSVUs efficient for multiple applications in chemical[51,67,68], heat transfer[49,69] and drying technologies[14,70]. The GSVU was studied computationally by several researchers indicating several possibilities for PI[23,53,71].

Of course GSVUs present disadvantages as well. Compared to RFBs where the vessel is rotating, the walls of GSVUs are static. Hence significant friction is caused between the static walls and the rotating particles and fluid. Furthermore, in GSVUs the azimuthal and radial velocities cannot be controlled independently. As a result, a change in fluid flow will affect both the centrifugal force and the drag force.

Although the GSVU concept is known and utilized, fundamental experimental studies of GSVUs are scarce. The use of different vortex chambers and the effects of the aspect ratio (exhaust to reactor diameter) on Vortex Unit behavior were investigated, and it was found that the aspect ratio should be in the range of 0.3 to 0.5[70]. It is also mentioned that the ratio of the axial reactor length and the reactor diameter should be less than 0.5. Furthermore, it was shown that the tangential inlet slots should be uniformly distributed over the circumferential wall[70]. Using X-rays, the flow behavior at various solid loadings was studied. The angular velocity of the rotating flow was measured at different radial positions, using 20 µm talc particles[49]. It was reported that by introducing just a few grams of powder, the rotational velocity in the vortex chamber significantly decreases. Moreover, a strongly non-uniform particle bed was observed at low solids capacities. A sufficient solids capacity was needed to obtain a well-defined fluidized bed. Theoretical and experimental research on the Vortex Unit aerodynamics, heat and mass transfer using 2-5 mm diameter wheat grains were also carried out[14,72]. The axial profile of radial velocity was simultaneously investigated, in particle-free and particulate flow[72]. It was observed that the non-uniformity in axial direction reduces when particles are present. High heat transfer coefficient values between gas and the grains were reported. Finally, it was shown that processes in vortex chambers can be intensified several times as compared to gravitational reactors[72]. The efficiency of drying can be increased by 45%, while drying expenditures can be reduced by 10%. A theoretical model based on local force and mass balances to calculate solids capacities in Vortex Units was suggested for both horizontal and vertical axis vortex chambers with one or more tangential inlets[73]. The comparison of the calculated solids capacities showed that for the same operating conditions the solids capacity of the horizontal axis GSVU is twice higher than that of the vertical axis GSVU. Additionally, the solids capacity in a horizontal axis GSVU can be increased by raising the gas flow rate, whereas in the vertical axis unit the solids capacity remained almost constant. Investigation on the radial and tangential fluidization behavior of a bed of Geldart-B particles showed that at lower bed mass, channeling is observed, while at higher bed mass, bubbling is found to be the main type of fluidization[74]. For Geldart-D particles both channeling and slugging were observed. With increasing solids capacity, a dense, stable and uniform bed is formed. The influence of a rotating chimney on the bed behavior was experimentally investigated using different types of particles[75]. Different reactor designs, changing the reactor diameter and number of inlet slots were studied. It was concluded that increasing the number of inlet slots has a positive effect on the bed fluidization[65]. The influence of the azimuthal slot thickness and the particle diameter and density on the bed behavior were aso investigated[76,77]. It was reported that a minimum solids capacity is required in order to obtain a stable rotating bed. Below that minimum bed mass, slugging and channeling was observed, a result which agrees with previous observations in literature[21]. The importance of the azimuthal injection slots height was also explored using FCC particles and 6 mm slot openings. A stable rotating bed could not be established[76]. By decreasing the slot opening to 2 mm and thus increasing the gas injection velocity for the same volumetric gas flow rate, a stable rotating bed was formed. The slot height has a huge influence on the maximum solids capacity as well. By decreasing the slot height, the maximum solids capacity increases. Dvornikov and Belousov used a cylindrical, a conical and a hybrid vortex chamber to investigate the heat and mass transfer processes[78]. Using Laser Doppler Anemometry to measure azimuthal velocities the authors showed that the particle velocity is a bit lower near the end-walls than in the center. It was shown experimentally that Geldart-C particles, which are difficult to fluidize under gravitational conditions, can be fluidized in a GSVR as they start behaving like Geldart-A particles in the gravitational field[79].

The GSVU literature is very limited in terms of the analysis of reacting flows, mainly because even the non-reacting bed dynamics are still not fully understood. There are many industrial processes that rely on multiphase contact and thus are potential candidates for GSVU implementation. Several important industrial chemical processes that may benefit are adsorption processes, gas-phase polymerization, biomass pyrolysis, biomass/coal gasification, and fast catalytic partial oxidation of hydrocarbons. Quite recently, a detailed computational study of fluid catalytic cracking in a GSVU[71,80] was performed. These papers highlighted the potential processes that could benefit from the GSVU technology and briefly discussed the process intensification potential. Gasification or pyrolysis of biomass to fuels or chemicals is another application in which GSVU technology may provide specific benefits. The performance of the GSVU as a candidate for biomass pyrolysis was recently computationally assessed to explore its PI abilities[53]. The product distribution from biomass pyrolysis between 450 and 500°C was reported and compared with traditional fluidization technologies. Calculated convective gas/solid heat transfer coefficients were shown to be 3 to 5 times higher than in non-rotating fluidized reactors.

1.4 Scope of the work

The present work aims at understanding the single phase and multiphase hydrodynamics in the Vortex Unit. A series of experimentally validated Computational Fluid Dynamics (CFD) simulations using the commercial finite volume package FLUENT® 14a are used to investigate the various primary and secondary flow features occurring in the Vortex Unit. Alongside the simulations, some theoretical aspects of the GSVU are also discussed in order to explain the origin of the various flow features observed in the unit and possible ways to quantify and characterize the flow. An overview of the work is presented below.

Chapter 2 provides a detailed numerical study of the cold-flow GVU, that is available in the Laboratory for Chemical Technology and that is used in the present study. The three-dimensional numerical model and the solution technique are elaborately discussed and model verification with experimental data obtained from the cold-flow setup is also included. A novel explanation regarding the formation of near-wall jets is provided. A three-dimensional visualization of the jets is attempted, combining the numerical simulations and an experimental oil flow visualization technique.

The formation of secondary flows in the GVU is studied next in *Chapter 3*. Axisymmetric simulations of the Vortex Unit reveal that recirculation regions develop both in the disc part and the exhaust line of the unit. The numerical model is used to investigate the origin of these secondary flows. An experimental Particle Image Velocimetry (PIV) technique is used to validate the observations obtained from the simulations.

Introducing the solids in the Vortex Unit significantly alters the flow topology. The gas-solid two phase flow is numerically studied in *Chapter 4*. To investigate the solids bed hydrodynamics in the GSVU, a three dimensional Eulerian-Eulerian numerical model is constructed. After validation with experimental PIV data, the model is used to investigate flow features such as unit pressure drop, bed voidage and solids velocities. The effect of gas flow rates, particle diameter and solids density on the fluidization is also studied.

Finally, in *Chapter 5* the thesis conclusions are discussed and recommendations for future work are made. A dimensional analysis of the Vortex Unit is briefly discussed to help future researchers in deriving scaling laws for the unit.

1.5 References

1. Stuchtey M. Growth within: A circular economy vision for a competitive Europe. 2015.

2. http://www.iea.org/newsroom/news/2016/november/world-energy-outlook-2016.html.

3. 2016: An Energy Outlook. British Petroleum. 2016.

4. Klein N. This changes everything: capitalism vs. climate. Simon and Schuster Paperbacks, New york. 2014.

5. http://www.nasa.gov/press-release/nasa-noaa-analyses-reveal-record-shattering-global-warm-temperatures-in-2015.

6. Process intensification – chemical sector focus technology assessment: United States Department Of Energy Information Agency; 2015.

7. Facts and figures 2012, the European chemicals industry in a worldwide perspective. CEFIC Chemical Engineering Council. 2012.

8. Ramshaw C. The incentive for process intensification. Paper presented at: 1st International Conference on Process Intensification for Chemical Industry; 1995; BHR Group, London.

9. Stankiewicz AI, Moulijn, JA. Process intensification: transforming chemical engineering. Chemical Engineering Progress. 2000;96(1):22-33.

10. Van Gerven T, Stankiewicz AI. Structure, energy, synergy, time - the fundamentals of process intensification. Industrial & engineering chemistry research. 2009;48(5):2465-2474.

11. Intensification ERfP. Creative-Energy;2011.

12. Visscher F. Liquid-liquid processes in spinning disc equipment. The Netherlands, Eindhoven University of Technology. 2013.

13. Visscher F, van der Schaaf J, Nijhuis TA, Schouten JC. Rotating reactors; A review. Chemical Engineering Research and Design. 2013;91(10):1923-1940.

14. Volchkov EP, Terekhov VI, Kaidanik AN, Yadykin AN. Aerodynamics and Heat and Mass Transfer of Fluidized Particle Beds in Vortex Chambers. Heat Transfer Engineering. 1993;14(3):36-47.

15. Tan IH, Stankiewicz AI, Moulijn JA. Performance of the monolithic stirrer reactor: applicability in multi-phase processes. Chemical Engineering Science. 2004;59:4975 – 4981.

16. Patwardhan AW, Joshi JB. Design of stirred vessels with gas entrained from free liquid surface. The Canadian Journal of Chemical Engineering. 1998;76(3):339-364.

17. Liu HS, Lin CC, Wu SC, Hsu HW. Characteristics of a Rotating Packed Bed. Industrial & Engineering Chemistry Research. 1996;35(10):3590-3596.

18. Rao DP, Bhowal A, Goswami PS. Process Intensification in Rotating Packed Beds (HIGEE): An Appraisal. Industrial & Engineering Chemistry Research. 2004;43(4):1150-1162.

19. Lewellen WS. A review of confined vortex flows: NASA. 1971; CR-1772.

20. Kroger DG, Abdelnour G, Levy EK, Chen JC. Centrifugal fluidization: effects of particle density and size distribution. Chemical Engineering Communications. 1980;5(1-4):55-67.

21. De Wilde J, de Broqueville A. Rotating fluidized beds in a static geometry: Experimental proof of concept. AIChE Journal. 2007;53(4):793-810.

22. Goldshtik M, Hussain F. Analysis of inviscid vortex breakdown in a semi-infinite pipe. Fluid Dynamics Research. 1998;23:189-234.

23. Ashcraft RW, Kovacevic J, Heynderickx GJ, Marin GB. Assessment of a Gas–Solid Vortex Reactor for $SO_{2/}$NOx Adsorption from Flue Gas. Industrial & Engineering Chemistry Research. 2013;52(2):861-875.

24. Sinkevich OA. A model of the flow in tornado vortex in view of phase transitions. Teplofizika vysokikh temperatur. 1996;34(6):936-941.

25. Vatistas GH, Fayed M, Soroardy JU. Strongly Swirling Turbulent Sink Flow Between Two Stationary Disks. Journal of Propulsion and Power. 2008;24(2):295-301.

26. Volchkov EP, Semenov SV, Terekov VI. Heat transfer and shear stress at the end wall of a vortex chamber. Experimental Thermal and Fluid Science. 1991;4(5):546-557.

27. Bain D. Vortex Amplifier. Heavy Current Fluidics: Course held at the Department of Fluid dynamics, October 1970. Vienna:47-56.

28. Syred N, Beér JM. Combustion in swirling flows: A review. Combustion and Flame. 1974;23(2):143-201.

29. Pandare A, Ranade VV. Flow in vortex diodes. Chemical Engineering Research and Design. 2015;102:274-285.

30. Savino JM, Keshock EG. Experimental Profiles of Velocity Components and Radial Pressure Distributions in a Vortex Contained in a Short Cylindrical Chamber. 1965;TN D-3072.

31. Taylor GI. The boundary layer in the converging nozzle of a swirl atomizer. The Quarterly Journal of Mechanics and Applied Mathematics. 1950;3:129-139.

32. Rietema K, Krajenbrink HJ. Theoretical derivation of tangential velocity profiles in a flat vortex chamber-influence of turbulence and wall friction. Applied Scientific Research, Section A. 1959;8(1):177-197.

33. Kerrebrock JL, Meghreblian RV. Vortex Containment for the Gaseous-Fission Rocket. Journal of the Aerospace Sciences. 1961;28(9):710-724.

34. Donaldson CD. The magnetohydrodynamic vortex power generator, basic principles and practical problems. Paper presented at: Proceedings of the Second Symposium on the Engineering Aspects of Magnetohydrodynamics; 1961; Philadelphia, USA.

35. Williamson GG, McCune JE. A preliminary study of the structure of turbulent vortices: Aeronautical Research Association of Princeton Incorporated. 1961;32.

36. Anderson OL, Utch CT.. Theoretical Solutions for the Secondary Flow on the End Wall of a Vortex Tube: Defense Technical Information Center. 1961; AD-0223952.

37. Lafferty JF. Two-phase vortex flow, University of Michigan; 1967.

38. Wormley DN. An Analytical Model for the Incompressible Flow in Short Vortex Chambers. Journal of Basic Engineering. 1969;91(2):264-272.

39. Kwok CCK. Vortex flow in a thin cylindrical chamber and its application in fluid amplifier technology. Montreal: Department of Mechanical Engineering, McGill University; 1966.

40. Farag EA. An investigation of the confined vortex flow of liquids. Montreal, Canada, Sir George Williams University; 1971.

41. Hashimoto H, Matsuya T. Characteristics of Gas-liquid Centrifugal Separation in a Short Vortex Chamber. Bulletin of JSME. 1983;26(211):64-71.

42. Claypole TC, Syred N. The effect of swirl burner aerodynamics on NOx formation. Symposium (International) on Combustion. 1981;18(1):81-89.

43. Vatistas GH, Lin S, Kwok CK. Reverse flow radius in vortex chambers. AIAA Journal. 1986;24(11):1872-1873.

44. Kostin NA. A short swirl chamber. Journal of Engineering Physics and Thermophysics. 1995;68(5):673-677.

45. Volchkov EP, Dvornikov NA, Lebedev VP, Lukashov VV. The investigation of vortex chamber aerodynamics. Paper presented at: Science and Technology, KORUS '99, The Third Russian-Korean International Symposium; 1999.

46. Wegner B, Maltsev A, Schneider C, Sadiki A, Dreizler A, Janicka J. Assessment of unsteady RANS in predicting swirl flow instability based on LES and experiments. International Journal of Heat and Fluid Flow 2004;25(3):528-536.

47. Anderson M, Valenzuela R, Bonazza R, Chiaverini M, Rom C. Vortex Chamber Flow Field Characterization for Gelled Propellant Combustor Applications. 39th AIAA/ASME/SAE/ASEE Joint Propulsion Conference and Exhibit: American Institute of Aeronautics and Astronautics; 2003.

48. Cheng JC, Olsen MG, Fox RO. A microscale multi-inlet vortex nanoprecipitation reactor: Turbulence measurement and simulation. Applied Physics Letters. 2009;94(20):204104.

49. Anderson LA, Hasinger SH, Turman BN. Two-Component Vortex Flow Studies of the Colloid Core Nuclear Rocket. Journal of Spacecraft and Rockets. 1972;9(5):311-317.

50. Lee JK, Hu CG, Shin YS, Chun HS. Combustion characteristics of a two-stage swirl-flow fluidized bed combustor. The Canadian Journal of Chemical Engineering. 1990;68(5):824-830.

51. Loftus PJ, Stickler DB, Diehl RC. A Confined Vortex Scrubber for fine particulate removal from flue gases. Environmental Progress. 1992;11(1):27-32.

52. Watano S, Nakamura H, Hamada K, et al. Fine particle coating by a novel rotating fluidized bed coater. Powder Technology. 2004;141(3):172-176.

53. Ashcraft RW, Heynderickx GJ, Marin GB. Modeling fast biomass pyrolysis in a gas-solid vortex reactor. Chemical Engineering Journal. 2012;207:195-208.

54. Levy EK, Martin N, Chen J. Minimum Fluidization and Startup of a Centrifugal Fluidized Bed, Fluidization. Cambrige: Cambridge University Press; 1979.

55. Chen YM. Fundamentals of a centrifugal fluidized bed. AIChE Journal. 1987;33(5):722-728.

56. Takahashi T, Tanaka Z, Itoshima A, Fan LT. Performance of a rotating fluidized bed. Journal of Chemical Engineering of Japan. 1984;17(3):333-336.

57. Fan LT, Chang CC, Yu YS, Takahashi T, Tanaka Z. Incipient fluidization condition for a centrifugal fluidized bed. AIChE Journal. 1985;31(6):999-1009.

58. Kao J, Pfeffer R, Tardos GI. On partial fluidization in rotating fluidized beds. AIChE Journal. 1987;33(5):858-861.

59. Zhu C, Lin CH, Qian GH, Pfeffer R. Modeling of the pressure drop and flow field in a rotating fluidized bed. Chemical Engineering Communications. 2003;190(9):1132-1154.

60. Qian G-H, B´gyi In, Pfeffer R, Shaw H, Stevens JG. Particle mixing in rotating fluidized beds: Inferences about the fluidized state. AIChE Journal. 1999;45(7):1401-1410.

61. Nakamura H, Watano S. Numerical modeling of particle fluidization behavior in a rotating fluidized bed. Powder Technology. 2007;171(2):106-117.

62. Saunders JH. Particle entrainment from rotating fluidized beds. Powder Technology. 1986;47(3):211-217.

63. Wong WY, Lu Y, Nasserzadeh VS, Swithenbank J, Shaw T, Madden M. Experimental investigation into the incineration of wool scouring sludges in a novel rotating fluidised bed. Journal of Hazardous Materials. 2000;73(2):143-160.

64. Zhang W. A Review of Techniques for the Process Intensification of Fluidized Bed Reactors. Chinese Journal of Chemical Engineering. 2009;17(4):688-702.

65. Dutta A, Ekatpure RP, Heynderickx GJ, de Broqueville A, Marin GB. Rotating fluidized bed with a static geometry: Guidelines for design and operating conditions. Chemical Engineering Science. 2010;65(5):1678-1693.

66. Ekatpure RD, Narote SP. Ocular Detection for Biometric Recognition. 2013 Ieee Second International Conference on Image Information Processing (Iciip). 2013;5:644-648.

67. Kuzmin AO, Pravdina MK, Yavorsky AI, Yavorsky NI, Parmon VN. Vortex centrifugal bubbling reactor. Chemical Engineering Journal. 2005;107(1–3):55-62.

68. Ryazantsev AA, Malikov AS, Batoeva AA, Faddeenkova GA. Liquid-phase oxidation of hydrogen sulfide in centrifugal bubbling apparatus. Russian Journal of Applied Chemistry. 2007;80(9):1544-1548.

69. Dickson P, Drawbaugh D. An engineering study of the colloid fueled reactor concept. 6th Propulsion Joint Specialist Conference: American Institute of Aeronautics and Astronautics; 1970.

70. Kochetov LM, Sazhin BS, Karlik EA. Experimental determination of the optimal ratios of structural dimensions in the whirl chamber for drying granular materials. Chemical and Petroleum Engineering. 1969;5(2):106-108.

71. Trujillo WR, De Wilde J. Computational Fluid Dynamics Simulation of Fluid Catalytic Cracking in a Rotating Fluidized Bed in a Static Geometry. Industrial & Engineering Chemistry Research. 2010;49(11):5288-5298.

72. Volchkov EP, Dvornikov NA, Yadykin AN. Characteristic Features of Heat and Mass Transfer in a Fluidized Bed in a Vortex Chamber. Heat Transfer Research. 2003;34(7&8):13.

73. Sazhin BS, Kochetov LM, Belousov AS. Retention capacities and flow patterns of vortex contactors. Theoretical Foundations of Chemical Engineering. 2008;42(2):125-135.

74. De Wilde J, de Broqueville A. Experimental investigation of a rotating fluidized bed in a static geometry. Powder Technology. 2008;183(3):426-435.

75. De Wilde J, de Broqueville A. A rotating chimney for compressing rotating fluidized beds. Powder Technology. 2010;199(1):87-94.

76. Ekatpure RP, Suryawanshi VU, Heynderickx GJ, de Broqueville A, Marin GB. Experimental investigation of a gas-solid rotating bed reactor with static geometry. Chemical Engineering Process. 2011;50(1):77-84.

77. Pantzali MN, Kovacevic JZ, Heynderickx GJ, Marin GB, Shtern VN. Radial pressure profiles in a cold-flow gas-solid vortex reactor. AIChE Journal. 2015;61(12):4114-4125.

78. Dvornikov NA, Belousov PP. Investigation of a fluidized bed in a vortex chamber. Journal of Applied Mechanics and Technical Physics. 2011;52(2):206-211.

79. Eliaers P, de Broqueville A, Poortinga A, van Hengstum T, De Wilde J. High-G, low-temperature coating of cohesive particles in a vortex chamber. Powder Technology. 2014;258:242-251.

80. Rosales Trujillo W, De Wilde J. Fluid catalytic cracking in a rotating fluidized bed in a static geometry: a CFD analysis accounting for the distribution of the catalyst coke content. Powder Technology. 2012;221:36-46.

Chapter 2

On near-wall jets in a disc-like Gas Vortex Unit

This work was published as:

On near-wall jets in a disc-like Gas Vortex Unit

Kaustav Niyogi[1], Maria Torregrosa[1], Maria N. Pantzali[1], Vladimir N. Shtern[2], Geraldine J. Heynderickx[1] and Guy B. Marin[1]

[1]Ghent University, Laboratory for Chemical Technology, Technologiepark 914, B-9052, Gent, Belgium

[2]Shtern Research and Consulting, Houston, TX 77096, USA

Abstract

To clarify the three-dimensional structure of near-wall jets observed in disc-like gas vortex units, experimental and numerical studies are performed. The experimental results are obtained using Particle Image Velocimetry (PIV), Laser Doppler Anemometry (LDA), pressure probes and surface oil flow visualization techniques. The first three techniques have been used to investigate the bulk flow hydrodynamics of the vortex unit. Surface oil flow visualization is adopted to visualize streamlines near the end-walls of the vortex unit. The surface streamlines help determine the azimuthal and radial velocity components of the radial near-wall jets. Simulations of the vortex unit using FLUENT® v.14a are simultaneously performed, computationally resolving the near-wall jet regions in the axial direction. The simulation results together with the surface oil flow visualization establish the three-dimensional structure of the near-wall jets in gas vortex units for the first time in literature. It is also conjectured that the near-wall jets develop due to combined effects of bulk flow acceleration and swirl. The centrifugal force diminishes in the vicinity of the end-walls. The radially inward pressure gradient in these regions, no longer balanced by the centrifugal force, pushes gas radially inward thus developing the near-wall jets.

Keywords:

Gas Vortex Unit, Near-wall Jets, Surface Oil Flow Visualization, Computational Fluid Dynamics, Swirling flow between parallel discs

2.1 Introduction

The development of near-wall jets in accelerating swirling flows in confined static geometries has been a topic of research for many decades[1,2]. An example of confined accelerating flow is found in the gas vortex unit (GVU). GVUs are a basic part of a wide variety of devices such as cyclone separators[3,4], vortex valves[5], Ranque-Hilsch tubes[6], nuclear rocket propellers[7] and gas vortex reactors[8,9]. A GVU is a stationary flow domain confined by two normal-to-unit-axis parallel flat discs, the end-walls, and by a lateral circumferential wall, as shown in Fig. 1(a-b). Gas is introduced through a series of azimuthally inclined rectangular injection slots along the circumferential wall (Fig. 1(a)). The radially converging flow results in a spatial acceleration of the radial velocity in the radial direction, due to a gradual decrease in cross-sectional circumferential flow surface area. The azimuthally inclined slots impart a strong azimuthal component to the injection gas velocity. This establishes a swirling flow structure inside the vortex unit. The gas leaves the unit through the axial (unidirectional/bidirectional) exhaust(s), centrally located in the end-wall(s). As will be shown later in the manuscript (Fig. 4), the rotating gas elements experience a “free-swirl” behavior in the disc part of the GVU, where the azimuthal gas velocity increases with decreasing radius resulting in a spatial acceleration of the azimuthal velocity as well. In such a flow condition, it has been observed that the radial velocity profile along the height of the unit at a particular radius from the central axis becomes non-uniform and shows two peaks near the end-walls[10], schematically shown in Fig. 1(c). Though in the GVU flow domain, the azimuthal velocity is the dominant velocity, nonetheless these near-wall peaks of the radial velocity present an interesting flow phenomenon and are regarded as the near-wall jets in the GVU. The gas elements close to the end-walls are “pushed” towards the exhaust and hence complete lesser turns inside the disc part of the GVU, as schematically shown in Fig. 1(d). The swirling flow inside the vortex unit can be characterized by (i) the injection swirl ratio (S_{in}) defined as the ratio of the azimuthal to the radial injection velocity component, and (ii) the Reynolds number (Re) with the gas injection velocity and the chamber half-length, that is half the distance between the end-walls, as the characteristic velocity and length scale[10]. Anderson[11] provided a comprehensive literature study on vortex flow devices for a large range of Re and S_{in} values. The present work focuses on GVU flow with S_{in}= 5.5 and Re of the order of $1x10^5$, values typical for industrial applications.

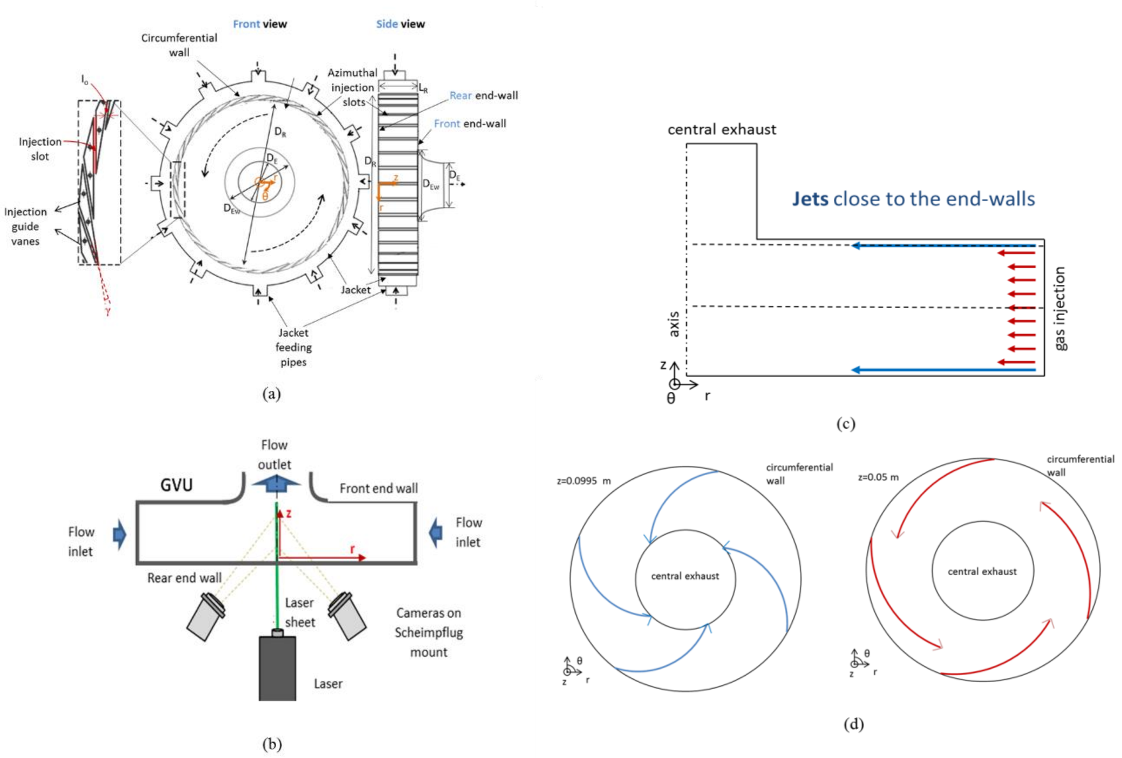

Fig. 1.(a) Schematics of the front and side view of the experimental pilot-scale GVU. (b) Schematics of the experimental Stereo PIV configuration on a side view of the GVU. Dimensions are provided in Table 1. (c) Schematic of the near-wall jets along an azimuthal plane in the GVU. (d) Schematic of velocity direction at different axial planes in the GVU, showcasing the effect of near-wall jets.

Given these values of S_{in} and Re, GVU flow is highly swirling and turbulent[12]. In accelerating swirling flows, the end-walls greatly affect the gas flow profile and turbulence inside the unit. As the gas flows inwards through the GVU, the circumferential flow surface area gradually decreases with decreasing radius, resulting in flow acceleration and a nearly uniform velocity distribution in the normal-to-flow direction as observed in converging channel flow[13]. However, the presence of swirl causes overshoots in the radial velocity component near the end-walls for $S_{in} > 1$, giving rise to the near-wall jets in the GVU[14]. Due to the jets, the radial velocity profile over the length of the GVU becomes non-uniform for moderate values of Re.

Hornbeck[14] showed that with increasing Re, the end-wall boundary layers become thinner and have less effect on the bulk flow. Consequently, at higher Re the radial velocity profile in the bulk of the unit was found to be uniform. However, for $S_{in}> 4$, a local flow reversal in the radial velocity was observed in the bulk of the unit. The aspect ratio (radius to length of the unit) was varied from 5 to 10. It was observed that the higher the aspect ratio, the narrower the geometry becomes, and the higher is the effect of end-wall jets on the bulk flow in between the discs.

For high-Re flow ($Re > 10^5$), the distance from the jet peak to the end-wall is about 1% of the GVU length[12]. Hence the near-wall jets are formed very close to the end-walls. As a result, the experimental resolution of the near-wall jets becomes a major challenge for highly turbulent GVU flows. Initially the experimental studies on GVU flow were carried out using pressure probes and pitot tube techniques[15,16]. However, the measured radial pressure and azimuthal velocity profiles were no more than suggestive for the presence of the jets near the end-walls. Kendall[17] was the first to observe the presence of near-wall jets by measuring the radial velocity profile along the length of the GVU using a flattened pitot tube technique. In spite of measuring radial velocity overshoots near the end-walls, the technique failed to resolve the entire jet region. Donaldson[18] and Williamson and McCune[19] used a combination of hot wire anemometry, yaw probe and pitot tube to obtain quantitative radial and azimuthal velocity data inside the unit. However, the probes failed to span the entire length of the unit due to mechanical construction limitations.

Savino and Keshock[10] presented the most reliable experimental work to date to measure radial and azimuthal velocity profiles over the length of a confined vortex unit. Savino and Keshock[10] performed a detailed experimental study using modified pitot tubes and yaw probes which revealed two striking flow features: (a) the radial peak jet velocity is one order of magnitude larger than the superficial radial velocity and (b) the peak is located so close to the end-wall that the peak-to-wall region cannot be fully resolved by the applied measuring techniques.

All the experimental techniques mentioned above are intrusive and can thus affect the local flow pattern and cause significant error in the measurement. Singh[20] investigated the bulk flow in a GVU using non-intrusive Laser Doppler Anemometry (LDA). A good understanding of the turbulence intensity of the bulk flow along the GVU end-wall was obtained. However, this technique remained usually restricted to bulk region measurements, due to the reflections from the walls and visual limitations related to the geometry of the unit.

The lack of sufficient experimental data to provide a direct visualization of the near-wall jets in the highly turbulent swirling flow necessitated a detailed numerical study of the GVU flow. The first CFD simulations of a GVU were carried out using a *laminar* flow approximation[14,21]. But the simulations suffered from numerical instabilities, particularly when flow reversal occurred in the central bulk flow of the GVU due to the presence of the jets.

Numerical methods, such as the momentum integral analysis, were also applied to understand the GVU hydrodynamics[5,12]. These methods modeled flow turbulence using an apparent viscosity formulation and failed to capture the turbulence anisotropy in the GVU with its streamline curvature. Singh et al.[22] performed turbulent flow simulations using the two parameter k-ε turbulence model[23] to analyze the GVU flow. Turbulent intensities were calculated to be maximum near the end-walls and to decrease towards the central bulk flow region. Turbulence suppression due to flow acceleration in the vortex unit was calculated and analyzed.

Modeling turbulent anisotropy arising in swirling flows can be challenging and two-parameter eddy-viscosity models may not be adequate. Second-order momentum closure models for turbulence perform better for swirling flows, but must be carefully applied as they may exhibit convergence issues and difficulty in flow predictions such as free-to-forced vortex transition and normal stress distribution in the core of the swirling flow[24]. Vatistas et al.[25] successfully implemented the second-order closure model, the Reynolds Stress Model (RSM)[26] in the GVU geometry, directly computing the Reynolds stresses and thus accounting for turbulence anisotropy in the swirling flow. The numerical and experimental data[10] showed better agreement than two-parameter turbulence models. The simulations demonstrated the capability of Computational Fluid Dynamics (CFD) software like FLUENT® to predict near-wall jets as well as secondary flow phenomena such as the flow reversal in the bulk region of GVU due to the near-wall jets. Though the simulations of Vatistas et al.[25] captured the near-wall jets, being two-dimensional (2D) axisymmetric in nature, could not provide a complete three-dimensional (3D) *visualization* of the observed near-wall jets. Unraveling the physical mechanisms resulting in near-wall jet formation remained incomplete.

The present work provides an in-depth analysis and explanation of the near-wall jet formation in GVUs. To build and support this explanation, the present study involves both experimental and numerical investigations of GVU hydrodynamics. Stereoscopic PIV is applied to gather quantitative data in the bulk flow region of the GVU. The results are cross-verified with 2D LDA data. Once the bulk flow data are acquired, a surface oil flow visualization technique to capture the near-wall jets is applied. Surface film on the transparent rear end-wall of the GVU, formed by tracer oil droplets guided by the flowing gas, allows a proper observation of the near-end-wall flow.

For the numerical simulations FLUENT® v 14.0 is used. Incompressible transient GVU flow is simulated using the RSM turbulence modeling approach. 3D simulations are preferred over 2D axisymmetric simulations, allowing to (i) compare the 3D nature of the near-wall jet formation with experimental data and (ii) to test how well the assumption of axisymmetry in the GVU holds when using azimuthal gas injection slots in the circumferential wall. Using combined numerical and experimental techniques, this paper investigates the origin and nature of near-wall jets in disc-like vortex units.

2.2 Experimental set-up and technique

Fig. 1(a-b) show the schematics of the experimental GVU and the Stereo PIV measurement configuration on a side view of the GVU. The pilot-scale setup is oriented such that the axis of the GVU unit passing through the center of the exhaust is horizontal in direction. Pressurized gas enters the GVU through 36 injection slots along its circumferential wall. The slots are inclined at a 10º angle with respect to the tangent of the circumferential wall. This makes the azimuthal velocity of the inflowing gas significantly higher than the radial and axial velocities. The gas swirls inward in the disc part of the GVU and exits the GVU through the tubular uni-directional exhaust along the central axis. The radii of the circumferential wall and exhaust opening with respect to the central axis are 0.27 m and 0.075 m, while the axial length of the disc part is 0.1 m. Near the exhaust pipe opening, at r=0.1 m, the front end-wall starts making a curvature towards the exhaust pipe. The details of the geometric dimensions of the pilot-scale experimental GVU setup used in the present study can be found in Table 1.

Table 1. Geometrical Dimensions of Experimental GVU

GVU geometrical dimensions:	
GVU circumferential wall diameter	0.54 m
GVU exhaust diameter	0.15 m
GVU length	0.1 m
Number of injection slots	36
Slot width	0.002 m
Slot angle with respect to circumferential wall	10°

Ekatpure et al.[9] and Kovacevic et al.[27] gave a detailed description of the experimental set-up used in this study. In the previous studies of Pantzali et al.[28] and Kovacevic et al.[27,29], two-phase gas-solid flow in the experimental setup was investigated. Two dimensional (2D) Particle Image Velocimetry (PIV) was used to monitor the radial and azimuthal particle velocities in the Gas-Solid Vortex Unit (GSVU).

In the single phase GVU of the current study the 2D PIV is extended to a stereoscopic PIV where two cameras are accurately aligned (Fig. 1b) focusing on a single light sheet. All three velocity components of the tracer particles can thus be captured.

The stereoscopic PIV measurements are done using a dual pulsed Nd: YAG laser (135 mJ, NewWave, LaVision), a set of sheet forming optics(~1.5mm laser thickness) and two CCD cameras. A LaVision Aerosol Generator is used to continuously inject a polydisperse aerosol of Di-Ethyl-Hexyl-Sebacat (DEHS) tracing droplets with a diameter between 0.2-2 μm in the gas feeding pipe, about 2 m upstream of the GVU. For turbulent gas flows, the flow tracking capacity of the tracer is quantified by the Stokes number, that compares the droplet response time with the Kolmogorov time scale of the flow. While the droplet response time is easily calculated from the droplet density, diameter and fluid viscosity; the determination of the smallest viscous scales is usually not easy to quantify precisely. Roughly, the Kolmogorov time scale of the flow can be estimated from the integral length scales of the flow according to the Turbulent Energy Cascade theory, assuming that the dissipation rate in the smallest scales is equal to the turbulent kinetic energy generation from large eddies. In our case, the estimated Stokes number is about 0.008. For the given density ratio, a good response from the oil droplet is expected for Stokes smaller than 0.05[30].

Stereoscopic PIV measurements are performed in 5 different (r,z) locations in a single azimuthal plane, θ=20° (Fig. 3). The angle between the two cameras is changed in between experiments in order to minimize light reflections. In each of the 5 data acquisition areas at least 3 statistically independent data sets of 200 stereoscopic PIV image pairs are acquired, for a mass flow rate of 0.4 Nm^3/s. The rear end wall is carefully cleaned between experiments in order to remove the tracer residues deposited on it, that otherwise would distort the stereoscopic PIV images. The visualization of the tracer droplets in the gas flow is improved using a pre-processing filter that subtracts from the instantaneous images, the time-averaged image, that is, the static background. The stereoscopic PIV processing method consists of a two-step process with a final interrogation window size of 48 x 48 pixels and a 50 % overlap. The particle density in each interrogation window is limited between 6 and 15 tracer droplets. The recorded images have 2 to 5 pixels per particle. The average particle displacement is kept at about 6 pixels. This corresponds to a time lapse from 2 to 5 μs between the images in the stereoscopic PIV pair, depending on the flow rate and the location of the measurement plane. The velocity vector fields are validated using standard velocity range criteria based on an universal outlier detection. Missing vectors are not interpolated. A more detailed description of the stereoscopic PIV measurement and data acquisition technique can be found in the form of supplementary material provided with this study.

When using oil droplets in the gas flow for a period of time much longer than the usual duration of the stereoscopic PIV measurements, eventually some of the tracing droplets stick on the end-walls and slide along them driven by the shear stresses, forming visible surface streamlines. These streamlines become more distinguished when increasing the oil droplet concentration, have been captured by the CCD camera and are compared with the corresponding numerical results. This technique is analogous to the Surface Oil Film Visualization[31,32], usually applied for qualitative visualization of flow patterns close to the surface of a solid body exposed to a gas flow[33]. Further processing of the images by Digital Image Analysis (DIA) is used to calculate of the angles of the surface streamlines.

A limited number of measurements of the azimuthal tracer velocities in the vortex unit is also performed with a 2D Laser Doppler Anemometer (LDA) for validation purposes. More information on the LDA measuring technique can be found in Pantzali et al.[28]. Gauge pressure values are acquired along 12 radial positions inside the GVU. Details on the equipment used can be found in Pantzali et al.[34].

2.3 Numerical technique and solution methodology

FLUENT® v.14a, finite-volume based CFD software, is used to numerically study the flow of a viscous incompressible gas in the GVU. 3D simulations of a 40° section of the complete GVU geometry are performed assuming rotational periodic boundary conditions. Results from initial simulations with the complete geometry but with coarser grid were compared with the 1/8th section (40°) of the GVU. No significant difference was observed in the mean velocity components and pressure drop over the unit. Moreover, previous studies have shown that the presence of multiple (36) injection slots suffices to assure a very uniform gas distribution over the circumference of the geometry[35]. Fig. 2(a) demonstrates this statement by showing the velocity contour lines in a plane at constant axial distance from the sectional GVU simulation. The figure shows that the injected gas develops fast over a small distance from the injection slots both radially and azimuthally, almost before reaching the next injection slot. The azimuthal asymmetry due to the presence of discrete injection slots along the GVU circumferential wall remains confined to the close vicinity of the circumferential wall. The downstream flow becomes axisymmetric. The near-wall jets develop further downstream in the unit and hence are not affected by the local injection asymmetry. The 40° section simulated in the present work includes sufficient number of injection slots (4) to capture this flow development region close to the injection slots of the GVU with reasonable computational cost[8,9,36]. One drawback is that the gravitational force has to be neglected in the sectional simulations of the GVU set-up with horizontal axis, as the gravity force direction changes in each section of the horizontal-axis GVU. Kovacevic et al.[27] have demonstrated that gravity has a minimal effect on the gas flow dynamics at the applied operating conditions.

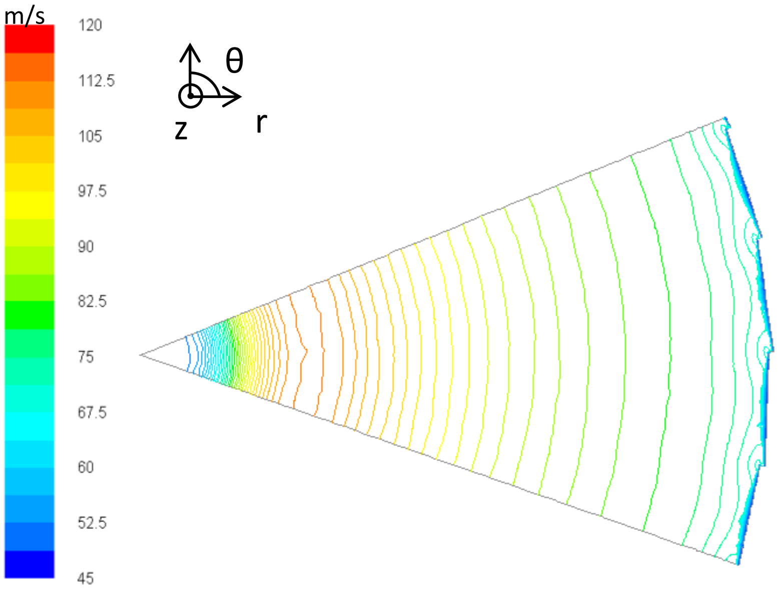

(a)

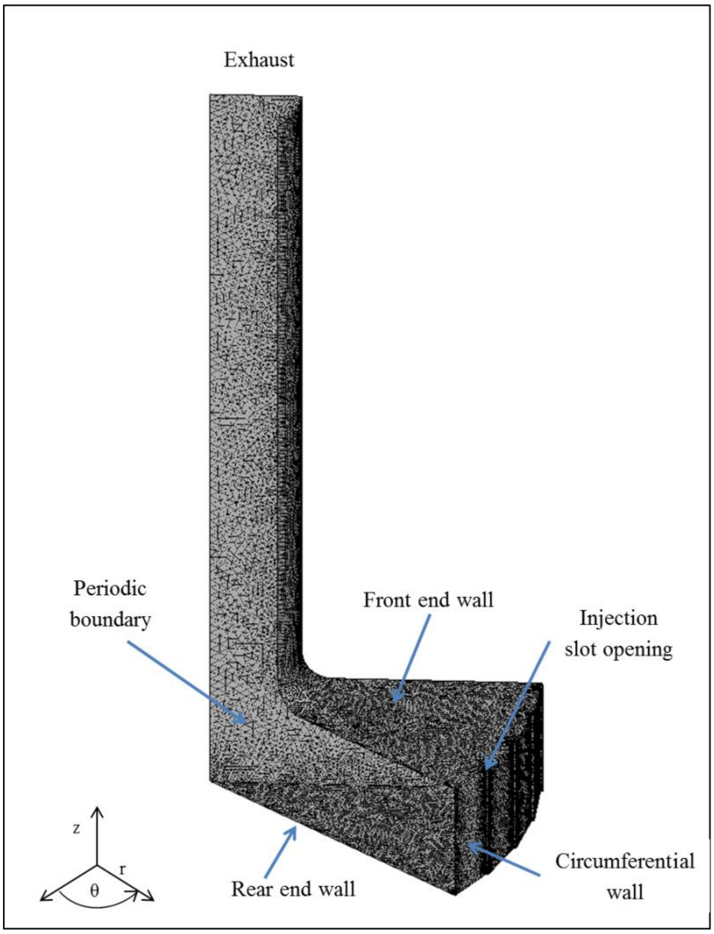

(b)

Fig. 2. (a) Velocity magnitude contour lines along the plane at constant axial position (z=0.05m), from numerical simulation calculated by solving the set of Eqs. (1.1)–(1.4) given in Table 2. (b) Mesh on 40° sectional geometry of GVU with periodic boundary conditions. Dimensions are provided in Table 1.

The reference mesh used, shown in Fig. 2, has approximately 9 million cells with a dimension of 0.5 mm near the gas injection slots and 4 mm near the gas exhaust, and in the bulk flow region between the end-walls. The region near the gas injection slots is more densely meshed because gas velocity gradients are expected to be highest there, and hence involve regions of smallest time and length scales of flow. Layers of 0.05 mm prism cells are used close to the end-walls of the GVU in order to accurately resolve the near-wall boundary layers. Mesh resolution in these regions results in wall y^+ values of the order of 1. Automatic wall treatment is simultaneously used at the walls as a part of the Stress-omega RSM turbulence model, which implies that for the given y^+ values, the near-wall mesh guidelines correspond to enhanced wall treatment accounting for the low-Re variants. Fine meshing near the end-walls is necessary to numerically resolve the near-wall jet region, as experimental techniques such as the PIV and LDA cannot provide enough resolution close to the end walls.

For swirling flows in the GVU with Re of the order of 1×10^5 and S_{in} higher than 0.5, the flow is turbulent[25]. The GVU injection slot angle of 10° in the present study results in values of S_{in} about the order of 5. Thus the flow inside the GVU in the present study is highly turbulent in nature and hence requires proper numerical turbulence modeling. The Reynolds Averaged Navier-Stokes (RANS) turbulence modeling approach is adopted, as the main goal of the present work is to obtain time-averaged GVU hydrodynamics. The Reynolds Stress Model (RSM) is used to model the GVU turbulence by resolving the Reynolds stresses and thus capturing the anisotropic nature of the Reynolds stresses owing to the curved nature of the flow in the GVU. The governing conservation and turbulence model equations are presented in Table 2.

Table 2. Steady-State Transport Equations for GVU Flow

Mass Conservation Equation:	
$\frac{\partial(U_i)}{\partial x_i} = 0$	1.1
Reynolds-averaged Momentum Conservation Equation:	
$\frac{\partial(U_i U_j)}{\partial x_i} = -\frac{1}{\rho}[\frac{\partial P}{\partial x_i} + \frac{\partial\left[\mu\left(\frac{\partial U_i}{\partial x_j} + \frac{\partial U_j}{\partial x_i} - \frac{2}{3}\delta_{ij}\frac{\partial U_i}{\partial x_i}\right)\right]}{\partial x_j} + \frac{\partial\left(-\rho\overline{u_i' u_j'}\right)}{\partial x_j}]$	1.2
Reynolds Stress Equation:	
$\frac{\partial(U_k\overline{u_i' u_j'})}{\partial x_k} = \frac{1}{\rho}\frac{\partial(\frac{\mu_t}{\sigma_k}\frac{\partial(\overline{u_i' u_j'})}{\partial x_k})}{\partial x_k} + \frac{1}{\rho}\frac{\partial[\mu\frac{\partial(\overline{u_i' u_j'})}{\partial x_k}]}{\partial x_k} - \left(\overline{u_i' u_j'}\frac{\partial U_j}{\partial x_k} + \overline{u_j' u_k'}\frac{\partial U_i}{\partial x_k}\right) + \frac{1}{\rho}p\overline{(\frac{\partial u_i'}{\partial x_j} + \frac{\partial u_j'}{\partial x_i})} - \frac{2}{3}\delta_{ij}\varepsilon$	1.3
Dissipation Rate Equation:	
$\frac{\partial(\varepsilon U_i)}{\partial x_i} = \frac{1}{\rho}\frac{\partial}{\partial x_j}\left[\left(\mu + \frac{\mu_t}{\sigma_\varepsilon}\right)\frac{\partial\varepsilon}{\partial x_j}\right]C_{\varepsilon 1}\frac{1}{2}P_{ij}\frac{\varepsilon}{k} - C_{\varepsilon 2}\frac{\varepsilon^2}{k} \quad (\sigma_\varepsilon=1.0, C_{\varepsilon 1}=1.44, C_{\varepsilon 2}=1.92)$	1.4

The governing equations are spatially discretized using third order Monotone Upstream-Centered Schemes for Conservation Laws (MUSCL)[37]. Pressure corrections are computed using the body force weighted Pressure Staggering Option (PRESTO!) scheme[38]. A segregated solver is used for the pressure-velocity coupling following the Semi-Implicit Method for Pressure-Linked Equations (SIMPLE) algorithm[23]. A second order implicit time stepping scheme is used. The time step size during the transient simulations varies from an initial 10^{-6} s to 10^{-3} s as steady state approaches, with 50 iterations per time step. The scaled residuals in mass and momentum balance are set to 10^{-5} as condition for convergence. The simulations are performed on AMD-based Linux 128-core clusters. A dynamic steady state solution for the 3D 40° periodic section requires about 1 week of CPU time. The operating conditions in the GVU, the physical properties of gas and the boundary conditions used are given in Table 3.

Table 3. Physical Properties of Gas and Boundary Conditions

Gas properties and operating conditions:	
Gas mass flow rate	0.4 Nm^3/s
Gas injection velocity at inlet slots	55 m/s
Gas density (25 °C, 101235 Pa)	1.225 kg/m^3
Turbulent intensity at injection slots/ exhaust	5 %
Hydraulic diameter at injection slots	0.004 m
Hydraulic diameter at exhaust	0.2 m

As the main focus of the present work is in the disc part of the GVU, where gas velocities are considerably lower than 0.3 Ma (Mach Number), the simulated flow is considered to be incompressible. No-slip boundary condition is considered at both the end-walls and the circumferential wall of the GVU.

The time-averaged data are exported to Tecplot® v.2015 for post-processing and further analysis. A normal-to-axis plane (z=0.05 m) and an azimuthal plane (θ=20°) are selected for analysis of the simulation results. They are indicated as colored planes in Fig. 3.

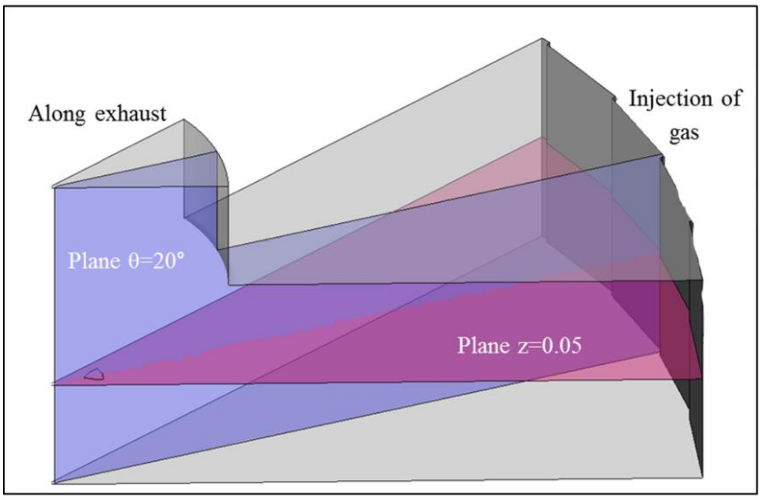

Fig. 3. Different analysis planes in the sectional GVU simulation geometry. Geometrical dimensions are provided in Table 1.

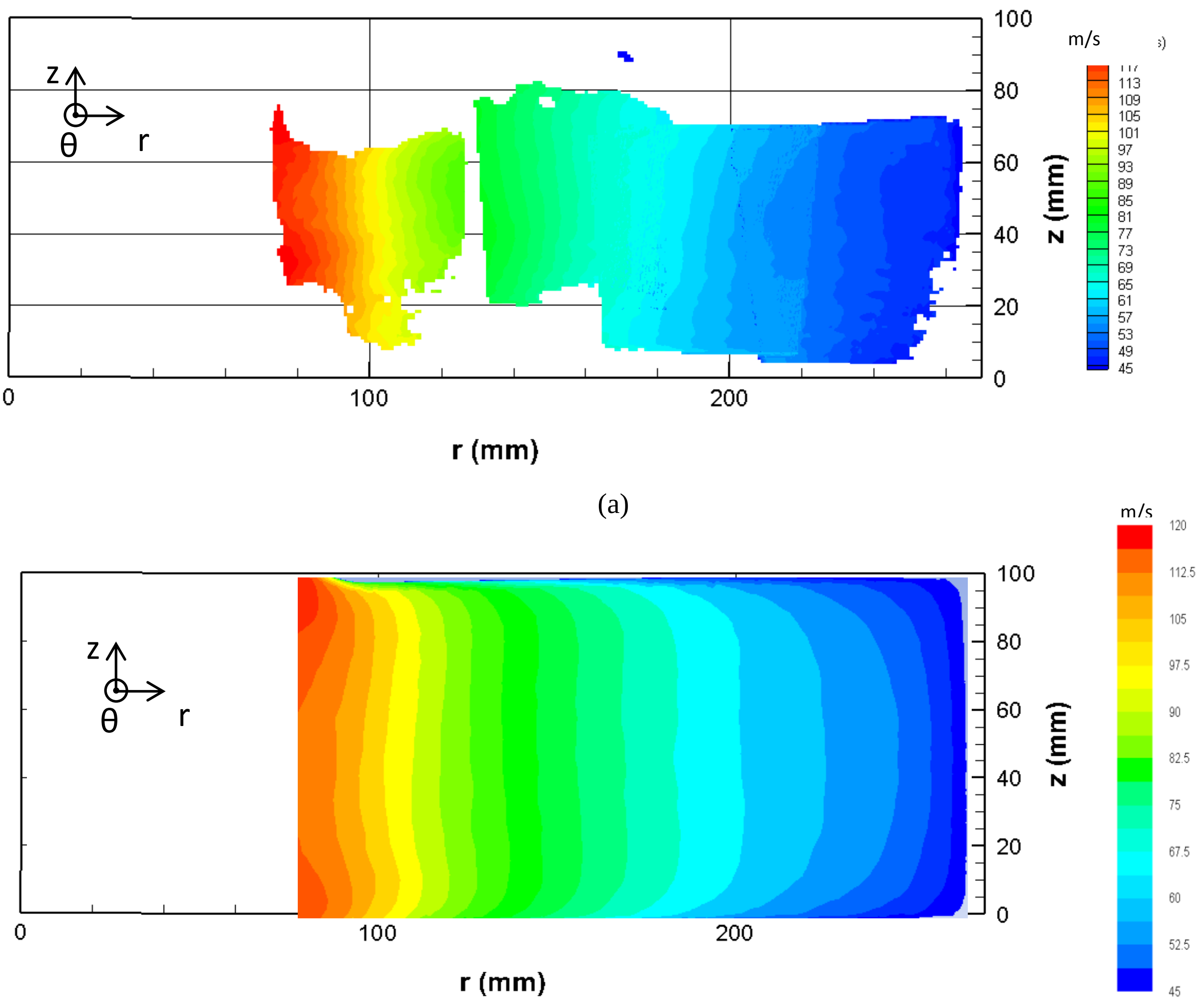

(a)

(b)

Fig. 4.1. Comparison of the azimuthal velocity field along the azimuthal plane (θ=20°) obtained from (a) experimental PIV technique and (b) numerical simulations calculated by solving the set of Eqs. (1.1)–(1.4) given in Table 2.

The azimuthal velocity field obtained from PIV measurements is compared with the simulation results in Fig. 4.1(a) and (b). Good *qualitative* agreement between the fields is observed. The azimuthal velocity remains nearly uniform along the length of the unit and increases radially inwards. Fig. 4.2 (a) and (b) show the axial profiles of azimuthal velocity component obtained from simulations and PIV measurements, at two different radii in the GVU.

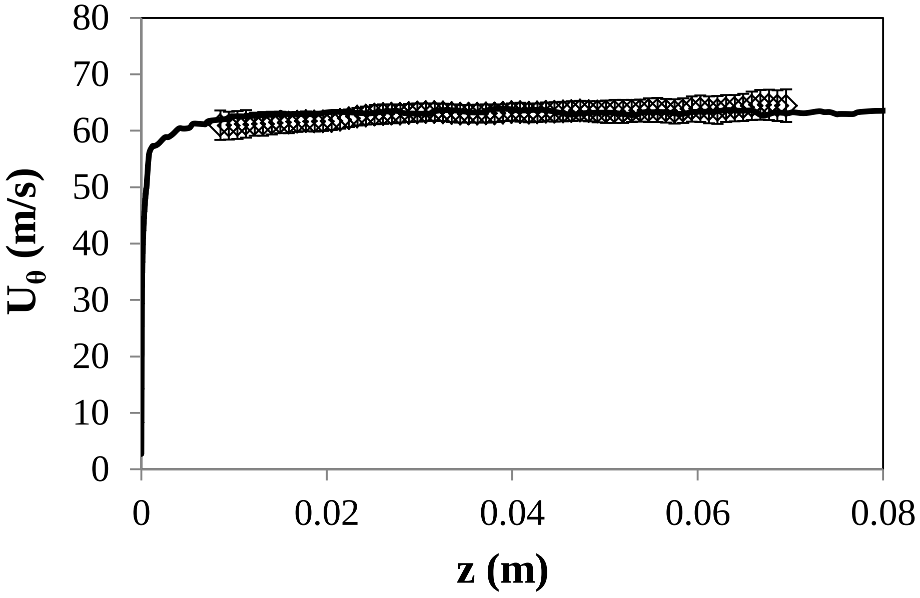

(a)

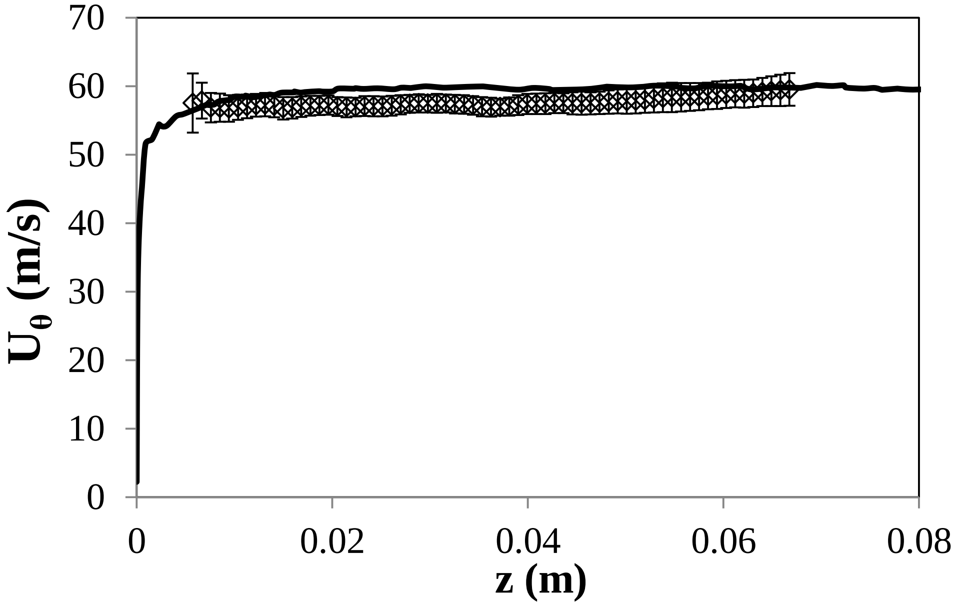

(b)

Fig. 4.2. Axial profile of azimuthal velocity: (◊) experimental PIV measurement; full line, from numerical simulations, calculated by solving the set of Eqs. (1.1)–(1.4) given in Table 2 along (a) the line (θ=20°, r=0.2m) and (b) the line (θ=20°, r=0.18m).

The experimental and simulation data show *quantitative* agreement in terms of the dominant azimuthal velocity in the GVU thus providing an initial validation of the numerical model used. It must be noted, that the PIV technique is limited to the bulk flow measurement. It cannot accurately the profiles in the thin boundary layers close to the end-walls of the unit, which are captured in the numerical simulations. Remark that only the azimuthal velocity component in the bulk GVU flow is essential for the goal of the study and hence has been used for validation of numerical data, as will be further developed in the subsequent sections of the manuscript.

2.4 Results and Discussions

2.4.1 Acceleration of azimuthal velocity in the GVU

As a first step, the bulk gas flow in the vortex unit is studied experimentally and numerically. The radial distribution of the azimuthal velocity component in the GVU at z=0.05 m and θ=20° for a gas flow rate of 0.4 Nm^3/s is presented in Fig. 4.3.

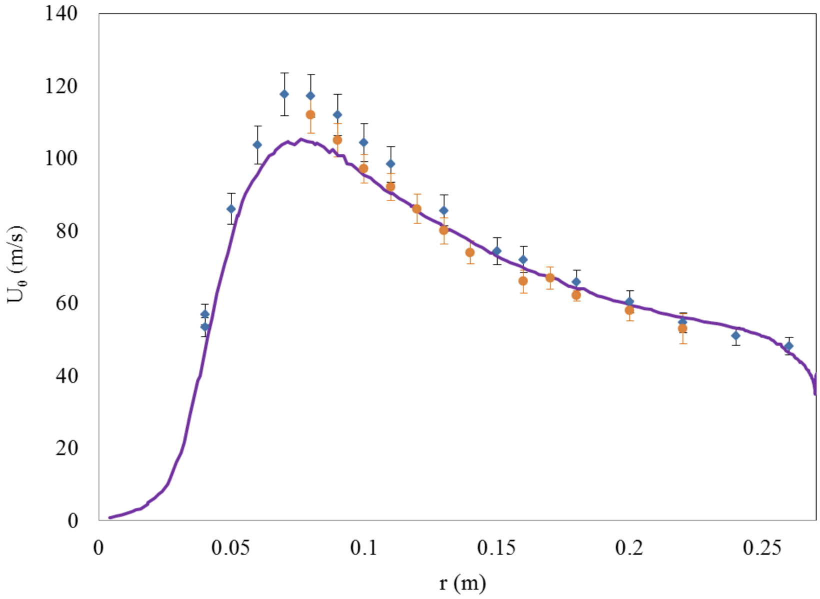

Fig. 4.3. Radial profile of azimuthal velocity along the line (θ =20°, z = 0.05 m): (●) experimental PIV; (♦) experimental LDA; full line, from numerical simulation calculated by solving the set of Eqs. (1.1)–(1.4) given in Table 2. Error bars represent the 95% confidence interval based on 3-7 repeated experiments for SPIV data. Error is shown in form of standard deviation for LDA experiments.

The simulation data agree well with the experimental results, obtained using both PIV and LDA (given the difficulty of properly aligning the LDA probe, only one set of LDA data was taken, and used to validate the stereoscopic PIV data). The deviation of the simulation data near the peak of the azimuthal velocity, observed close to the edge of the exhaust region (r=0.075 m) can be attributed to either the difference between the experimental exhaust geometry and simulation setup or the fact that the numerical simulations consider the gas to be incompressible. As the main objective of the experimental GVU geometry is to study gas-solid multiphase flows at a later stage, it possesses a solids filter at the exhaust. However, the simulated exhaust line is devoid of any solids filter for gas-only flow simulations as the mesh is simplified and reduces the computational expense of the simulations. Secondly, the gas used in the experiments, air, is compressible. The effect of compressibility on the gas density becomes more prominent as the gas velocity rises to values higher than 100 m/s (Mach number of about 0.3), which is seen in the peak region of the azimuthal velocity, near the exhaust (r=0.075 m). Under isothermal conditions, the density of the gas will decrease with decreasing gauge pressure near the gas exhaust (gauge pressure profile in Fig. 6), for compressible flow. Lower gas density for a given mass flow rate will result in an increase in the local gas velocity magnitude. Hence compressible flow simulations should theoretically predict slightly higher values of gas velocity near the exhaust. However, as gas velocities near the exhaust are still lower than 0.3Ma, this effect is not considered to be significant. Moreover, as the primary focus of the present work is to study flow phenomena in the disc-part of the GVU and good agreement between the experimental data and numerical results for the dominant azimuthal velocity component in the GVU bulk flow in the disc part of the unit is obtained, the present CFD model is adequate for further flow analysis.

Both the numerical and experimental data in Fig. 4.3 show a radial distribution of the azimuthal velocity typical for swirling flow in the disc part of a vortex unit, as reported in literature[10]. It is important here to understand the difference between the bulk hydrodynamics occurring in rotor (rotating disc-like chamber) and vortex (stationary disc-like chamber) units. In rotor units, the azimuthal velocity and, consequently, the centrifugal force increases proportionally with the distance from the rotor unit axis when the angular velocity (ω) is kept constant in the system. This behavior is representative of solid body-like rotation. On the contrary, in vortex units the azimuthal velocity and the centrifugal force are nearly inversely proportional to the distance. In such a system, the angular momentum (rU_θ) remains constant. This behavior is characteristic of free-vortex flow. The GVU seems to exhibit both solid-body rotation and free-vortex flow features depending on the radial position inside the unit. In Fig. 4.3 it can be seen that for r>0.075 m, that is sufficiently far away from the exhaust, a free-vortex flow structure is present. In the region r < 0.1 m, the flow is essentially of solid-body rotation nature.

To further analyze the flow behavior in the GVU the radial profile of the azimuthal velocity is compared in Fig. 5 with the profiles arising in free-vortex flow and solid body-like rotation. The free-vortex flow line is calculated using the equation

$$rU_\theta = c \tag{2}$$

with the azimuthal gas velocity value at the injection slots used to calculate the value of constant, c. The solid-body rotation line is drawn based on the following equation

$$\omega = k \tag{3}$$

where, the maximum azimuthal velocity (at r=0.075 m) is used to calculate the value of constant, k. In the region 0.1<r<0.27 m of the GVU, the simulated azimuthal velocity component increases with decreasing radius.

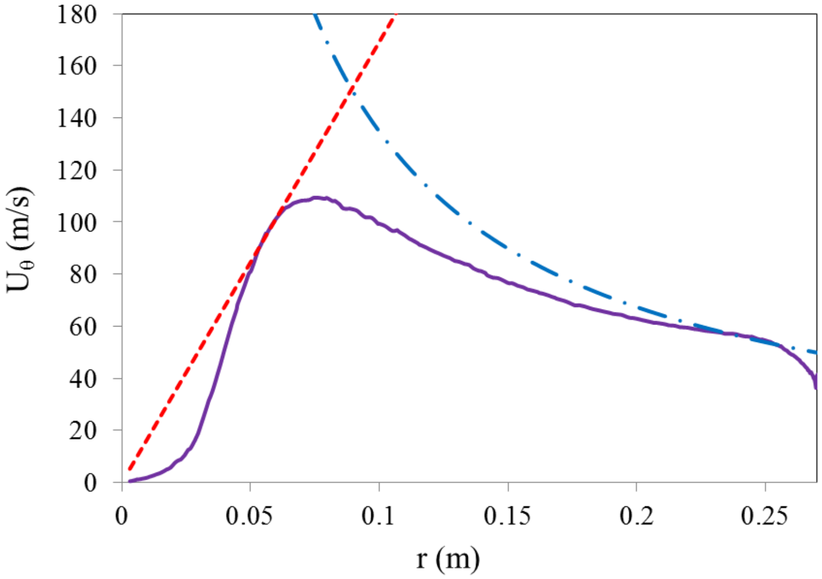

Fig. 5. Comparison of azimuthal velocity profiles obtained along the line (θ=20°, z=0.05 m): (- • -) free vortex flow, calculated by solving Eq. (2); (---) solid body rotation, calculated by solving Eq. (3); full line, from numerical simulation calculated by solving the set of Eqs. (1.1)–(1.4) given in Table 2.

However, the increase is slower than in the free-vortex profile, presumably due to the end-wall friction. As the gas reaches the exhaust region (0<r<0.075 m), the flow deviates from the free vortex flow-like pattern. The unidirectional exhaust causes a large positive axial velocity component to develop as the gas flows out of the GVU through the exhaust pipe. In turn, the swirl structure of the gas breaks resulting in a drop in the azimuthal velocity. Hence, in the region 0<r<0.075 m, the azimuthal velocity component decreases with decreasing radius. This decrease of the azimuthal velocity compares well with the solid body-like rotation, as seen in Fig. 5. The deviation from the solid body-like rotation, near the axis in the region 0<r<0.02 m, is due to the presence of a back flow region near the axis in the GVU exhaust region, as explained in the next paragraph. Fig. 6 shows the radial profile of simulated and experimental gauge pressure in the GVU. The good agreement of the pressure data between simulated and experimental pressure values in the region r>0.075 m corroborates further the validity of the simulations.

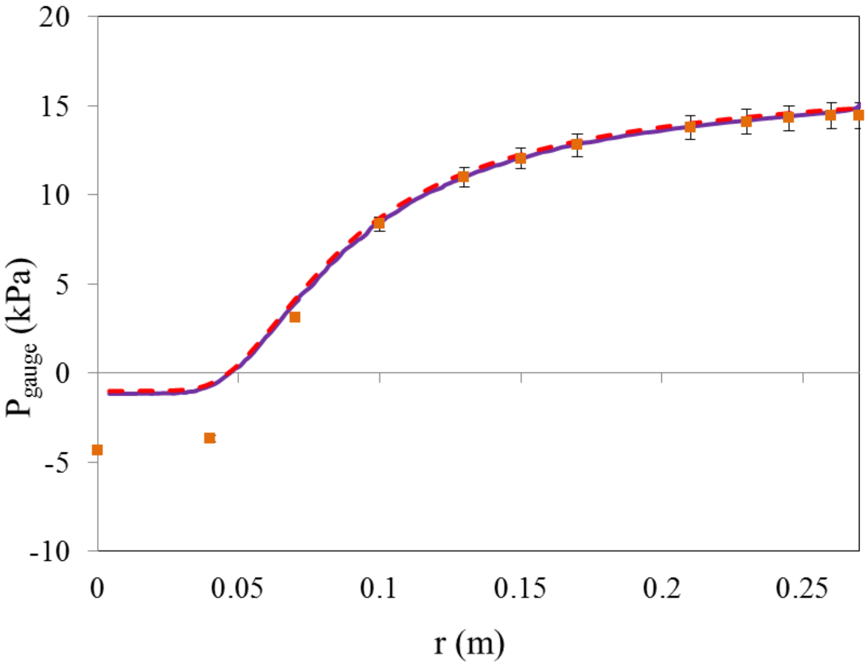

Fig. 6. Radial profile of static gauge pressure along the line (θ=20°, z=0.05 m): (■) experimental pressure measurement; (---) from cyclostrophic balance, calculated by solving Eq. (5) with azimuthal velocity values obtained from numerical simulation; full line, from numerical simulation calculated by solving the set of Eqs. (1.1)–(1.4) given in Table 2. Error bars represent the 95% confidence interval based on several experiments.

The dashed line corresponding to the cyclostrophic balance will be commented in a next section of the paper. The negative gauge pressure in the gas exhaust region 0<r<0.05 m indicates the possibility of gas flowing in the reverse direction near the axis, i.e. from the GVU exhaust pipe towards the rear end-wall, giving rise to a so-called backflow region. The presence of a backflow region in the exhaust is highlighted in Fig. 7(a) by the negative gauge pressure color contours along the azimuthal plane at θ=20°. The negative gauge pressure values extend in the GVU core region along the entire exhaust pipe length.

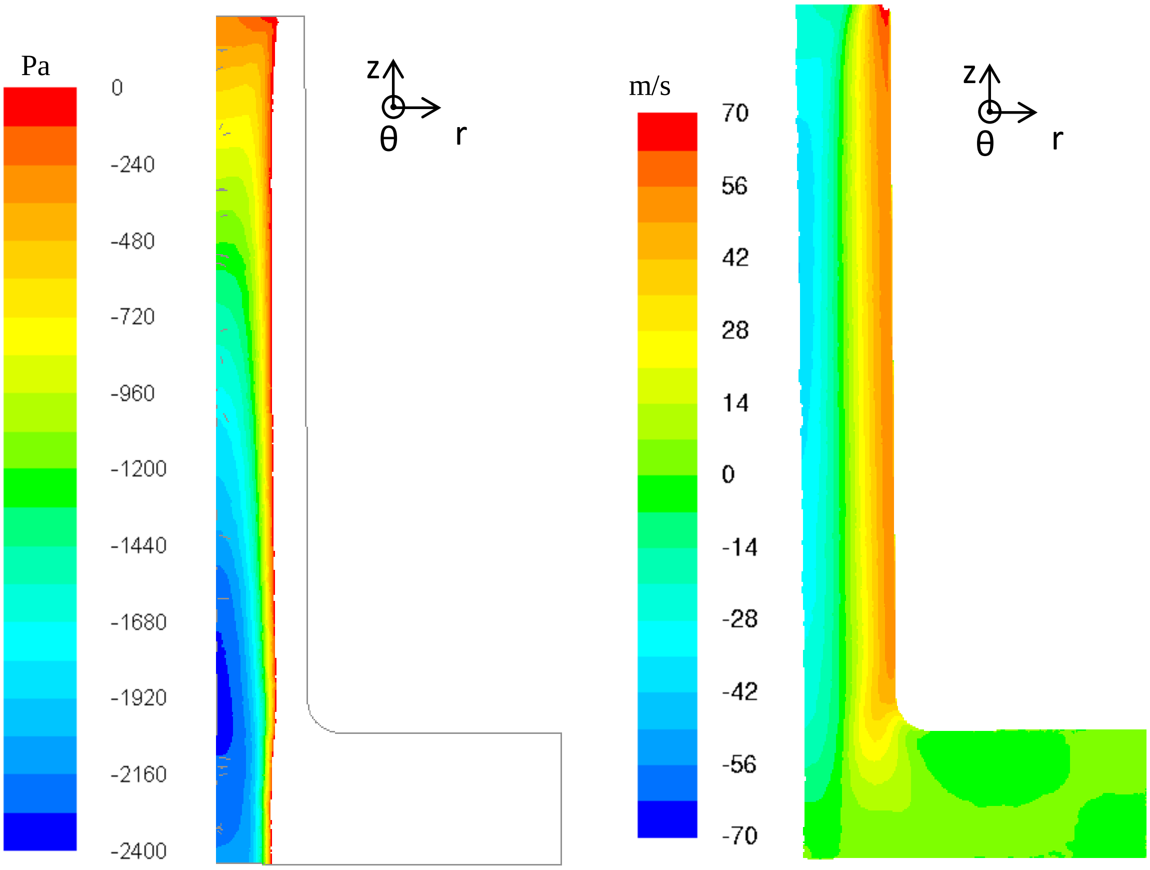

(a) (b)

Fig. 7. (a) Gauge pressure field (colored online) and (b) Axial velocity field (colored online) along the azimuthal plane (θ=20°), from numerical simulation calculated by solving the set of Eqs. (1.1)–(1.4) given in Table 2.

The static gauge pressure minimum is seen to be located slightly above the GVU disc length ($0.1<z<0.2$ m), suggesting that there is a pressure gradient in the negative z direction, from the exhaust outlet towards the rear end-wall of the unit. Fig. 7(b) shows the axial velocity field along the same azimuthal plane. The negative values of the axial velocity in the core of the exhaust pipe further verifies flow reversal in the exhaust and the formation of an extensive backflow region. The gas flow exits the GVU through a narrow peripheral annular region of the exhaust pipe near the exhaust wall ($0.05<r<0.075$ m). Ambient gas is sucked into the GVU through the central core of the exhaust. The presence of backflow near the axis of vortex units has been previously reported in literature[25]. Backflow transports swirl-free ambient gas to the rear end-wall of the GVU thus explaining the decrease in the azimuthal velocity component, in the exhaust region, to values lower than those corresponding to solid body-like behavior, seen in Fig. 5. It must be mentioned here, that a deviation between the experimental and simulation data in the backflow region, can be seen in the gauge pressure profiles shown in Fig. 6. The experimental data shows much lower gauge pressure values inside the exhaust region ($r<0.05$ m) than the simulation results. This difference arises from the fact that a shorter GVU exhaust pipe length has been simulated compared to the experimental setup. The experimental GVU setup has about 5 m of exhaust pipe length. Simulating the entire pipe would require excessive computational resources. Hence about 1 m of the exhaust length is simulated. Some preliminary simulations have indicated that the negative gauge pressure in the exhaust region increases with increasing the length of the exhaust. However, the length of the exhaust pipe is observed not to affect the near-wall jets.

2.4.2 Axial distribution of azimuthal and radial velocity components

Flow acceleration in confined flows is known to result in a uniform velocity distribution in the normal-to-flow direction[39]. Laminar flow in a cylindrical pipe, as an example, has a parabolic velocity profile over the cross-section of the channel. In contrast, in a converging pipe the flow spatially accelerates due to the gradual reduction in cross-sectional surface area. In such flows, the velocity profile over the channel cross-section is flat, except very close to the walls where the velocity drops to zero due to no-slip condition leading to the formation of the boundary layers[13]. In Fig. 8 the numerically simulated profile of the azimuthal velocity over the length of the disc part of the GVU is presented for different radii.

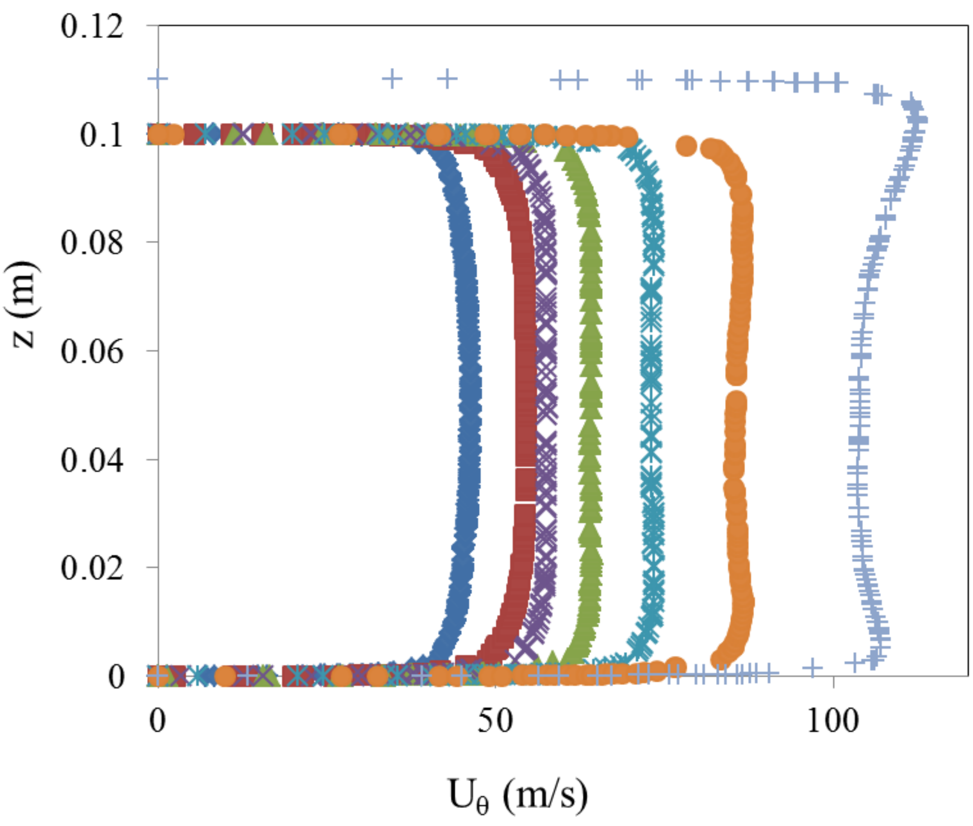

Fig. 8. Axial profiles of azimuthal velocity at different radii along the plane (θ=20°), from numerical simulation calculated by solving the set of Eqs. (1.1)–(1.4) given in Table 2: (+) r=0.08 m; (●) r=0.12 m; (*) r=0.15 m; (▲) r=0.18 m; (×) r=0.21 m; (■) r=0.23 m; (♦) r=0.26 m.

Due to the end-wall curvature at the exhaust of the unit, the length of the vortex unit has slightly increased at r = 0.08 m as can be seen in Fig. 8. The r = 0.26 m azimuthal velocity profile in Fig. 8 is most close to a typical turbulent profile in a channel. The boundary layers near the end-walls are thin and the azimuthal velocity profile is nearly flat with a slight convex bulge near the bulk region in between the two end-walls. The downstream velocity profiles in Fig. 8 gradually become more flat, particularly in the bulk region due to the acceleration effect in the GVU: due to the gradual reduction in circumferential flow surface area when flowing from the gas injection slots to the exhaust, the gas accelerates and the azimuthal velocity is nearly uniform in the axial direction over the length of the unit. The figure indicates that flow behavior downstream of r = 0.26 m in the GVU is similar to that in a converging pipe[13]. The azimuthal velocity profiles are nearly symmetric with respect to the z=0.05 m mid-plane. However, at r=0.08 m the symmetry deteriorates due to the front end-wall curvature towards the exhaust pipe. Two (small) peaks in all the azimuthal velocity profiles appear in the vicinity of the two end-walls. The azimuthal velocity peak near the front end-wall (z=0.1m), where the exhaust is located, is due to the fact that the exhaust bend creates a local pressure minimum. Following Bernoulli's principle, the velocity around the bend increases and the velocity curve peaks near this region. Near the rear end-wall (z=0 m), and at radii close to the exhaust region, the radially converging gas flow meets the backflow region and experiences a 90^0 turn, flowing towards the exhaust. This abrupt change in flow direction results in another virtual flow "bend" and gives rise to another local pressure minimum. The latter accelerates the flow near the rear end-wall in the exhaust region resulting in the second peak in the azimuthal velocity profile. To maintain a uniform mass flow rate throughout the GVU, the azimuthal velocity in the bulk of the GVU at r=0.08 m slightly diminishes to balance the two (small) velocity peaks. This results in the concave velocity profile as shown by the r=0.08 m curve in Fig. 8. Fig. 8 also shows that the azimuthal velocity drops to zero only in the thin boundary layers present near the end-walls. The Reynolds number

$$Re = \frac{\rho U_{\theta,slot}(H/2)}{\mu} \tag{4}$$

is calculated using as characteristic velocity the injection slot azimuthal velocity, being the dominant velocity component, and the half-length of the disc as characteristic dimension[12]. For a gas flow rate of 0.4 Nm^3/s, Re is 1.225×10^5. This large Re value means that the flow is highly turbulent. Even though the GVU flow is turbulent, the bulk flow acceleration (see Fig. 4 and Fig. 8) typically tends to suppress turbulence close to the end-walls[25]. Estimating the boundary layer thickness based on the Prandtl boundary layer theory[40] can be instructive.

According to Prandtl's theory, the boundary layer thickness (δ) is inversely proportional to the square of Re. This indicates that for the GVU pilot setup used in this work, the boundary layer thickness is of the order 10^{-4} m. Such thin boundary layers near the end-walls make it challenging for experimental techniques such as PIV and LDA to capture near-wall flow behavior, namely the presence of the near-wall radial jets. Numerical simulations nonetheless can give detailed description of the near-wall jets when using a high mesh refinement near the end-walls.

Fig. 9(a) shows the radial velocity profile along z at r=0.21 m. The dashed line in the figure represents the superficial radial velocity at r=0.21 m in the GVU, calculated as the total volumetric flow rate divided by the total circumferential surface area available for flow at r=0.21 m.

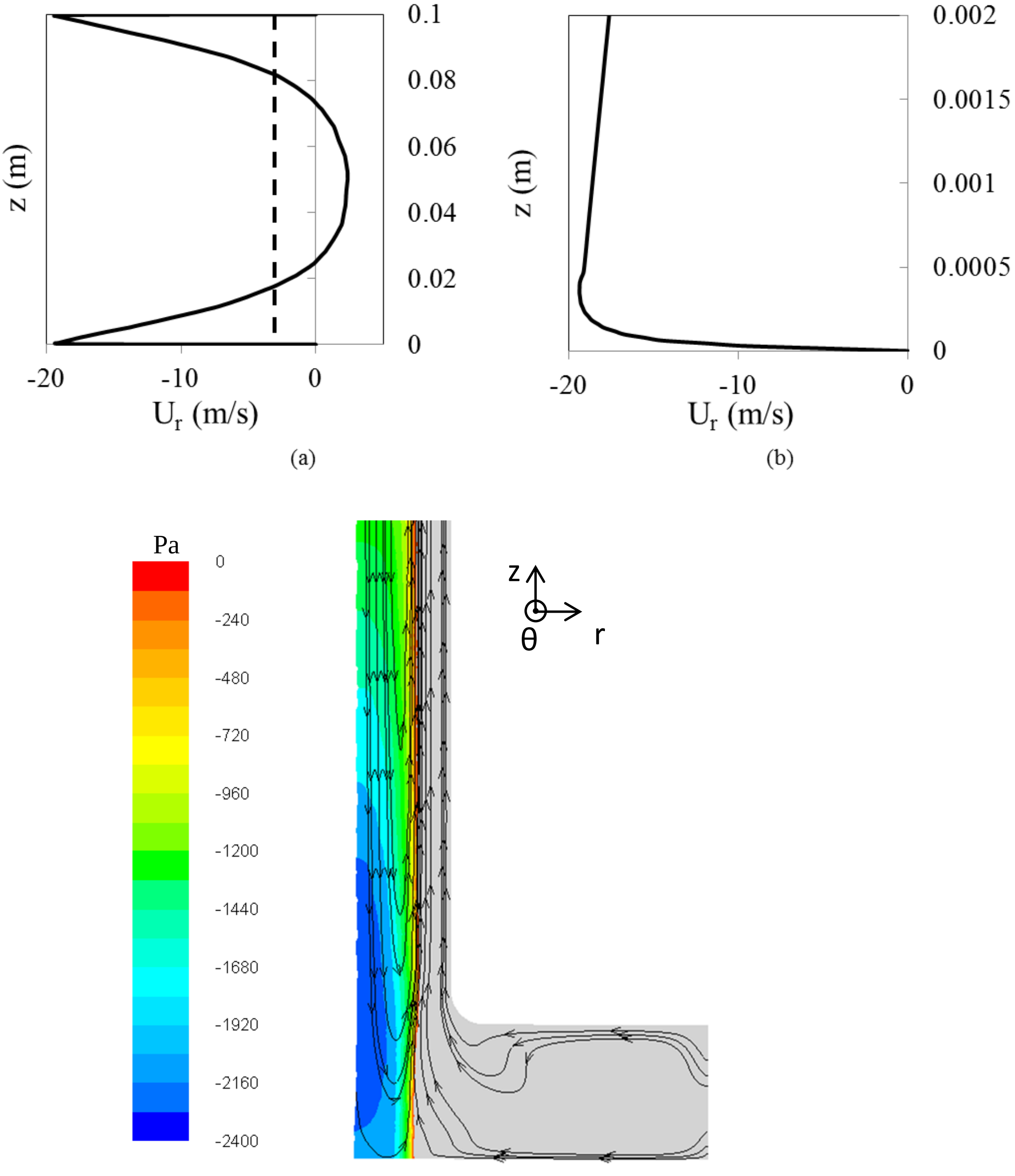

(a)

(b)

(c)

Fig. 9. (a) Axial profile of radial velocity along the line (θ=20°, r=0.21 m) (dashed line indicates the superficial radial velocity). (b) zoomed-in axial profile of jet peak velocity close to the rear end-wall

along the line (θ=20°, r=0.21 m). (c) Gauge pressure field (colored online) and streamlines of *in-plane* velocity components along the azimuthal plane (θ=20°); arrows show the flow directions, from numerical simulation calculated by solving the set of Eqs. (1.1)–(1.4) given in Table 2.

Similar to the profile of azimuthal velocity profile shown in Fig. 8, the profile of the radial velocity shows that the boundary layers near the end-walls are also thin (around 10^{-4} m, as seen in Fig. 9(b)). But while the azimuthal velocity is nearly constant over the length of the GVU, the axial profiles of the radial velocity are significantly altered by the swirling flow. Without swirl, the radial velocity would be nearly uniform along the GVU length due to the radially converging nature of the flow. Firstly, Fig. 9(a) shows that the axial profile of the radial velocity has sharp overshoots near the end-walls as compared to the superficial velocity. Secondly, a zoom-in of the radial velocity profile in the boundary layer near the rear end-wall as seen in Fig. 9(b) shows that the peak value in the radial velocity overshoot (≈20 m/s) occurs at a distance from the rear end-wall of about 2×10^{-4} m. Interestingly, this distance has the same order of magnitude as the above-estimated boundary layer thickness (10^{-4} m), using Prandtl's theory. The peaks of the radial velocity near the two end-walls are what the authors term as the near-wall jets formed in the GVU. The near-wall jets can also be visualized using the *in-plane* velocity streamlines shown in Fig. 9(c). The close packing of the in-plane streamlines near the two end-walls of the unit suggest regions of high radial gas flow rate taking place through the near-wall jets. It must be mentioned here, that Fig. 7(a) is a representation of the *in-plane* velocity (radial and axial velocity components without the azimuthal component) streamlines along the azimuthal plane, highlighting the near-wall jets in the radial direction. However, due to the high swirl nature of the GVU flow, the velocity streamlines shown in fig. 7(a) possess an azimuthal component as well. For complete visualization of the flow field, reference is made to the section '3D Features of near-wall jets' further into the manuscript. Fig. 9(a) also reveals that as a consequence of the near-wall jets, the radial velocity profile in the bulk flow of the GVU can no longer remain uniform. To balance the effect of radial velocity overshoots in the conservation of mass in the radial flow direction, the radial velocity in the bulk region of the GVU falls below the superficial radial velocity (shown by dashed line in fig. 9(a)). Thus the presence of near-wall jets in the GVU may cause a reversal in radial gas flow towards the circumferential wall observed in the central bulk region of the unit. When a vortex unit is used in single phase applications like combustion the presence of the near-wall jets can actually be beneficial and cool down the walls of the unit[41]. Therefore there is a strong need to elucidate the physical mechanism behind the formation of these near-wall jets. In order to achieve that understanding, a study of the cyclostrophic balance in the GVU is essential, as explained in the next section.

2.4.3 Cyclostrophic balance

Fig. 10(a) shows the radial profile of the swirl ratio S defined as the ratio of the azimuthal velocity to the superficial radial velocity at a fixed r.

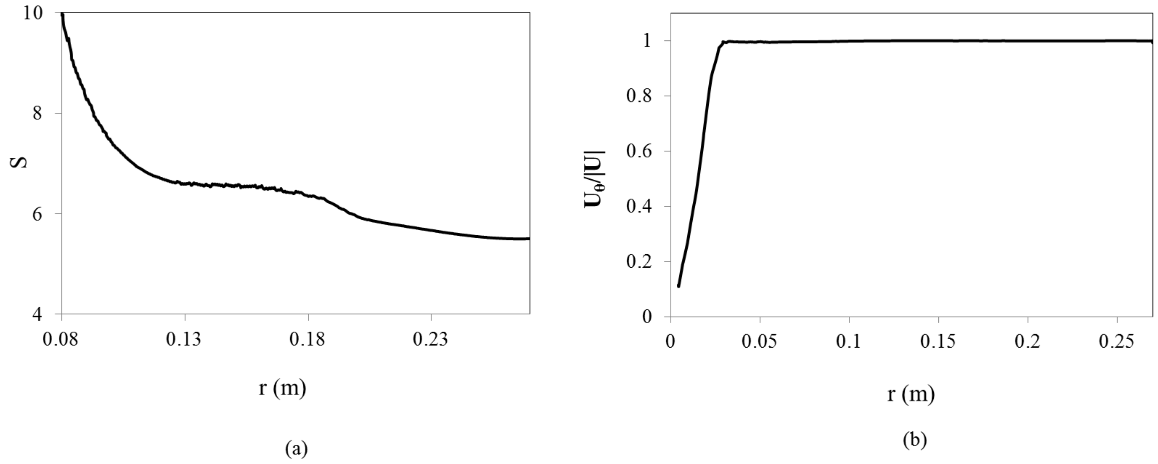

Fig. 10.(a) Radial profile of swirl ratio along the line (θ=20°, z=0.05 m), from numerical simulation calculated by solving the set of Eqs. (1.1)–(1.4) given in Table 2 and (b) azimuthal velocity component, normalized with respect to the velocity magnitude along the line (θ=20°, z=0.05 m), from numerical simulation calculated by solving the set of Eqs. (1.1)–(1.4) given in Table 2.

Since S>>1, the azimuthal velocity dominates the radial velocity at z=0.05 m over the entire disc part of the GVU. Accordingly the contribution of the radial velocity in the momentum conservation equation (Table 1, Eq. 1.2) becomes negligible as compared to the centrifugal acceleration contribution. Additionally, as the flow is bounded by two end-walls, the axial velocity component inside the GVU is close to zero. Due to the high gas injection velocity (55 m/s) the viscous contribution can be neglected as the flow is highly convective in nature. Hence, Eq. 1.2 reduces to:

$$\frac{\partial P}{\partial r} = \frac{\rho U_\theta^2}{r} \tag{5}$$

referred to as the cyclostrophic balance. The equation expresses that the radial pressure gradient in the bulk flow in the GVU is mainly balanced by the centrifugal force. Remark that, in the cyclostrophic balance analysis, it is assumed that radial and axial velocity are negligible compared to the azimuthal component. Now, away from the geometry axis, close to the circumferential wall, the gas enters the GVU geometry through slots, 10° azimuthally inclined with respect to the circumferential wall. Hence, right from the point of injection, the azimuthal velocity dominates the radial velocity. The presence of end-walls confines the flow and prevents any significant axial velocity components to develop. Fig. 10(b) shows that for r>0.05m, that is in the entire GVU except the central backflow region, azimuthal velocity comprises of almost the entire velocity magnitude. In the backflow region the azimuthal and radial velocity components drop to zero at the axis and significant axial velocity component develops due to the backflow. However, as Figure 6 shows, the pressure is nearly r-independent for r<0.03 m. In the range 0<r<0.03m, the overall velocity magnitude diminishes significantly such that the velocity differences in the backflow region make negligible contribution to the pressure variation. This explains why cyclostrophic balance seems to work well over the entire range 0<r<0.27 m at z=0.05 m.

Referring to Fig. 6, it can be seen that the simulated radial static gauge pressure profile in the GVU compares well with the calculated pressure profile using the cyclostrophic balance, based on the simulated azimuthal velocity profile. Quantitative agreement between the two profiles indicates that the cyclostrophic balance holds well for the bulk flow of the GVU unit. It can thus be concluded that the flow inside the bulk region of the disc part of the GVU is indeed highly swirling in nature and that the centrifugal acceleration mainly governs the radial pressure drop.

Near the end-walls, however, the azimuthal velocity drops to zero (no-slip boundary condition) over the thin boundary layer as discussed in Fig. 8. The centrifugal acceleration thus rapidly diminishes near the end-walls. However, the radial pressure gradient remains nearly invariant over the boundary layer as it follows from Fig. 11 showing the simulated axial profiles of static gauge pressure at 5 different radii in the region between the injection slots and the central gas exhaust.

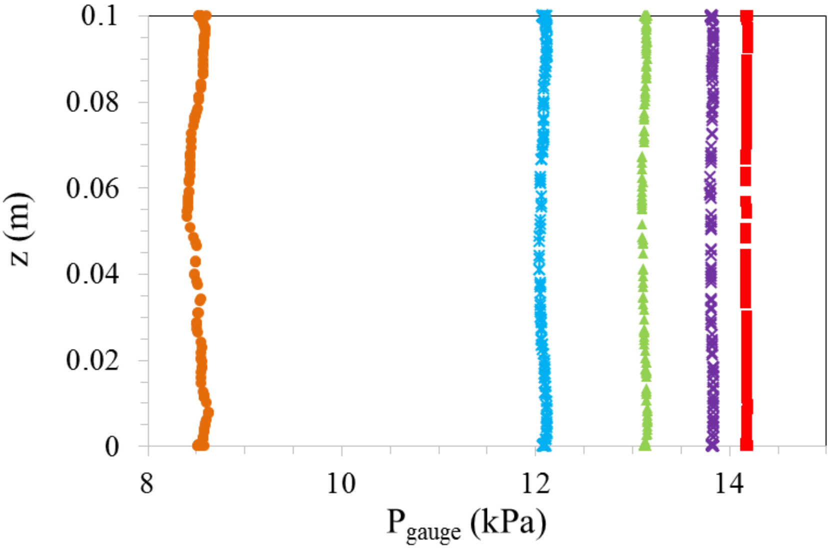

Fig. 11. Axial profiles of static gauge pressure at different radii along the plane (θ=20°), from numerical simulation calculated by solving the set of Eqs. (1.1)–(1.4) given in Table 2: (●) r=0.1 m; (*) r=0.15 m; (▲) r=0.18 m; (×) r=0.21 m; (■) r=0.23 m.

From the figure it can be seen that the pressure remains nearly uniform over the entire length of the GVU at a given radius. The profile becomes slightly non-uniform for r=0.1 m due to the presence of the unidirectional exhaust, while no pressure variation is visible within the drawing accuracy for r≥0.18 m. Therefore, it can be concluded from Fig. 11 that ∂p/∂r is nearly constant in axial direction, even inside the boundary layers close to the respective end-walls.

To further investigate the height of the GVU over which the cyclostrophic balance holds, a cyclostrophic function *f* is defined:

$$f = (\partial p/\partial r - \rho U_\theta^2/r)/\partial p/\partial r \qquad (5)$$

such that *f* becomes zero wherever the cyclostrophic balance holds in the flow domain. Fig. 12(a) presents the axial profile of *f* at r=0.21 m. It can be seen from the figure that *f* is close to zero, that is the cyclostrophic balance holds, in the bulk region of the GVU.

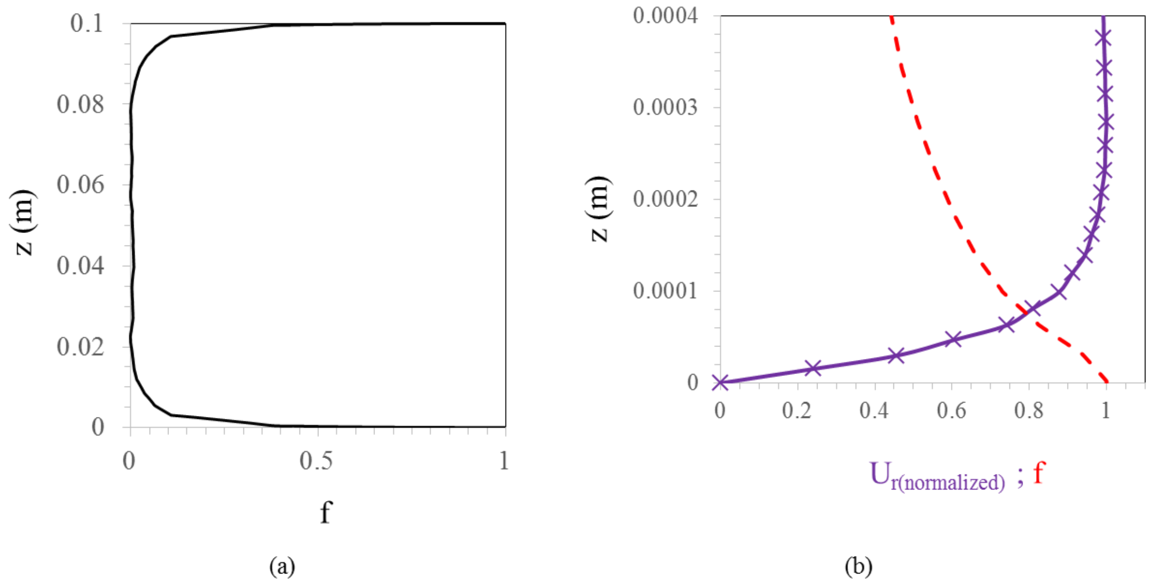

Fig. 12. (a) Axial profile of cyclostrophic ratio function f along the line (θ=20°, r=0.21m), from numerical simulation calculated by solving the set of Eqs. (1.1)–(1.4) given in Table 2 and (b) zoomed-in axial profile of function f and normalized radial velocity close to the rear end wall. (---) function f; (×) normalized radial velocity.

However in the regions very close to the end-walls, *f* increases to a value of 1 at the end-walls. From the zoom-in in Fig. 12(b) it can be seen that the cyclostrophic balance no longer holds over a distance of about 2×10^{-4} m from the end-wall, corresponding to the radial velocity peak location in Fig. 9(b) and to the estimated boundary layer thickness as calculated above. Thus, in the boundary layer, the pressure gradient $\partial p/\partial r$ is no longer balanced by $\rho U_\theta^2/r$. The unbalanced radial gradient of pressure propels the gas radially inwards towards the exhaust (r=0.075 m), resulting in the formation of the near-wall jets. Fig. 12(b) reveals this formation of near wall jets by plotting the radial velocity close to the end-wall. The radial velocity in Fig. 12(b) is normalized by the peak jet velocity occurring at r=0.21 m in order to bring the velocity values to comparable scale as the cyclostrophic function *f*. Close to the end-wall due to the no-slip condition, the radial velocity component also drops to zero. However, in the region just adjacent to the end-wall, the radial velocity component increases sharply and forms the near-wall jet.

2.4.4 3D Features of near-wall jets

The end-wall jets are highly asymmetric in their shape with respect to their peak velocity magnitude location. Fig. 9(a) shows that the gas radial velocity in the bulk flow side of the jet increases to approximately half-peak value at a distance of about 1×10^{-2} m from the adjacent end-wall. The jet velocity then peaks at about $z=2\times10^{-4}$ m from the end-wall and then drops drastically to zero within this small distance of about 2×10^{-4} m (Fig. 9(b)). This difference in jet thickness on two sides of the jet peak velocity is due to the entrainment of ambient gas which only occurs from the bulk flow in the GVU.

The near-wall jets develop so close to the end-walls that locating their exact position and resolving the boundary layer of the jet region cannot be achieved using experimental techniques like LDA and stereoscopic PIV. In the present work, prism layers of meshing near the end-walls help to achieve a finer level of resolution and to visualize the 3D structure of the jets near the end-walls. The jets, although mainly characterized by their high radial velocity component, are highly swirling as well because they possess a strong azimuthal velocity component. This renders the near-wall jets in the GVU a 3D structure.

To better understand the 3D structure of the near wall jets and their influence on the hydrodynamics of the GVU, the in-plane velocity streamlines along different constant axial position planes inside the GVU, are shown in Fig. 13.

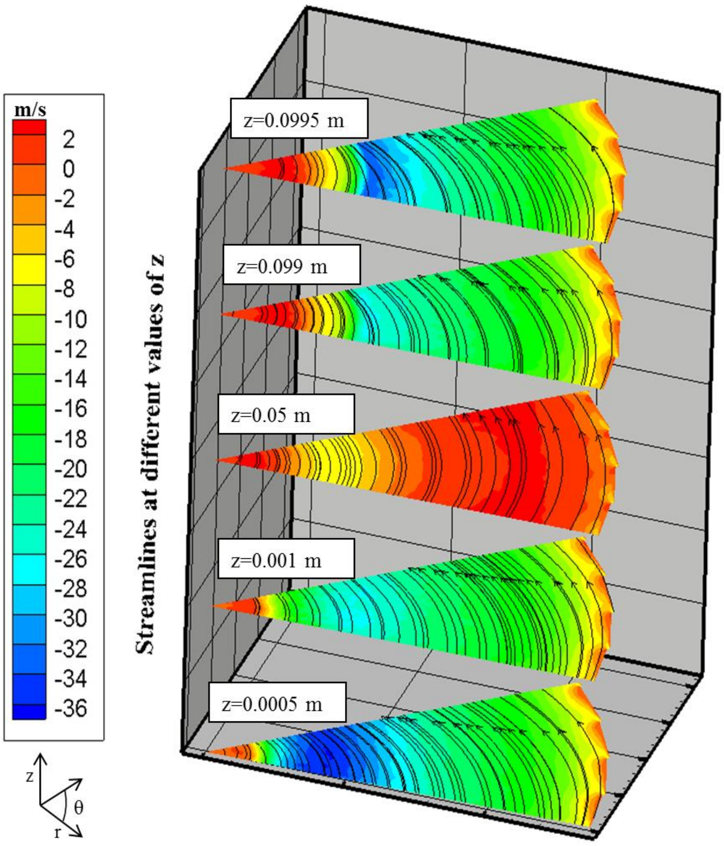

Fig. 13. Streamlines projected on planes at constant axial positions, from numerical simulation calculated by solving the set of Eqs. (1.1)–(1.4) given in Table 2; z value of each plane provided in the figure. Colored contours indicate the radial velocity field along different axial planes. Gas properties and operating conditions given in Table 3.

The streamlines in the central plane (z=0.05m) are nearly concentric circular arcs illustrating the strong dominance of the azimuthal velocity component compared to the radial velocity component in the bulk flow. Due to the reduced radial velocity component in the bulk flow in the central region of the vortex unit, the gas completes more number of turns in the unit before leaving the GVU through the central exhaust. As one moves from the central region (z=0.05 m) towards the end-walls (z=0 m and z=0.1 m) of the vortex unit, the streamlines start to increasingly spiral inward. The latter implies that the azimuthal velocity component becomes less dominant as compared to the radial velocity component. As a result, the number of full turns in the vortex unit completed by the gas before leaving the GVU through the exhaust reduces near the end-walls of the GVU. The streamlines in the planes shown in Fig. 13, thus provide a visualization of the combined effect of near-wall jets and swirling motion near the two end-walls in the GVU.

Conventional experimental techniques fail to capture near-wall jets in vortex units. Therefore, in order to validate the numerical observations with experimental data, the surface oil flow technique on the surface of the rear wall is applied. The oil droplets are very small (Stokesian) and hence, follow the gas flow. Some droplets travelling with the gas close to the end-wall stick to the surface. Their tracks on the wall correspond to the gas streamlines in the near-wall region. Fig. 14 compares the experimental oil tracks on the rear end-wall of the GVU (Fig. 14(a)) with the gas streamlines obtained from the simulation (Fig. 14(b)).

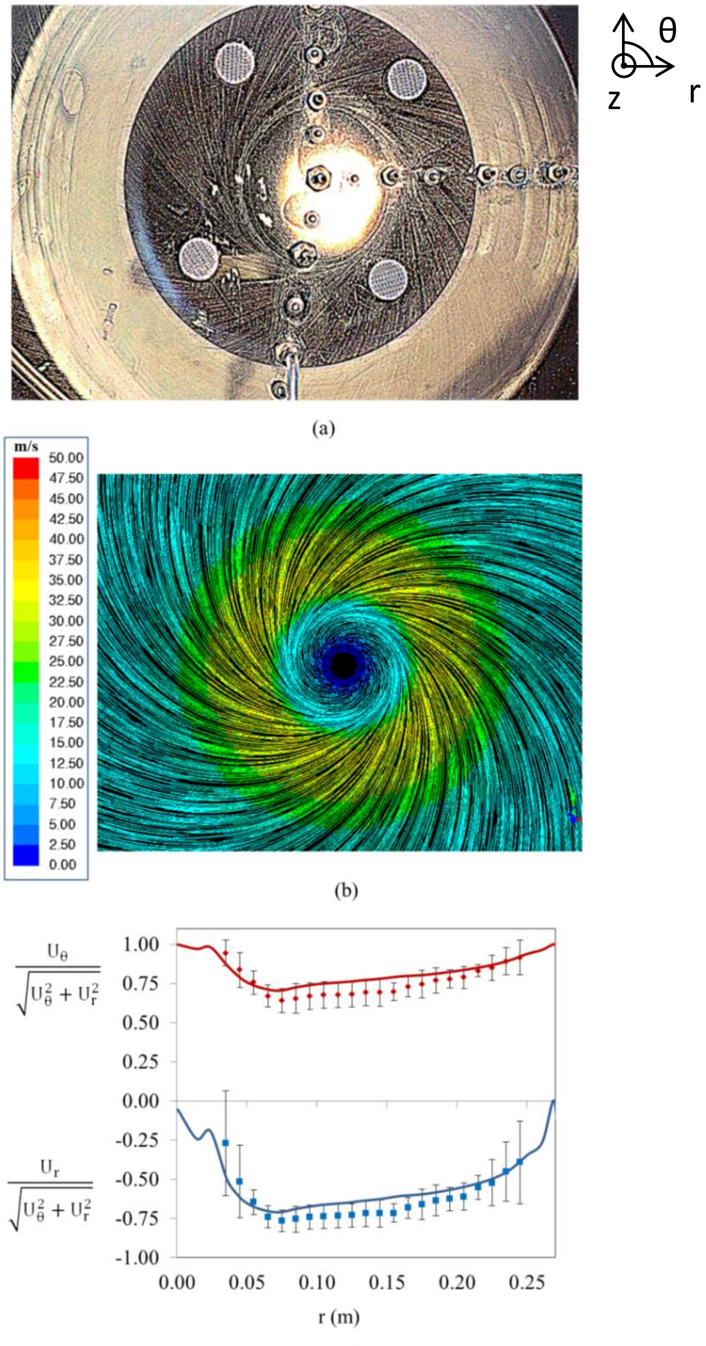

(a)

(b)

(c)

Fig. 14. Comparison of flow streamlines generated by (a) experimental oil droplet traces at the rear end wall, (b) numerical simulation along a plane with constant axial position (z=0.0001 m) (color indicates the velocity magnitude of the gas along the plane) and (c) comparison of azimuthal and radial velocity components, normalized with respect to the velocity magnitude from (a) and (b): (♦) normalized azimuthal velocity component derived from experimental surface oil flow visualization; (■) normalized radial velocity component derived from experimental surface oil flow visualization;

full lines, from numerical simulation calculated by solving the set of Eqs. (1.1)–(1.4) given in Table 2. Error bars represent the 95% confidence interval based on 5 repeated experiments.

The recorded and simulated streamlines agree well with each other. The peripheral streamlines converge inward from the circumferential wall to a limiting circle with a radius somewhat smaller than the exhaust radius. The spiraling nature of the converging streamline patterns experimentally confirms the presence of the near-wall jets and their 3D structure as observed in Fig. 13. The surface oil flow technique thus provides a first ever experimental visual proof of the presence of near-wall jets in vortex units. Fig. 14 also shows that both experimentally and numerically obtained streamlines converge to a limiting circle with a radius of about 0.07 m. The presence of the limiting circle can be linked to the backflow region that develops in the exhaust of the GVU and reaches all the way to the rear end-wall, as described in section 4.1 and seen in Fig. 6. The ambient gas flowing into the GVU via the backflow region reaches the GVU rear end-wall, expands laterally and is forced to make a 180^0 turn at the interface with the gas swirling radially inwards from the circumferential wall. This interface where the ambient gas meets the in flowing gas can be seen as the limiting circle in Fig. 14(b). Therefore, the flow approaches the interface from both sides and then separates from the rear end-wall at the position of the interface (limiting circle).

Fig. 14(c) depicts the velocity direction near the rear wall, z=0 m, depending on the distance from the GVU axis. Velocities U_r and U_θ both are zero at z=0 m, but their ratio has a non-zero limiting value as $z \to 0$, because $U_r = z\tau_{rZ}(0)/\mu$ and $U_\theta = z\tau_{\theta Z}(0)/\mu$ for small z; $\tau_{rZ}(0)$ and $\tau_{\theta Z}(0)$ are the corresponding stresses at the rear end-wall (z=0 m) and μ is the dynamic viscosity of the flowing gas. In Fig. 14(c) the symbols represent the experimental data extracted from the oil tracks and the dashed curves depicts the numerical results. The experimental and numerical results agree well and validate the numerical accuracy in description of the near-wall jets.

Next, the radial propagation of the near-wall jets in the GVU is studied. More specifically, the development and weakening of the near wall jet as a function of the radial position r is investigated. Therefore, in Fig. 15 the axial profiles of the radial gas velocity component at different r inside the GVU are plotted.

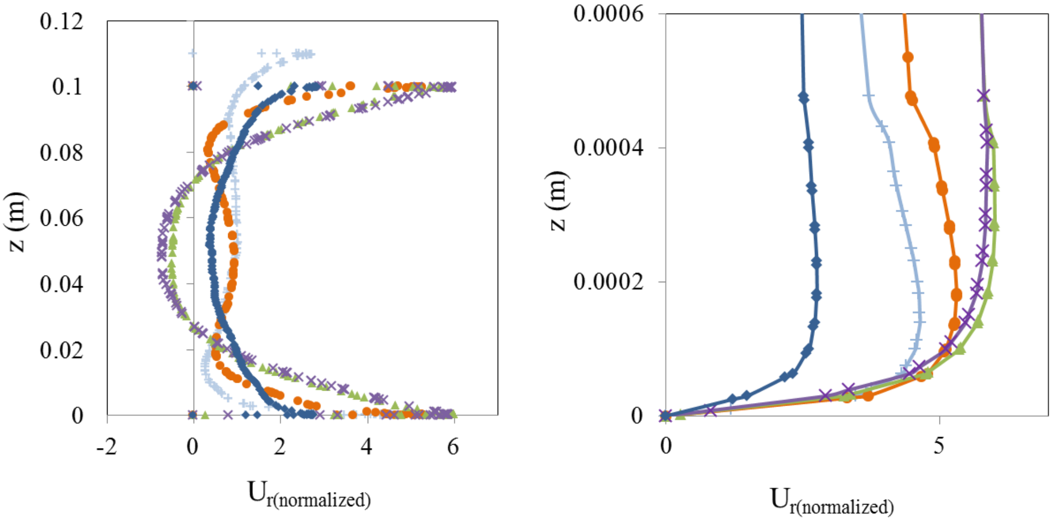

(a) (b)

Fig. 15. (a) Axial profiles of normalized radial velocity at different radii along plane (θ=20°), from numerical simulation calculated by solving the set of Eqs. (1.1)–(1.4) given in Table 2: and (b) zoomed in axial profile of jet peaks close to bottom end wall: (+) r=0.08 m; (●) r=0.1 m; (▲) r=0.18 m; (×) r=0.21 m; (♦) r=0.26 m.

As the effect of the increase in superficial radial velocity with decreasing circumferential surface area in direction of flow propagation needs to be accounted for, the local radial gas velocity at each r is normalized by the superficial radial gas velocity at that respective r. From Fig. 15 it can be seen that near the circumferential wall, r=0.26 m, the jets are not fully developed yet. With decreasing radius, as the flow penetrates in the GVU, the jets gain strength. The jet peak normalized velocity magnitude reaches its maximum value near r=0.20 m. With further decreasing radius, the jets start to weaken due to the expansion of the jets in the axial direction. This expansion for radii below r = 0.18 m is confirmed by the normalized velocity curves which have a more uniform profile for a broader range of z. Lateral expansion takes place near both end-walls of the GVU. Furthermore, Fig. 15 shows that the radial velocity profiles are quite symmetric with respect to the z=0.05 m plane, except for r=0.08 m where the curved exhaust is present on the front end-wall. The peak velocity at the rear end-wall (~4 m/s) is higher than at the front end-wall (~2.5 m/s) for r=0.08 m. This non-symmetric behavior of radial velocity is mainly a consequence of the unidirectional exhaust geometry of the

GVU. Due to the gas exiting through the exhaust, the gas flow develops a strong axial velocity component which diminishes the swirl behavior near the front end-wall.

The strength of the end-wall jets is studied next by comparing the normalized peak velocity of a jet at the different radii. Fig. 16 shows the profile of the jet peak normalized velocity along the radial distance normalized with the circumferential wall of the GVU.

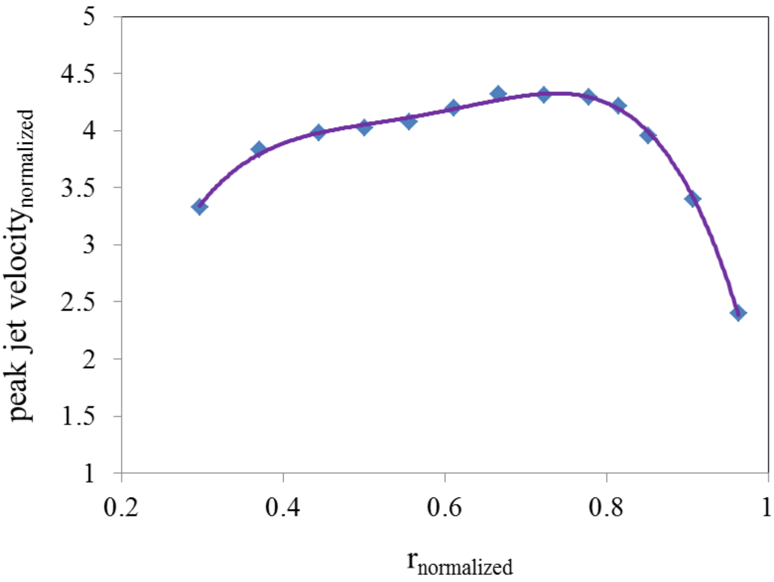

Fig. 16. Radial profile of variation of peak jet velocity along azimuthal plane (θ=20°), , from numerical simulation calculated by solving the set of Eqs. (1.1)–(1.4) given in Table 2. Full line represents the fourth order polynomial-fit trend line of the peak jet velocity data.

The figure clearly shows that the jet becomes fully developed at $r_{normalized}=0.8$. So about two-fifth volume of the disc part of the GVU is used up as the jet development region. The slight decrease in the peak velocity magnitude for $r_{normalized}<0.8$ can be attributed to the lateral expansion of the jet as explained in the previous paragraph.

2.5 Conclusions

This paper explains the physical nature of jets developing near the end-walls of a disc-like gas vortex unit. To this end, both experimental and numerical studies are performed to obtain a 3D visualization of the near-wall jets.

LDA and stereoscopic PIV velocity measurements are performed in the central bulk zone of a pilot setup, verifying one another, and validating the numerical results obtained by 3D simulations of the setup, using FLUENT v.14a. Using PIV and LDA techniques, experimental data cannot be obtained in the thin boundary layers near the end-walls. Hence, the surface oil flow visualization technique on an end-wall of the vortex unit is used for near-wall jet visualization, showing flow streamlines near the rear end-wall. Numerical data in the jet region near the end-walls are also obtained by performing 3D simulations on a highly dense layer of prism cells close to the end-walls.

The physical understanding of jet formation is based on three key components: (i) flow acceleration in the disc part of the unit, (ii) cyclostrophic balance of centrifugal force and radial pressure gradient and (iii) no-slip condition at the end-walls.

The gas flowing in the GVU forms a free swirl structure before leaving the unit through a central unidirectional exhaust. The azimuthal gas velocity increases with decreasing radius in the free swirl flow to maintain constant angular momentum, resulting in flow acceleration. As a consequence of this flow acceleration, the azimuthal velocity profile along the height of the unit becomes nearly constant for a given radius between the end-walls of the vortex unit, except in the thin boundary layers where the azimuthal velocity component drops to zero due to the no-slip wall boundary condition. The pressure gradient acting radially inwards, on the other hand, is constant over the height of the unit, even in the thin boundary layers. The cyclostrophic balance thus only holds in the bulk of the vortex unit. In the boundary layer near the end-walls the pressure gradient is no longer balanced by the centrifugal force. This pushes the gas radially towards the axis of the vortex unit, resulting in jet formation near the end-walls. However, even in the boundary layer region some part of the azimuthal velocity component is still present, which renders 3D characteristics to the jets. The gas elements close to the end walls also swirl towards the exhaust. However, due to larger radial velocity component, the number of rotations by the gas before leaving the unit is lower than by the gas in the bulk of the GVU.

The radial propagation of the near-wall jets is explored. The normalized jet peak velocity reaches its maximum halfway between the circumferential wall and the central exhaust of the vortex unit. The detailed 3D simulation of the near-wall jet formation combined with the velocity streamlines obtained from experimental surface oil flow visualization allow visualizing and understanding the physical mechanism of the near-wall flow behavior of the flow in vortex units. This study captures the 3D nature of the near wall jets occurring in highly swirling confined flows such as the GVU and can support optimizing existing vortex units and designing new vortex units for chemical technology and combustion applications, in view of process intensification.

2.6 Acknowledgments

This work was supported by the European Research Council FP7/2007-2013/ ERC grant agreement n° 290793. We are grateful for the use of the Stevin Supercomputer Infrastructure at Ghent University, funded by Ghent University, the Hercules Foundation, and the Flemish Government – department EWI.

2.7 References

1. Lewellen WS. A review of confined vortex flows. NASA. 1971;CR-1772.
2. Long RR. A vortex in an infinite viscous fluid. Journal of Fluid Mechanics. 1961;11(04):611-624.
3. Dahlstrom DA. Cyclone operating factors and capacities on coal and refuse slurries. Transactions of the American Institute of Mining, Metallurgical and Petroleum Engine. 1949;184:331-344.
4. Gupta AK, Lilley DG, Syred N. Swirl Flows. Abacus Press, 1984.
5. Wormley DN. An analytical model for the incompressible flow in short vortex chambers. Journal of Basic Engineering. 1969;91(2):264-272.
6. Hilsch R. The use of the expansion of gases in a centrifugal field as cooling process. Review of Scientific Instruments. 1947;18(2):108-113.
7. Kerrebrock JL, Meghreblian RV. Vortex containment for the gaseous-fission rocket. Journal of the Aerospace Sciences. 1961;28(9):710-724.
8. Ashcraft RW, Heynderickx GJ, Marin GB. Modeling fast biomass pyrolysis in a gas-solid vortex reactor. Chemical Engineering Journal. 2012;207:195-208.

9. Ekatpure RP, Suryawanshi VU, Heynderickx GJ, de Broqueville A, Marin GB. Experimental investigation of a gas-solid rotating bed reactor with static geometry. Chemical Engineering and Processing: Process Intensification. 2011;50(1):77-84.
10. Savino JM, Keshock EG. Experimental profiles of velocity components and radial pressure distributions in a vortex contained in a short cylindrical chamber. NASA. 1965;TN D-3072.
11. Anderson OL, Utch CT. Theoretical solutions for the secondary flow on the end wall of a vortex tube. Defense Technical Information Center. 1961.
12. Sorokin VV. Calculation of compressible flow in a short vortex chamber. Journal of Engineering Physics and Thermophysics.2006;79(5):999-1005.
13. Shtern V. Counterflows. Cambridge University Press, 2012.
14. Hornbeck RW. Viscous flow in a short cylindrical vortex chamber with a finite swirl ratio. Lewis Research Center, NASA. 1968;TN D-5132.
15. Beverloo WA, Leniger HA, Weldering JAG. Potentialities of the flat vortex hydrosifter. British Chemical Engineering Journal. 1963;8:678-682.
16. Ragsdale RG. NASA research on the hydrodynamics of the gaseous vortex reactor. NASA. 1959;NSA-15-001058.
17. Kendall JMJ. Experimental study of a compressible viscous vortex. 1962;NSA-16-023818.
18. Donaldson CD. The magnetohydrodynamic vortex power generator, basic principles and practical problems. Paper presented at: Proceedings of the Second Symposium on the Engineering Aspects of Magnetohydrodynamics. March, 1961; Philadelphia.
19. Williamson GG, McCune JE. A preliminary study of the structure of turbulent vortices. Aeronautical Research Association of Princeton Incorporated. 1961; 32.
20. Singh A. Theoritical and experimental investigations and decelerating flows within two flat discs, IIT Bombay; 1993.
21. Murphy HD, Coxon M, McEligot DM. Symmetric Sink Flow Between Parallel Plates. Journal of Fluids Engineering. 1978;100(4):477-484.
22. Singh A, Vyas BD, Powle US. Investigations on inward flow between two stationary parallel disks. International Journal of Heat and Fluid Flow. 1999;20(4):395-401.

23. Launder BE, Spalding DB. The numerical computation of turbulent flows. Computer Methods in Applied Mechanics and Engineering. 1974;3(2):269-289.
24. Jakirlic S, Hanjalic K, Tropea C. Modeling Rotating and Swirling Turbulent Flows: A Perpetual Challenge. AIAA Journal. 2002;40(10):1984-1996.
25. Vatistas GH, Fayed M, Soroardy JU. Strongly swirling turbulent sink flow between two stationary disks. Journal of Propulsion and Power. 2008;24(2):295-301.
26. Launder BE, Reece GJ, Rodi W. Progress in the development of a Reynolds-stress turbulence closure. Journal of Fluid Mechanics. 1975;68(03):537-566.
27. Kovacevic JZ, Pantzali MN, Heynderickx GJ, Marin GB. Bed stability and maximum solids capacity in a gas-solid vortex reactor: experimental study. Chemical Engineering Science. 2014;106:293-303.
28. Pantzali MN, Lozano BN, Heynderickx GJ, Marin GB. Three-component solids velocity measurements in the middle section of a riser. Chemical Engineering Science. 2013;101:412-423.
29. Kovacevic JZ, Pantzali MN, Niyogi K, Deen NG, Heynderickx GJ, Marin GB. Solids velocity fields in a cold-flow gas-solid vortex reactor. Chemical Engineering Science. 2015;123:220-230.
30. Mei R. Velocity fidelity of flow tracer particles. Experiments in Fluids. 1996;22(1):1-13.
31. Maltby RL, Keating RFA. The surface oil flow technique for use in low speed wind tunnels. AGARDograph, 1962:70:87-109.
32. Adam P, Frank L, Daniel B, Yusi S. New developments in surface oil flow visualization. Paper presented at: 27th AIAA Aerodynamic Measurement Technology and Ground Testing Conference: American Institute of Aeronautics and Astronautics; 2010; Chicago, USA.
33. Merzkirch W. Optical flow visualization. Flow Visualization (Second Edition). San Diego: Academic Press, 1987:115-231.
34. Pantzali MN, Kovacevic JZ, Heynderickx GJ, Marin GB, Shtern VN. Radial pressure profiles in a cold-flow gas-solid vortex reactor. AIChE Journal. 2015;61(12):4114-4125.

35. De Wilde J. Gas–solid fluidized beds in vortex chambers. Chemical Engineering and Processing: Process Intensification. 2014;85:256-290.
36. Rosales Trujillo W, De Wilde J. Fluid catalytic cracking in a rotating fluidized bed in a static geometry: a CFD analysis accounting for the distribution of the catalyst coke content. Powder Technology. 2012;221:36-46.
37. van Leer B. Towards the ultimate conservative difference scheme. V. A second-order sequel to Godunov's method. Journal of Computational Physics. 1979;32(1):101-136.
38. Patankar SV. Numerical Heat Transfer and Fluid Flow. New York: McGraw-Hill, 1980.
39. Yuan J, Piomelli U. Numerical simulation of a spatially developing accelerating boundary layer over roughness. Journal of Fluid Mechanics. 2015;780:192-214.
40. Schlichting H. Boundary Layer Theory. New York: McGraw-Hill, 1960.
41. Borissov A, Shtern V, Gonzalez H, Yrausquin A. Volume distributed high-temperature-air combustion for turbine. Paper presented at: Proceedings of 8th International Symposium on High Temperature Air Combustion and Gasification; 5-7 July 2010; Poznan, Poland.

Chapter 3

On the secondary flow mechanisms in a Gas Vortex Unit

Abstract

The present study investigates the hydrodynamics of secondary flow phenomena occurring in a radially converging swirling flow through a disc-shaped stationary Gas Vortex Unit (GVU), using experimentally validated numerical simulations. The turbulent two-dimensional axisymmetric flow along an azimuthal plane of the GVU is simulated using the finite-volume based commercial fluid dynamics software FLUENT® v.14a. A highly refined mesh resolving the near-wall boundary layers together with the Reynolds Stress Model (RSM) for turbulence reveals interesting flow features, such as a backflow region along the core of the central gas exhaust, and a counterflow region with radially diverging flow in the bulk of the disc part of the unit. The numerical technique is validated with experimental data obtained from Stereoscopic Particle Image Velocimetry (SPIV) and surface oil flow visualization measurements. Under the tested operating conditions, the bulk GVU flow is found to be highly spiraling with dominant azimuthal velocity components in a major section of the GVU. As the swirl becomes stronger, secondary flows develop. As the Reynolds number (Re) characterizing the gas flow rate increases, a backflow region first develops via the swirl-decay mechanism in the exhaust line. As Re further increases, for a given injection swirl-to-radial velocity ratio (S), the flow pattern gets established and becomes Re-independent. As S increases, the radial velocity profile shows a formation of near-wall jets appearing in the thin boundary layers near the GVU end-walls. As the jets get stronger, they result in the formation of a flow reversal in the bulk flow in between the two end-walls, referred to as the counterflow region. It is argued that counterflow occurs due to jet entrainment. At a sufficiently large S, the jet entrainment flow rate exceeds the injection flow rate, resulting in downstream gas being sucked in the reverse direction, i.e. radially outward, causing a counterflow region to develop. With increasing S, the counterflow region first develops near the GVU exhaust line, then gradually progresses upstream into the disc part of the unit until it occupies the entire disc bulk region. Further increase in S does not change the size of the counterflow region. However, the counterflow itself becomes multicellular with the appearance of multiple vortices. As the number of vortices increases, it is conjectured that the flow becomes more turbulent in the bulk of the GVU and will result in better mixing of gases for industrial applications.

Keywords:

Gas Vortex Unit, secondary recirculation flows, computational fluid dynamics, Reynolds Stress Model, swirling flow

3.1 Introduction

A Gas Vortex Unit (GVU) is the basic design unit for several engineering applications ranging from nuclear rocket propulsion[1], vortex diodic valves[2], vortex scrubbing[3], nano-precipitation reactors[4], vortex amplifiers[5] and combustion[6]. The unit, schematically shown in Fig. 1(a), consists of a disc-shaped (aspect ratio, $L_R/D_R << 1$) geometry confined on either side by two normal-to-unit-axis parallel flat plates, referred to as the end-walls. The distance between the two end-walls constitutes the length of the unit, L_R. A series of azimuthally inclined rectangular gas injection slots are located along the circumferential wall, through which the gas is introduced into the unit. The inclination of the slots imparts a strong azimuthal component to the inflowing gas. As a result, a strong swirling flow is established within the unit as the gas spirals towards the central unidirectional exhaust located on the front end-wall. The extended exhaust line (not shown in the schematic) finally directs the gas towards the outlet into the atmosphere. The degree of swirl imparted to the flowing gas in the GVU is determined by the injection slot angle (γ), highlighted in Fig. 1 (inset: zoomed-in view of the slots where $\gamma = 10°$ for the presented unit).

Although the primary flow in the GVU is swirling in nature, secondary flows may get developed under specific operating conditions and geometrical design of the unit. Fig. 1(b) schematically shows the secondary flow patterns that may appear in the GVU in form of in-plane velocity streamlines in an azimuthal plane (θ=constant). The figure reveals that two distinct recirculation regions can develop in the unit: one in between the two end-walls referred to as Counterflow Region (CR) and another in the core of the exhaust region along the exhaust line, referred to as the Backflow Region (BR). As the gas swirls towards the central exhaust axis, the small aspect ratio of the unit causes the two end-walls to significantly affect the flow topology resulting in the formation of a toroidal recirculation region (Counterflow Region, CR in Fig. 1(b)) in between the two end-walls. In the core of the CR, the radial gas velocity is found to be directed radially outwards, opposite to the main throughput flow direction in the GVU. The radially converging gas entering from the injection slots, thus splits in two parts (referred to as through-flow) flowing close to the two end-walls of the unit, while the bulk region is occupied by a flow reversal region. Remark that the gas flowing in the CR possesses a strong azimuthal velocity component as well. This azimuthal velocity component causes the CR to stretch along the entire circumference of the unit, in the form of a toroidal flow reversal zone. Fig. 1(b) also shows that in the vicinity of the central axis, in the core of the exhaust line, the gas flows axially downwards, from the exhaust outlet towards the GVU rear end-wall. Meanwhile the gas, flowing in from the injection slots, leaves the unit through a peripheral annular region near the exhaust wall surrounding this recirculation zone. This second recirculation zone constitutes the Backflow Region, (BR in Fig. 1(b)) and extends along the entire exhaust line. In the BR, the gas flows downwards, sucked in from the ambient atmosphere.

The near-axis flow reversal in the form of the BR is a well-known hydrodynamic phenomenon commonly applied for solid-liquid and liquid-liquid separation in hydro-cyclones[7] and effluent treatment by cavitation[2,8]. The formation of the Backflow Region in swirling flows, discovered around the 1960s, is known as Vortex Breakdown (VB)[9]. The effects of VB on flow hydrodynamics can be considered positive or negative depending on the application of the GVU. For instance, in delta-wing aircrafts, VB can prove to be dangerous as it may cause abrupt variations in lift and drag forces on the aircraft wings [10]. In combustion chambers however, VB can be beneficial to stabilize flames[11]. In natural swirling flows such as tornadoes, VB is known to decrease the destructive strength of the twister[12]. A number of explanations for the appearance of the VB have been proposed in literature: (a) inertial wave roll-up[13], (b) collapse of the near-axis boundary layer[14], (c) flow separation[15] (d) transition from convective to absolute instability[16]. A recent view is that VB develops via the swirl-decay mechanism[10,17]. The present study also shows that the swirl-decay mechanism can explain the formation of the BR, as discussed in more details in the results section.

The Counterflow Region (CR) is a comparatively less researched hydrodynamic phenomenon. It was accidentally detected in a series of experimental studies conducted on a Vortex Unit for the development of a nuclear rocket propulsion engine conceived in 1960s[1]. The presence of the CR was experimentally detected using techniques such as pitot tubes[18] and hot wire anemometry[19]. The reversal of the radial velocity in the CR was unexpected and was initially considered to be an artifact of the measurement inaccuracy[19]. The detailed experimental study by Savino and Keshok[20] however confirmed the radial velocity reversal in the bulk of the disc part of the GVU[20]. It also revealed that the CR occupies a major part of the GVU disc volume (Fig. 1(b)). The authors postulated that the CR develops in the GVU due to entrainment of the bulk flow gas by the near-wall jets that develop in the boundary layers adjacent to the two end-walls of the unit. Initial tracer experiments were carried out using air bubbles and concentrated milk powder to visualize the CR in between the end-walls of the GVU[21]. It was observed that when a strong swirl component is imparted to the injected gas, a persistent “donut”-shaped, toroidal ring of tracers is formed in the bulk disc part of the GVU. The author concluded that, since the tracer particles were retained inside the cavity for prolonged times, the bulk region of the GVU is devoid of any net radially inward gas flow. That is, all injected gas actually flows through two boundary layers formed near the end-walls of the unit. As the observations were mostly visual, the author associated the CR with zero radial velocity rather than flow reversal. Laser Doppler Anemometry (LDA) measurements of GVU flow turbulence confirmed that at high Reynolds numbers (Re~7000-13000) the swirling flow in the GVU is highly turbulent[22]. The turbulent kinetic energy of the gas increases radially inwards along the disc part of the unit and peaks upon entering the exhaust region. To better understand the complex GVU flow hydrodynamics, analytical models describing the azimuthal and radial velocity distributions in the GVU were formulated and compared the results with experimental data[20,21,23]. Although the model predicted GVU bulk flow quantities well, the disagreement between the model and experimental data near the end-walls resulted in speculation on the accuracy of the experimental measurements close to the end-walls. Intrusive flow measurement techniques such as pitot tubes or yaw probes disrupt the flow, while techniques such as LDA and PIV have limited accuracy in the near-wall regions due to wall reflections. Hence, a numerical investigation into the complex secondary flow hydrodynamics in the GVU becomes essential.

Initial simulations were performed using a laminar approximation of the GVU flow and a finite difference methodology[24,25]. The simulations qualitatively showed that the swirl structure in the GVU is irrotational in nature in the bulk flow rather than solid-body rotational. The effect of varying gas injection slot angles was investigated. With increasing swirl, the radial flow reversal was located close to the chamber outer periphery. However, as the model used a laminar approximation, its accuracy was limited to low Reynolds numbers. Turbulent flow simulations, using the two-parameter k-ε turbulence model in radially converging confined flows, demonstrated that turbulence modeling is crucial in predicting the flow field[26]. Radially converging non-swirling flow results in flow laminarization due to acceleration. In the presence of swirl, the boundary layers in the GVU for a given Re become comparatively thinner, intensifying the local turbulence production near the walls and increasing the numerical complexity of turbulence modeling in the GVU. One major drawback of the two-parameter eddy viscosity models is that the scalar eddy viscosity cannot account for the turbulent anisotropy arising from the strong streamline curvature in the GVU. Second order turbulence models such as the Reynolds Stress Model (RSM) prove to be highly applicable in this regard. A turbulence model such as RSM directly solves the Reynolds stresses in the flow field and captures the effect of streamline bending on turbulence. A successful implementation of RSM turbulence modeling in GVU simulations by Vatistas et al.[27] demonstrated the capability of Computational Fluid Dynamics (CFD) software FLUENT® to predict both bulk and secondary flows in the GVU. Their numerical results quantitatively agreed with the experimental data thus strongly validating the numerical code[27].

The present work provides an in-depth analysis of swirling flows and more specifically the associated secondary flow phenomena in GVUs. Two-dimensional (2D) axisymmetric simulations of an azimuthal plane of the GVU are performed with the commercial finite volume software package FLUENT® v 14.0. Incompressible steady-state simulations are performed using the RSM turbulence modeling approach. The numerical model is first validated with experimental data provided by Stereoscopic Particle Image Velocimetry (SPIV) and surface oil flow visualization in a GVU setup in the authors' laboratory. Additionally, a comparison is made between swirl-free purely radially converging flow and swirling flow in the GVU.

3.2 Methodology

3.2.1 GVU setup description

The schematic of the GVU experimental setup simulated in the present work is shown in Fig. 1(a).

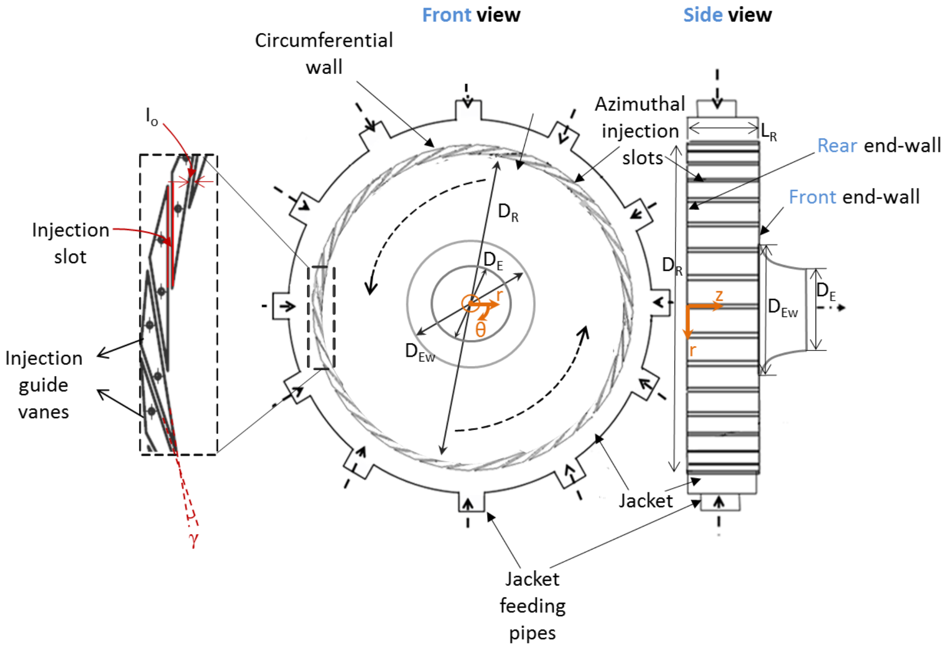

(a)

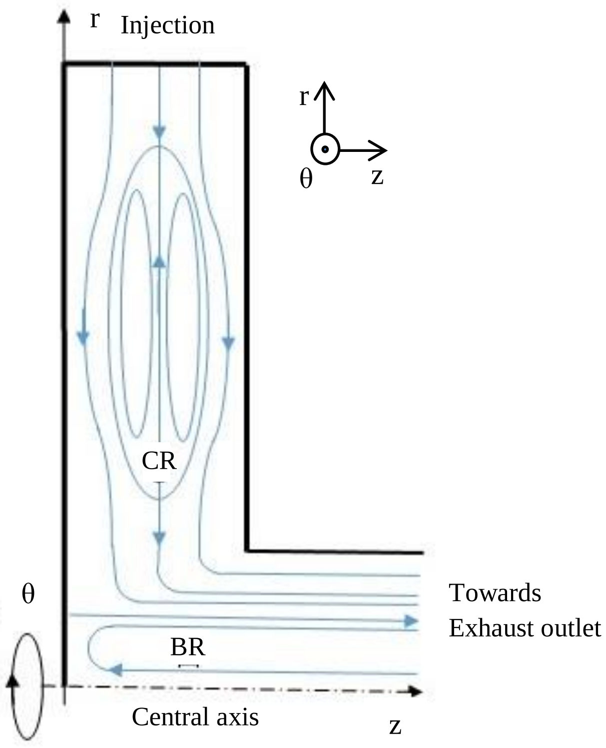

(b)

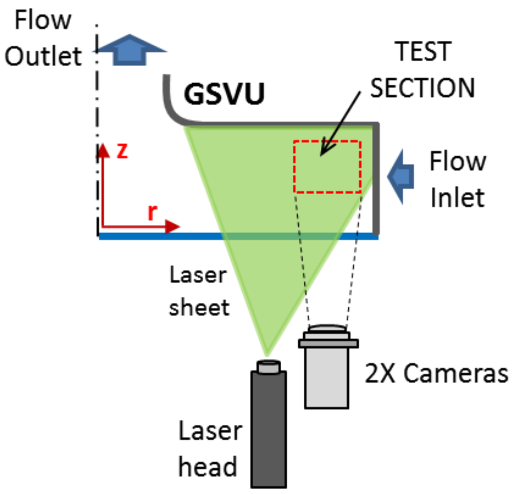

(c)

Fig. 1. (a) Schematics of the front and side view of the experimental GVU. (b) Schematic of secondary flows in the GVU along an azimuthal plane. (c) Schematics of the experimental Stereo PIV configuration on a side view of the GVU. Dimensions are provided in Table 1.

The GVU consists of a disc-shaped confined static geometry positioned along a horizontal axis. The geometrical dimensions of the experimental GVU can be found in Table 1. Pressurized gas (in the presented study, air: ρ=1.225 kg/m^3, μ=1.75x10^{-5} kg/m-s) is sent through twelve feeding pipes into a distributor jacket. From the jacket, the gas is directed into the main unit through 36 equidistant injection slots uniformly located along the circumferential wall of the unit. The slots are azimuthally inclined at an angle of 10º, thereby imparting a strong azimuthal velocity component to the injected gas. The gas spirals inwards in the disc part and leaves the unit axially through a centrally located unidirectional exhaust. Under the specified operating conditions, the gas velocities obtained in the geometry are lower than 0.3 Mach number (Ma), and hence the flow is considered to be incompressible.

Table 1. Geometrical Dimensions of Experimental GVU

GVU geometrical dimensions:	
GVU Jacket diameter	0.7 m
GVU Circumferential wall diameter	0.54 m
GVU exhaust diameter	0.15 m
GVU length	0.1 m
Number of injection slots	36
Slot width	0.002 m
Exhaust line length	1 m

Fig. 1(c) shows the Stereoscopic Particle Image Velocimetry (SPIV) measurement configuration, with two cameras that are angularly positioned to measure the three gas velocity components on a single laser sheet illuminating a two-dimensional azimuthal plane passing through the GVU. In order to measure the gas flow field, tracer oil droplets are injected along with the gas from the injection slots in the GVU. The size of the droplets is chosen such that the Stokes number is less than 1, ensuring that the droplets follow the azimuthal gas flow. The SPIV technique is useful in getting a visual proof of the presence of the Counterflow Region and validating the numerical technique used in the presented study. Also, it is the first time in literature that a two-dimensional visualization of the CR on an azimuthal plane in the GVU is attempted using the SPIV technique. However, as shown in the present study, the experimental technique has its own limitations. In fast-swirling flow the large centrifugal force increases the measuring error in the radial direction. The significantly denser oil tracer droplets are subject to stronger centrifugal forces as compared to the gas molecules, causing a radially outwards shift in the SPIV measured radial and axial flow fields. This is further explained in the results and discussions section.

3.2.2 Numerical model

In the present study, steady 2D axisymmetric flow simulations in an azimuthal (θ=constant) plane of the GVU are performed, using the commercial CFD software package Fluent 14.a®. The simulated plane corresponds to a GVU section shown in Fig. 1(b). The effect of the gravitational force on the flow hydrodynamics is negligible due to the low gas density and the dominant centrifugal force. Hence gravity is not considered in the present study. The axisymmetric assumption is considered valid, based on previous work (Niyogi et al., 2016), where it was shown that the use of multiple equidistant injection slots (36) uniformly distributes the gas in the GVU and makes the flow nearly axisymmetric even in the vicinity of the injection slots. The no-slip boundary condition is imposed at the end-walls of the GVU. The Reynolds Averaged Navier-Stokes (RANS) turbulence modeling approach is adopted, as the main goal of the present work is to obtain ensemble-averaged GVU hydrodynamics. Turbulence modeling for highly swirling flows can be challenging. Swirling flows often encounter high streamline curvature and the Reynolds stresses exhibit anisotropy owing to this curvilinear motion. Two-parameter eddy-viscosity turbulence models quantify turbulence using a scalar in the form of turbulent viscosity and fail to account for the directional dependence of the turbulent stresses[27]. Hence, the Reynolds Stress Model (RSM) is used in the present study as it directly calculates the Reynolds stresses in the flow domain, and captures the turbulence anisotropy. The governing conservation and turbulence model equations are presented in Table 2.

Table 2. Steady-State Transport Equations for GVU Flow

Mass Conservation Equation:	
$\frac{\partial(U_i)}{\partial x_i} = 0$	2.1
Reynolds-averaged Momentum Conservation Equation:	

$$\frac{\partial(U_iU_j)}{\partial x_i} = -\frac{1}{\rho}[\frac{\partial P}{\partial x_i} + \frac{\partial\left[\mu\left(\frac{\partial U_i}{\partial x_j}+\frac{\partial U_j}{\partial x_i}-\frac{2}{3}\delta_{ij}\frac{\partial U_i}{\partial x_i}\right)\right]}{\partial x_j} + \frac{\partial\left(-\rho\overline{u_i'u_j'}\right)}{\partial x_j}] \tag{2.2}$$

Reynolds Stress Equation:

$$\frac{\partial(U_k\overline{u_i'u_j'})}{\partial x_k} = \frac{1}{\rho}\frac{\partial(\frac{\mu_t}{\sigma_k}\frac{\partial(\overline{u_i'u_j'})}{\partial x_k})}{\partial x_k} + \frac{1}{\rho}\frac{\partial[\mu\frac{\partial(\overline{u_i'u_j'})}{\partial x_k}]}{\partial x_k} - \left(\overline{u_i'u_j'}\frac{\partial U_j}{\partial x_k} + \overline{u_j'u_k'}\frac{\partial U_i}{\partial x_k}\right) + \frac{1}{\rho}\overline{p(\frac{\partial u_i'}{\partial x_j}+\frac{\partial u_j'}{\partial x_i})} - \frac{2}{3}\delta_{ij}\varepsilon \tag{2.3}$$

Pressure-strain Equation: (Wilcox, 1988)

$$\begin{aligned}
&pressure-strain\ term\ (\Phi_{ij}) = \frac{1}{\rho}\overline{p(\frac{\partial u_i'}{\partial x_j}+\frac{\partial u_j'}{\partial x_i})}\\
&\Phi_{ij} = -(C_1\rho\epsilon + C_1^*P)b_{ij} + C_2\rho\epsilon\left(b_{ik}b_{kj} - \frac{1}{3}b_{mn}b_{mn}\delta_{ij}\right) + \left(C_3 - C_3^*\sqrt{b_{ij}b_{ij}}\right)\rho k S_{ij}\\
&\qquad + C_4\rho k\left(b_{ik}S_{kj} + b_{jk}S_{ik} - \frac{2}{3}b_{mn}S_{mn}\delta_{ij}\right) + C_5\rho k\left(b_{ik}\Omega_{jk} + b_{jk}\Omega_{ik}\right)\\
&where,\\
&Reynolds-stress\ anisotropy\ tensor\ \left(b_{ij}\right) = -\left(\frac{\rho\overline{u_i'u_j'} + \frac{2}{3}\rho k\delta_{ij}}{2\rho k}\right)\\
&mean\ strain\ rate\ \left(S_{ij}\right) = \frac{1}{2}\left(\frac{\partial U_i}{\partial x_j} + \frac{\partial U_j}{\partial x_i}\right)\\
&mean\ rate-of-rotation\ tensor\ \left(\Omega_{ij}\right) = \frac{1}{2}\left(\frac{\partial U_i}{\partial x_j} - \frac{\partial U_j}{\partial x_i}\right)
\end{aligned} \tag{2.4}$$

$(\mathrm{C}_1{=}3.4,\ \mathrm{C}_1^* = 1.8, \mathrm{C}_2 = 4.2, \mathrm{C}_3 = 0.8, \mathrm{C}_3^* = 1.3, \mathrm{C}_4 = 1.25, \mathrm{C}_5 = 0.4)$

Dissipation Rate Equation:

$$\frac{\partial(\varepsilon U_i)}{\partial x_i} = \frac{1}{\rho}\frac{\partial}{\partial x_j}\left[\left(\mu + \frac{\mu_t}{\sigma_\varepsilon}\right)\frac{\partial\varepsilon}{\partial x_j}\right] C_{\varepsilon 1}\frac{1}{2}P_{ij}\frac{\varepsilon}{k} - C_{\varepsilon 2}\frac{\varepsilon^2}{k} \tag{2.5}$$

$(\sigma_\varepsilon{=}1.0,\ C_{\varepsilon 1}{=}1.44,\ C_{\varepsilon 2}{=}1.92)$

By virtue of an initial systematic mesh study, the optimal mesh for resolving the primary and secondary flow characteristics in the GVU is found to consist of 200,000 quadrilateral cells as shown in Fig. 2.

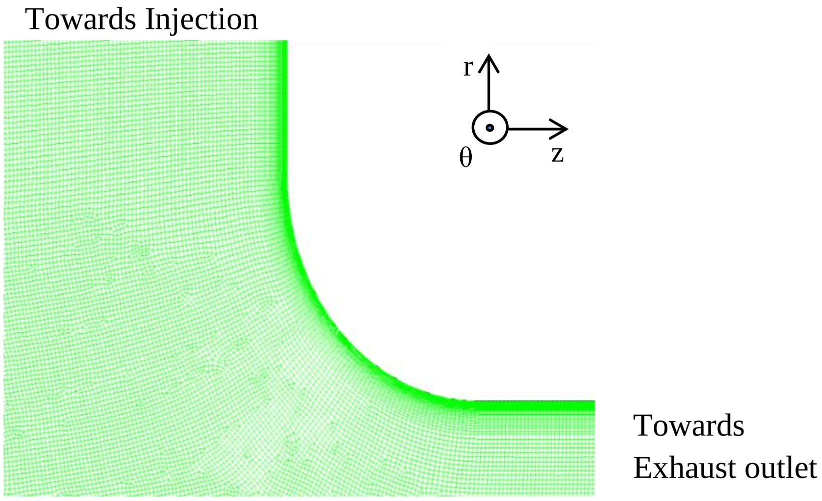

Fig. 2. Zoomed-in section of the mesh in an axisymmetric azimuthal plane (θ=constant) of the GVU geometry highlighting the inflation layers used along the wall to capture the thin boundary layer. Dimensions are provided in Table 1.

The cell size varies from 1 mm in the bulk region to approximately 0.001 mm inflation layer cells near the GVU end-walls. The inflation layers are added near the end-walls to accurately capture the near-wall flow. Mesh resolution results in wall y^+ values of the order of 1. The automatic wall treatment, implemented through the Stress-omega RSM turbulence model applies enhanced wall treatment for resolving the flow near the walls of the geometry. The turbulence model and wall modeling used in the present study is validated in great detail with experimental data for both the near-wall and bulk flow quantities in a previous publication from the authors' group[28]. The measured and calculated radial profiles of the azimuthal velocity component in the GVU bulk flow were shown to quantitatively agree, indicating that the numerical model correctly predicts bulk flow hydrodynamics in the GVU. The velocity streamlines obtained from simulations were compared with the oil droplet tracks on the rear end-wall of the GVU. The qualitative and quantitative agreement between the two sets of data validated the applicability of the numerical model in the boundary layers in the near-wall regions as well. Thus the simulations of GVU flow were validated both in the bulk region and close to the end-walls in the boundary layers in the unit.

3.2.3 Solution methodology

A second-order accurate spatial discretization scheme is applied to solve the momentum and turbulence equations. Pressure corrections are computed using the body force weighted Pressure Staggering Option (PRESTO!) scheme. To solve the set of equations the segregated pressure-based Semi-Implicit Method for Pressure-Linked Equations (SIMPLE) algorithm[29] is used. The scaled residuals in the mass and momentum balances are set to 10^{-5} as condition for convergence. The simulations are performed on an AMD-based Linux 16-core clusters. One simulation for the 2D axisymmetric GVU flow requires about 2 hours of CPU time. The simulation data are exported to MS Excel® and Tecplot® v.2015 for post-processing and further analysis.

3.3 Results and discussions

3.3.1 GVU flow characterization

The azimuthally inclined injection of the gas in the GVU imparts a strong swirling motion in the disc part of the GVU while the overall gas mass flow rate through the unit is radially inwards. Moreover, as the circumferential flow surface area of the GVU decreases with decreasing radius, the superficial radial gas velocity increases as the gas approaches the central exhaust in order to maintain constant mass flow rate through consecutive cross-sectional flow areas. Meanwhile, the azimuthal gas velocity in the bulk flow increases with decreasing radius exhibiting a flow pattern similar to a potential vortex-sink behavior[30]. The no-slip condition at the end-walls causes both the radial and azimuthal velocity components to drop to zero in the near-wall boundary layers. The azimuthal velocity decrease from the bulk flow value to zero in the boundary layers shows a monotonic smooth profile. In contrast, the radial velocity profile changes counter-intuitively. Sharp peaks of the radial velocity in the form of near-wall jets appear near the end-walls[20]. The converging radial flow, the high degree of swirl and the presence of the end-walls result in the formation of near-wall boundary layers, thus resulting in a highly complicated flow pattern in the GVU geometry. To better understand all these flow phenomena, it is helpful to decouple the effects of the converging radial throughput and the swirl. This is achieved by defining two control parameters in the form of characteristic numbers describing the GVU flow.

The first parameter is the *radial Reynolds number (Re)* which is defined as

$$Re = \frac{\rho_g U_{r,i} L}{\mu} = \frac{\rho_g G_M L}{A_i \mu} \tag{1}$$

where $U_{r,i}$ is the superficial radial gas velocity component at the GVU injection slots, G_M is the gas mass flow rate, L is the length of the unit, A_i is the circumferential area at injection and ρ and μ are the density and dynamic viscosity of the operating gas respectively. For a given aspect ratio of the geometry and a given gas mass flow rate, Re remains constant, independent of the degree of swirl in the flow.

The second control parameter is the *swirl ratio (S)*, defined as

$$S = \frac{U_{\theta,i}}{U_{r,i}} \tag{2}$$

where, $U_{\theta,i}$ is the azimuthal gas velocity component at the GVU injection. An S value of 0, for a given Re, corresponds to a swirl-free flow through the unit. Remark that S is indicative of the injection angle (α) of the injection slots. An increase in S, at constant Re, imparts a higher degree of swirl to the flow in the GVU for a constant gas mass flow rate. It is interesting to mention here that at high Re values, the flow becomes predominantly convective and the viscous contribution of gas becomes negligible making the flow topology independent of Re. In contrast, a variation of S can significantly change the flow topology even at high Re values. More detailed elaboration on this topic is presented further in the manuscript.

Since the main focus of the present work is to investigate highly swirling flow features in the GVU, S is set to be greater than 1 for most simulation cases. However, it is instructive to first investigate a swirl-free flow (S=0) case for reasons of comparison.

3.3.2 Swirl-free flow in the GVU (Re=13700; S=0)

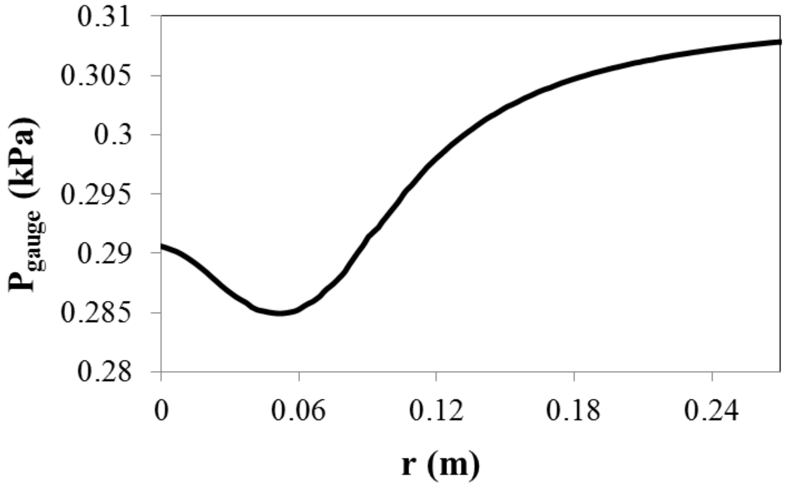

(a)

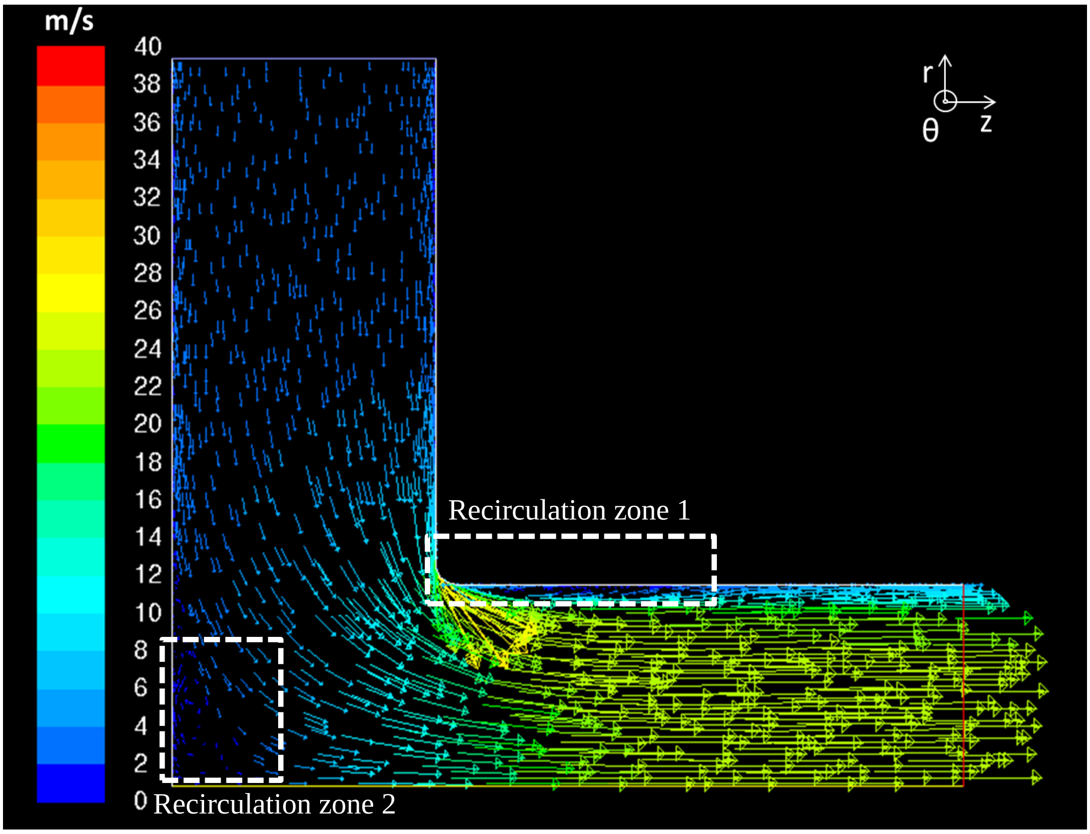

(b)

Fig.3. (a) Radial profile of static gauge pressure along z=0.05 m, calculated by solving the set of Eqs. (2.1)–(2.5) given in Table 2, and (b) in-plane velocity vector field along axisymmetric azimuthal plane, calculated by solving the set of Eqs. (2.1)–(2.5) given in Table 2, under operating conditions (G_M=0.4 kg/s, Re=13700, S=0). Color indicates the velocity magnitude of the gas.

Fig. 3(a) shows the calculated radial gauge pressure profile along the centerline (z=0.05m) of the GVU for swirl-free, purely radially converging flow. The positive pressure gradient ($\partial P/\partial r > 0$) from the circumferential wall to the central exhaust of the disc ($0.06 < r < 0.27$m) directs the injected gas towards the exhaust. The figure shows that in the exhaust region ($r < 0.06$m) an adverse pressure gradient develops. In order to understand the origin of this adverse pressure gradient, the in-plane gas velocity vector field along the azimuthal plane is plotted in Fig. 3(b). It can be seen from the figure, that the radially converging gas experiences a strong streamline curvature from the radial to the axial direction in the exhaust region in order to align the flow with respect to the central exhaust line. This streamline bending compounded with the high Re flow results in the formation of two local recirculation regions, highlighted in Fig. 3(b). As the radially converging gas reaches the exhaust line, the bulk flow makes a 90° anticlockwise turn, causing a local flow separation just downstream of the point of intersection of the exhaust wall and the front end-wall (z=0.1 m) of the unit. This results in the development of an adjacent thin recirculation region (Recirculation zone 1, Fig. 3(b)). The drastic change in the flow direction causes the flow to locally accelerate in accordance with the inviscid flow theory[30]. The color change of the velocity vectors in the vicinity of the abovementioned intersection, shown in Fig. 3(b), highlights this increase in the gas velocity. The flow acceleration decreases the local static pressure in the vicinity of the intersection, and generates an adverse pressure gradient after the exhaust bend, resulting in the formation of a local Recirculation zone 1.

The second recirculation zone develops near the intersection of the rear end-wall of the disc and the axis of the unit (Recirculation zone 2, Fig. 3(b)). The gas approaches the axis at high Re condition which causes flow separation near the axis due to the streamline curvature of the flow. The flow separation generates an adverse pressure gradient and a local pressure maximum near the axis-wall intersection, corresponding to the inviscid fluid theory, as seen in the radial pressure profile ($r < 0.06$m) in Fig. 3(a). The elevated pressure values direct the gas away from the rear end-wall (z=0.1 m), resulting in the formation of a local recirculation zone. Remark that this zone remains confined to the vicinity of the GVU rear end-wall and does not extend extensively into the exhaust line. Recirculation zone 2 does not significantly constrict the area for gas flow in the exhaust.

Fig. 4(a) shows the axial profile of the radial velocity at different radial positions in the disc part of the unit. As the flow approaches the exhaust the radial velocity of the gas increases with decreasing radius.

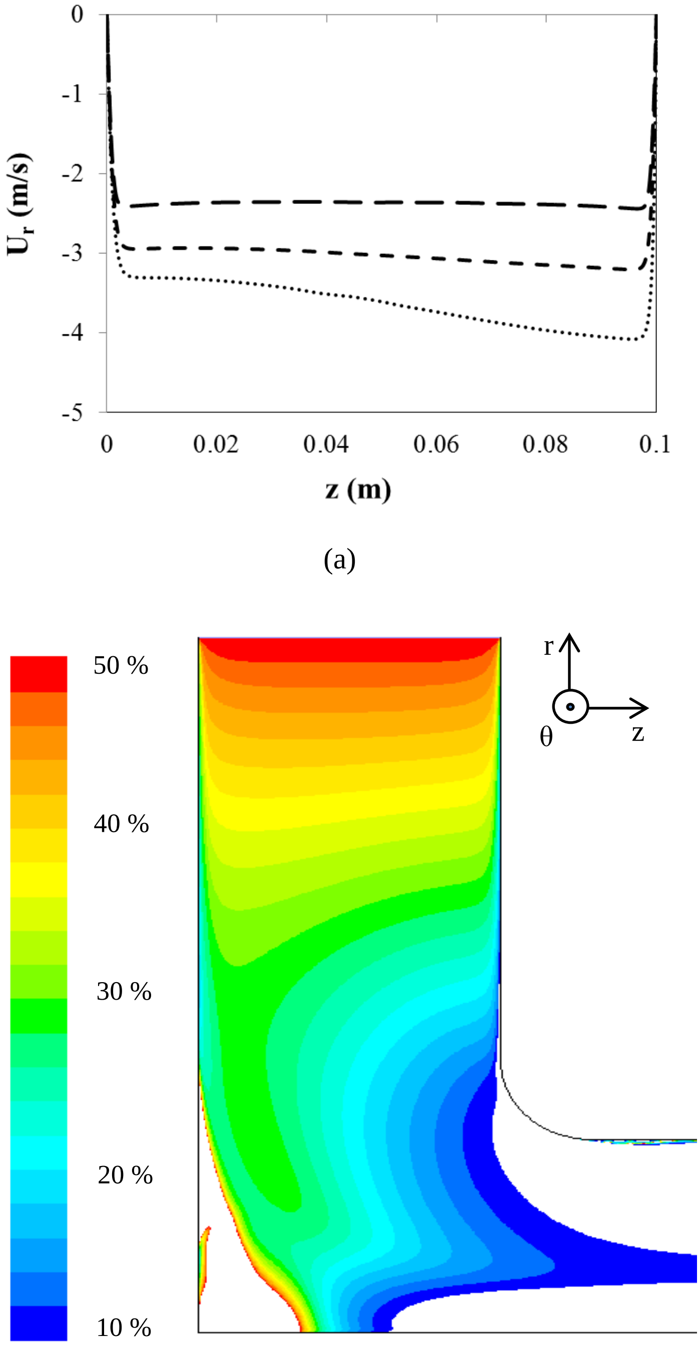

(a)

(b)

Fig.4. (a) Axial profile of radial velocity at different radii in the GVU, (b) contours of turbulent intensity in the azimuthal GVU plane calculated by solving the set of Eqs. (2.1)–(2.5) given in Table 2 under operating conditions (G_M=0.4 kg/s, Re=13700, S=0).

This flow acceleration causes the radial velocity profile to be nearly uniform over almost the entire length of the unit (at r=0.23 m and 0.18 m). Only in the thin boundary layers formed near the two end-walls, the no-slip boundary condition causes the radial gas velocity to monotonically decrease to zero, as can be seen more clearly in the zoomed-in near-wall profiles in Fig.5.

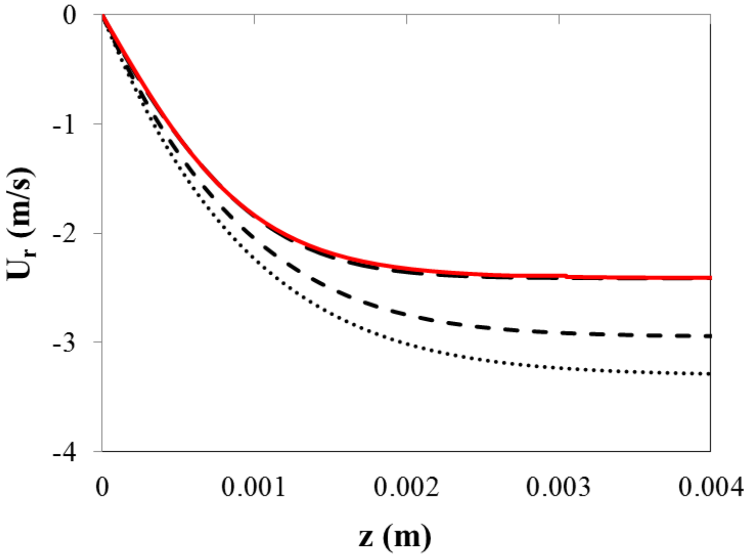

Fig.5. Zoomed-in axial profile of radial velocity close to the rear end-wall at different radii in the GVU: (-) r=0.23 m; (---) r=0.18 m; (···) r=0.15 m, calculated by solving the set of Eqs. (2.1)–(2.5) given in Table 2 under operating conditions (G_M=0.4 kg/s, Re=13700, S=0). Full line represents the analytical solution curve for radial velocity profile calculated by solving Eq. (9).

Further downstream, closer towards the exhaust, the axial symmetry of the radial velocity profile with respect to the centerline (z=0.05 m) breaks. Suction generated due to the flow acceleration near the intersection of the front end-wall (z=0.1 m) and the exhaust increases the radial velocity near the front end-wall (z=0.1 m) as compared to the rear end-wall (z=0).

For swirl-free flow in the GVU, the radial flow acceleration significantly affects the turbulent characteristics of the gas as well. In converging flows, fluid acceleration results in relaminarization of the turbulence in the downstream direction[10]. The kinetic energy required by the mean flow to accelerate is obtained from its turbulent counterpart. Hence the turbulence gradually decreases downstream. The gradually reducing circumferential area in the GVU geometry in the direction of flow represents a similar converging flow scenario. Hence, the acceleration of the radial velocity is expected to cause flow relaminarization in a swirl-free GVU flow. To test this hypothesis, the contours of turbulent intensity in the disc part of the unit are plotted in Fig. 4(b). The turbulent intensity, set at 5% at the injection, is seen to decrease downstream in the GVU disc part, confirming flow relaminarization. The non-colored region in Fig. 4(b) near the rear end-wall of the unit towards the central axis corresponds to the high turbulence region due to the presence of Recirculation zone 2. As turbulence significantly increases in this part of the geometry, Recirculation zone 2 is excluded from the turbulence intensity color map in order to capture the lower values in the turbulence field in the disc part of the GVU. Owing to this laminar nature (turbulence intensity < 5%) of swirl-free flow in the GVU, an analytical solution of the velocity profile in the near wall boundary layer regions can be obtained.

For radially converging sink flow, mass conservation yields

$$U_r(bulk) = -\frac{Q}{2\pi r L} = -\frac{f_0}{r} \tag{3}$$

where Q is the volumetric gas flow rate and f_0 is a constant for a given gas flow rate and unit length. This equation remains valid for the bulk flow inside the GVU disc part, except in the vicinity of the end-walls where boundary layers develop as the radial velocity, U_r, drops to zero. The pressure field in the unit is linked with the velocity field through the Navier-Stokes equation in the radial direction as shown in Table 2, Eq. 1.2. In radial direction the equation reduces to

$$\rho U_r \frac{\partial U_r}{\partial r} = -\frac{\partial P}{\partial r} + \mu\left[\frac{1}{r}\frac{\partial}{\partial r}\left(r\frac{\partial U_r}{\partial r}\right) - \frac{U_r}{r^2} + \frac{\partial^2 U_r}{\partial z^2}\right] \tag{4}$$

for swirl-free steady flow.

At high Re, the bulk flow is dominantly convective in nature and viscous contributions can be neglected, simplifying Eq. 4 to

$$\frac{\partial P}{\partial r} = -\rho U_r \frac{\partial U_r}{\partial r} = \frac{\rho {f_0}^2}{r^3} \tag{5}$$

Over the boundary layer, the radial velocity can be expressed as $U_r = -f(z)/r$. Since dP/dr is nearly uniform across the boundary layer, its bulk-flow value, $dp/dr = \rho f_0^2/r^3$ can be used henceforth. Combining all, Eq. 5 results in

$$\frac{(f_0^2 - f^2)}{r^3} = -\frac{\nu f_{zz}}{r} \tag{6}$$

where $\nu = \mu/\rho$ is the kinematic viscosity of the gas and the subscript "zz" denotes the second order derivative with respect to z. Since the boundary layer thickness is small compared to the radial coordinate in the GVU, r can be approximated by a local value r_0 (say, $r_0 = 0.23$ m). Introducing the dimensionless variables $\varphi = f/f_0$, and $\zeta = ((f_0/\nu)^{1/2} z)/r_0$ transforms Eq. 6 into

$$\varphi_{\zeta\zeta} = \varphi^2 - 1 \tag{7}$$

where the subscript "ζ" denote the differentiation with respect to ζ. The boundary conditions are $\varphi = 0$ at $\zeta = 0$ (no-slip) and $\varphi \to 1$ as $\zeta \to \infty$ (the radial velocity tends to its bulk value). Multiplying all terms of Eq. 7 with φ_ζ and integrating results in

$$\frac{{\varphi_\zeta}^2}{2} = \frac{\varphi^3}{3} - \varphi + \frac{2}{3} \tag{8}$$

where the last term on the right hand side of the equation is an integration constant satisfying the boundary condition, $\varphi \to 1$ as $\zeta \to \infty$. One more integration, satisfying the no-slip condition yields that

$$\zeta = \int \left(\frac{4}{3} - 2u + 2\frac{u^3}{3}\right)^{-\frac{1}{2}} du \tag{9}$$

where the integration runs from 0 to φ.

In Fig. 5 this analytical solution (red line) for r=0.23m is compared with the corresponding radial velocity profile obtained from the numerical simulations (dashed). As can be seen from the figure, the two profiles match quantitatively, validating that laminarization holds for swirl-free (S=0) flow. Eq. 9 demonstrates that for swirl-free flow in the GVU, due to the relaminarization phenomenon, an analytical solution of the near-wall transformation of the radial velocity can be obtained.

3.3.3 Swirling flow in the GVU (Re=13700; S=5, 12)

3.2.3.1 Bulk flow hydrodynamics

Adding an azimuthal velocity component to the injection of the GVU significantly alters the flow pattern in the unit. As the superficial radial velocity, or the gas mass flow rate for incompressible flow at injection remains constant, Re remains unchanged and the net throughput in the unit remains constant. However, a finite injection swirl ratio imparts additional azimuthal momentum to the gas causing it to start spiraling towards the exhaust. The larger the swirl ratio, the higher is the number of rotations the gas completes inside the disc part of the geometry before exiting through the central exhaust. Since the value of S is always considered to be higher than 1 in the present study, the gas undergoes multiple *complete* rotations in the unit before reaching the exhaust. Fig. 6 shows the radial profile of the azimuthal velocity component along the centerline (z=0.05m) in the steady-state swirl flow inside the unit.

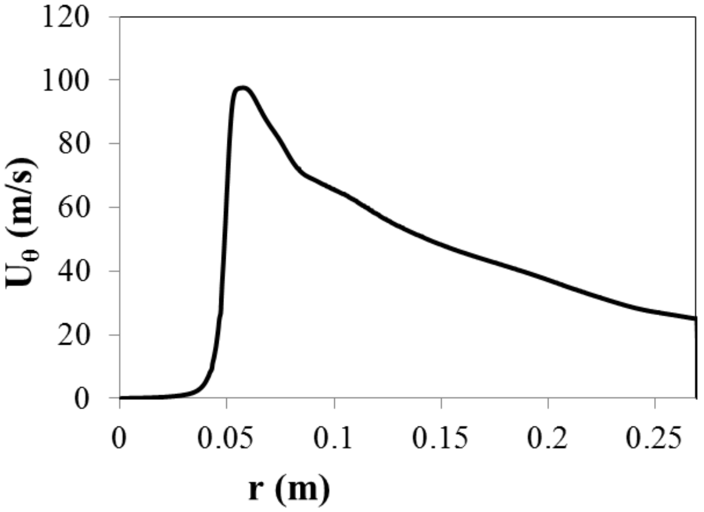

Fig.6. Radial profile of azimuthal velocity along z=0.05 m, calculated by solving the set of Eqs. (2.1)–(2.5) given in Table 2 under operating conditions (G_M=0.4 kg/s, Re=13700, S=12).

In the disc part of the unit (0.075<r<0.27m) the azimuthal velocity component increases with decreasing radius. This flow behavior has been shown previously to *qualitatively* represent free-vortex flow, where the gas angular momentum is nearly conserved in radial direction (Niyogi et al., 2016). The quantitative deviation of the azimuthal velocity profile from the hyperbolic free-vortex flow profile arises from the fact that the friction losses encountered by the gas at the end-walls reduce U_θ to some extent[31]. However, the qualitative trend of increasing U_θ with decreasing radius is retained. In the exhaust region of the unit (0<r<0.0075m), the BR and an intense turbulence develop (discussed in a subsequent section) causing the swirling structure to break. This explains the steep drop in the azimuthal velocity component for r < 0.06 m observed Fig. 6.

3.2.3.2 Formation of backflow in the exhaust line of the GVU

Fig. 7(a) shows the radial profile of the static gauge pressure along the unit centerline (z=0.05m). Compared to the swirl-free flow (Fig. 3(a)), the pressure drop over the disc part significantly increases for when swirl is imparted to the flowing gas. This increase in pressure drop across the unit partly arises from a balance between the centrifugal force generated on the gas and the radial pressure drop, and partly arises due to the formation of an extended BR in the exhaust line as explained below.

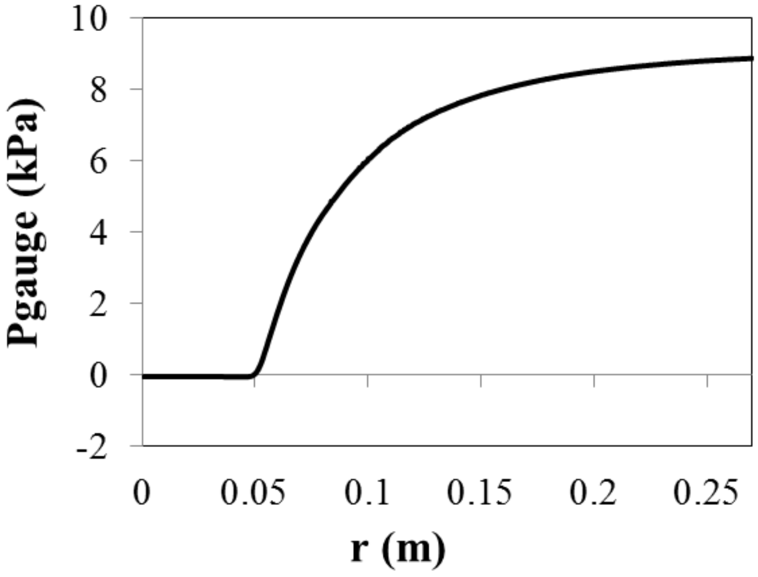

(a)

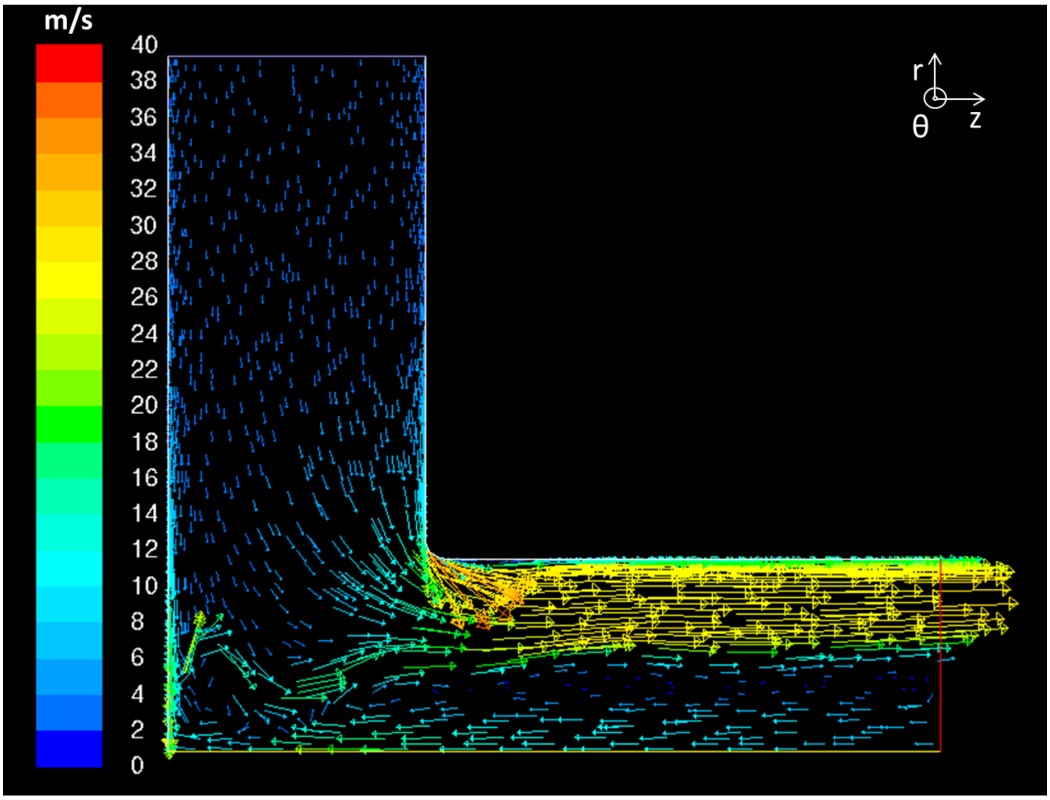

(b)

Fig.7. (a) Radial profile of static gauge pressure along z=0.05 m, calculated by solving the set of Eqs. (2.1)–(2.5) given in Table 2, and (b) in-plane velocity vector field along axisymmetric azimuthal plane, calculated by solving the set of Eqs. (2.1)–(2.5) given in Table 2, under operating conditions (G_M=0.4 kg/s, Re=13700, S=12). Color indicates the velocity magnitude values of the gas.

The velocity vector field along the azimuthal plane for swirling flow in the GVU is shown in Fig. 7(b) for S=12. Two interesting phenomena can be observed. First, Recirculation zone 1 near the exhaust wall as seen in Fig. 3(b) significantly diminishes in size. For the swirling flow case, the gas exiting the GVU geometry through the exhaust possesses a high degree of azimuthal velocity component. This azimuthal velocity of the gas generates a centrifugal force which is sufficiently large to push the gas elements towards the wall of the exhaust line causing Recirculation zone 1 to diminish. The second interesting feature that Fig. 7(b) highlights is the presence of an elongated BR along the central axis of the unit over the entire simulated exhaust line, denoted by velocity vectors directed in the reverse direction (from the exhaust outlet to the rear end-wall of the unit). This BR extends along the entire exhaust line, in contrast to the small Recirculation zone 2 for swirl-free flow, which remains restricted to the vicinity of the rear end-wall of the unit (Fig. 3(a)). The extended BR is not merely a result of the streamline bending near the axis of the unit. Its origin can be traced back to the decay mechanism of the swirling motion of the gas due to friction with the wall of the exhaust line of the unit. In Fig. 8, the azimuthal velocity component of the gas is found to decrease along the exhaust line.

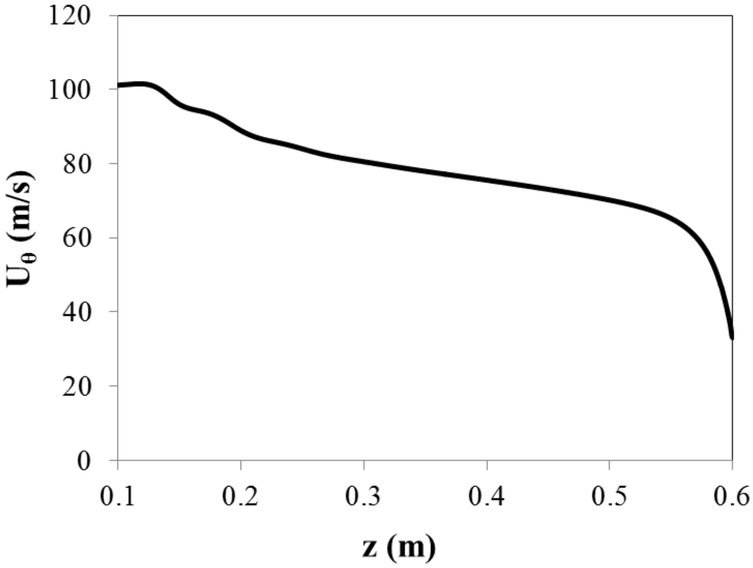

Fig.8. Axial profile of azimuthal velocity along r=0.06 m, calculated by solving the set of Eqs. (2.1)–(2.5) given in Table 2 under operating conditions (G_M=0.4 kg/s, Re=13700, S=12).

The velocity profile suggests that in the initial section of the exhaust line, near z=0.1 m, the gas is swirling comparatively stronger with respect to the gas near the outlet of the exhaust line (z=0.6 m). A swirling vortex possesses a static pressure minimum at its center on the axis of rotation[10]. The stronger the rotation of the elements, the lower is the local pressure at the axis. Naturally it follows, that the stronger swirling structure near z=0.1 m reduces the local static gauge pressure value at the GVU axis at z=0.1 m to a lower value than the near-axis pressure value at z=0.6 m. This reverse pressure gradient along the axis of the unit causes flow reversal by sucking ambient gas into the exhaust line and pushing it towards the rear-end wall of the unit. This flow reversal constitutes the BR in the GVU as seen in Fig. 7(b). One of the major consequences of this BR is that its presence considerably constricts the net flow surface area in the exhaust line available for the gas to leave the unit. This flow area constriction is one of the causes for the overall pressure drop increase across the unit, as seen in Fig. 7(a).

As previously mentioned, another reason for the pressure drop increase can be attributed to the influence of the centrifugal force on the pressure-velocity coupling in the GVU swirling flow. To better understand this mechanism, the radial steady-state Navier-Stokes equation in cylindrical coordinates is analyzed. The Navier Stokes equation (Table 2, Eq. 1.2) can be expressed in radial coordinates as

$$\rho(U_r \frac{\partial U_r}{\partial r} + \frac{U_\theta}{r}\frac{\partial U_r}{\partial \theta} - \frac{U_\theta^2}{r} + U_z \frac{\partial U_r}{\partial z}) = -\frac{\partial P}{\partial r} + \mu[\frac{1}{r}\frac{\partial}{\partial r}\left(r\frac{\partial U_r}{\partial r}\right) - \frac{U_r}{r^2} + \frac{1}{r^2}\frac{\partial^2 U_r}{\partial \theta^2} - \frac{2}{r^2}\frac{\partial U_\theta}{\partial \theta} + \frac{\partial^2 U_r}{\partial z^2}] \qquad (10)$$

As the GVU flow can be considered to be axisymmetric, the azimuthal velocity and the azimuthal gradients can be neglected. The viscous contribution can also be neglected as, given the high Re, the flow is highly convective in nature. For axisymmetric swirl-free flow through the GVU (S=0), the centrifugal acceleration term ($\frac{U_\theta^2}{r}$) is absent and the pressure drop over the GVU unit can be approximated as

$$\frac{\partial P}{\partial r} = -\rho(U_r \frac{\partial U_r}{\partial r} + U_z \frac{\partial U_r}{\partial z}) \qquad (11)$$

Fig. 9(a) validates these assumptions by comparing the pressure gradient obtained from numerical simulations to the pressure gradient as computed from Eq. 11. Excellent agreement is seen between the two curves.

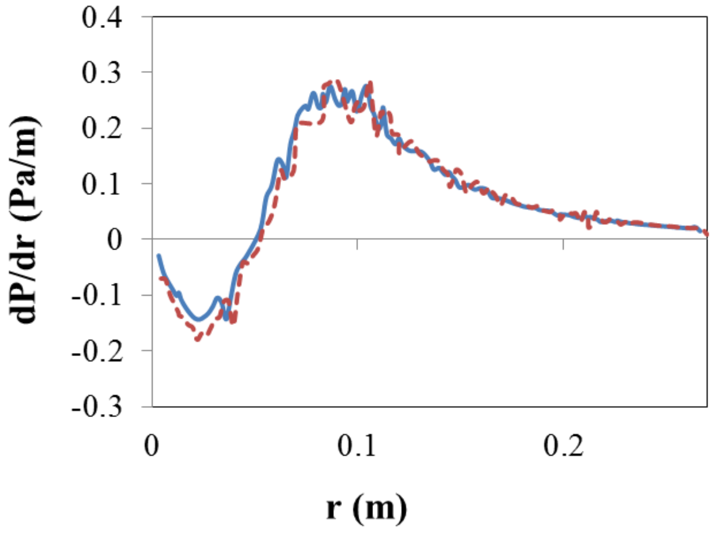

(a)

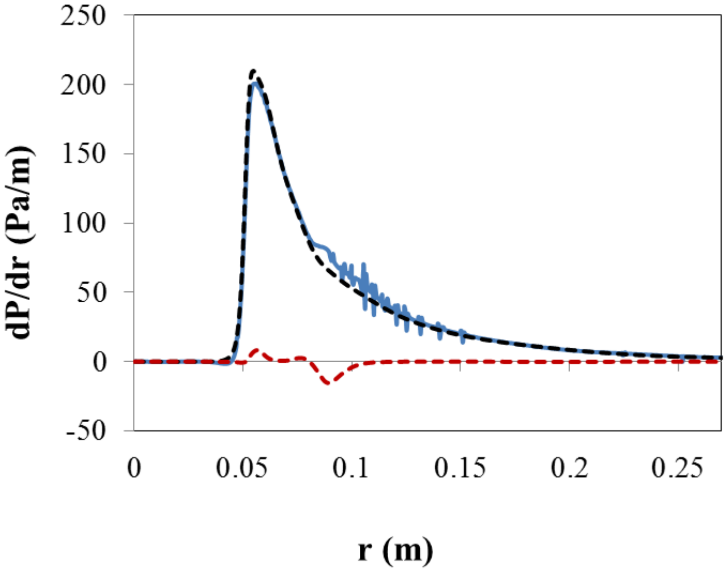

(b)

Fig. 9. (a) Radial profile of static pressure gradient along z=0.05 m: (---) calculated by solving Eq. (2); full line, from numerical simulation, calculated by solving the set of Eqs. (2.1)–(2.5) given in Table 2 under operating conditions (G_M=0.4 kg/s, Re=13700, S=0), and (b) radial profile of static pressure gradient along z=0.05 m: (---) calculated by solving Eq. (2); (---) calculated by solving Eq. (4); full line, from numerical simulation, calculated by solving the set of Eqs. (2.1)–(2.5) given in Table 2 under operating conditions (G_M=0.4 kg/s, Re=13700, S=12).

When swirl is introduced in the GVU flow (S=12), the centrifugal acceleration term is retained in Eq. (10), resulting in

$$\rho(U_r\frac{\partial U_r}{\partial r}+U_z\frac{\partial U_r}{\partial z}-\frac{U_\theta^2}{r})=-\frac{\partial P}{\partial r} \tag{12}$$

To understand the extent of influence of the centrifugal term on the overall pressure drop of the unit, Fig. 9(b) is plotted. The figure separately compares the pressure drop obtained from simulations of swirling GVU flow with the contribution from the centrifugal acceleration term $(\frac{U_\theta^2}{r})$ in Eq. 12 on the one hand, and the radial and axial velocity gradient terms $(U_r\frac{\partial U_r}{\partial r}+U_z\frac{\partial U_r}{\partial z})$ in Eq. 12 on the other hand. The figure shows that the contribution of the centrifugal term significantly exceeds its radial and axial counterparts, and singularly accounts for the entire pressure drop over the disc part of the unit. This helps to simplify Eq. 12 further, resulting in the cyclostrophic balance, given by

$$\rho \frac{U_\theta^2}{r} = \frac{\partial P}{\partial r} \tag{13}$$

Thus, the high azimuthal velocity imparted to the flowing gas in the GVU increases the unit pressure drop as compared to swirl-free flow (S=0). This effect, compounded with the reduction of the cross-sectional flow surface area near the exhaust due to the formation of the BR, elevates the total pressure drop across the GVU for the swirling flow case.

3.2.3.3 Formation of counterflow in the disc part of the GVU

In the bulk flow through the disc part of the GVU, the cyclostrophic balance (Eq. 13) between the *radially inwards* pressure force and the *radially outwards* centrifugal force on the gas holds well. However, the cyclostrophic balance does not hold in the close vicinity of the end-walls due to the boundary layer formation[28]. Imposing the no-slip boundary condition sets the azimuthal velocity component to zero at the end-walls, as seen in Fig. 10 where the axial profile of the scaled azimuthal velocity is plotted for r=0.21m.

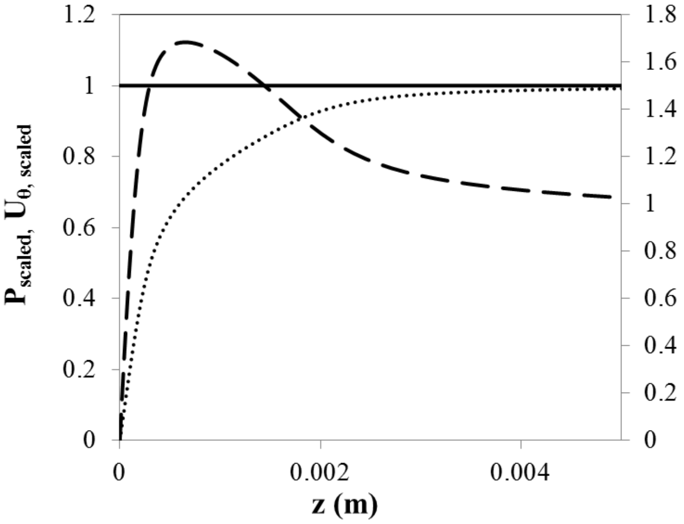

Fig. 10. Axial profiles of scaled static gauge pressure and azimuthal velocity and normalized radial velocity at r=0.21 m: (•••) azimuthal velocity, scaled by its maximum value along GVU length at r=0.21 m, calculated by solving Eq. (3); (---) radial velocity, normalized by the superficial velocity at

r=0.21 m cross-sectional surface area in the GVU; full line, static gauge pressure, scaled by its maximum value along GVU length at r=0.21 m, calculated by solving the set of Eqs. (2.1)–(2.5) given in Table 2 under operating conditions (G_M=0.4 kg/s, Re=13700, S=12).

Since U_θ diminishes in the boundary layers, there is in a corresponding drop in centrifugal force exerted on the gas elements. In contrast, the static gauge pressure remains unaffected by the near-wall boundary layer. The scaled static gauge pressure profile in the near-wall region in Fig. 10 illustrates this. For convenient comparison, both the static gauge pressure and the azimuthal velocity in Fig. 10 are scaled with respect to their maximal values along the length of the unit at r=0.21m. The drop in the centrifugal force near the end-walls causes the cyclostrophic balance to break. The gas in this region is directed radially inwards by the unbalanced pressure gradient. The monotonic near-wall profile of the radial velocity in swirl-free flow (S=0), seen in Fig. 4(a), is lost resulting in the development of a local radial velocity peak in the vicinity of each end-wall boundary layer. This local radial velocity peak near the rear end-wall can be seen in Fig. 10, where the radial velocity, normalized by the superficial radial velocity at r=0.21m, is plotted along the length of the unit. The near-wall peaks in the radial velocity profile when swirl is introduced in the GVU flow are referred to as the near-wall jets. More details regarding the physics and experimental proof regarding the near-wall jet formation in the GVU can be found in previous work by the authors[28].

The axial profiles of the radial velocity component of the gas at r=0.21m are shown in Fig. 11(a) for two different swirl ratio cases S=5 (solid line) and S=12 (dashed line). The figure shows that for a comparatively lower degree of swirl (S=5), the effect of the near-wall jets remains confined to the close vicinity of the end-walls. The radial velocity in the bulk flow for S=5 is slightly lower than the superficial gas velocity magnitude (2.47 m/s) at the given cross-sectional area (r=0.21m) to account for the excess gas entrained by the near-wall jets.

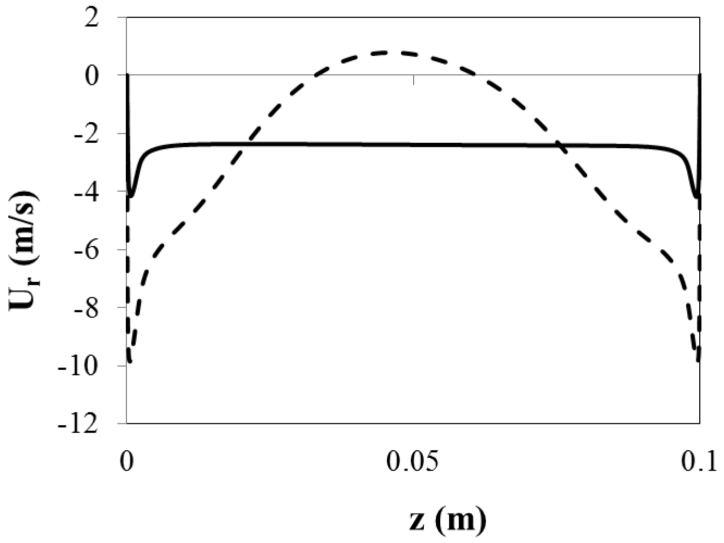

(a)

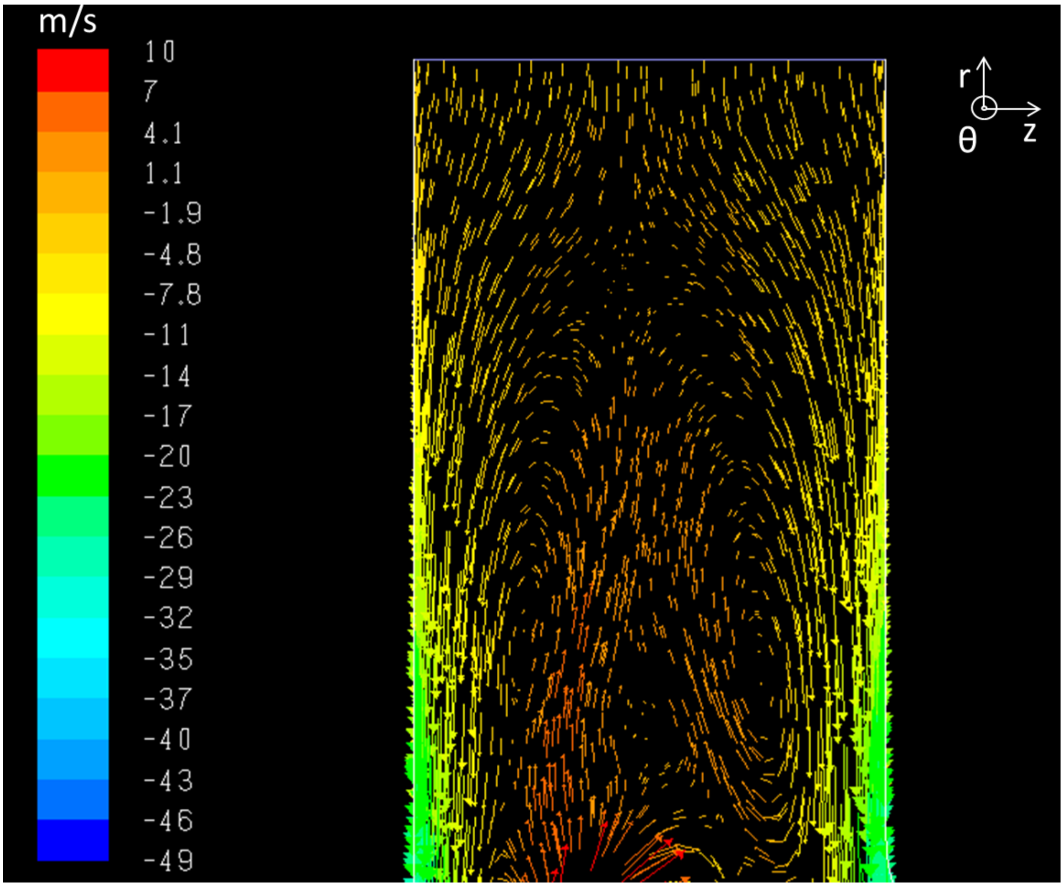

(b)

Fig.11 (a) Axial profile of radial velocity along r=0.21 m for different swirl ratios: (---) S=12; full line S=5, calculated by solving the set of Eqs. (2.1)–(2.5) given in Table 2, and (b) in-plane velocity vector field along axisymmetric azimuthal plane, calculated by solving the set of Eqs. (2.1)–(2.5) given in

Table 2, under operating conditions (G_M=0.4 kg/s, Re=13700, S=12). Color indicates radial velocity values of the gas.

However, the radial velocity along the entire length of the unit remains negative as seen in Fig. 11(a) indicating that the gas flow throughout the entire length of the unit remains radially inwards. However, for an increased value of the swirl ratio (S=12), the near-wall jets become stronger as indicated by the radial peak velocity magnitudes in Fig. 11(a). As a consequence, the jets entrain a higher volume of gas along with them towards the central exhaust. Also, Fig. 11(a) reveals that the radial velocity in the bulk region for S=12 becomes positive indicating a local flow reversal, from the central axis towards the GVU injection. This radial flow reversal between the two end-walls of the GVU constitutes the CR. Fig. 11(b), showing the in-plane velocity vector field in an azimuthal plane, helps to visualize this CR. In the figure it can be seen that a pair of counter-rotating vortices develop in the bulk region of the flow. Remark that, in the entire disc part of the GVU, the azimuthal velocity component still remains the dominant velocity component. It is one order of magnitude higher than the corresponding local radial velocity component (not shown). This implies that the 2D representation of the CR as seen in Fig. 11(b) is actually an in-plane projection of a toroidal ring-like 3D structure in the GVU geometry.

The CR in the GVU has previously been observed in literature through pitot tube measurements[20]. However, this intrusive experimental technique could provide velocity data only at specific sections of the geometry, and at the expense of disrupting the local flow phenomena. The authors clearly demonstrated how immensely challenging it is to experimentally quantify the CR and produced an in-plane velocity field as shown in Fig. 12(b). Nonetheless, obtaining experimental data on secondary flow phenomena in the GVU is highly crucial for the validation of simulated GVU hydrodynamics as in the present study. Hence, the more rigorous SPIV technique is adopted for the first time in literature to validate the numerical model used to simulate counterflow fields. Fig. 12 compares the experimental in-plane (axial and radial) velocity streamlines along the azimuthal plane of the GVU generated using SPIV (Fig. 12(a)) with those obtained from the simulations (Fig. 12(b)).

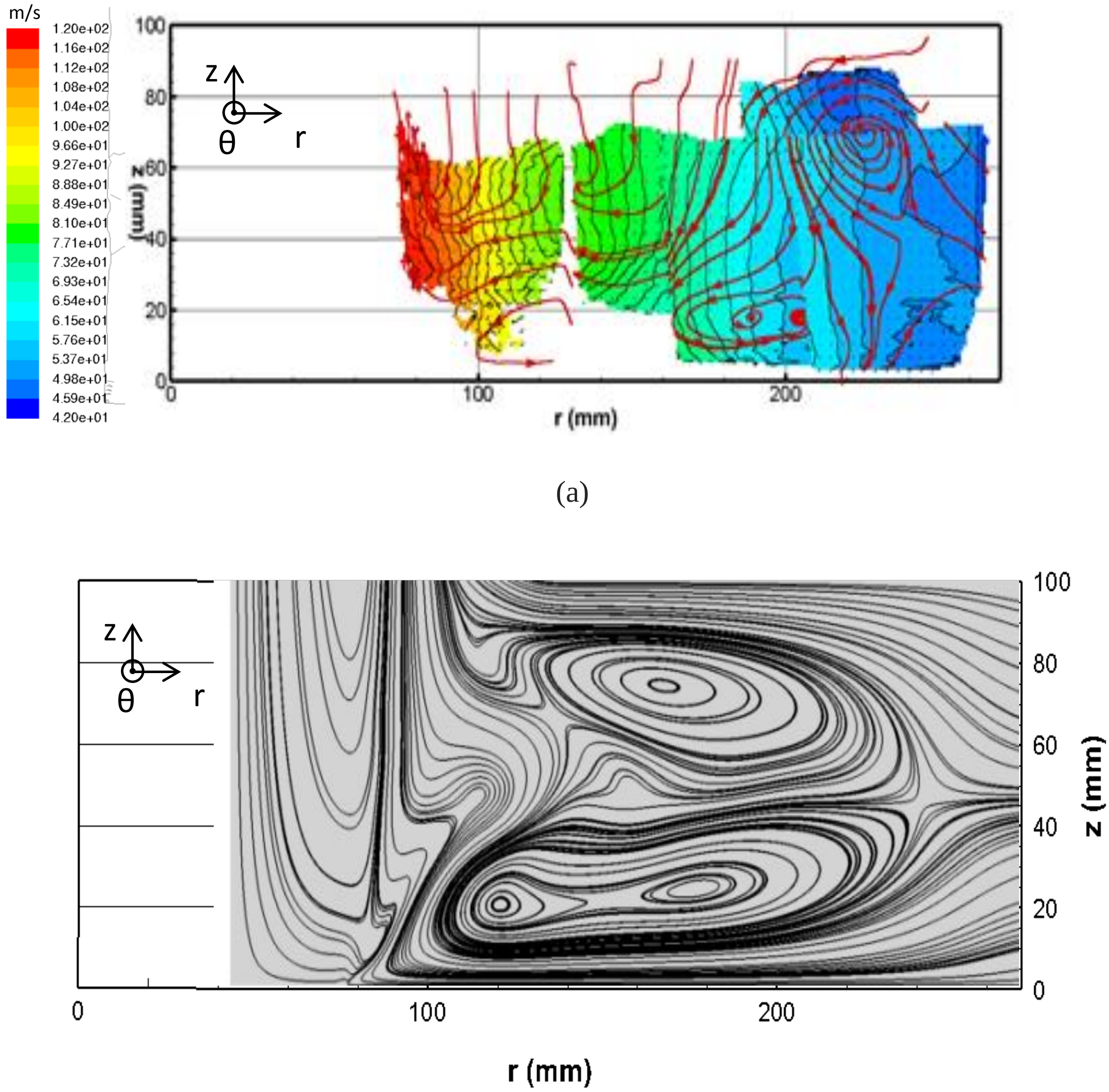

(a)

(b)

Fig. 12. In-plane velocity streamlines along the azimuthal plane (θ=20°), from (a) SPIV measurements (color contours represents azimuthal velocity values) and (b) numerical simulation calculated by solving the set of Eqs. (2.1)–(2.5) given in Table 2.

The experimental and simulated streamlines both show the formation of counter-rotating vortices and radially outwards reverse flow in the bulk region in between the end-walls of the unit. However, the *quantitative* agreement between experiment and simulation is not completely satisfactory. The authors believe that this discrepancy can be explained as follows. The Stokes number for the tracer droplets being less than 1 is a strong indication that the droplets will follow the gas along the main velocity component direction which, in the case of the swirling GVU flow, is azimuthally oriented. It is questionable, however, whether the tracer droplets will accurately follow the bulk gas flow in the radial and axial direction. The axial and radial velocity components (0.5-2 m/s) in the bulk region of the GVU are two orders of magnitude smaller than the azimuthal velocity (45-100 m/s). The magnitude of the radial and axial velocities in the bulk flow are so low that they may be in the inaccuracy range of SPIV measurements (3% for azimuthal velocities). It is known from literature that the SPIV error can be high for radial velocity measurements in highly swirling flows[32] due to the tracers In the bulk region, the centrifugal force on a gas element is balanced by the radial pressure gradient (Eq. 13). The centrifugal force acting on an oil droplet, however, is significantly higher and is not balanced by the radial pressure gradient. The latter results in a radially outward shift towards the circumferential wall of the in-plane velocity field (axial and radial) of tracer droplets in an azimuthal plane. Comparing the in-plane (radial and axial) velocity fields in Fig. 12(a) and (b) confirms this conjecture. Nevertheless, the SPIV data qualitatively capture the presence of a CR in the bulk of the GVU without any measurement intrusion into the flow field, validating the numerical prediction of the recirculation region. Moreover, the numerical results compare well with the velocity flow fields obtained in previous numerical studies[27].

The presence of near-wall jets significantly alters the turbulence characteristics of the swirling GVU flow. Fig. 13(a) shows the profile of the turbulent intensity along the length of the unit at r=0.21 m for S=12. It can be seen that close to the two end-walls of the unit, high turbulence production takes place. These regions correspond to the locations where the near-wall jet peaks are located.

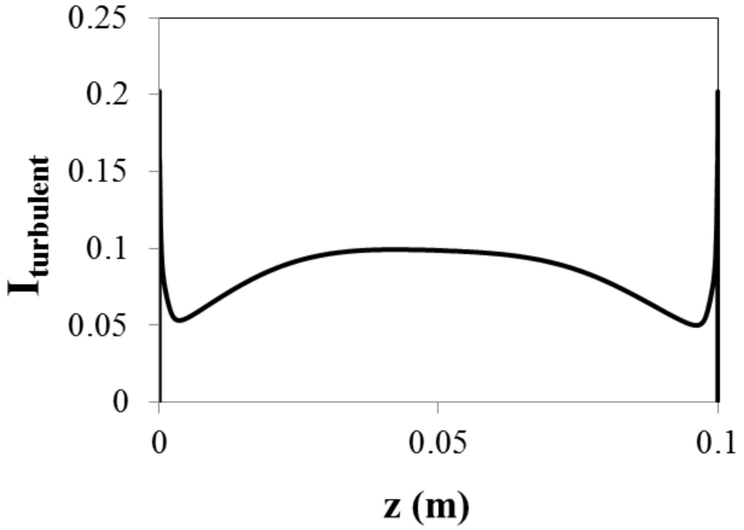

(a)

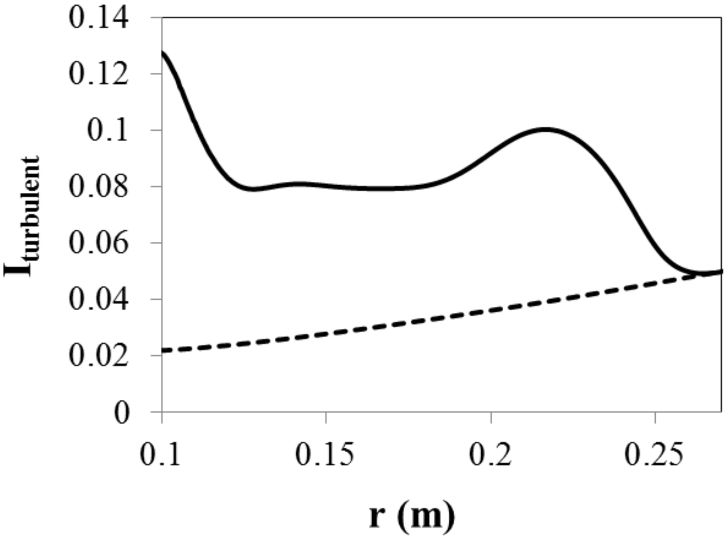

(b)

Fig.13. (a) Axial profile of turbulence intensity along r=0.21 m for S=12 and (b) radial profile of turbulent intensity along z=0.05 m for different swirl ratios: (---) S=0; full line S=12, calculated by solving the set of Eqs. (2.1)–(2.5) given in Table 2, under operating conditions (G_M=0.4 kg/s, Re=13700).

The jets result in high velocity gradients in the end-wall boundary layers. The corresponding intense shear between the gas layers results in turbulence production. Due to such high values of turbulence, the near-wall axial profile of the radial velocity can no longer be analytically derived, as was possible for the swirl-free (S=0) GVU flow (Eq. 9). Furthermore, the presence of the CR significantly alters the turbulence characteristics in the bulk flow as well. Fig. 4(b) has already demonstrated the relaminarization effect of flow acceleration on swirl-free (S=0) flow in the GVU. Fig. 13(b), comparing the turbulence intensities of swirl-free (S=0) and swirling (S=12) GVU flow, attests to this observation. The turbulent intensity, set at 5% at injection, decreases with decreasing radius for swirl-free flow (S=0). In strongly swirling flow (S=12) however, the CR prevents the downstream flow from laminarizing. The turbulent intensity increases with decreasing radius as the solid curve in Fig. 13(b) illustrates. The turbulent intensity shows a local maximum near r=0.22 m for S=12. For reasons of comparison this cross-section is highlighted in Fig. 11(b). By comparing Fig. 11(b) and 13(b), it is seen that the turbulent intensity maximum coincides with the GVU region where the injected gas stream meets the reverse flowing (radially outwards flowing) gas that is brought in by the counterflow vortices. This collision of oppositely directed streams results in the formation of a flow stagnation saddle point and generates high shear rates resulting in a significant turbulence production. As the gas flow approaches the central exhaust it collides with the boundary of the BR causing turbulence to increase once again at the interface.

Fig. 11(a) indicates that for a given Re, the swirl ratio S will have a cutoff value above which the CR develops (no CR for S=5, Fig. 11(a)). To investigate the operating conditions for the emergence of the counterflow phenomenon, it is instructive to compare the injection gas flow rate in the GVU on the one hand, and the gas entrainment flow rate by the near-wall jets on the other hand. To this end, Fig. 14 shows the *cumulative* gas flow rate calculated from the rear to the front end-wall of the GVU plotted along the unit length, at r=0.21m for S=0, 5 and 12.

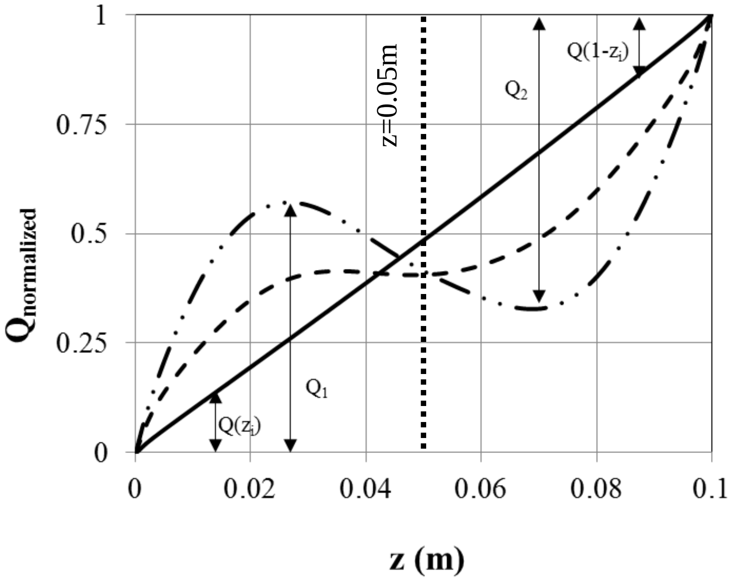

Fig.14. Axial profile of cumulative normalized gas flow rate along r=0.21 m for different swirl ratios: (-··-) S=12; (---) S=5; full line S=0, calculated by solving the set of Eqs. (2.1)–(2.5) given in Table 2, under operating conditions (G_M=0.4 kg/s, Re=13700). Q_1 and Q_2 denote the jet entrainment flow rate in the GVU.

The gas flow rate at the given radius (r=0.21m), for each swirl ratio, has been normalized by the injected gas flow rate. For swirl-free flow (S=0), the cumulative gas flow rate shows a linear monotonic growth starting from one end-wall (z=0) to the other (z=0.1m). The monotonicity of the curve indicates that the gas flows in one direction only: radially inwards and without any flow reversal.

When limited swirl is introduced in the flow (S = 5), it can be seen from Fig. 14 that the formation of the near-wall jet increases the local gas flow rate near th end-wall due to jet entrainment, causing the cumulative gas flow rate profile to increase more sharply than in the absence of swirl (S = 0). As more gas flows near the walls of the unit, the local flow rate of the gas in the bulk region decreases (Fig. 11(a)), explaining the central plateau in the S = 5 curve in Fig. 14.

For higher swirl ratios (S=12), the cumulative gas flow rate curve loses its monotonic behavior and two extrema are formed on both sides of the centerline (z=0.05m) as seen in Fig. 14. The formation of an extremum in the cumulative gas flow rate curve is indicative of the flow reversal resulting in the formation of the CR in the bulk flow through the disc part of the GVU. The near-wall jets entrain the adjacent gas thus causing a steep rise in the cumulative gas flow rate near the end-wall until a maximum is reached. Counterflow in the bulk causes the local radial gas velocities to reverse direction and change sign, such that the local gas flow rates are “subtracted” from the cumulative gas flow rate. This explains the decrease in the cumulative gas flow rate profile seen for S=12 in Fig. 14. After crossing the centerline (z=0.05m), the radial gas velocities again change direction on reaching the other boundary of the CR towards the front end-wall, and the second extremum appears in Fig. 14. The peak value Q_1=0.572 achieved at around z=0.027 m, equals the normalized gas flow rate entrained by the jet located near the rear end-wall, while Q_2=0.672, achieved at z=0.069 m, is the normalized gas flow rate entrained by the jet adjacent to the front end-wall. The axial distance in between the two peaks corresponds to the CR where the gas flows radially outwards. The sum Q_1+Q_2 is larger than one, indicating that the total jet entrainment flow rate exceeds the injection gas flow rate. This physically implies that at high swirl ratios (S=12), the near-wall jets have become so strong that the injected quantity of gas is not sufficient to feed the jets. Gas is sucked back into the jets from the upstream bulk region resulting in the formation of a CR. The above discussion provides a proper physical explanation regarding the origin of the CR in the GVU flow. A counterflow rate (Q_{cf}) can be further quantified as Q_{cf} = (Q1+Q2-1)*100 (=24.4%). Q_{cf} gives a percentage measure of the jet entrainment overshoot over the injection gas flow rate and characterizes the flow rate of the GVU counterflow.

In the next section, some light is shed on the effect of the swirl ratio and Reynolds number on the formation of these GVU secondary flow features. Fig. 15 shows in great detail the evolution of flow topology in the GVU with increasing swirl ratio. At low values of the swirl ratio (S=5) the gas streamlines become packed near the two end-walls indicating the formation of near-wall jets.

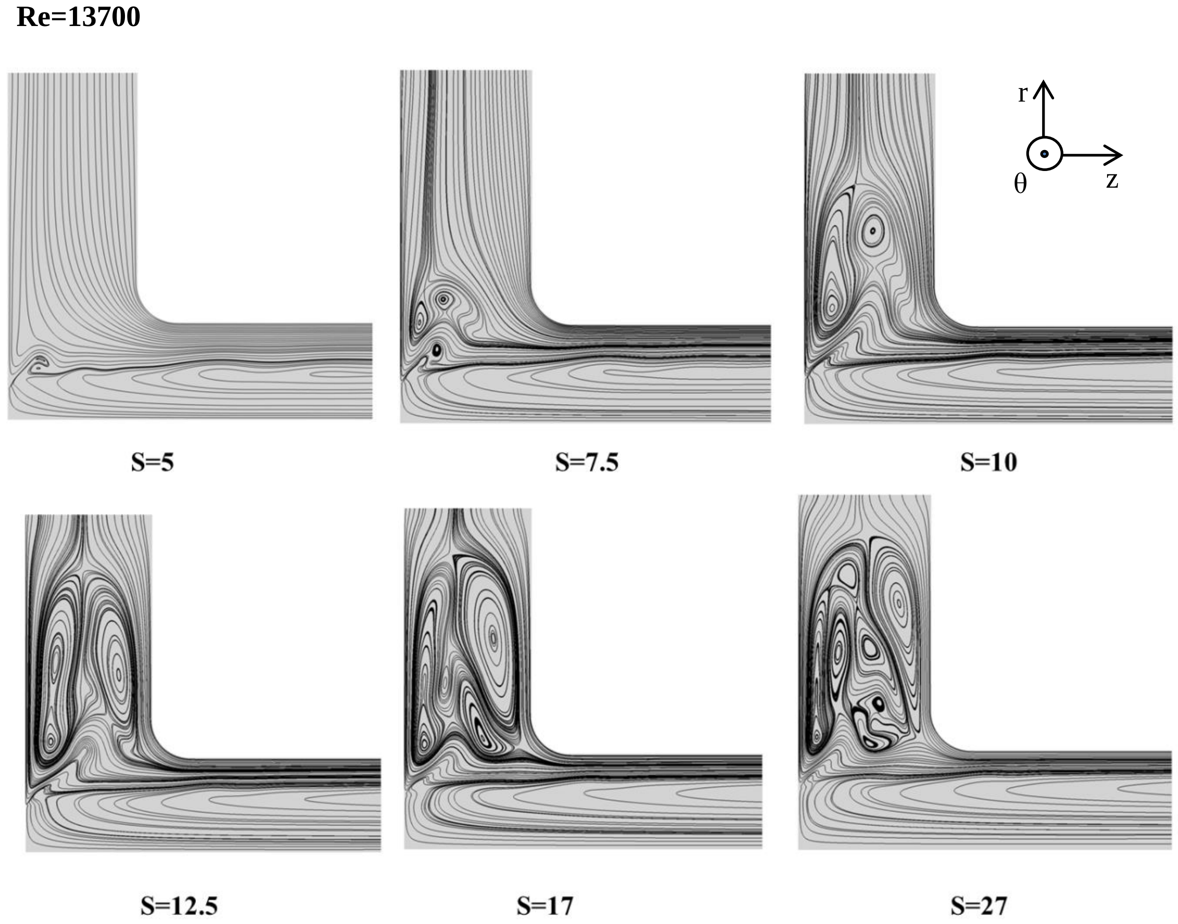

S=5 **S=7.5** **S=10**

S=12.5 **S=17** **S=27**

Fig.15. In-plane velocity streamlines along the azimuthal plane (θ=20°) for different swirl ratios at constant Reynolds number, from numerical simulations calculated by solving the set of Eqs. (2.1)–(2.5) given in Table 2. The colored arrows for S=10 show the flow direction of three branches of gas flow in the disc part of the GVU.

The swirl strength is not yet sufficient to form a CR in the bulk flow of GVU. Nonetheless, in the region near the exhaust, where the inflowing gas from the disc part of the unit and the BR meet, a local eddy formation is observed as the local fluid layers slide over one another. At S=7.5, two counter-rotating vortices are seen to develop in the GVU disc part close to the rear end-wall. The injected gas splits into two branches which encompass the vortices in the CR. The counter-rotating vortices become more elongated and shift towards the circumferential wall, penetrating further into the GVU disc part as the degree of swirl increases, as observed for S =10 case. This shift of the CR from the exhaust region towards the circumferential wall of the unit has also been experimentally reported in previous literature and helps strengthen the prediction from the simulations[21].

The gas through-flow is seen to split into three branches of at these high values of S (highlighted in Fig. 15 (S=10)). The first two branches can be clearly discerned as being attached to either end-wall as they reach the exhaust and leave. The third branch has a more complicated flow path. It initially remains attached to the rear end-wall. When reaching the exhaust region, the third branch turns back towards the circumferential wall and in between the counter-rotating vortices of the CR. Next, the third branch makes a U-turn and converges, now with the second branch near the front end-wall and proceeds radially inwards. Finally it leaves the GVU disc part through the exhaust line.

For S=12.5, the CR further grows and occupies nearly half of the GVU disc part volume. The flow topology, however, is identical to that for S=10. The topology becomes more complicated at S=17 where four vortices are observed in the CR of the GVU. Nevertheless, all vortices constitute a united recirculation domain in the GVU disc part separating the through-flow of the injected gas into two major branches: one adjacent to the rear end-wall and another adjacent the front end-wall.

At S=27, Fig. 15 shows that the overall size of the CR has reached saturation, being bounded: in the axial direction by the two near-wall jets and in the radial direction by the incoming gas flow near the circumferential wall and by the BR near the exhaust. Larger swirl ratios further increase the number of vortices within the Counterflow Region. The plurality of vortices and saddle points indicates the intense mixing within the Counterflow Region which can be beneficial for applications in combustion and chemical vortex devices.

The variation of the GVU flow topology with respect to Re is shown in Fig. 16. For all studied cases, the swirl ratio is set at a value of 12.5. At small Re, no CR occurs (Fig. 16, at Re=3.5).

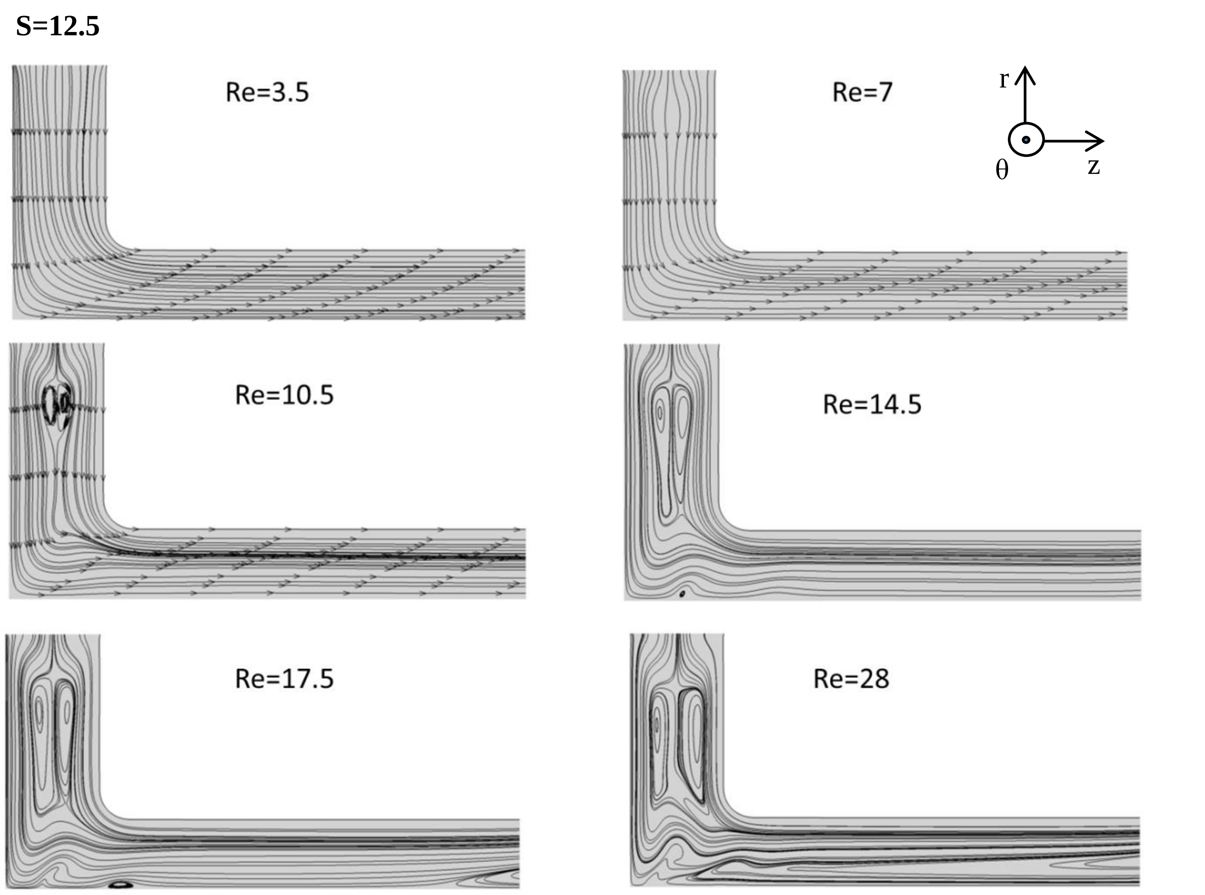

Fig.16. In-plane velocity streamlines along the azimuthal plane (θ=20°) for different Reynolds numbers at constant swirl ratio, from numerical simulations calculated by solving the set of Eqs. (2.1)–(2.5) given in Table 2.

The flow is viscous in nature. No detachment of streamlines is observed near the axis of the GVU. As Re increases, the streamlines downstream of the injection slots in the bulk region of the disc part of the GVU seem to shift towards the end walls (Fig. 16, at Re=7), with an increased packing of streamlines near the two end-walls. This shift of the streamlines suggests entrainment of the bulk gas by the near-wall jets and is a precursor for the emergence of the CR which appears at Re=10.5. The jet entrainment causes a part of the downstream gas to flow back towards the circumferential wall causing the CR to form (Re>10). The CR consists of a pair of counter-rotating vortices. As Re further increases, the counterflow expands radially inwards (Fig. 16, at Re=14.5). This figure also shows the appearance of a small recirculation region at the GVU central axis some distance away from the rear end-wall. The small recirculation is a precursor for the BR. As Re increases the BR develops by the swirl decay mechanism, and gets extended over the entire exhaust line very quickly from Re=14.5 to Re=28 (Fig. 16). As Re further increases, the vortices in the GVU CR become separated by a through-flow branch (Fig. 17, at Re=700).

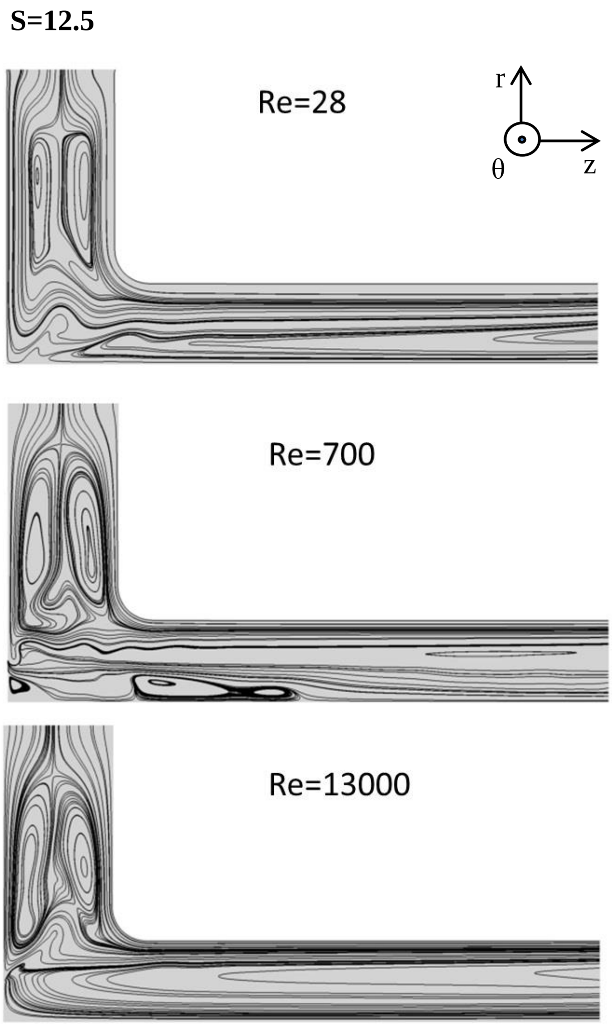

Fig.17. In-plane velocity streamlines along the azimuthal plane (θ=20°) for different Reynolds numbers at constant swirl ratio, from numerical simulations calculated by solving the set of Eqs. (2.1)–(2.5) given in Table 2.

Beyond this Re, however, the flow topology saturates with respect to Re, as can be seen by comparing the in-plane streamlines for Re=7000 and 13000 in Fig. 17. Since Re is usually high in technological applications[8,31], Re=13700 is the range in focus in this study where the flow topology becomes independent with respect to Re, and in turn the gas flow rate through the GVU.

3.4 Conclusion

This paper studies secondary flow phenomena arising due to swirling motion of gas in a Vortex Unit with the help of experimentally validated numerical simulations. Both the formation of a backflow region in the central exhaust and a Counterflow Region in the bulk flow in the disc part of the unit are investigated in detail. The backflow region develops due to the swirl decay mechanism along the exhaust line of the unit. As the gas proceeds through the exhaust line, it loses its azimuthal momentum. An axial pressure gradient is established along the exhaust line due to this difference in swirl structure and causes gas to flow back in the unit. The Counterflow Region in the disc part of the unit appears due to the strengthening of the near-wall jets observed in the unit. The near-wall jets form as a result of the breakdown of the cyclostrophic balance between the radial pressure gradient and the centrifugal force exerted on the gas elements. As the near-wall jets get stronger they entrain the adjacent gas from the bulk causing a local flow reversal. This constitutes the Counterflow Region. A first ever experimental validation of the presence of a Counterflow Region using Stereoscopic Particle Image Velocimetry is carried out to further validate the applied numerical model. To highlight the effect of swirl on the flow topology, first a swirl-free fast flow is numerically explored as a reference. It is shown that the flow acceleration in the GVU disc part causes the injected turbulent flow to get laminarized downstream of the unit without the formation of a counterflow or backflow region. To explore the evolution of the flow topology in the swirling flow, two strategies are applied: (a) the swirl ration S is increased at a fixed gas flow rate, characterized by the Reynolds number Re, and (b) the Reynolds number Re is increased at a fixed swirl ratio S. Increasing Re shows that the topology initially is Re–dependent, shifting from a laminar to a turbulent regime through a short transition zone, and finally becomes viscosity-independent for large Re values (Re>13000), typical of technological applications. Changing S significantly affects the flow topology as the secondary flows are more sensitive to the degree of swirl in the unit. At higher values of S, the Counterflow Region becomes multicellular with multiple vortices appearing. The numerical simulations reveal seven vortices in the GVU disk part at S=27. The plurality of vortices and related saddle stagnation points of the meridional motion should cause the fast and fine mixing of flow ingredients, which is beneficial for a variety of technological applications.

3.5 Acknowledgments

This work was supported by the European Research Council FP7/2007-2013/ ERC grant agreement n° 290793. We are grateful for the use of the Stevin Supercomputer Infrastructure at Ghent University, funded by Ghent University, the Hercules Foundation, and the Flemish Government − department EWI.

3.6 References

1. Ragsdale RG. NASA Research on the hydrodynamics of the gas vortex reactor. 1959; NP-9150 NSA-15-001058.

2. Priestman GH. A Study of Vortex Throttles Part 1: Experimental. Proceedings of the Institution of Mechanical Engineers, Part C: Journal of Mechanical Engineering Science. 1987;201(5):331-336.

3. Loftus PJ, Stickler DB, Diehl RC. A Confined Vortex Scrubber for fine particulate removal from flue gases. Environmental Progress. 1992;11(1):27-32.

4. Cheng JC, Olsen MG, Fox RO. A microscale multi-inlet vortex nanoprecipitation reactor: Turbulence measurement and simulation. Applied Physics Letters. 2009;94(20):204104.

5. Parker D, Birch MJ, Francis J. Computational Fluid Dynamic Studies of Vortex Amplifier Design for the Nuclear Industry—I. Steady-State Conditions. Journal of Fluids Engineering. 2011;133(4):041103.

6. Volchkov ÉP, Dvornikov NA, Lukashov VV, Borodulya VA, Teplitskii YS, Pitsukha EA. Study of swirling gas-dispersed flows in vortex chambers of various structures in the presence and absence of combustion. Journal of Engineering Physics and Thermophysics. 2012;85(4):856-866.

7. Schütz S, Gorbach G, Piesche M. Modeling fluid behavior and droplet interactions during liquid–liquid separation in hydrocyclones. Chemical Engineering Science. 2009;64(18):3935-3952.

8. Pandare A, Ranade VV. Flow in vortex diodes. Chemical Engineering Research and Design. 2015;102:274-285.

9. Council AR. Preliminary Results of Low Speed Wind Tunnel Tests on a Gothic Wing of Aspect Ratio 1.0: H.M. Stationery Office; 1960.

10. Shtern V. Counterflows. Cambridge University Press, 2012.

11. Claypole TC, Syred N. The effect of swirl burner aerodynamics on NOx formation. Symposium (International) on Combustion. 1981;18(1):81-89.

12. Escudier MP, Bornstein J, Maxworthy T. The Dynamics of Confined Vortices. Proceedings of the Royal Society of London. A. Mathematical and Physical Sciences. 1982;382(1783):335-360.

13. Benjamin TB. Theory of the vortex breakdown phenomenon. Journal of Fluid Mechanics. 1962;14(4):593-629.

14. Hall MG. Vortex Breakdown. Annual Review of Fluid Mechanics. 1972;4(1):195-218.

15. Leibovich S. Vortex stability and breakdown - Survey and extension. AIAA Journal. 1984;22(9):1192-1206.

16. Olendraru C, Sellier A. Absolute/Convective Instabilities in the Batchelor Vortex: Viscous Case. Paper presented in: Seventh European Turbulence Conference; 1998; Saint-Jean Cap Ferrat, France.

17. Herrada MA, Shtern VN, Torregrosa MM. The instability nature of the Vogel–Escudier flow. Journal of Fluid Mechanics. 2015;766:590-610.

18. Kendall JMJ. Experimental study of a compressible viscous vortex. NASA. 1962; JPL-TR-32-290.

19. duP Donaldson C, Williamson GG. An Experimental Study of Turbulence in a Driven Vortex: Aeronautical Research Associates of Princeton Incorporated. 1964; AD-0609460 .

20. Savino JM, Keshok EG. Experimental profiles of velocity components and radial pressure distributions in a vortex contained in a short cylindrical chamber. NASA. 1965; TN D-3072.

21. Wormley DN. An Analytical Model for the Incompressible Flow in Short Vortex Chambers. Journal of Basic Engineering. 1969;91(2):264-272.

22. Yan L, Vatistas GH, Lin S. Experimental studies on turbulence kinetic energy in confined vortex flows. Journal of Thermal Science. 2000;9(1):10-22.

23. Kwok CCK, Thinh ND, Lin S. An Investigation of Confined Vortex Flow Phenomena. Journal of Basic Engineering. 1972;94(3):689-696.

24. Hornbeck RW. Viscous flow in a short cylindrical vortex chamber with a finite swirl ratio: NASA Lewis Research Center. 1969; TN-D-5132.

25. Leschziner MA, Hogg S. Computation of highly swirling confined flow with a Reynolds stress turbulence model. AIAA Journal. 1989;27(1):57-63.

26. Singh A, Vyas BD, Powle US. Investigations on inward flow between two stationary parallel disks. International Journal of Heat and Fluid Flow. 1999;20(4):395-401.

27. Vatistas GH, Fayed M, Soroardy JU. Strongly Swirling Turbulent Sink Flow Between Two Stationary Disks. Journal of Propulsion and Power. 2008;24(2):295-301.

28. Niyogi K, Torregrosa MM, Pantzali MN, Heynderickx GJ, Marin GB, Shtern VN. On near-wall jets in a disc-like gas vortex unit. AIChE Journal. 2016; DOI: 10.1002/aic.15533.

29. Patankar SV. Numerical Heat Transfer and Fluid Flow. McGraw-Hill, 1980; New York.

30. Batchelor GK. An Introduction to Fluid Dynamic. Cambridge University Press, 2000.

31. Volchkov EP, Terekhov VI, Kaidanik AN, Yadykin AN. Aerodynamics and Heat and Mass Transfer of Fluidized Particle Beds in Vortex Chambers. Heat Transfer Engineering. 1993;14(3):36-47.

32. Birch DM, Martin N. Tracer particle momentum effects in vortex flows. Journal of Fluid Mechanics. 2013;723:665-691.

Chapter 4

Numerical Study of Gas-Solid Vortex Unit Hydrodynamics

This work was published as:

Experimentally Validated Numerical Study of Gas-Solid Vortex Unit Hydrodynamics

K. Niyogi[1], Maria Torregrosa[1], Maria N. Pantzali[1], Geraldine J. Heynderickx[1*], Guy B. Marin[1]

[1]Ghent University, Laboratory for Chemical Technology, Technologiepark 914, B-9052, Gent, Belgium
*corresponding author

Abstract

A three-dimensional numerical analysis of the flow in a Gas-Solid Vortex Unit (GSVU) is carried out. The numerical model is first validated by comparing the bed pressure drop and solids velocity with experimental data. Next, the influence of gas flow rate, solids density, and particle diameter on the pressure drop, solids velocity, bed void fraction and slip velocity between the two phases is studied. A stable, solids bed is achieved for the entire range of gas flow rates tested (0.1-0.6 Nm3/s). No particle entrainment is observed when varying the solid density (1800-450 kg/m3) or the particle diameter (2-0.5 mm). A shift to bubbling fluidization regime is observed for small particle diameters (0.5 mm). The observed changes in the GSVU flow patterns are discussed by analyzing the changes in the cumulative centrifugal to drag force ratio over the bed.

Keywords:
Gas-Solid Vortex Unit, Rotating fluidized bed, Computational Fluid Dynamics, Eulerian multiphase modeling

4.1 Introduction

Gas-solid Fluidized Beds (FB) are widely used in chemical industry as they enhance heat and mass transfer and solids mixing. The applications range from physical operations such as drying of solids[1], adsorption of dilute components from carrier gas[2] and particle coating[3] to reactive operations such as fluid catalytic cracking of hydrocarbons[4] and polymerization of olefins[5]. Heat and mass transfer efficiency in FBs is determined by the relative velocity between both phases, the so-called slip velocity. In conventional gravitational FBs, where the drag force is balanced by the gravitational force, the slip velocity cannot exceed the terminal free-falling velocity of the particles in a uniform bed operation[6]. Higher gas velocities in gravitational beds results in the formation of bubbles and slugs. Extensive gas bypass decreases gas-solid contact and thus the corresponding heat and mass transfer drops. Further increase in gas flow rate causes particle entrainment[7] and may affect the compactness of the industrial-scale fluidization setups[8].

Centrifugal force can reach much higher values than the gravitational force allowing feasible operation in the 7-40g regime, which is suitable for high gas throughput, more uniform fluidization, higher slip velocities and, hence, much higher heat and mass transfer[9-13]. Centrifugal FBs cause a shift in the Geldart classification of particles[14] and have been successfully used in fluidization of cohesive particles[15,16]. Consequently the centrifugal bed technology is more energy efficient, increasing the gas flow rate per reactor volume and making the fluidization process more compact. Hence, a centrifugally fluidized bed is an ideal candidate for Process Intensification (PI).

A centrifugal FB can be achieved in two ways: by setting the particles in motion by rotating the operating vessel itself, known as Rotating Fluidized Bed (RFB)[13,17,18] or by introducing the particles in a swirling flow field of azimuthally injected gas in a static vessel (Gas-Solid Vortex Unit) (GSVU)[10,19-21]. In the RFB, the independent control over the rotational velocity of the vessel and the injected gas flow rate imply that the azimuthal and radial velocity components can be varied in a decoupled manner[13]. However, RFBs involve mechanically moving parts and are prone to mechanical abrasion. In GSVU’s on the other hand, the fluidizing gas is injected from a number of azimuthally inclined rectangular slots at the circumferential wall. Azimuthal momentum is transferred from the swirling gas to particles fed into the unit, which start rotating and experience an outward centrifugal force. The particles rotating in a GSVR achieve a ‘fluidized state’ when the radially inward drag force exerted by the gas overcomes the apparent weight of solids in the centrifugal field[22]. Unlike the RFB, in the GSVU the particle velocity components cannot be independently controlled. However, the absence of mechanically moving parts significantly reduces the abrasion in the GSVU and makes the device more suitable for scale-up[19,23].

As the centrifugal force in a GSVU is a function of reactor geometry, operating conditions and solids properties, it can be tailored to establish a desired fluidization regime[17]. The latter cannot be achieved in gravitational FBs, as gravitational force is constant. All these features make the GSVU a potential device for PI of selected processes such as combustion of hydrocarbon fuels[24,25], drying of fine pored materials like food grains, pharmaceutical products or polymers[26,27], biomass pyrolysis[28] and SO_2-NO_x adsorption[29]. Excellent reviews of GSVU design as well as potential applications of single phase and multiphase vortex devices reference can be found in literature[16,30].

Reports on experimental studies carried out in GSVU setups to investigate the cold gas–solid hydrodynamics, i.e. in the absence of reactions, have improved the understanding of the nature of the flow field in the unit[11,12,19,31,32]. Kochetov et al.[33] ran experiments with varying length-to-diameter ratios of the GSVU and prescribed optimal values for its construction. Anderson et al.[19] performed experiments on GSVU bed hydrodynamics with talc, tungsten and zinc particles using X-ray absorption techniques to measure solids volume fractions in the bed and using a paddle wheel to measure angular bed velocities at various radii. Heat and mass transfer intensification when drying wheat grains in a GSVU was demonstrated by Volchkov et al.[34]. Particle entrainment close to the end-walls of the GSVU was observed as gas and solids centrifugal acceleration decrease in the wall boundary layers. Their work thus demonstrated the need for a 3D description of the GSVU bed hydrodynamics. Volchkov et al.[12] studied changes in the GSVU bed porosity behavior in the GSVU with varying gas flow rate and concluded that the bed becomes more dense with increasing gas flow rate. The authors also found the centrifugal force to be larger than the radial drag force in the GSVU under given flow conditions, indicating that, if centrifugal force and drag force do not balance each other, particles are pushed towards the wall resulting in increased wall shear stresses. De Wilde and de

Broqueville[10,11] experimentally demonstrated by fast digital camera image analysis that the GSVU shows different fluidization behavior for different Geldart classified materials. Kovacevic et al.[31,32] used Particle Image Velocimetry (PIV) and pressure probing techniques to measure the pressure drop and solids velocity in a cold flow GSVU. The authors observed higher solids velocities with increasing gas flow rate and decreasing solids density. Depending on the solids loading, the GSVU bed exhibited bubbling characteristics for smaller sized particles.

Although the experimental work carried out by different researchers highlighted important GSVU flow characteristics, two major drawbacks of the experimental data acquisition remain. Firstly, the range of operating conditions is limited by equipment design. More importantly, the non-intrusive measurements techniques employed limit experimental data collection to locations near the end-walls due to the dense nature of the bed[32]. However, for a complete description of the GSVU bed hydrodynamics various interactions at multiple scales (viz. at particle scale, bubble/slug scale and reactor scale) need to be accounted for[34-36]. The lack of complete information on the internal bed hydrodynamics of centrifugal FBs necessitates the need for a numerical study[13]. de Broqueville and De Wilde[37] performed two-dimensional (2D) numerical heat transfer studies in a GSVU. The authors theoretically demonstrated an increased heat transfer thereby achieving a more uniform heat distribution and a higher bed-averaged heat transfer rate compared to the conventional gravitational bed riser. Rosales and De Wilde[36] captured the appearance of slugs and non-uniformities in the bed for small sized catalyst particles (80 μm) in a 2D numerical study. Ashcraft et al.[28] implemented 2D simulations for biomass pyrolysis and demonstrated PI in a GSVU. These numerical studies although highly insightful, are 2D in nature and cannot capture the effect of a unidirectional gas exhaust or the presence of the end-walls on bed hydrodynamics. Moreover, bubble formation and slugging in fluidized beds may possess 3D propagation tendencies[38]. Hence, in order to properly investigate the bed (non-)uniformity in the GSVU, 3D simulations are needed. Preliminary 3D simulations using various geometrical designs of the GSVU have been carried out by Dutta et al.[23]. However, elaborate studies on the effect of gas flow rates and different solids properties were not performed. Furthermore, the validation of the applied CFD model was purely qualitative, requiring further calibration of the numerical model.

In the present work, the commercial Computational Fluid Dynamics (CFD) code FLUENT® 14.0 is used to perform a three-dimensional (3D) numerical study of the hydrodynamic behavior of the GSVU. First, the CFD model is validated by comparing simulated pressure and velocity data with experimental data. Next, the validated numerical model is used to study the gas-solid hydrodynamics in the GSVU over a wide range of conditions. Gas flow rate, particle diameter and solids density are individually varied to estimate their effect on various flow variables such as pressure drop, solids velocity, bed-averaged solids volume fraction and slip velocity.

4.2 Methodology

4.2.1 GSVU setup

A photographic view of the experimental GSVU setup, simulated in this work, is shown in Fig. 1(a). A schematic of the setup, shown in Fig. 1(b) [39], clearly highlights the important sections of the geometry. It basically consists of a cylindrical unit positioned along a horizontal axis with thirty-six gas injection slots azimuthally inclined at a 10° angle, equally distributed over the circumferential wall.

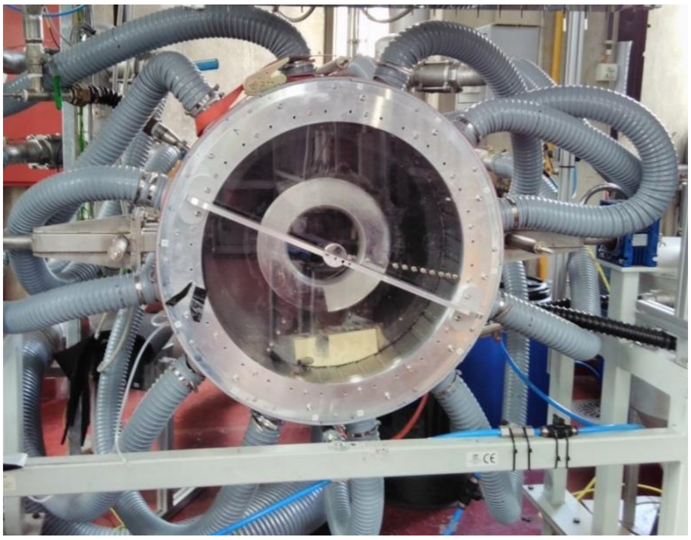

(a)

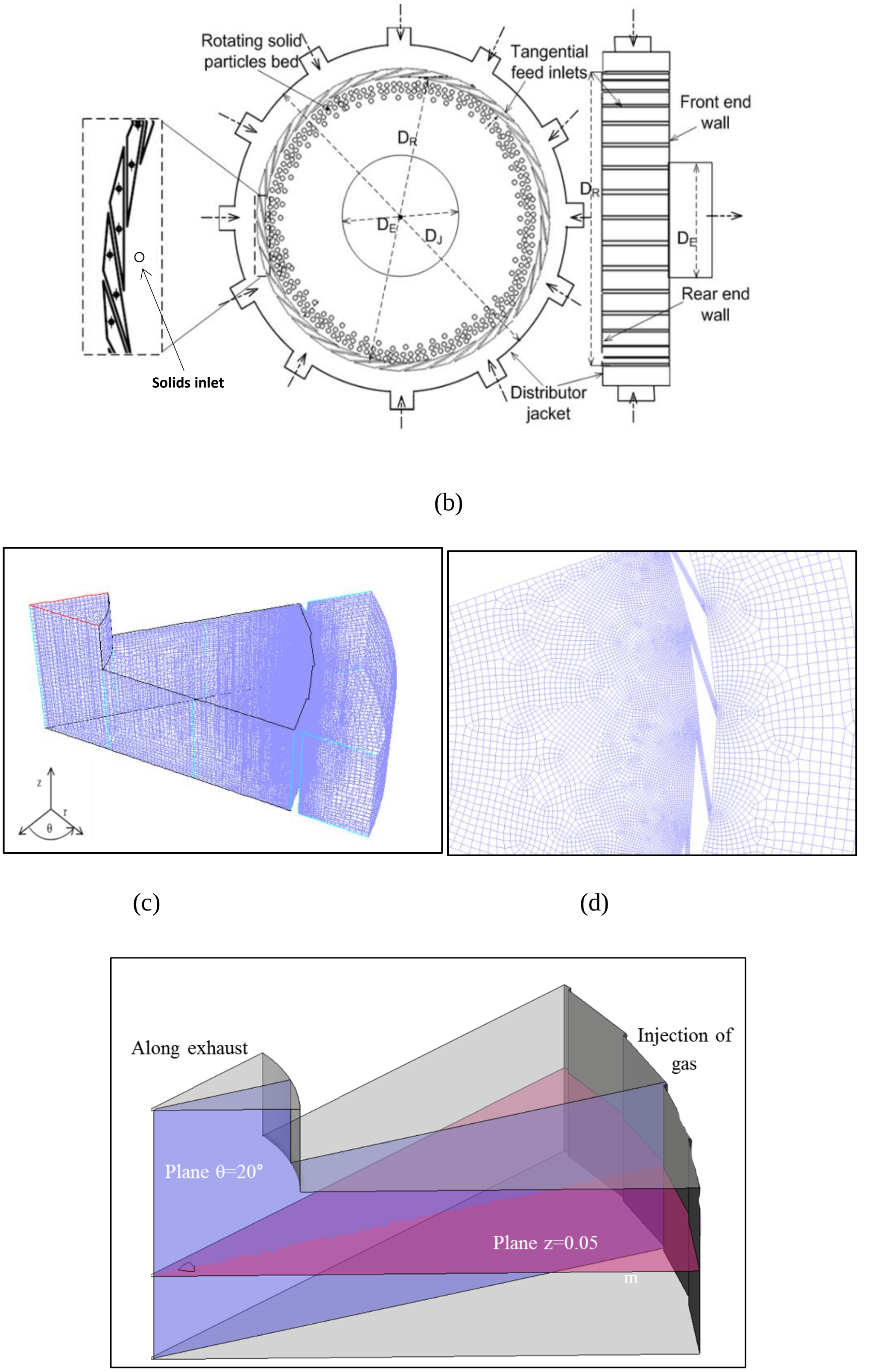

(b)

(c) (d)

(e)

Fig. 1. (a) Photographic view of the Gas-Solid Vortex Unit; (b) front view and side view of the pilot-scale GSVU[21]; (c) 3D periodic mesh used to simulate GSVU hydrodynamics; (d) zoomed-in view of

mesh refinement near slots and (e) different analysis planes in the sectional GVU simulation geometry. Geometrical dimensions given in Table 1.

The unit is confined on two sides by two parallel flat end-walls made from transparent polycarbonate glass (Makrolon®), allowing visual inspection of the solids bed formed in the GSVU as well as PIV measurements. The distance in between the end-walls determines the length of the GSVU. On the front end-wall (see Fig. 1(b)) an unidirectional gas exhaust is present. The fluidizing gas is first sent to an outer concentric distributor jacket through 12 feeding pipes positioned normally with respect to the jacket wall. The distribution jacket ensures that the gas approaching each injection slot has a nearly similar velocity. For a given gas flow rate, the thickness of the injection slots determines the magnitude of the gas injection velocity while the injection angle determines its radial and azimuthal components. For instance, in the given GSVU geometry with thirty-six 2mm injection slots, a gas flow rate of 0.5 Nm^3/s approximately corresponds to 70 m/s average injection velocity magnitude at the slots. The 10° injection angle of the azimuthally inclined slots then results in approximately 68 m/s average azimuthal gas injection velocity and 12 m/s average radial gas injection velocity at the slot opening. Table 1 lists up the main dimensions of the GSVU.

Table 1. Geometrical data for the pilot-scale experimental GSVU

GSVU circumferential wall diameter	0.54 m
GSVU exhaust diameter	0.15 m
GSVU length	0.1 m
Number of injection slots	36
Slot thickness	0.002 m
Slot angle with respect to circumferential wall	10°

The GSVU is operated in semi-batch mode. At the start of the experiment, the fluidizing gas is fed to the unit until a steady-state swirling gas flow is established inside the chamber. A more detailed description of the experimental setup and experimental procedure can be found in previous Kovacevic et al.[31,32]. Some details of the experimental procedure, relevant for the numerical study of the GSVU are discussed next.

Pressure measurements are carried out using radially aligned pressure taps on the rear end-wall of the unit, with milliampere output pressure sensors (Unik 5000). A two-dimensional standard PIV system from LaVision® with a 4 MP Charge Couple Device Camera and a 135mJ Nd-YAG laser are used to measure the solids velocity through the transparent rear end-wall of the unit. A more detailed description of the measurement techniques can be found in Kovacevic et al.[31] and Pantzali et al. [40]. The pressure and velocity measurements performed for different operating conditions and particle properties are used to validate the CFD model proposed for the numerical study of the GSVU.

4.2.2 Numerical model

In the present numerical study the Eulerian-Eulerian approach [41] is adopted to simulate the two-phase flow, using the commercial CFD software package Fluent 14.a®. In this approach, the gas and solid phases are treated as interpenetrating continua. Table 2 summarizes the conservation equations for both phases.

Table 2. Conservation equations

Mass Conservation:	
$\frac{\partial}{\partial t}(\varepsilon_i \rho_i) + \nabla \cdot \left(\varepsilon_i \rho_i \overline{U_i}\right) = 0$ (i = g, s)	(2.1)
Momentum Conservation:	
Gas: $\frac{\partial}{\partial t}\left(\varepsilon_g \rho_g \overline{U_g}\right) + \nabla \cdot \left(\varepsilon_g \rho_g \overline{U_g}\,\overline{U_g}\right) = -\varepsilon_g \nabla P + \nabla \cdot \overline{\overline{\tau_g}} + \varepsilon_g \rho_g \overline{g} - \beta\left(\overline{U_g} - \overline{U_s}\right)$	(2.2)

Solids: $$\frac{\partial}{\partial t}\left(\varepsilon_s\rho_s\overline{U_s}\right)+\nabla\cdot\left(\varepsilon_s\rho_s\overline{U_s}\,\overline{U_s}\right)=-\varepsilon_s\nabla P-\nabla P_s+\nabla\cdot\overline{\overline{\tau}}_s+\varepsilon_s\rho_s\bar{g}-\beta\left(\overline{U_s}-\overline{U_g}\right) \qquad (2.3)$$

Transport equation for k, turbulent kinetic energy:

$$\frac{\partial}{\partial t}\left(\varepsilon_i\rho_i k\right)+\nabla\cdot\left(\varepsilon_i\rho_i k\overline{U_i}\right)=\nabla\cdot\left(\varepsilon_i\frac{\mu_{t,i}}{\sigma_j}\nabla k\right)+\left(\varepsilon_i\mu_{t,i}\left(\nabla\overline{U_i}+\overline{U_i}^T\right):\nabla\overline{U_i}-\varepsilon_i\rho_i e\right)-\beta\left(2k\right) \qquad (2.4)$$

(i = g, s)

Transport equation for e, dissipation rate of turbulent kinetic energy:

$$\frac{\partial}{\partial t}\left(\varepsilon_i\rho_i e\right)+\nabla\cdot\left(\varepsilon_i\rho_i e\overline{U_i}\right)=\nabla\cdot\left(\varepsilon_i\frac{\mu_{t,i}}{\sigma_j}\nabla e\right)+C_{1s}\frac{e}{k}\left(\varepsilon_i\mu_{t,i}\left(\nabla\overline{U_i}+\overline{U_i}^T\right):\nabla\overline{U_i}\right)-C_{2s}\varepsilon_i\rho_i\frac{e^2}{k}-\beta\left(2k\right)C_{3s}\frac{e}{k} \qquad (2.5)$$

(i = g, s)

The turbulent viscosity $\mu_{t,i}$ in equations (2.3-2.4) can then be computed from:

$$\mu_{t,i}=\rho_i C_\mu\frac{k^2}{e} \qquad \text{(i = g, s)} \qquad (2.6)$$

The mass and momentum conservation equations are Reynolds-averaged. For the solid phase, the conservation equations for mass, momentum and granular temperature are obtained via the Kinetic Theory of Granular Flow (KTGF)[42,43]. The effect of turbulence is taken into account for each phase via a Re-Normalization Group (RNG) k-ε model[44], adapted for gas-solid interactions. No energy conservation equations are applied since isothermal operation is assumed for both phases in the present study.

Simulating the whole GSVU geometry is computationally expensive. Ashcraft et al.[28] confirmed that simulating a 40° section of the GSVU, using rotational periodic boundary conditions, suffices to obtain correct values for primary flow variables such as pressure drop, solids volume fraction and solids velocity. Hence, 3D simulations of a 40° section of the unit are performed. The 3D simulations help to capture the effect of the end-walls on the gas-solid flow behavior and to make the simulation results accurate. Initially a mesh study is performed to verify the grid independence of the presented simulation data. Three mesh resolutions (I, II and III) are used (Table 3). The consecutive mesh size is decreased by a factor of 2.

Table 3. Mesh study for the GSVU simulations

Mesh	Number of cells	Variable values		
		ΔP_{gauge} (kPa)	$U_{\theta,s}$ (m/s)	ε_s (-)
I	124,420	3.1	6.1	0.44
II	256,000	4.2	7.84	0.49
III	557,330	4.4	7.92	0.51

In Table 3 the change in the calculated values for the time-averaged GSVU pressure drop, solids velocity magnitude and solids volume fractions are presented. The difference in flow variable values between mesh II and III is found to be small (<5%) and hence, mesh II (shown in Fig. 1(c)-(d)) is chosen as the standard mesh for further analysis in order to save computational cost. The cell size in the mesh varies from 0.5 mm near the gas injection slots to 4.0 mm near the central gas exhaust. Cell sizes are smaller near the circumferential wall to capture the small time- and space-scale hydrodynamics near the solids bed [31]. The cells close to the end-walls of the GVU are more densely packed to give a grid resolution with wall y^+ values in the order of 30. The standard wall function model proposed by Launder and Spalding[45] is used to model the near-wall flow. Remark that simulation of a sectional GSVU geometry with horizontal axis implies that the gravitational force cannot be accounted for correctly as the gravitational acceleration direction changes in different sections of the geometry. Gravity was shown to have a minimal effect on the flow dynamics at the applied operating conditions[31]. During simulations only the dominant forces, that is centrifugal force, drag force, inter-particle and particle-wall forces, are taken into consideration.

An overview of the constitutive equations is found in Table 4. The gas is considered to be incompressible (air, density: 1.225 kg/m^3) and the no-slip boundary condition is imposed at both end-walls and circumferential wall for the gas phase.

Table 4. Constitutive equations

Gas phase stress tensor:	
$\overline{\overline{\tau_g}} = \varepsilon_g \left(\mu_g + \mu_{t,g}\right)\left(\nabla\overline{U_g} + \nabla\overline{U_g}^{T}\right)$	(3.1)
Granular Temperature[42]*:*	
$\left(-P_s \overline{\overline{I}} + \overline{\overline{\tau_s}}\right) : \nabla\overline{U_s} - \gamma\Theta_s + 3\beta\Theta_s = 0$	(3.2)
Solids pressure [46]*:*	
$P_s = \rho_p \varepsilon_s \theta + 2(1+e_{ss})\rho_p \theta g_{0,ss}\left(\varepsilon_s\right)\varepsilon_s^{\;2}$	(3.3)
Gas-solid drag coefficient [47]*:*	
$\beta = \frac{3}{4} C_D \frac{\varepsilon_g \varepsilon_s \rho_g \left\lvert\overline{U_{slip}}\right\rvert}{d_p} \varepsilon_g^{\;-2.65}$ (for $\varepsilon_g>0.8$) where $C_D = 150 \frac{24}{\varepsilon_g \mathrm{Re}_s}\left[1 + 0.15\left(\varepsilon_g \mathrm{Re}_s\right)^{0.687}\right]$; $\mathrm{Re}_s = \frac{\rho_g d_p \left\lvert\overline{U_{slip}}\right\rvert}{\mu_g}$ $\beta = 150 \frac{\varepsilon_s^2 \mu_g}{\varepsilon_g d_p^2} + 1.75 \frac{\rho_g \varepsilon_s \left\lvert\overline{U_{slip}}\right\rvert}{d_p}$ (for $\varepsilon_g \le 0.8$)	(3.4)
Radial distribution function[48]*:*	
$g_{0,ss} = \left[1 - \left(\frac{\varepsilon_s}{\varepsilon_{s,\max}}\right)^{\frac{1}{3}}\right]^{-1}$	(3.5)
Solid-phase shear stress tensor:	

$$\overline{\overline{\tau}}_s = \varepsilon_s \mu_s \left(\nabla \overline{U}_s + \nabla \overline{U}_s^{\,T} \right) + \varepsilon_s \left(\lambda_s - \frac{2}{3} \left(\mu_{s,col} + \mu_{s,kin} + \mu_{s,fr} + \mu_{t,s} \right) \right) \nabla \cdot \overline{U}_s \overline{\overline{I}} \qquad (3.6)$$

Solids collision viscosity[47]*:*

$$\mu_{s,col} = \frac{4}{5} \varepsilon_s \rho_s d_p g_{0,ss} (1 + e_{ss}) \left(\frac{\Theta_s}{\pi} \right)^{1/2} \qquad (3.7)$$

Solids kinetic viscosity[49]*:*

$$\mu_{s,kin} = \frac{\varepsilon_s \rho_s d_p \sqrt{\Theta_s \pi}}{6(3 - e_{ss})} \left[1 + \frac{2}{5} \varepsilon_s g_{0,ss} (1 + e_{ss})(3e_{ss} - 1) \right] \qquad (3.8)$$

Solids frictional viscosity[50]*:*

$$\mu_{s,fr} = \frac{P_s \sin\delta}{2\sqrt{I}} \qquad (3.9)$$

Solids bulk viscosity[46]*:*

$$\lambda_s = \frac{4}{3} \varepsilon_s \rho_s d_p g_{0,ss} (1 + e_{ss}) \left(\frac{\Theta_s}{\pi} \right)^{1/2} \qquad (3.10)$$

Shear stress at the wall[51]*:*

$$\overline{\overline{\tau}}_s = -\frac{\pi}{6} \sqrt{3} \phi \frac{\alpha_s}{\alpha_{s,\max}} \rho_s g_{0,ss} \sqrt{\Theta_s} \left| \overline{U_{slip}} \right| \qquad (3.11)$$

where φ is the specularity coefficient

In order to reduce the computational cost, the exhaust tube is simulated over a length of 0.1 m only. The radial equilibrium pressure distribution condition is imposed at the exhaust outlet as previous studies have shown that the outflowing gas still retains its swirling structure at this height[52]. Experimental observations have shown that the solids bed formed in the GSVU is dense in nature[23,32].

Particle collisions are modeled as highly elastic imposing a restitution coefficient (e_{ss}) value of 0.9. Remark that the collision dynamics between two polymeric particles primarily depends on impact velocity[53,54]. The cold flow experimental GSVU studies have been performed with materials such as high density polyethylene (HDPE), a semi-crystalline material and polycarbonate (PC), a more amorphous material. However, both materials exhibit a similar elastic collision tendency with a restitution coefficient close to 0.9 for low impact velocities (<1 m/s)[53]. The solids bed formed in the GSVU is shown to be dense, with layers of solids rotating in very close proximity to each other near the circumferential wall of the unit[32]. For dense flow, direct inter-particle collisions at velocities higher than 1 m/s are less likely. The inter-particle momentum transfer primarily takes place through shear. Consequently the frictional forces between the particle layers become important rather than collisional dynamics. The partial-slip wall boundary condition developed by Johnson and Jackson[51] is used to calculate the solid shear stress near the wall. The specularity coefficient used differs for the circumferential wall (φ_c=0.02) and the end-walls (φ_e=0.004). Different wall construction materials (circumferential wall: steel, end-wall: polycarbonate glass, Makrolon®) explain the need for different values of specularity coefficients. All CFD model parameters are presented in Table 5.

Table 5. Optimized CFD model parameters

Parameter	Value
Particle end-wall specularity coefficient (φ_e)	0.004
Particle circumferential-wall specularity coefficient (φ_c)	0.02
Particle restitution coefficient (e_{ss})	0.9
Maximum packing limit	0.63
Turbulent intensity at injection slots/ exhaust	5 %

The turbulent intensity is set at a value of 5% at the jacket outer periphery (r=0.35 m). The high value artificially replicates the high turbulence due to the sudden expansion of the fluidizing gas entering the jacket through discrete feeder pipes in (r=0.35 m) the experimental setup. The possibility of flow reversal near the exhaust of the unit due to vortex breakdown may result in increased turbulence at the exhaust, explaining the high turbulent intensity value imposed at the exhaust. Remark that, with both the jacket wall and the central gas exhaust being sufficiently away from the solids bed region in the GSVU, the turbulence boundary conditions will only have a minor influence on the overall time-averaged solids bed hydrodynamics. The conditions for the complete numerical study, comprising of 12 simulation cases, are presented in Table 6.

Table 6. Simulation cases for parametric study

		Gas flow rate (G_M) Nm^3/s	Particle diameter (d_p) mm	Particle density (ρ_s) kg/m^3
Effect of gas flow rate	Case 1	0.11	1	950
	Case 2	0.23		
	Case 3	0.32		
	Case 4	0.41		
	Case 5	0.52		
	Case 6	0.64		
Effect of particle density	Case 7	0.32	1	450
	Case 8			950
	Case 9			1800
Effect of particle	Case 10	0.32	2	950

diameter	Case 11		1	
	Case 12		0.5	

The experimentally measured and computationally determined gauge pressures and azimuthal solids velocities for different gas flow rates, particle diameters and solid densities (corresponding to simulation cases 3, 4, 10 in Table 6) are compared in Fig. 2(a)-(e).

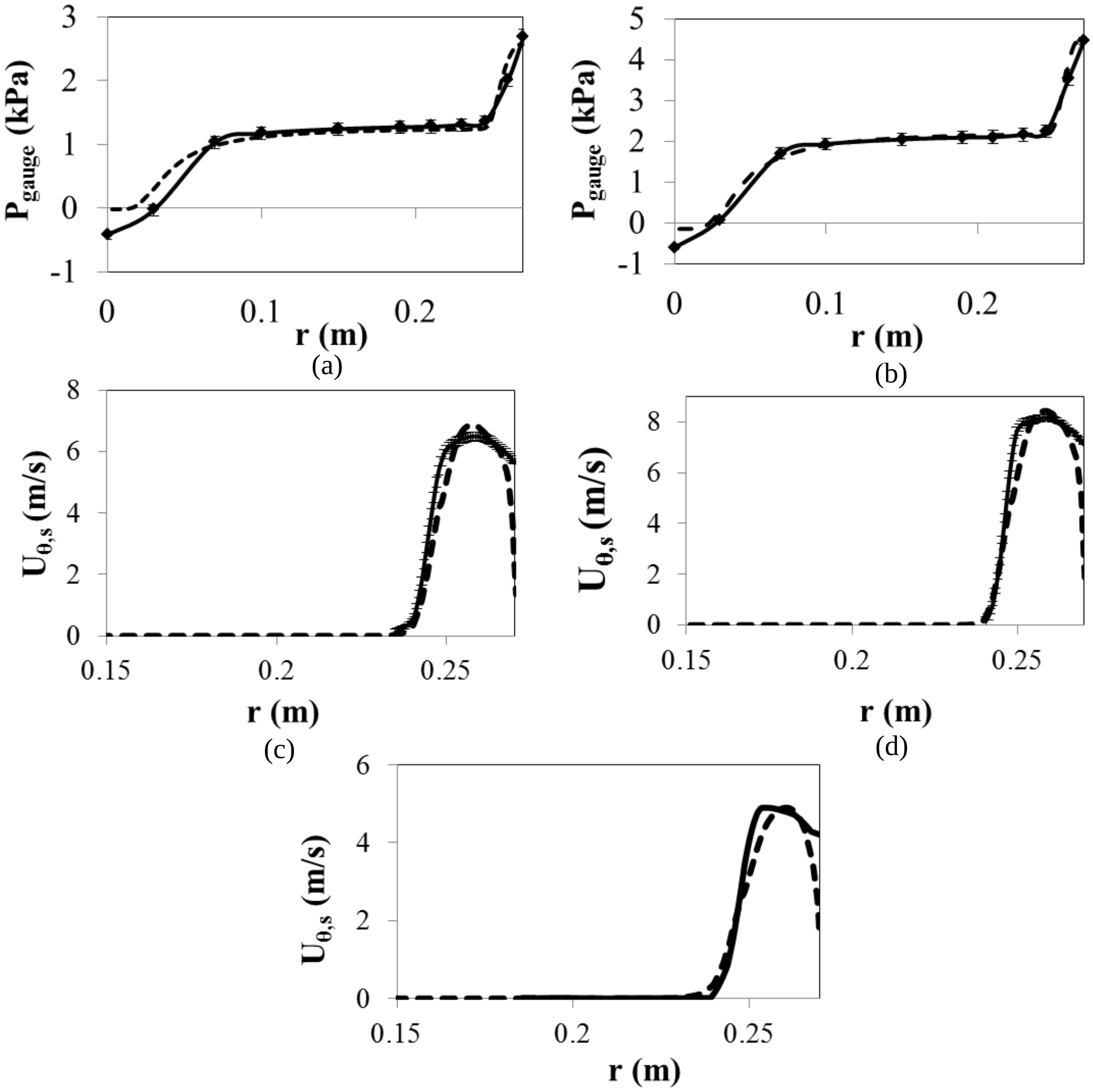

(a)

(b)

(c)

(d)

(e)

Fig. 2. Radial profiles of static gauge pressure for particulate flow along z=0.05m line in θ=20° plane: full line, experimental data and (---) numerical data calculated by solving Eqs. (2.1)–(3.11) in Tables 2 and 4 with parameter values in Table 5, for (a) G_M=0.39 Nm^3/s, d_p=1 mm, ρ_s=950 kg/m^3; (b) G_M=0.5

Nm^3/s, d_p=1 mm, ρ_s=950 kg/m^3. Radial profiles of azimuthal solids velocity for particulate flow along the θ=20° plane, z=0.05m line: full line, experimental data; (---) numerical simulation calculated by solving Eqs. (2.1)–(3.11) in Tables 2 and 4 with parameter values in Table 5, for (c) G_M=0.39 Nm^3/s, d_p=1 mm, ρ_s=950 kg/m^3; (d) G_M=0.5 Nm^3/s, d_p=1 mm, ρ_s=950 kg/m^3 and (e) G_M=0.39 Nm^3/s, d_p=2 mm, ρ_s=950 kg/m^3. Bed mass=2 kg. Error bars represent the 95% confidence interval based on three repeated experiments.

The gauge pressure data from simulations and experiments compare well in the disc part of the GSVU ($0.06<r<0.27$ m), as seen in Fig. 2(a)-(b). The average percentage deviation between the experimental and simulated pressure data is around 5% in the main disc part of the GSVU. It significantly increases near the core of the exhaust region ($r<0.06$ m). The latter can be attributed to the shortening of the simulated exhaust line as compared to the experimental setup to reduce computational cost. As the main focus of the manuscript is on the solids bed hydrodynamics in the disc part of the unit, differences near the exhaust do not exert any significant influence on the results discussed in the presented study. The experimental and simulated solids velocities are compared in Fig. 2(c)-(e). With an average percentage deviation of 7%, the data sets agree well for the main part of the solids bed. The deviation increases towards the free board of the solids bed and in the vicinity of the circumferential wall (~20%). In these particular regions the differences can be attributed to the inability of the experimental technique to provide mass-averaged velocity values, as calculated from simulations. The PIV technique indeed cannot account for local solids volume fractions in the solids bed. The difference between the experimental and simulated data close to the circumferential wall stems from a calculated narrow region of dilute solids flow close to the circumferential wall of the unit. As mass-averaged solids velocities are calculated in the simulations, the solids velocities near the circumferential wall of the GSVU are low. The PIV technique only provides absolute velocities of particle clusters without accounting for the fact that lesser number of particles near the circumferential wall will result in a decrease in the local solids volume fractions. Also, the geometrical design of the GSVU makes it difficult to accurately measure local solids volume fractions at such close distance to the circumferential wall. Hence, the main objective of the presented study is the analysis of the overall GSVU solids bed characteristics. Difference of local velocity data close to the circumferential wall between experiments and simulations lies within acceptable limit. The pressure and velocity data presented in Fig. 2 (a)-(e) validates the CFD model for further numerical study of the GSVU hydrodynamics. After validating the numerical model, a parametric study under varying conditions of gas flow rate and particle properties is carried out to obtain a better understanding of the gas-solid hydrodynamic behavior in the GSVU. The effect of one parameter on the hydrodynamic performance of the GSVU is studied in detail, meanwhile keeping the others constant.

4.2.3 Solution Method

To solve the set of equations the segregated pressure-based Phase Coupled SIMPLE (PC-SIMPLE) algorithm[55] is used. A second-order implicit time stepping scheme is applied for the transient simulations. Reaching the steady-state semi-batch fluidized bed condition is a two-step process. The first step involves establishing a steady-state gas-only flow inside the GSVU (previously described as the start of an experiment). Once the steady-state swirling gas flow is reached (about 5 s simulation time), the particles are fed with the gas through the injection slots until a stable solids bed is established. Remark that this feeding mechanism differs from the experimental one. However, the focus of the present study is on the analysis of steady-state *semi-batch* hydrodynamics in the GSVU, the simulation results will not be affected by the procedure through which the particles are fed into the geometry. In the semi-batch mode, particles are fed until a designated mass of solids has accumulated in the unit (2 kg in the presented cases). Next, solids feeding is stopped. Experimental data on solids bed hydrodynamics is collected when sufficient time has elapsed to reach steady-state operation. In the simulations, solids feeding is monitored by tracking the solids accumulation in the main unit. When the designated bed mass is reached and steady state solids flow is achieved, time-averaging of flow characteristics is performed. The semi-batch operation of the GSVU thus ensures that the hydrodynamic data from experiments and simulations are not influenced by the solids feeding mechanism. Feeding is stopped once the required bed mass is obtained (about 2s simulation time). Once the gas-solid flow has reached steady-state, another 10 s of simulation time is required for the time-averaging of the bed hydrodynamics. The time step during the transient simulations varies from an initial 10^{-3}s during gas and solids feeding, to 10^{-2}s as stable bed operation approaches. Each time step takes 50 iterations. The simulations are performed on AMD-based Linux 32-core clusters. A 3D time-averaged steady-state solution for a 40° sectional volume of the GSVU requires about 2 weeks of CPU time. The time-averaged data are exported for post-processing and further analysis. A normal-to-axis $z=0.05$m plane and an $\theta=20°$ azimuthal plane are selected for analysis of the simulation results. They are indicated as colored planes in Fig. 1(e).

4.3 Results and discussions

4.3.1 Particle-free GSVU hydrodynamics

As previously mentioned, both GSVU experiments and simulations start by establishing a steady-state swirling gas flow inside the unit. Therefore, as an introduction to the two-phase study and for means of comparison with the particulate flow hydrodynamics, a short overview of particle-free GSVU hydrodynamics is provided. The results discussed in this section are obtained for a gas flow rate (G_M) of 0.39 Nm^3/s.

Fig. 3(a) shows the steady-state azimuthal gas velocity profile in the particle-free GSVU along the radial coordinate. From the circumferential wall to the gas exhaust ($0.075<r<0.27$m) the azimuthal gas velocity increases with decreasing radial coordinate, a behavior representative of free-vortex flow dynamics.

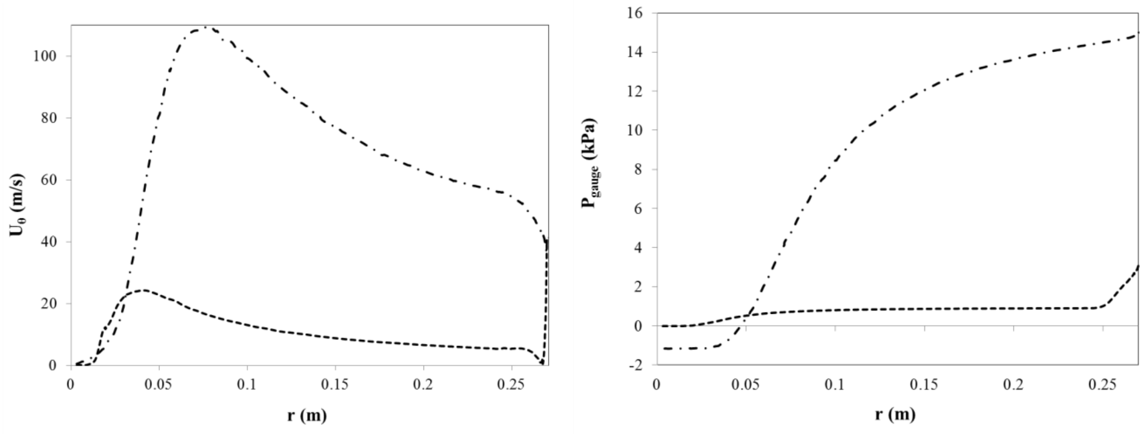

(a) (b)

Fig. 3. (a) Radial profiles of (a) azimuthal gas velocity and (b) static gauge pressure along $z=0.05$m line in $\theta=20°$ plane: (-●-) particle-free flow calculated by solving the set of Eqs. (2.1)–(2.2), (2.4)–(2.6) in Table 2, for $G_M=0.39$ Nm^3/s and (---) particulate flow, calculated by solving the set of Eqs.

(2.1)–(3.11) in Tables 2 and 4 with parameter values in Table 5, for G_M=0.39 Nm^3/s, d_p=1 mm, ρ_s=950 kg/m^3. Bed mass=2 kg.

This free-vortex flow behavior in the disc part of the GSVU, predicted by the simulations, compare well with LDA velocity data from experiments by Volchkov et al.[12]. The azimuthally injected gas spirals its way, radially converging, towards the central gas exhaust forming a free-vortex flow region in the disc part of the GSVU. Upon reaching the unidirectional central gas exhaust a strong positive axial velocity component develops and disrupts the swirling structure of the gas flow resulting in a drastic reduction of the azimuthal velocity.

Fig. 3(b) shows the steady-state static gauge pressure profile plotted along the radial coordinate for particle-free flow. The pressure drop over the unit is computed to be about 15 kPa. The free-vortex structure in the GSVU causes the azimuthal gas velocity component to dominate the axial and radial components by an order of magnitude, thus reducing the single-phase Navier-Stokes equation for the radial coordinate to the cyclostrophic balance[40]:

$$\frac{\partial P}{\partial r} = \frac{\rho U_{\theta,g}^2}{r} \tag{1}$$

The cyclostrophic balance indicates that the radial pressure gradient inside the GSVU in particle-free flow is balanced by the strong centrifugal acceleration of the gas. In other words, the high azimuthal velocity component of the free swirling gas causes the high pressure drop over the unit.

The negative static gauge pressure for r<0.05m indicates flow reversal in the central gas exhaust region of the GSVU (0<r<0.05m). This flow reversal zone is referred to as the backflow region in the GSVU. As the swirling gas, approaching from the injection slots, reaches the central gas exhaust, it has to bend 90° towards the unidirectional exhaust. This high degree of streamline bending around the axis of the exhaust causes flow acceleration due to an abrupt change in velocity direction and creates a local low pressure region. A gas recirculation zone develops in the exhaust region in the GSVU, reducing the net exit area of the gas flowing through the exhaust tube. The gas leaves the GSVU only through an annular ring-like cross-section of the exhaust pipe. This decrease in the exhaust area increases the overall pressure drop over the unit.

4.3.2 Particulate GSVU hydrodynamics

4.3.2.1 Pressure drop and gas dynamics

Once steady-state gas flow has been established in the GSVU, particles with 1mm diameter (d_p) and 950 kg/m^3 (ρ_s) solids density are fed until a bed mass of 2 kg is achieved. As more particles are fed into the GSVU, the "height" of the solids bed increases radially inwards. When sufficient particles are fed, a dense stable solids bed is formed near the circumferential wall. The present study focuses on stable bed hydrodynamics only. Bed stability is discussed in more detail by Kovacevic et al.[31].

As seen in Fig. 3(b), the total pressure drop over the GSVU is seen to decrease from 15 kPa in particle-free flow to 3 kPa in particulate flow. In gravitational fluidized beds, the presence of particles provides a physical barrier for the gas flow and the pressure drop increases as compared to particle-free flow. The pressure profiles for the GSVU show a reverse trend as can be seen in Fig. 3(b) and as experimentally observed[40,56]. For particulate flow, the pressure drop is mainly localized over the solids bed (ΔP_{bed}). From the freeboard region to the central exhaust the pressure remains nearly constant. In the exhaust zone, a slight pressure drop is observed. Introduction of particles in the GSVU immediately disrupts the swirling structure of the gas in the particle-free GSVU. This can be observed in Fig. 3(a), where the azimuthal gas velocity is significantly reduced (around 80%) when the particles fed form a stable bed. The gas loses the major part of its azimuthal momentum by imparting rotational momentum to the particles. When the gas leaves the bed, the gas velocity is of the order of 5 m/s, that is one order of magnitude smaller than the values in particle-free flow (Fig. 3(a)). The reduced azimuthal gas velocity component fails to generate a strong swirling structure in the particle-free zone between the freeboard and the central gas exhaust ($0.075<r<0.24$m). The weaker swirling structure results in a lower radial pressure drop, following the cyclostrophic balance (Eq. 1). From Fig. 3(b) it can also be seen, that in the exhaust region ($0<r<0.075$m) the negative gauge pressure values observed in particle-free flow becomes negligible when particles are introduced. This provides an indication that the presence of particles diminishes the backflow region around the exhaust axis (discussed in previous section). To further confirm this hypothesis, an in-plane gas velocity vector field in the $\theta=20°$ plane in the GSVU for particle-free flow (Fig. 4(a)) and particulate flow (Fig. 4(b)) are compared.

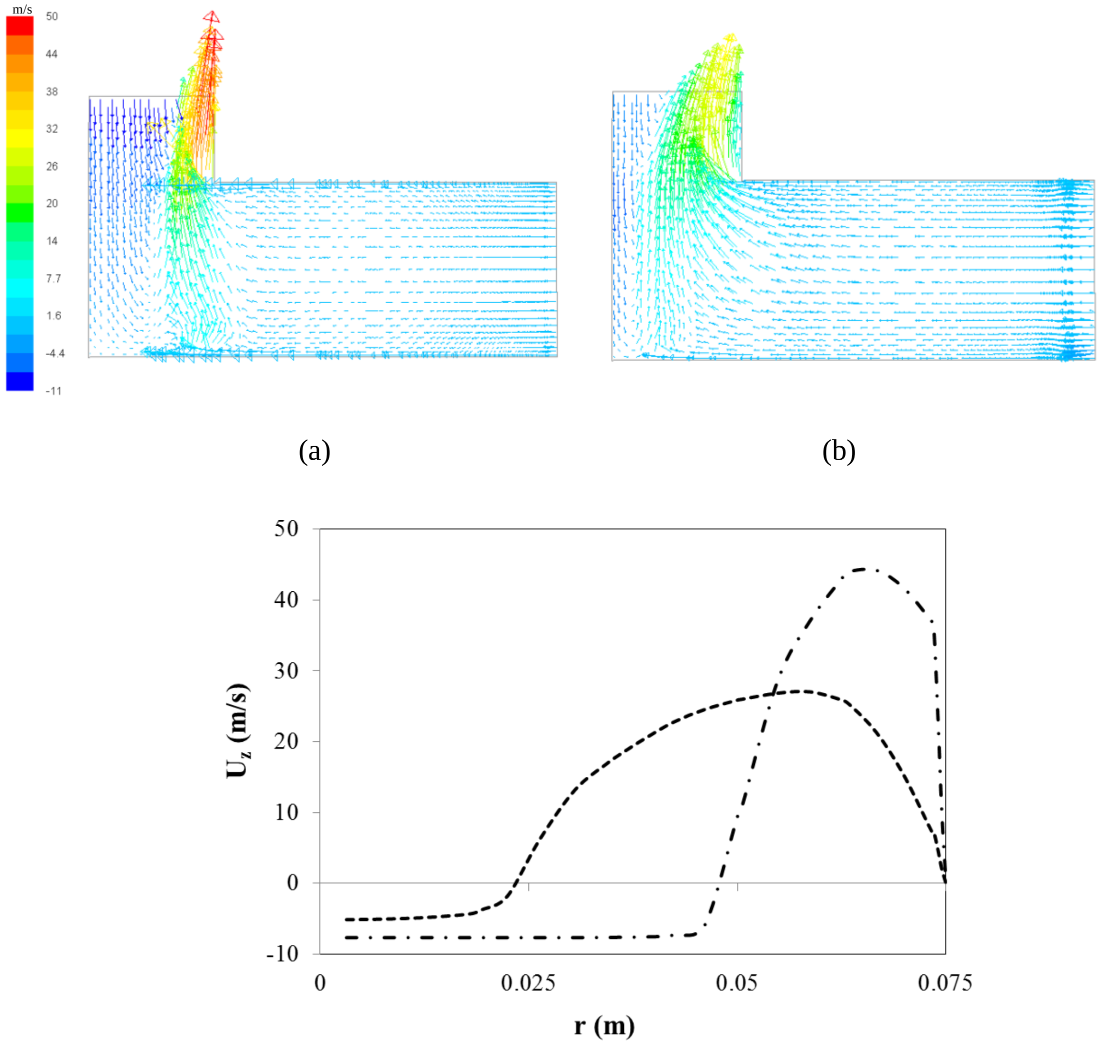

(a)

(b)

(c)

Fig. 4. Velocity vector field in θ=20° plane for (a) particle-free flow calculated by solving the set of Eqs. (2.1)–(2.2), (2.4)–(2.6) in Table 2, for G_M=0.39 Nm^3/s and (b) particulate flow calculated by solving Eqs. (2.1)–(3.11) given in Tables 2 and 4 with parameter values in Table 5, for G_M=0.39 Nm^3/s, d_p=1 mm, ρ_s=950 kg/m^3 (colors indicate axial velocity values). (c) Radial profile of axial velocity along z=0.12 m line in θ=20° plane: (-●-) particle-free flow calculated by solving the set of Eqs. (2.1)–(2.2), (2.4)–(2.6) in Table 2, for G_M=0.39 Nm^3/s and (---) particulate flow, calculated by solving the set of Eqs. (2.1)–(3.11) in Tables 2 and 4 with parameter values in Table 5, for G_M=0.39 Nm^3/s, d_p=1 mm, ρ_s=950 kg/m^3. Bed mass=2 kg.

It can be clearly seen from the figure, that the backflow region is substantially reduced by the introduction of particles in the GSVU, increasing the net cross-sectional area for the gas to leave. Fig.

4(c), showing the axial gas velocity profiles with respect to the radial coordinate in the exhaust tube in the θ=20° plane at z=0.12m, shows that the presence of particles reduces the radius of the backflow region (indicated by negative axial velocity values). The width of the annular region where the gas leaves from the unit increases from around 0.02m (particle-free flow) to 0.05m (particulate flow). Thus the cross-sectional area for the gas to leave the unit increases by a factor of 1.7. The axial gas velocities in the exhaust tube decrease accordingly. According to Bernoulli's law, a reduced gas velocity results in an increased local gauge pressure value. Consequently, the static gauge pressure drop in the exhaust region decreases (Fig. 3(b)). The total decrease in pressure drop over the entire GSVU when introducing particles is thus explained both by the disruption of the swirling gas flow structure and by the size-reduction of the backflow region.

4.3.2.2 Solids volume fraction and velocity

The radial solids volume fraction distribution along the bed in the GSVU is presented in Fig. 5(a). The bed shows a dense middle part and becomes diluted towards the circumferential wall (r=0.27m) and towards the freeboard (r<0.25m).

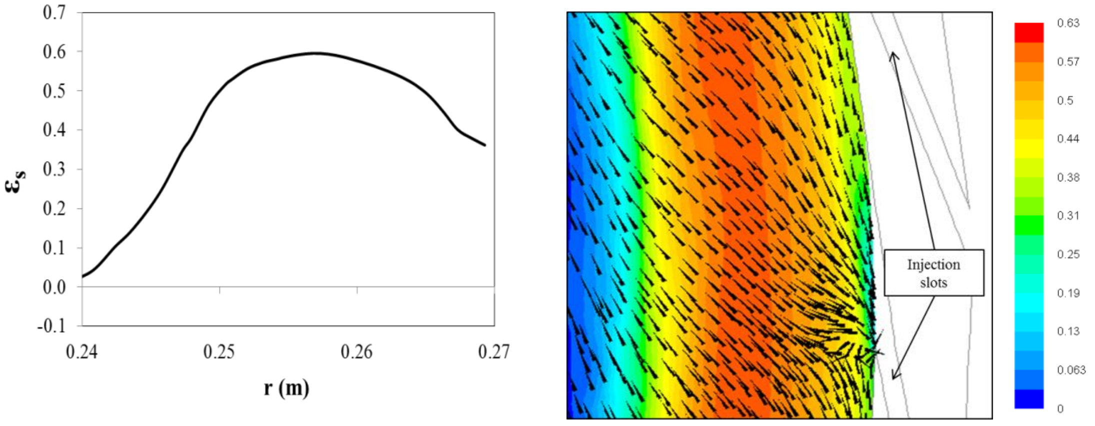

(a) (b)

Fig. 5. (a) Radial profile of solids volume fraction along z=0.05m line in θ=20° plane and (b) gas velocity vector field in z=0.05m plane superimposed on contour of solids volume fractions for particulate flow calculated by solving Eqs. (2.1)–(3.11) in Tables 2 and 4 with parameter values in Table 5, for G_M=0.39 Nm^3/s, d_p=1mm, ρ_s=950 kg/m^3. Bed mass=2 kg.

In the middle of the bed, solids volume fractions are close to 0.63, the maximum packing limit for spherical monodisperse particles[18]. A solids volume fraction of 0.05 is considered to be the cut-off value to locate the bed freeboard. From Fig. 5(a), it is seen that the bed height is about 0.03m. An experimental value of bed height with value of 0.026m was observed and previously reported[32]. The bed is calculated to be most dense at a radius of 0.255m. At the circumferential wall the solids volume fraction is as low as 0.4 due to the injection of gas through the slots. The dense solids bed acts like a gas distributor, splitting the inflowing gas into multiple streams. A gas stream flowing close to the circumferential wall induces a decrease in the solids volume fraction in the proximity of the circumferential wall. To verify this hypothesis, the gas velocity vectors are plotted along with the solids volume fraction field in the z=0.05m plane in Fig. 5(b). It is indeed discerned that although most of the azimuthally entering gas flows radially inwards through the bed towards the central gas exhaust, a part of it flows azimuthally very close to the circumferential wall. The lowering of solids volume fractions predicted by the simulations compare qualitatively well with experimental X-ray absorption data obtained by Anderson et al.[19].

A profile of the azimuthal solids velocity along the radial coordinate was already plotted in Fig. 2 (c), when comparing the simulated and experimental solids velocity data. Near the circumferential wall the azimuthal solids velocity is reduced due to particle-wall friction. The subsequent particle layers away from the wall accelerate and a maximum azimuthal solids velocity of about 7 m/s is obtained at r=0.255m where the bed is most dense (ε_s=0.61) (Fig. 5(a)). Beyond this point, the azimuthal solids velocity gradually decreases. This can be attributed to shear between the particle layers on the one hand and reduced momentum transfer between the phases on the other. The reduction in azimuthal solids velocity near the freeboard was also experimentally observed by Kovacevic et al.[32].

4.3.2.3 Slip velocity between gas and solid phases

As the gas flows through the bed it exerts a drag force on the particles. The slip velocity between both phases, on particle scale, is a prime variable to determine the value of this drag force. Studying the GSVU hydrodynamics based on the balance between drag force and centrifugal force thus requires determination of proper slip velocity values. Since the gas-solid hydrodynamics in the GSVU is not purely radial nor azimuthal, the slip velocity will first be analyzed in the respective components.

To estimate the slip velocities, the profiles of the azimuthal and radial velocity of each phase along the radial coordinate are shown in Fig. 6(a) and (b) respectively.

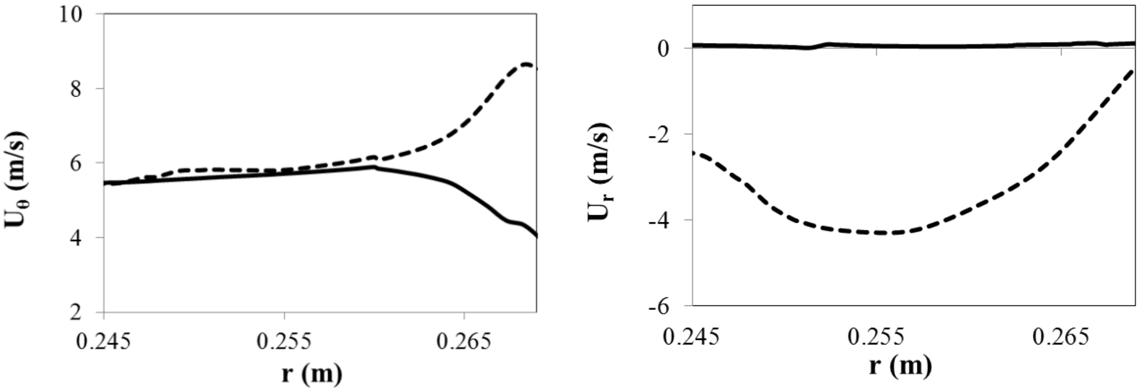

(a) (b)

Fig. 6. Radial profiles of (a) azimuthal velocity and (b) radial velocity along z=0.05m line in θ=20° plane: full line, solids and (---) gas, for particulate flow calculated by solving Eqs. (2.1)–(3.11) in Tables 2 and 4 with parameter values in Table 5, for G_M=0.39 Nm^3/s, d_p=1 mm, ρ_s=950 kg/m^3. Bed mass=2 kg.

In Fig. 6(a), it can be seen that near the circumferential wall (0.26<r<0.27m) where the gas injection slots are located, the gas azimuthal velocity is higher than the solids azimuthal velocity. This is the region where the injected gas transfers most of its momentum to the particles. The entire azimuthal momentum transfer is seen to be transferred over this initial 40% of the bed height starting from the circumferential wall. Beyond this radial position (r<0.26m), the azimuthal velocity of both gas phase and solid phase are equal, indicating that the azimuthal slip velocity falls off to zero. Fig. 6(b) shows that in radial direction the solids have zero velocity, as the rotating particles lack any overall radial motion in a *stable* bed operation. The radial slip velocity thus equals the radial gas velocity. The overall slip velocity is calculated from its radial and azimuthal component as

$$U_{slip} = \sqrt{U_{\theta,slip}^2 + U_{r,slip}^2} \tag{2}$$

The change in the main flow features of the GSVU particulate flow, discussed in this section, namely i) pressure drop over the solids bed, ii) solids velocity iii) bed solids volume fraction and iv) slip velocity will next be studied for varying gas flow rate, solids density and particle diameter. The study is performed for a bed with mass of 2 kg for all simulation cases.

4.3.4 Effect of gas flow rate on GSVU hydrodynamics

Contrary to gravitational fluidized beds, a constant mass fluidized bed in the GSVU, as in the present study, will remain stable with increasing gas flow rate [31]. To investigate this claim, the gas flow rate is extended over a wide range (Table 6, cases 1-6) while particle diameter, solids density and bed mass (2 kg) are kept constant. The range of gas flow rates (Cases 1-6, Table 6) is selected such that a stable dense rotating solids bed is established while ensuring a low energy cost for sending pressurized gas through the GSVU in large quantities. The effect on the flow features described in the previous section is studied.

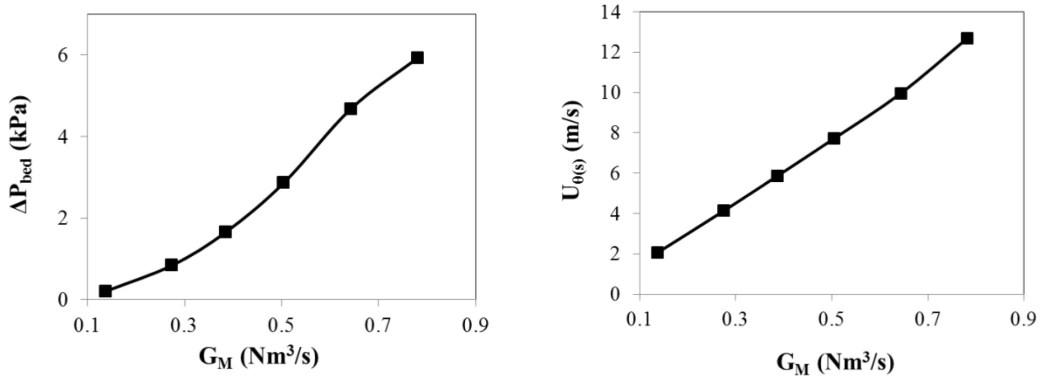

(a) (b)

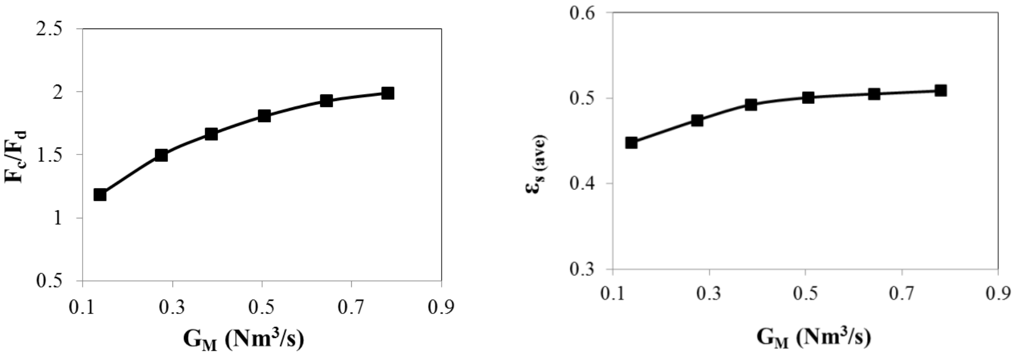

(c) (d)

Fig. 7. (a) Bed pressure drop; (b) bed-averaged azimuthal solids velocity; (c) cumulative centrifugal force to radial drag force ratio and (d) bed-averaged solids volume fraction as a function of gas flow rate for particulate flow calculated by solving Eqs. (2.1)–(3.11) in Tables 2 and 4 with parameter values in Table 5, for d_p=1 mm, ρ_s=950 kg/m^3. Bed mass=2 kg.

Fig. 7(a) shows an almost proportional increase of the pressure drop over the GSVU bed with increasing gas flow rate. Assuming the radial gas velocity gradients not to be significant and the viscosity of the gas being low, the gas momentum balance (Table 2, Eq. 2.2) over the radial coordinate can be simplified to:

$$\int_{P_0}^{P_i} dP = \int_{r_0}^{r_i} \left(\frac{1}{\varepsilon_g}\beta U_{slip}\right) dr \tag{3a}$$

with r_0 and r_i being the outer radius (circumferential wall) and inner radius (freeboard) of the bed respectively. The equation suggests that the radial pressure drop over the bed is a function of the radial drag force per unit volume acting on the particles. The cumulative drag force acting on the particles can be expressed as:

$$F_d = \int_{r_0}^{r_i} (2\pi r L)\beta U_{slip} dr \tag{3b}$$

Eq. 3(a)-(b) indicate that an increase of the drag force on the particles results in an increase in the pressure drop over the bed. When increasing the gas flow through a gravitationally fluidized bed, the increasing drag force on the particles will eventually result in entrainment of the particles, as the gravitational force on the particles remains unaffected. In the GSVU however, the centrifugal force on the particles increases with increasing gas flow rate as more azimuthal momentum is transferred to an invariant number of particles (constant bed mass). Consequently, the particles rotate with a higher azimuthal velocity as seen in Fig. 7(b). The proportional increase in azimuthal solids velocity with increasing gas flow rate has also been experimentally observed by De Wilde and de Broqueville[11]. With increasing azimuthal solids velocity the cumulative centrifugal force acting on the particles also increases in magnitude:

$$F_c = \int_{r_0}^{r_i} (2\pi r L) \rho_s \varepsilon_s \frac{U_{\theta,s}^{\ 2}}{r} dr \tag{4}$$

Therefore, in a GSVU, both the drag force and centrifugal force are altered with changing gas flow rate. Bed stability and particle entrainment for given operating conditions depend on the variation in the ratio of the two forces. It must be highlighted here that the densification of the bed in the GSVU is different from the fluidization behavior observed in a RFB. In a RFB, layer-by-layer fluidization is reported with increasing gas flow rate in RFBs[22,57].

From Fig. 7(c) the centrifugal to radial drag force ratio is seen to increase with increasing gas flow rate. As the ratio remains higher than one the particles will not be entrained and a stable solids bed is maintained for all gas flow rates investigated. With increasing gas flow rate, both the drag force and the centrifugal force increase. The increase in centrifugal force thus overcompensates the increase in radial drag force. Hence, the particles are pushed more strongly towards the circumferential wall and the bed is expected to become more compact. Fig. 7(d) shows that the bed-averaged solids volume fraction initially increases with increasing gas flow rate, making the bed more compact, in agreement with previous experimental studies[11]. Once the maximum packing limit is reached, the solids volume fraction remains nearly constant with increasing gas flow rate. Remark that the solids volume fraction presented in Fig. 7(d) is a bed-averaged value. Although in the middle part of the bed the solids volume fractions approach the maximum packing limit, the dilution of the bed towards the circumferential wall and towards the freeboard (Fig. 5(a)) reduces the bed-averaged solids volume fraction. From Fig. 8(a)-(c) it is found that with increasing gas flow rate, the azimuthal, radial and total slip velocity increase.

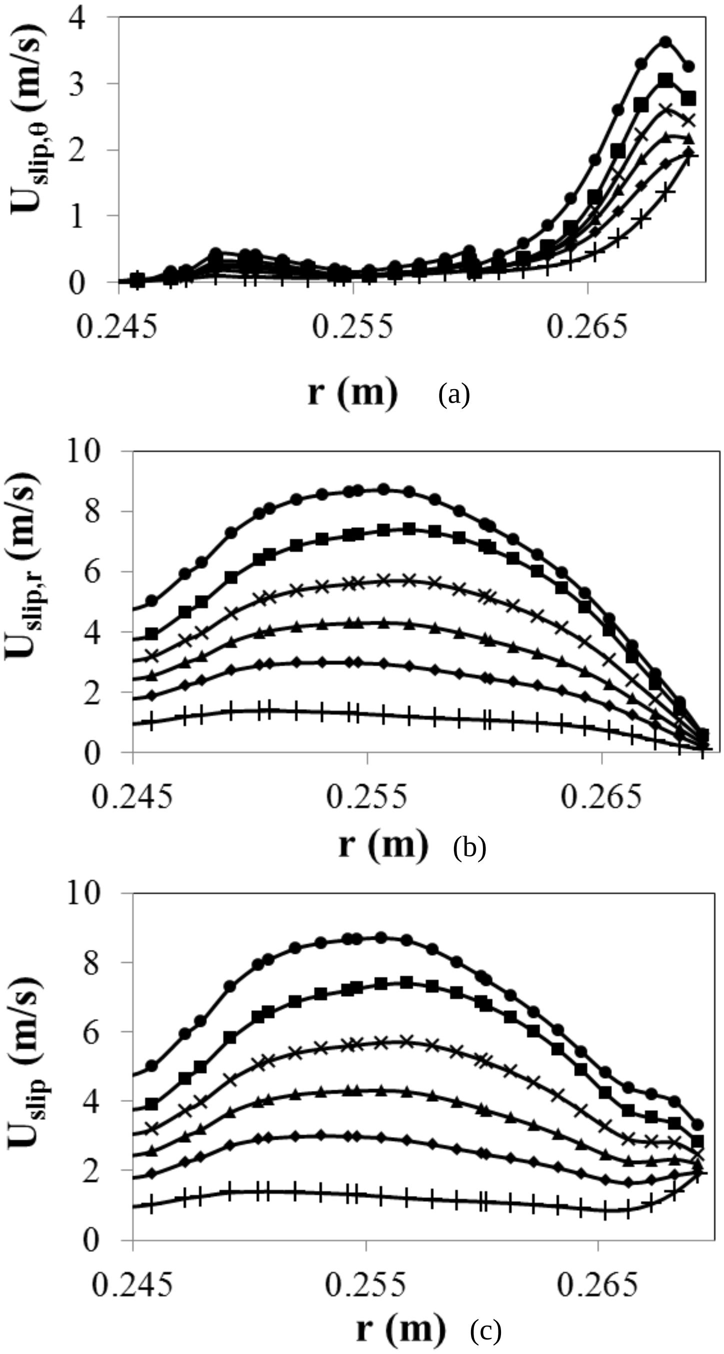

(a)

(b)

(c)

Fig. 8. Radial profiles of (a) azimuthal; (b) radial and (c) total slip velocity obtained along z=0.05m line in θ=20° plane, calculated by solving Eqs. (2.1)–(3.11) in Tables 2 and 4 with parameter values in Table 5, for (-+-) G_M=0.14 Nm^3/s; (-♦-) G_M=0.28 Nm^3/s; (-▲-) G_M=0.39 Nm^3/s; (-×-) G_M=0.5 Nm^3/s; (-■-) G_M=0.64 Nm^3/s and (-●-) G_M=0.78 Nm^3/s, d_p=1 mm, ρ_s=950 kg/m^3. Bed mass=2 kg.

In azimuthal direction, the slip velocity varies in a small part of the bed ($0.263<r<0.27$m) only. In the remaining part of the bed, the gas and solids azimuthal velocity are equal and the azimuthal slip velocity drops to zero (Fig. 6(a)). It is also observed that the radius where the azimuthal slip velocity drops to zero decreases with higher gas flow rates. In the radial direction however the interstitial gas velocity increases with increasing gas flow rate while the radial solids velocity is zero at all stable bed conditions (Fig. 6(b)). The increase in slip velocity with increasing gas flow rate, highlights one of the major strengths of the GSVU for process intensification. Increased slip velocities result in improved heat and mass transfer between the phases, without particle entrainment or bed dilution as observed in gravitational fluidized beds.

4.3.3 Effect of solids properties on GSVU bed hydrodynamics

The effect of solids properties on the GSVU bed hydrodynamics is studied under constant gas flow rate (0.39 Nm^3/s) and constant total bed mas (2 kg). As the centrifugal force acting on the particles is a function of both particle diameter and solids density, while the drag force is *primarily* but not uniquely influenced by the particle diameter but hardly by the solids density, both are varied independently in the present study.

4.3.4.1 Variation in solids density

A study with three solids densities is performed as shown in Table 6 (Cases 7-9). The solids densities are representative of biomass (450 kg/m^3), high density polyethylene (HDPE) (950 kg/m^3) and polyvinyl difluoride (PVDF) (1800 kg/m^3). The latter two have been used in previous experimental studies [32] on the effect of solids properties on GSVU bed hydrodynamics. As one of the currently investigated applications for the GSVU technology is fast biomass pyrolysis, a material density representative of the bulk density of biomass is also considered for analysis[28]. The particle diameter is kept constant at 1mm.

In order to analyze the effect of solids density on the GSVU bed hydrodynamics, the changes in the drag force exerted by the gas on the particles in the solids bed need to be understood. The overall cumulative radial drag force exerted on the solids bed is primarily influenced by the total area available for momentum transfer between the phases. This transfer surface area A_T is calculated as

$$A_T = (\frac{A_P}{V_P})V_T \qquad (5)$$

with $\left(\frac{A_P}{V_P}\right)$ being the volumetric cross-sectional area for momentum transfer per particle and V_T the total volume of particles in the bed. For spherical monodisperse particles the specific cross-sectional area per particle is calculated as

$$\left(\frac{A_P}{V_P}\right) = \frac{3}{2}\frac{1}{d_p} \qquad (6)$$

with d_p the particle diameter. In the solids density case study, the particle diameter is kept constant, thus the volumetric cross-sectional area per particle remains unchanged. Lowering the solids density implies that more particles are needed to keep the bed mass at 2 kg. Thus the total volume of particles V_T in the bed increases with decreasing solids density. This can be clearly seen in Figure 9, which shows the calculated contours of solids volume fraction in the θ=20° plane for different density materials and a bed mass of 2 kg.

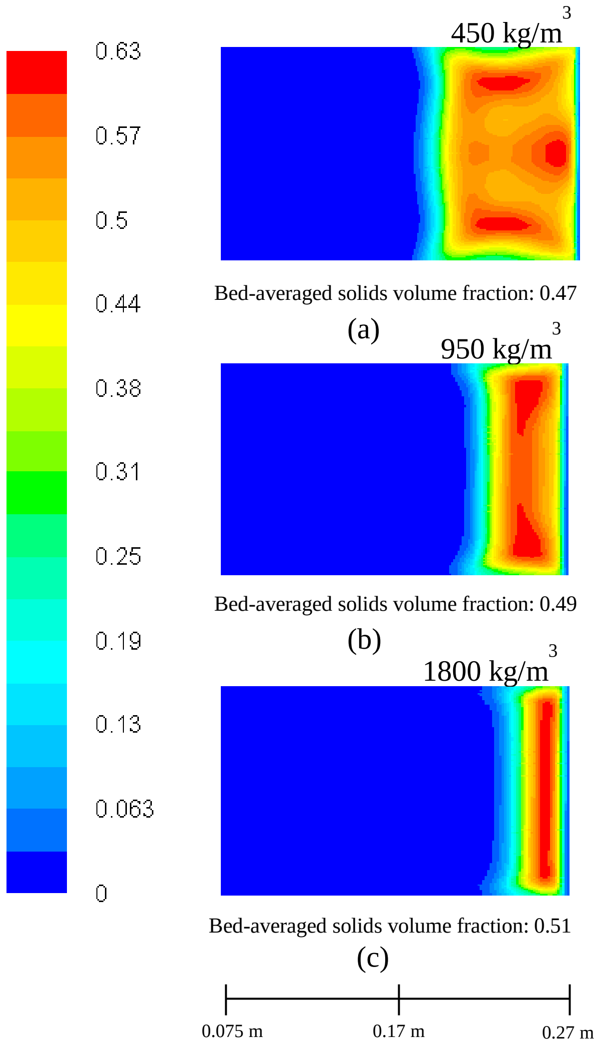

Fig. 9. Contours of solids volume fraction in θ=20° plane for different solids densities for particulate flow calculated by solving the set of Eqs. (2.1)–(3.11) given in Tables 2 and 4 with parameter values in Table 5, for G_M=0.39 Nm^3/s, d_p=1 mm, (a) 450 kg/m^3; (b) 950 kg/m^3 and (c) 1800 kg/m^3. Bed mass=2 kg.

With increasing number of particle layers, the total available surface area (A_T) for momentum transfer (Eq. 5) increases, which will cause the net drag force on the bed to increase. Indeed from the static gauge pressure profile along the radial coordinate, shown in Fig. 10(a), the pressure drop over the bed is seen to increase with decreasing solids density.

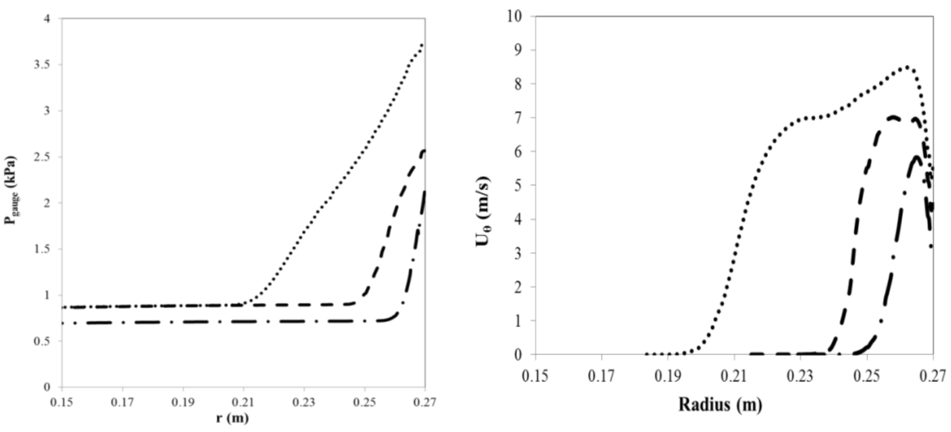

(a) (b)

Fig. 10. Radial profiles of (a) static gauge pressure and (b) solids azimuthal velocity obtained along z=0.05m line in θ=20° plane, calculated by solving Eqs. (2.1)–(3.11) in Tables 2 and 4 with parameter values in Table 5, for G_M=0.39 Nm^3/s, d_p=1 mm, (●●●) ρ_s=450 kg/m^3; (---) ρ_s=950 kg/m^3 and (-●-) ρ_s=1800 kg/m^3. Bed mass=2 kg.

As already discussed (Eq. 3), an increased pressure drop over the bed corresponds to an increase in the net drag force experienced by the particles. In Fig. 10(b) the azimuthal solids velocity in the θ=20° plane is seen to increase with decreasing solids density. This seems controversial at first glance. The gas flow rate remaining constant, a constant amount of azimuthal momentum is fed to the GSVU by the gas phase while the total bed mass in the unit is kept constant. Therefore, the velocity of the particles is not expected to vary with solids density. The trend can be explained however by considering the change in the ratio of centrifugal force to radial drag force for different densities, shown in Fig. 11(a).

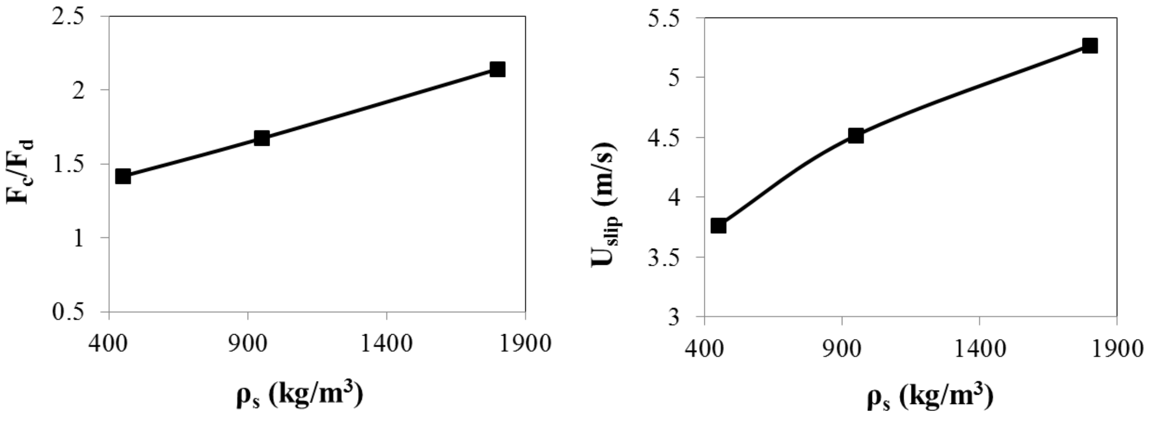

(a) (b)

Fig. 11. (a) Cumulative centrifugal force to radial drag force ratio and (b) bed-averaged slip velocity as a function of solids density for particulate flow calculated by solving Eqs. (2.1)–(3.11) in Tables 2 and 4 with parameter values in Table 5, for G_M=0.39 Nm^3/s, d_p=1 mm. Bed mass=2 kg.

A first observation is that, as the ratio is greater than 1, the bed is pushed towards the circumferential wall due to an unbalanced radially outward force. This results in a wall-normal force pushing the particles against the wall, generating particle-wall friction and hence, slowing down the particles. As the ratio of centrifugal to radial drag force decreases with decreasing solids density, the unbalanced force exerted on the circumferential wall diminishes, resulting in a reduction in particle-wall friction for decreasing solids density. The reduced frictional force on the low density particles will allow them to rotate with higher velocities, as observed in Fig. 10(b). Following this line of argument, the particles should have slowed down with increasing gas flow rate, which was not observed in the previous section (Fig. 7(b)). An increase in the gas flow rate increases the centrifugal to radial drag force ratio, thereby increasing the particle-wall friction. However, the net azimuthal momentum transferred to the particles from the gas phase also increases with increasing gas flow rate. This increase compensates the losses due to particle-wall friction. In the solids density case study the gas flow rate is kept constant and hence, there is no compensation.

The bed-averaged solids volume fractions only slightly decrease with decreasing solids density as can be seen in Fig. 9. Although the bed height increases and the solids volume fraction distribution becomes slightly non-uniform with decreasing solids density, the dense nature of the bed is retained and no macroscopic non-homogeneities such as bubble formation are observed. This can be explained by decreasing centrifugal to radial drag force ratio over the bed (Fig. 11(a)). As the cumulative centrifugal to radial drag force ratio over the entire bed decreases with decreasing solids density, the bed shows a higher degree of radial fluidization resulting in a decrease in the bed-averaged solids volume fractions. Nonetheless, for different solids densities the solids bed is sufficiently dense and stable without particle entrainment or bubble formation, demonstrating the capability of the GSVU to handle a wide range of density in materials.

In Fig. 11(b) the average slip velocity is seen to decrease with decreasing solids density. Since the gas flow rate is kept constant at 0.39 Nm^3/s, the fed radial and azimuthal gas momentum is constant for all beds. Furthermore, the change in the solids volume fractions inside the bed is not significantly altered (Fig. 9). Hence, the *radial* slip velocity remains mostly unaffected by a change in solids density, as confirmed by the simulations (not shown). However, with decreasing density, the bed rotates faster (Fig. 10(b)) and the *azimuthal* slip velocity between the gas and the particles diminishes (not shown). This causes a net decrease in the *total* slip velocity with decreasing solids density (Fig. 11(b)).

4.3.4.2 Variation in particle diameter

A study with three particle diameters is performed as shown in Table 6 (Cases 10-12). The solids density is set at 950 kg/m^3. The particle diameters chosen are 2, 1 and 0.5 mm. The 2 mm and 1 mm particle sizes constitute the size of polymeric materials experimentally investigated. As solids (in form of soft biomass pellets for future reactive flow applications such as fast biomass pyrolysis [28]) will become smaller in diameter due to breakage, a smaller particle diameter (0.05 mm) case has been considered. Remark that, for even smaller sized particles, additional van Der Waals' forces may be generated in between them. Since this force has not been accounted for in the present study, the lower range of the particle diameter is kept limited to 0.05 m.

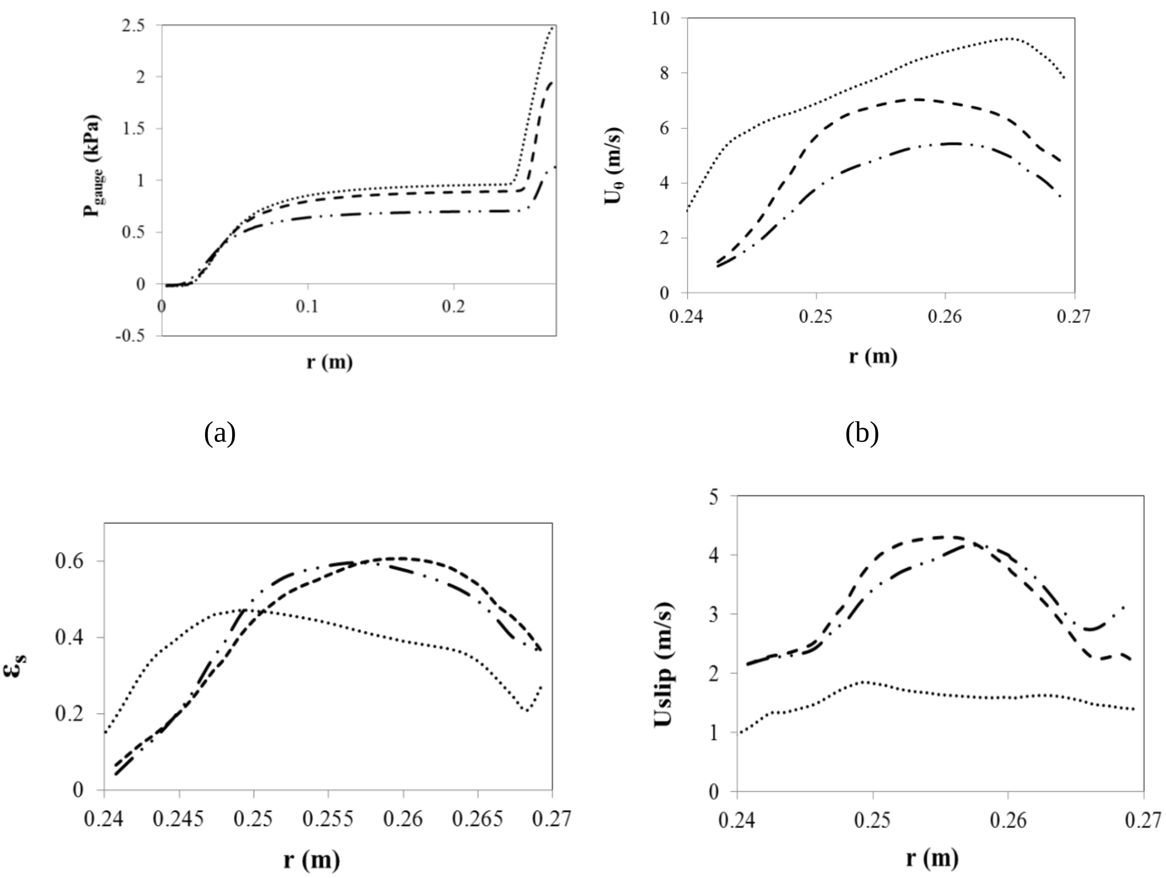

(a) (b)

(c) (d)

Fig. 12. Radial profiles of (a) static gauge pressure, (b) azimuthal solids velocity, (c) solids volume fraction and (d) slip velocity obtained along z=0.05m line in θ=20° plane, calculated by solving Eqs. (2.1)–(3.11) in Tables 2 and 4 with parameter values in Table 5, for G_M=0.39 Nm^3/s, (●●●) d_p=0.5 mm; (---) d_p=1 mm and (-●●-) d_p=2 mm, ρ_s=950 kg/m^3. Bed mass=2 kg.

In Fig. 12(a), the static gauge pressure drop along the radial coordinate in the θ=20° plane is seen to increase with decreasing particle diameter, indicating an increase in the overall drag force over the bed (Eq. 3). Accounting for the drag model proposed by Gidaspow [47] (Table 3, Eq. 3.4), the local drag force on the particles in the solids bed is an inverse function of the particle diameter. With decreasing particle diameter the number of particles required to keep the bed mass at 2 kg increases (as for decreasing solids density). However, since the particle diameter decreases the total bed volume hardly changes (V_T), as seen in Fig. 13.

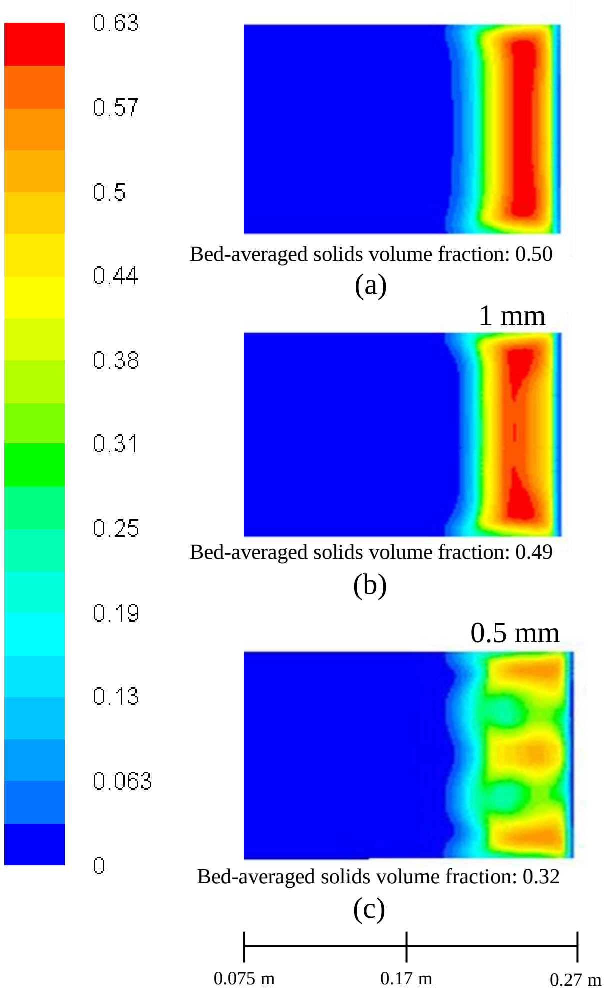

Bed-averaged solids volume fraction: 0.50
(a)

Bed-averaged solids volume fraction: 0.49
(b)

Bed-averaged solids volume fraction: 0.32
(c)

Fig. 13. Contours of solids volume fraction in θ=20° plane for different particle diameters for particulate flow calculated by solving the set of Eqs. (2.1)–(3.11) given in Tables 2 and 4 with parameter values in Table 5, for G_M=0.39 Nm^3/s, (a) 2 mm; (b) 1 mm and (c) 0.5 mm, ρ_s=950 kg/m^3. Bed mass=2 kg.

Moreover, reducing the particle diameter from 2 to 1 mm does not affect the uniformity of the dense bed significantly. Although the solids volume fractions near the central region of the bed decrease slightly with decreasing particle diameter, no macroscopic non-uniformities such as bubble formation are observed. The volume fractions in almost the entire bed reach nearly as high as the maximum packing limit. Reducing the particle diameter from 1 to 0.5 mm however, induces non-uniformity in the solids bed. The decrease in particle diameter to 0.5 mm causes a shift from a uniformly dense solids bed to a bubbling fluidized bed. The appearance of bubbles in the GSVU solids bed with decrease in particle diameter has previously been also observed in experiments[10], thus validating the qualitative trend in the bed behavior observed in the numerical simulations.

Bubble formation in the bed can be explained by investigating the variation in drag force with decreasing particle diameter. As discussed in the previous section, the drag force acting on the bed is a function of the total surface area A_T for momentum transfer between the phases (Eq. 5). From Fig. 13, it is already seen that the total solids volume V_T is not significantly affected by a change in particle diameter. The volumetric cross-sectional area $\left(\frac{A_P}{V_P}\right)$ per particle however, being inversely related to d_p for spherical particles (Eq. 6), increases with decreasing particle diameter. Thus the drag force *acting on a particle* increases with decreasing diameter. The centrifugal force acting on a particle however decreases due to the smaller diameter and hence mass, for constant density, of the particles. This local change in the centrifugal to radial drag force ratio, affects the balance over the *entire* bed. The calculated force ratio over the bed significantly decreases with decreasing particle diameter as shown in Fig. 14.

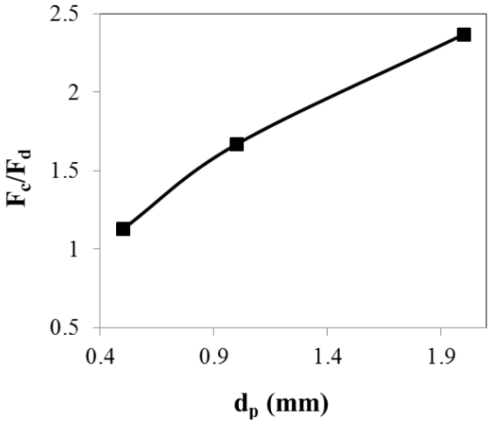

Fig. 14. Cumulative centrifugal force to radial drag force ratio as a function of particle diameter for particulate flow from calculated by solving Eqs. (2.1)–(3.11) in Tables 2 and 4 with parameter values in Table 5, for G_M=0.39 Nm^3/s, ρ_s=950 kg/m^3. Bed mass=2 kg.

The gas entering through the injection slots forces its way through the particles to form bubbles. For smaller particles (more drag, less apparent weight), gas bubbles will more easily be formed in the bed. This causes a shift to bubbling fluidization as observed in Fig. 13.

In Fig. 12(b), showing the profiles of the azimuthal solids velocity along the radial coordinate for different particle diameters, it is seen that for smaller particles the solids rotate with a higher azimuthal velocity. The reduced centrifugal to radial drag force ratio over the bed for smaller particles (Fig. 14) results in a reduction of the wall-normal force and causes the particles to accelerate as discussed above.

Fig. 12(c) shows the radial profile of the solids volume fraction for different particle diameters. Bubble formation in the bed of 0.5 mm particles causes the bed to expand and become more diluted as gas bubbles entrain small particles in their wake when travelling from the circumferential wall towards the freeboard region of the bed. As the gas passes through the bed in the form of bubbles, the gas-solid contacting area is diminished. Furthermore, bubbles induce radial solids recirculation in the bed. The corresponding reduction in radial velocity significantly reduces the total slip velocity in the bed as seen in Fig. 12(d). A reduction in the total slip velocity will result in a decrease of the heat and mass transfer efficiency of the GSVU. Thus, the bubbling fluidization regime is counterproductive for PI. Remark that the present study is performed in an imposed GSVU geometry. The minimum gas flow rate at which bubbling fluidization shifts to uniformly dense bed, for different particle diameters needs further study.

4.4 Conclusions

This paper explains the gas-solid bed hydrodynamics developing in a Gas-Solid Vortex Unit. To this end, a 3D Eulerian two-phase numerical study using FLUENT v.14a® of a 40° section of a GSVU unit is performed to obtain a proper visualization of the fluidization behavior.

Simulated radial profiles of static gauge pressure and solids velocity are compared with experimental data obtained in a GSVU. The model is found to predict well the pressure drop and solids velocity over a wide range of operating conditions. The validated model is then used for a study of the GSVU fluidization behavior for a range of operating conditions. Flow variables such as the bed pressure drop, solids volume fraction, solids velocity and slip velocity are calculated and analyzed. The simulations indicate that a stable uniformly dense bed can be formed inside the unit at high gas flow rates over a wide range of gas flow rates, solids densities and particle diameters, establishing the GSVU to be suitable for process intensification.

During the case study, no particle entrainment is observed, elaborating the flexibility of operation of the GSVU. With increasing gas flow rate, for constant solids density, particle diameter and bed mass, the increasing centrifugal to radial drag force ratio results in higher solids velocities, more compact beds and higher slip velocities. Contrary to Rotating Fluidized Beds, no radial layer-by-layer fluidization is observed in the GSVU as both azimuthal and radial momentum input of the gas increase simultaneously with increasing gas flow rate. Decreasing the solids density, for constant gas flow rate, particle diameter and bed mass, results in higher solids velocities due to a decrease of friction between the particles and the circumferential wall of the GSVU. At the same time, slip velocity is seen to decrease as the azimuthal solids velocity increases while the gas flow rate remains constant. Decreasing the particle diameter for constant gas flow rate, solids density and bed mass, eventually causes a shift in the fluidization regime and the GSVU bed exhibits bubbling behavior, due to the local reduction of centrifugal to radial drag force ratio. Meanwhile, the slip velocity is seen to decrease due to gas bypassing suggesting a possible decrease in heat and mass transfer efficiency in the GSVU. The model predicts changes in fluidization regime and can thus be used for further studying the fluidization regime maps for the GSVU at different operating conditions and for different types of materials.

4.5 Acknowledgments

This work was supported by the European Research Council FP7/2007-2013/ ERC grant agreement n° 290793. We are grateful for the use of the Stevin Supercomputer Infrastructure at Ghent University, funded by Ghent University, the Hercules Foundation, and the Flemish Government − department EWI.

4.6 References

1. Jensen AS. Pressurized drying in a fluid bed with steam. Paper presented at: Proceedings of the Eighth International Drying Symposium. March 1992; Montreal, Canada.

2. Avery DA, Tracey DH. Application of fluidized beds of activated carbon in solvent recovery from air or gas streams. Paper presented at: Tripartite Chemical Engineering Conference. April 1968; Montreal, Canada.

3. Maronga SJ, Wnukowski P. The use of humidity and temperature profiles in optimizing the size of fluidized bed in a coating process. Chemical Engineering and Processing: Process Intensification. 1998;37(5):423-432.

4. Nakaishi H. Paper presented at: Chemical Reactors.1984; Baifukan.

5. Karol FJ. Studies with High Activity Catalysts for Olefin Polymerization. Catalysis Reviews. 1984;26(3-4):557-595.

6. Froment G, Bischoff KB, DeWilde J. Chemical Reactor Analysis and Design. John Wiley & Sons, Inc., 2010.

7. Ahmadzadeh A, Arastoopour H. Three-dimensional numerical simulation of a horizontal rotating fluidized bed. Powder Technology. 2008;183(3):410-416.

8. Zhang W. A Review of Techniques for the Process Intensification of Fluidized Bed Reactors. Chinese Journal of Chemical Engineering. 2009;17(4):688-702.

9. Ahmadzadeh A, Arastoopour H, Teymoour F. Rotating Fluidized Bed an Efficient Polymerization Reactor. Paper presented at: AIChE Annual Meeting. November 2005; Cincinnati, USA.

10. De Wilde J, de Broqueville A. Rotating fluidized beds in a static geometry: Experimental proof of concept. AIChE Journal. 2007;53(4):793-810.

11. De Wilde J, de Broqueville A. Experimental study of fluidization of 1G-Geldart D-type particles in a rotating fluidized bed with a rotating chimney. AIChE Journal. 2008;54(8):2029-2044.

12. Volchkov EP, Dvornikov NA, Yadykin AN. Characteristic Features of Heat and Mass Transfer in a Fluidized Bed in a Vortex Chamber. Heat Transfer Research. 2003;34(78):13.

13. Kroger DG, Abdelnour G, Levy EK, Chen JC. Centrifugal fluidization: effects of particle density and size distribution. Chemical Engineering Communications. 1980/01/01 1980;5(1-4):55-67.

14. Qian G-H, Bágyi I, Burdick IW, Pfeffer R, Shaw H, Stevens JG. Gas–solid fluidization in a centrifugal field. AIChE Journal. 2001;47(5):1022-1034.

15. Matsuda S, Hatano H, Muramoto T, Tsutsumi A. Modeling for size reduction of agglomerates in nanoparticle fluidization. AIChE Journal. 2004;50(11):2763-2771.

16. Eliaers P, de Broqueville A, Poortinga A, van Hengstum T, De Wilde J. High-G, low-temperature coating of cohesive particles in a vortex chamber. Powder Technology. 2014;258:242-251.

17. Fan LT, Chang CC, Yu YS, Takahashi T, Tanaka Z. Incipient fluidization condition for a centrifugal fluidized bed. AIChE Journal. 1985;31(6):999-1009.

18. Nakamura H, Iwasaki T, Watano S. Experimental analysis of bubble velocity in a rotating fluidized bed. Chemical Engineering and Processing: Process Intensification. 2009;48(1):178-186.

19. Anderson LA, Hasinger SH, Turman BN. Two-Component Vortex Flow Studies of the Colloid Core Nuclear Rocket. Journal of Spacecraft and Rockets. 1972;9(5):311-317.

20. Smulsky JJ. The aerodynamics and process in the vortex chamber. Tyumen, Russia: Science; 1992.

21. Ekatpure R, Heynderickx G, Broqueville AD, Marin GB. Experimental Investigation of Rotating Fluidized Bed in Static Geometry. Paper presented at: 2nd European Process Intensification Conference. 2009; Venice, Italy.

22. Chen YM. Fundamentals of a centrifugal fluidized bed. AIChE Journal. 1987;33(5):722-728.

23. Dutta A, Ekatpure RP, Heynderickx GJ, de Broqueville A, Marin GB. Rotating fluidized bed with a static geometry: Guidelines for design and operating conditions. Chemical Engineering Science. 2010;65(5):1678-1693.

24. Bykovskii FA, Zhdan SA, Mitrofanov VV, Vedernikov EF. Self-ignition and special features of flow in a planar vortex chamber. Combustion, Explosion and Shock Waves. 1999;35(6):622-636.

25. Lukashov VV, Mostovoi AV. Investigation of a Vortex Combustion Chamber with a Centrifugal Fluidized Bed. 2006;37(8):685-690.

26. Timonin AS, Mushtaev VI, Nguen ZT, Pakhomov AA, Ryauzov AG. Spiral-vortex apparatus — effective equipment for the heat treatment of disperse materials. Chemical and Petroleum Engineering. 1997;33(1):7-10.

27. Belousov AS, Sazhin BS. Characteristics of flow structures in units for processing fibre-forming polymers inactive hydrodynamic regimes. Fibre Chemistry. 2007;39(6):475-479.

28. Ashcraft RW, Heynderickx GJ, Marin GB. Modeling fast biomass pyrolysis in a gas–solid vortex reactor. Chemical Engineering Journal. 2012;207–208:195-208.

29. Ashcraft RW, Kovacevic J, Heynderickx GJ, Marin GB. Assessment of a Gas–Solid Vortex Reactor for SO2/NOx Adsorption from Flue Gas. Industrial & Engineering Chemistry Research. 2013;52(2):861-875.

30. Shtern V. Counterflows: paradoxical fluid mechanics phenomena: Cambridge University Press, 2012.

31. Kovacevic JZ, Pantzali MN, Heynderickx GJ, Marin GB. Bed stability and maximum solids capacity in a Gas–Solid Vortex Reactor: Experimental study. Chemical Engineering Science. 2014;106:293-303.

32. Kovacevic JZ, Pantzali MN, Niyogi K, Deen NG, Heynderickx GJ, Marin GB. Solids velocity fields in a cold-flow Gas–Solid Vortex Reactor. Chemical Engineering Science. 2015;123:220-230.

33. Kochetov LM, Sazhin BS, Karlik EA. Hydrodynamics and heat exchange in vortex drying chambers. Chemical and Petroleum Engineering. 1969;5(9):688-690.

34. Volchkov EP, Terekhov VI, Kaidanik AN, Yadykin AN. Aerodynamics and Heat and Mass Transfer of Fluidized Particle Beds in Vortex Chambers. Heat Transfer Engineering. 1993;14(3):36-47.

35. Sinclair JL, Jackson R. Gas-particle flow in a vertical pipe with particle-particle interactions. AIChE Journal. 1989;35(9):1473-1486.

36. Rosales Trujillo W, De Wilde J. Fluid catalytic cracking in a rotating fluidized bed in a static geometry: a CFD analysis accounting for the distribution of the catalyst coke content. Powder Technology. 2012;221:36-46.

37. de Broqueville A, De Wilde J. Numerical investigation of gas-solid heat transfer in rotating fluidized beds in a static geometry. Chemical Engineering Science. 3/16/ 2009;64(6):1232-1248.

38. Baeyens J, Geldart D. An investigation into slugging fluidized beds. Chemical Engineering Science. 1974;29(1):255-265.

39. Ekatpure RP, Suryawanshi VU, Heynderickx GJ, de Broqueville A, Marin GB. Experimental investigation of a gas–solid rotating bed reactor with static geometry. Chemical Engineering and Processing: Process Intensification. 2011;50(1):77-84.

40. Pantzali MN, Kovacevic JZ, Heynderickx GJ, Marin GB, Shtern V. Radial pressure profiles in a cold-flow gas-solid vortex reactor. AIChE Journal. 2015;61(12):4114-4125.

41. Anderson TB, Jackson R. Fluid Mechanical Description of Fluidized Beds. Equations of Motion. Industrial & Engineering Chemistry Fundamentals. 1967;6(4):527-539.

42. Jenkins JT, Savage SB. A theory for the rapid flow of identical, smooth, nearly elastic, spherical particles. Journal of Fluid Mechanics. 1983;130:187-202.

43. Gidaspow D. Multiphase flow and fluidization: continuum and kinetic theory descriptions. Academic press, 1994.

44. Yakhot V, Orszag SA. Renormalization group analysis of turbulence. I. Basic theory. Journal of Scientific Computing. 1986;1(1):3-51.

45. Launder BE, Spalding DB. The numerical computation of turbulent flows. Computer Methods in Applied Mechanics and Engineering. 1974;3(2):269-289.

46. Lun CKK, Savage SB, Jeffrey DJ, Chepurniy N. Kinetic theories for granular flow: inelastic particles in Couette flow and slightly inelastic particles in a general flowfield. Journal of Fluid Mechanics. 1984;140:223-256.

47. Gidaspow D, Bezburuah R, Ding J. Hydrodynamics of circulating fluidized beds: Kinetic theory approach. Paper presented at: Fluidization VII, Proceedings of the 7th Engineering Foundation Conference on Fluidization1992.

48. Ogawa S, Umemura A, Oshima N. On the equations of fully fluidized granular materials. Zeitschrift für angewandte Mathematik und Physik ZAMP. 1979;31(4):483-493.

49. Syamlal M, Rogers W, O`Brien TJ. MFIX documentation theory guide. 1993.

50. Schaeffer DG. Instability in the evolution equations describing incompressible granular flow. Journal of Differential Equations. 1987;66(1):19-50.

51. Johnson PC, Jackson R. Frictional–collisional constitutive relations for granular materials, with application to plane shearing. Journal of Fluid Mechanics. 1987;176:67-93.

52. Vatistas GH, Fayed M, Soroardy JU. Strongly Swirling Turbulent Sink Flow Between Two Stationary Disks. Journal of Propulsion and Power. 2008;24(2):295-301.

53. Moysey PA, Thompson MR. Determining the collision properties of semi-crystalline and amorphous thermoplastics for DEM simulations of solids transport in an extruder. Chemical Engineering Science. 2007;62(14):3699-3709.

54. Goro K, Kimitoshi K. Restitution Coefficient in a Collision between Two Spheres. Japanese Journal of Applied Physics. 1987;26(8):1230.

55. Patankar SV. Numerical Heat Transfer and Fluid Flow. New York: McGraw-Hill; 1980.

56. De Wilde J. Gas–solid fluidized beds in vortex chambers. Chemical Engineering and Processing: Process Intensification. 2014;85:256-290.

57. Ahmadzadeh A, Arastoopour H, Teymour F. Numerical Simulation of Gas and Particle Flow in a Rotating Fluidized Bed. Industrial & Engineering Chemistry Research. 2003;42(12):2627-2633.

Chapter 5

Conclusions and future work

5.1 Conclusions

The present numerical study provides an in-depth analysis of the various hydrodynamic flow features arising in a Vortex Unit over a wide range of operating conditions for both single phase and multiphase flows. Experimental measurements in the vortex unit are highly complicated as any intrusive measurement technique may disrupt the local flow. Surface flow measurements through the transparent end-wall of the unit can be carried out. However, the near-wall hydrodynamics in the vortex unit may not represent the bulk flow due to secondary flow formations. As such, ae numerical investigation of the vortex unit flow reveals various hydrodynamic aspects that experiments cannot measure.

In the first part of this study, single phase gas-only flow is investigated using the commercial finite volume package, Fluent® v.14a. Both three-dimensional and axisymmetric flow simulations are carried out using Reynolds Stress Modeling for closing the flow turbulence. Simulations with considerable mesh refinement reveal interesting secondary flow phenomena. The second part of the thesis focuses on the numerical investigation of two-phase flow, where particles introduced into the geometry through a solids inlet, obtain an azimuthal momentum from the swirling gas flow, and form a rotating fluidized bed. The hydrodynamics of the single and two-phase flows are significantly different and are studied separately. The computational models used for the complete numerical flow analysis are first validated using experimental data obtained in a laboratory GSVU using various experimental techniques such as pressure probes, Stereoscopic Particle Image Velocimetry (PIV) and oil flow visualization.

The numerical simulation of the swirling gas-only flow through the Vortex Unit reveals various interesting secondary flow features. The azimuthal velocity of the gas is the dominant velocity in the unit as the gas spirals towards the central unidirectional exhaust. However, the numerical simulations show that close to the end-walls of the unit, where the azimuthal velocity drops to zero in the thin boundary layers, radially directed gas jets are formed. The development of the near-wall jets is found to be based on three important flow features occurring simultaneously in the GVU: (i) the spatial flow acceleration behavior of the gas in the disc part of the unit, such that the angular momentum is conserved, and the azimuthal velocity increases with decreasing radius of the unit; while the free-swirling behavior of the gas makes the azimuthal velocity significantly dominant in the GVU flow over the radial and axial counterparts; (ii) the establishment of the cyclostrophic balance between the radially outward centrifugal force generated on the rotating gas elements and the radially inward pressure gradient; (iii) the no-slip condition at the end-walls. The end-walls cause the gas azimuthal velocity to decrease in the near-wall boundary layers, thereby reducing the centrifugal force acting on the gas elements. The cyclostrophic balance is broken and the unbalanced radially inward pressure gradient pushes the gas elements towards the central exhaust in the form of two thin near-wall jets. The formation of the near-wall jets is a numerical finding and requires experimental validation. The high Reynolds number of the flow, however, causes these boundary layers to be extremely thin and hence conventional techniques such as PIV and LDA (Laser Doppler Anemometry) cannot be used to study the near-wall jet formation. Hence, the surface oil flow visualization technique on an end-wall of the Vortex Unit is applied for the jet observation, tracing flow streamlines near the (rear) end-wall of the pilot-scale set-up. This technique, together with the extremely refined prism cells (meshing) in the numerical modeling, resolves the three velocity components of the near-wall jets and helps to render a first ever 3D visualization of the near-wall jets in the GVU. The propagation of the near-wall jets in the radial direction is also investigated. It is found that the jets become strongest halfway between the circumferential wall and the central gas exhaust of the Vortex Unit.

The numerical study of the GVU flow also reveals two secondary recirculation flows in the unit. The main throughput in the unit is oriented radially inward through the disc part, followed by an axially outward flow through the central unidirectional gas exhaust. However, the high degree of swirl in the flow results in the formation of recirculation regions in both the disc part and the exhaust pipe of the geometry. As the swirling gas leaves the unit through the exhaust line, the rotational momentum of the gas gradually decays due to friction with the walls of the exhaust pipe. A static pressure gradient in the reverse direction develops (from the outlet of the exhaust pipe to the rear-end wall of the unit), resulting in the formation of a recirculation region referred to as the GVU Backflow Region. Experimental static pressure measurements help to validate the numerical prediction of the Backflow Region. The simulations also show the development of a strong recirculation region between the two end-walls in the disc part of the unit, referred to as the Counterflow Region. A closer study of the Counterflow Region reveals that the counterflow is induced as a result of the entrainment of gas from the bulk of the unit by the near-wall jets. When the jets are sufficiently strong, the jet entrainment flow rate exceeds the gas injection flow rate in the GVU, causing the jets to suck gas from the downstream section of the unit, resulting in a radially outward flow in between the two end-walls of the unit. This analysis helps to explain the formation of the Counterflow Region.

The Stereoscopic PIV technique, tracing oil droplets injected in the gas bulk flow, is used to validate the numerical predictions. Although S-PIV tracer droplets are found to be influenced by the strong centrifugal force acting on them, thereby slightly distorting the counterflow visualization, the technique qualitatively verify the presence of this Counterflow recirculation Region in the unit. Once the numerical model is validated, the effect of different swirl ratios (S) and Reynolds numbers (Re) on the secondary flow features is investigated. At a cutoff swirl ratio S, for a given Re number, the formation of the Counterflow Region is observed. With increasing degree of swirl in the geometry, the Counterflow Region grows in size till saturation is reached. Beyond this value of swirl ratio, though the counterflow did not increase in size, the Counterflow Region becomes multicellular, thus indicating intense mixing in the bulk region of the GVU. When increasing Re for a constant S, both the Backflow and the Counterflow regions are formed and become saturated very fast. At Re values typical for industrial applications, the flow topology and in turn, the secondary flow phenomena in the GVU, are found to become independent of Re.

After analyzing the gas-only flow hydrodynamics, the numerical study shifts its focus to the two-phase (gas-solid) flow investigation in the vortex unit (regarded henceforth as GSVU). 3D Eulerian two-phase simulations are carried out using FLUENT v.14a® for a 40° section of a GSVU in order to obtain a proper visualization of the fluidization behavior. An Eulerian-Eulerian simulation framework is implemented. It treats the solid and gas phases as interpenetrating continuous media and hence, is less computational expensive as compared to Eulerian-Lagrangian simulations.

Introduction of solids in the swirling gas flow reduces the strong swirl structure of the gas. The solids start rotating and the centrifugal force acting on the individual particles pushes them close to the circumferential wall, resulting in the formation of an annular dense rotating solids bed. The numerical model is again first validated by comparing the simulated radial profiles of static gauge pressure and solids velocity magnitude with experimental data obtained using S-PIV in the experimental GSVU setup. The model predictions are found to be in good agreement with the experimental data. The validated model is then used to study differences in the fluidization behavior in the GSVU over a wide range of operating conditions.

The simulations predict the formation of a stable, dense (ε_s=0.5 approx.) bed over the entire wide range of gas flow rates investigated. This strengthens the claim that the GSVU has process intensification potential for fluidization, as it enables uniform dense bed operation at high gas flow rates without causing any particle elutriation, as observed in a conventional gravitational fluidized beds. The pressure drop over the GVSU as compared to the GVU is found to decrease due to the introduction of the particles in the swirling gas flow field. It is conjectured that the particles break the swirling flow structure of the gas in the unit. This, in turn, reduces the Backflow Region near the exhaust, thereby increasing the net cross-sectional area available in the gas exhaust line for the gas to leave the unit. As a result, the pressure drop in the GSVU drops. This change in pressure drop behavior is particularly unique for the GSVU and is counter-intuitive, as in conventional fluidized beds the pressure drop increases when particles are introduced in the geometry.

Next, a host of flow conditions such as gas flow rate, solid density and particle diameter are varied in a systematic study of their effect on the fluidization behavior in the GSVU. No particle entrainment is observed, even at higher gas flow rates, thus further highlighting the extended range of operation of the GSVU. Particle elutriation in the GSVU is closely linked to the centrifugal-to-drag force ratio on the particles in the solids bed. Simulations show that increasing the gas flow rate in the unit actually increases the centrifugal-to-drag force ratio acting on the solids bed making the bed more stable and compact. Radial layer-by-layer fluidization however, as commonly seen in mechanically rotating packed beds, is not observed in the GSVU, highlighting an interesting contrast between the two fluidization technologies.

The fluidization behavior of different materials in the Vortex Unit is studied next. The solids density is varied, for a constant gas flow rate, particle diameter and bed mass. Lighter solids do not affect the dense nature of the solids bed. However, the solids bed is found to rotate faster in the GSVU when the solids density decreases. Under the simulated operating conditions in the GSVU, the net centrifugal-to-drag force ratio on the solids bed is shown to be higher than unity. This causes the particles to be pushed against the circumferential wall, resulting in wall friction on the sliding particles. Decreasing the solids density results in an increase in the drag force exerted on the particles. As a result, the centrifugal-to-drag force ratio decreases, and consequently the net unbalanced wall force on the particles also decreases. The friction acting on the particles is reduced, increasing the solids velocities. However, as the net gas flow rate remains constant, the slip velocity between the two phases decreases slightly. The reduced slip velocity is expected to negatively affect the heat and mass transfer rate between the two phases.

The simulations also reveal a remarkable GSVU bed flow phenomenon, when studying the effect of decreasing the particle diameter for constant gas flow rate, solids density and bed mass. Decreasing the particle diameter eventually causes a shift in the fluidization regime. The dense nature of the bed is lost and it starts to exhibit bubbling behavior. This regime shift is supposed to be a consequence of the change in the *local* centrifugal-to-drag ratio on the particles. On particle scale, the drag force is linked to the cross-sectional area of a particle, while the centrifugal force is linked to the density and volume of the material. As the particle becomes smaller, the *local* centrifugal-to-drag force ratio decreases, enabling the gas to form bubbles in the solids bed. Due to bubbling, the gas-solid contact is found to deteriorate and the slip velocity between the phases is observed to decrease due to gas bypassing. This is indicative of a possible decrease in heat and mass transfer efficiency in the GSVU, at given combinations of operating conditions and particle properties. Interestingly, when increasing the gas flow rate through the bubbling solids bed in the GSVU, the bed becomes more dense and homogenous. This highlights yet another unique characteristic of the GSVU flow hydrodynamics. In conventional gravitational fluidized beds, and even in mechanically rotated fluidized beds, increasing the gas flow rate through a solids bed that exhibits bubbling behavior will result in particle elutriation. However, in the GSVU increasing the gas flow rate will restore the homogenous character of the solids bed.

Considering all these findings on GSVU hydrodynamics, it can be concluded that the present numerical study suggests that the fluidization regime map for a centrifugally fluidized bed will differ from its gravitational counterpart. This paves the way for further cold-flow exploration of the GSVU hydrodynamics through future numerical and experimental studies.

5.2 Future work

The present numerical study indicates the potential of the Vortex Unit technology to qualify as an interesting tool for process intensification in chemical and energy industry. The Vortex Unit provides the unique opportunity of harnessing the centrifugal force in order to significantly increase heat and mass transfer rates in reactive and unit operation applications without the need for mechanically moving parts. However, process intensification in a Vortex Unit comes at a cost. For instance, the gas flow rates necessary for generating the solids bed in a Vortex Unit is quite high, which makes the scaling of a Vortex Unit quite challenging. Additionally, flow features such as the near-wall jets, can entrain fine particles in a multiphase GSVU flow, resulting in a loss of valuable catalyst particles, for instance. Furthermore, due to the gas injection through inclined inlet slots, the radial and azimuthal components are always coupled, decreasing the degrees of freedom as compared to the mechanically moving rotating fluidized beds, where centrifugal and drag force can be set independently. Each of these challenges requires separate attention and proper experimental investigation. But experimental measurements in the Vortex Unit can be quite challenging due to geometrical design limitations. Hence, numerical simulations have to go hand-in hand with experimental studies to assure a thorough analysis of the vortex unit hydrodynamics. Only then, the true process intensification potential of the vortex unit can be determined.

In an attempt to chalk out a future research plan for the Vortex Unit technology the following suggestions for possible research directions are made. The research suggestions are broadly divided in three categories for ease of parallel project development:

5.2.1 Gas Vortex Unit

The present study analyzes in depth the various hydrodynamic secondary flow phenomena that may arise in the GVU under a high degree of swirl. The study also characterizes the GVU flow through dimensionless groups, such that a chosen set of flow conditions and geometrical parameters, giving the same Reynolds number and swirl ratio, is expected to result in similar hydrodynamic characteristics and flow topology for different GVU setups. However, the study does not separately consider the effect of the unit length-to-diameter aspect ratio, or the ratio of total gas injection slots area to total circumferential unit area, on the flow topology. This provides a clear avenue for further research into the GVU flow topology using the already benchmarked CFD code, as building separate setups for this study may prove expensive. Additionally, the intense mixing and recirculation zones in the GVU make the Vortex Unit an ideal candidate for combustion and stable flame generation. Including comprehensive kinetic models in the cold flow CFD code as developed, and studying the effect of hydrodynamics on the reaction kinetics, will further clarify the efficiency of the GVU as a process intensification tool.

5.2.2 Gas Solid Vortex Unit

The Gas Solid Vortex Unit promises to be an ideal process intensification device for the present day fluidization technology. It will allow the formation of dense uniform solids beds, with solid volume fractions as high as packed beds, at much higher gas flow rates as compared to the conventional gravitational fluidized beds. However, unlike a packed bed, the GSVU provides an opportunity for the particles to be operated in a continuous mode with constant feeding and removal. This can be significantly beneficial for processes such as catalytic reactions where the catalyst can be recycled rather easily. As compared to a mechanically rotating packed bed, the GSVU again proves advantageous since the latter does not involve any mechanical moving parts and thus is safe from mechanical abrasion. This can make scalingof the unit less challenging. However, even though the GSVU seems to outperform all other competitors in fluidization technology, there are some unmet challenges that need to be addressed to allow its commercialization.

So far the GSVU simulations have been carried out in a cold flow framework, without the inclusion of detailed kinetics such as, eg, biomass pyrolysis. An initial 2D simulation study of the latter has been carried out (Ashcraft et al., 2014) to demonstrate the potential of the Vortex Unit for process intensification of fast biomass pyrolysis. However, in the present work it is concluded that the end-walls of the unit significantly affect the flow and may cause, for instance, entrainment of finer particles as the biomass gets pyrolysed in the unit. Hence the present cold flow 3D simulation model can be coupled with kinetic models to evaluate the true process intensification potential of the GSVU technology.

Another interesting direction for the future study can be the implementation of more than one type of particles in the Vortex Unit to test the particle segregation characteristics. As reactive GSVU flows will often involve particles with not just a constant size, but rather a particle size distribution, this study can help to analyze the mixing and segregation capacity of the device for reactive applications. For instance, the variable centrifugal force on different types of particles may result in elutriation of fines, a feature particularly appealing for biomass pyrolysis. The fines in the pyrolysis process mostly constitute the char which can cause undesired secondary reactions deteriorating the quality of the bio-oil. The GSVU can provide a stable operation by which char is entrained very quickly from the unit preventing detrimental reactions to start.

5.2.3 Scale-Up Study

The GSVU has already been shown to be an ideal reactor for fast reactions such as biomass pyrolysis (Ashcraft et al., 2014). Biomass pyrolysis is endothermic in nature and the high temperatures (around 500°C) can alter the properties of the fluidizing gas such as gas density and viscosity as compared to the cold flow operation values. This in turn may alter the fluidization regimes observed at the same gas flow rates in the cold flow studies. Moreover, the quantity of fluidizing gas for the pyrolysis process is one of the most crucial cost determining factors. As the Vortex Unit already needs a quite high quantity of gas for fluidizing the solids, scaling-up the unit to an industrial-scale set-up might prove to be not very cost-effective. Using a network of smaller units for the pyrolysis process could solve this drawback. All these challenges indicate that a proper scale-up study is required to ensure cost- effectiveness of the commercial vortex unit technology. The scale-up study is initiated by deriving the dimensionless groups governing the GVU/ GSVU flow. It can be found in Appendix 1.

Appendix A: Dimensional groups

As a guide for the future researchers working on vortex unit technology, two methods to derive the dimensionless groups describing the unit hydrodynamics have been documented in the subsequent section, a first approach to scale-up studies.

A.1 Dimensional analysis using the Buckingham PI theorem

A first method is applying the Buckingham Pi Theorem (Bertrand, 1878). The theorem states that

> *"If a physical process depends on n independent parameters, it can be simplified to a relationship between (n-k) dimensionless parameters (pi groups), where, k is the number of dimensionally independent parameters which is less than or equal to the number of dimensions (mass, time and length)."*

In a first step the demarcation between process parameter and variable is highlighted. The definitions pertain to the convention commonly used for fluidization systems as suggested by Kline (1965). By this convention, quantities that vary in space or time for a particular problem are termed as variables (particle position, time, local velocities), whereas quantities that are constant for a particular problem but can vary between two of the same types of problems are termed as parameters (superficial injection gas velocity, total pressure drop over the unit, particle diameter, solids density).

Applying the Pi Theorem to determine the significant dimensionless groups for a vortex unit, a step-by-step guideline is demonstrated *for the GVU*. The method can be extended to the GSVU hydrodynamics, although not demonstrated in the present work.

A.1.1 Choosing the parameter space

In a process, any dependent parameter is a function of a set of dimensional independent parameters. The first step when applying the Pi theorem is to express this functionality such that *all* the independent parameters are included in the relationship. For the GVU, this relation can be of the form

$$\Delta P_{reactor} = f(D_R, D_E, L_R, A_{in}, \gamma, \rho_f, \mu_f, U_{0_i}) \tag{1}$$

where,

$$A_{in} = (I_0 \times L_R) \times n \tag{2}$$

It is important to note here that total unit pressure drop instead of local pressure has been designated as a process parameter. While the local pressure in the unit may change depending on the position, the total pressure drop is unique for a given set of operating conditions. The parameters are enlisted in Table 1 with the corresponding geometrical parameters graphically represented in Fig. 1.

Table 1. List of independent parameters in the GVU

Geometrical parameters	
D_R	Unit diameter
D_E	Exhaust diameter
L_R	Unit length
A_{in}	Total area of injection slots
γ	Injection slot angle
Fluid properties	
ρ_f	Fluid density
μ_f	Fluid viscosity
Operational conditions	
U_{0i}	Superficial injection velocity

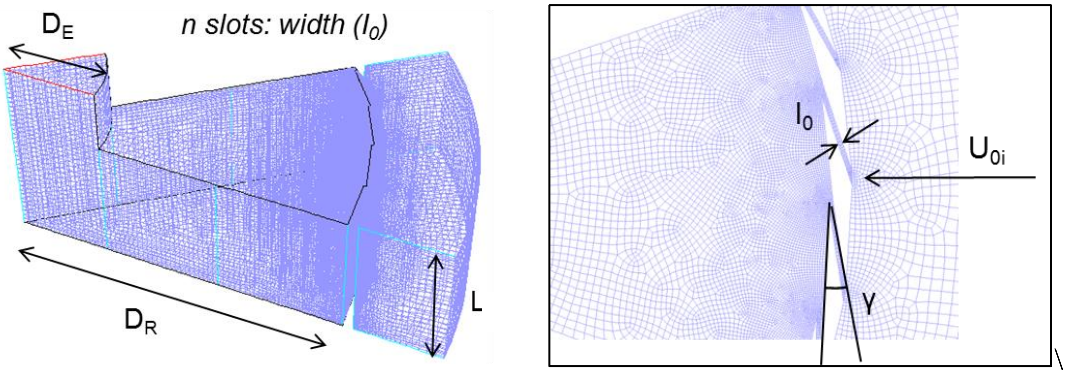

Fig. 1. Geometrical parameters in the Gas Vortex Unit

A.1.2 Listing the dimensions of in the parameter space

The next step is to express each of the parameters in a the form of the independent dimensions (length, time and mass) that constitute them. For the GVU, this is shown in Table 2.

Table 2. Dimensional form of the independent parameters in the GVU

ΔP	$ML^{-1}T^{-2}$
Geometrical parameters	
D_R	L
D_E	L
L_R	L
A_{in}	L^2
γ	-
Fluid properties	
ρ_f	ML^{-3}
μ_f	$ML^{-1}T^{-1}$
Operational conditions	
U_{0i}	LT^{-1}

From Table 2 it follows that for the particular case of the GVU, there are in total 9 parameters in the parameter space and 3 independent dimensions. Following the Pi theorem, therefore, should result in the formulation of (9-3) = 6 dimensionless groups.

A.1.3 Choosing the dimensionally independent subset

The next step is to choose an equal number of dimensionally independent parameters from the entire parameter space as the number of dimensions in the system (3, in the present case). For the GVU, one such set can be formed, including the following: the unit diameter (D_R), the gas density (ρ_f) and the superficial injection velocity (U_{oi}).

A.1.4 Forming the dimensionless Π groups

A Π group can be expressed as a product of the other parameters in the parameter space with the dimensionally independent parameters, chosen in step 3, each raised to an unknown exponent. For instance, the first parameter, the total unit pressure drop, can be used to derive the first dimensionless group as follows

$$\pi_1 = \Delta P \times {D_R}^a \times {\rho_f}^b \times {U_{0_i}}^c \tag{3}$$

$$\pi_1 = \frac{M}{LT^2} \times L^a \times \frac{M^b}{L^{3b}} \times \frac{L^c}{T^c} \tag{4}$$

The LHS of the above equation is dimensionless thus suggesting that the exponents for each of the dimensions of the RHS parameters should add up to zero. This results in a set of simultaneous equations which, when solved, gives the values of the exponents needed to build the dimensionless groups. This is demonstrated as follows

$$c + 2 = 0 \tag{5}$$

$$1 + b = 0 \tag{6}$$

$$a + c + 2 = 0 \tag{7}$$

which results in

$$c = -2 \tag{8}$$

$$b = -1 \tag{9}$$

$$a = 0 \tag{10}$$

These values of the exponents results in the first dimensionless group for the gas vortex unit

$$\pi_1 = \frac{\Delta P}{\rho_f U_{0_i}^2}\ (dimensionless\ pressure\ drop) \tag{11}$$

This procedure can be carried out for each of the parameters in Table 1, helping in the formulation of the other dimensionless groups. In case of the GVU, these groups are obtained as

$$\pi_2 = \frac{D_E}{D_R}\ (exhaust\ to\ reactor\ diamter\ ratio) \tag{12}$$

$$\pi_3 = \frac{L_R}{D_R}\ (reactor\ length\ to\ diameter\ ratio) \tag{13}$$

$$\pi_4 = \frac{A_{in}}{D_R^2} = \left(\frac{I_0 \times n}{D_R}\right)\left(\frac{L_R}{D_R}\right) = \left(\frac{I_0 \times n}{D_R}\right) \times \pi_3$$

$$= \left(\frac{I_0 \times n}{D_R}\right) \tag{14}$$

$$(cumulative\ slot\ thickness\ to\ reactor\ diameter\ ratio)$$

$$\pi_5 = \frac{U_{0_i}\rho_f D_R}{\mu_f}\ \ (reactor\ Reynolds\ number) \tag{15}$$

$$\pi_6 = \gamma\ \ (injection\ slot\ angle) \tag{16}$$

Therefore, the complete set of dimensionless groups describing the GVU flow can be summarized as follows

$$\frac{\Delta P_{reactor}}{\rho_f U_{0_i}^2} = f\left(\frac{D_E}{D_R}, \frac{L_R}{D_R}, \frac{I_0 \times n}{D_R}, \frac{U_{0_i}\rho_f D_R}{\mu_f},\ \gamma\right) \tag{17}$$

A.2 Non-dimensionalizing the governing equations

A second approach to determine the dimensionless groups, this time illustrated for *the GSVU* flow, is to start with the governing equations and boundary conditions describing the process and non-dimensionalizing them using a characteristic length and velocity scale. This method is demonstrated with respect to the Gas Solid Vortex Unit as follows.

For the GSVU flow simulations the Eulerian-Eulerian method is adopted treating the phases as interpenetrating continua, the governing equations of both the gas and the solid phases are derived from the Navier Stokes equations. Remark that a Lagrangian approach will alter the governing equations and will thus result in a different non-dimensionalization approach[1].

In the Eulerian-Eulerian approach the gas and the solid phase governing equations are stated as follows. The mass conservation equations for the gas and the solid phases respectively are

$$\nabla \cdot (\varepsilon \overline{u}) = 0 \qquad (gas\, phase) \tag{18}$$

$$\nabla \cdot [(1-\varepsilon)\overline{v}] = 0 \qquad (solid\, phase) \tag{19}$$

While the momentum conservation equations for the gas and solid phases are

$$\rho_f \varepsilon[\overline{u} \cdot \nabla \overline{u}] + \overline{\imath}\rho_f g \varepsilon - \varepsilon \nabla \cdot \overline{E_f} + \overline{F} = 0 \qquad (gas\, phase) \tag{20}$$

$$\rho_s (1-\varepsilon)[\overline{v} \cdot \nabla \overline{v}] + \overline{\imath}\rho_s g(1-\varepsilon) - (1-\varepsilon)\nabla \cdot \overline{E_f} - \nabla \cdot \overline{E_s} - \overline{F} = 0 \;\; (solids\, phase) \tag{21}$$

In the momentum conservation equations, the first term denotes the convective momentum transfer contribution, the second one denotes the gravity force acting on the gas/solids, the third term accounts for the stresses generated due to apparent viscosity, collisions and compression in the material and the final term represents the momentum interchange between the corresponding phases due to drag forces.

As the GSVU governing equations are in cylindrical coordinates, the gradient operator in the cylindrical coordinate system corresponds to

$$\nabla = \frac{\partial}{\partial r}\hat{r} + \frac{1}{r}\frac{\partial}{\partial \theta}\hat{\theta} + \frac{\partial}{\partial z}\hat{z} \tag{22}$$

To non-dimensionalize the gradient operator, the vortex unit radius ($\mathrm{R_R}$) and the superficial injection velocity ($\mathrm{U_{0_i}}$) are chosen as the characteristic length and velocity scales. The GSVU length scales and flow velocities can be expressed in the form of the corresponding non-dimensional quantities as follows

$$r = r^* \times R_r \tag{23}$$

$$z = z^* \times R_r \tag{24}$$

$$\overline{u} = \overline{u}^{*} \times U_{0_i} \qquad (25)$$

$$\overline{v} = \overline{v}^{*} \times U_{0_i} \qquad (26)$$

Utilizing the dimensionless length scales, the gradient operator can be expressed in non-dimensional form as

$$\nabla = \frac{1}{R_r}\frac{\partial}{\partial r^{*}}\hat{r} + \frac{1}{r^{*}R_r}\frac{\partial}{\partial \theta}\hat{\theta} + \frac{1}{R_r}\frac{\partial}{\partial z^{*}}\hat{z} \qquad (27)$$

When the non-dimensional variables and operators are substituted in the governing equations, their non-dimensional forms are obtained as follows. The mass conservation equations become

$$\nabla^{*} \cdot \left(\varepsilon \overline{u}^{*}\right) = 0 \qquad (gas\,phase) \qquad (28)$$

$$\nabla^{*} \cdot \left[(1-\varepsilon)\overline{v}^{*}\right] = 0 \qquad (solid\,phase) \qquad (29)$$

The momentum conservation equations become

$$\varepsilon\left[\overline{u}^{*} \cdot \nabla^{*}\overline{u}^{*}\right] + \bar{i}\left(\frac{R_r}{U_{0_i}^{2}}\right)g\varepsilon - \varepsilon\nabla^{*} \cdot \frac{\overline{E_f}}{\rho_f U_{0_i}^{2}} + \frac{R_r}{\rho_f U_{0_i}^{2}}\overline{F} = 0 \qquad (gas\,phase) \qquad (30)$$

$$(1-\varepsilon)\left[\overline{v}^{*} \cdot \nabla^{*}\overline{v}^{*}\right] + \bar{i}\left(\frac{R_r}{U_{0_i}^{2}}\right)g(1-\varepsilon) - (1-\varepsilon)\nabla^{*} \cdot \frac{\overline{E_f}}{\rho_f U_{0_i}^{2}} - \left(\frac{\rho_f}{\rho_s}\right)\nabla^{*} \cdot \frac{\overline{E_s}}{\rho_f U_{0_i}^{2}} -$$

$$\left(\frac{\rho_f}{\rho_s}\right)\frac{R_r}{\rho_f U_{0_i}^{2}}\overline{F} = 0 \qquad (solid\,phase) \qquad (31)$$

The above equations represent the non-dimensional form of the governing equations. Expanding the convective term in cylindrical coordinates will result in the centrifugal acceleration term which, when non-dimensionalized, will provide the first dimensionless group in the GSVU system as

$$Centrifugal\,Froude\,number = \frac{U_{0_i}^{2} r}{v^{2}R_R} \qquad (32)$$

The non-dimensional gravitational term gives the second non-dimensional group relevant to the flow physics, the gravitational Froude number, given as

$$Gravitational\ Froude\ number = \frac{U_{0_i}^2}{gR_R} \tag{33}$$

The centrifugal Froude number is of crucial importance for the GSVU hydrodynamics and may be several orders of magnitude higher than its gravitational counterpart.

As a next step the stress term and momentum exchange terms can be further expanded to obtain the remaining dimensionless groups. The stress term in both gas and solid phases can be expanded to

$$\overline{E_f} = -P_f + \mu_f(\nabla\overline{u} + \nabla\overline{u}^T - \frac{2}{3}\nabla \cdot \overline{u}) \tag{34}$$

$$\overline{E_s} = -P_s + \zeta_s\nabla \cdot \overline{v} + \mu_s(\nabla\overline{v} + \nabla\overline{v}^T - \frac{2}{3}\nabla \cdot \overline{v}) \tag{35}$$

where Pg and P$_S$ are the gas and solid phase pressures, μ_g and μ_s correspond to the gas phase and solid phase viscosities and ζ_s is the solid phase bulk viscosity in the unit. Remark that the solid phase pressure and viscosity terms can be expanded using constitutive model equations taken from literature. The stress terms, when non-dimensionalized, result in the following equations

$$\overline{E_f}^* = \frac{E_f}{\rho_f U_{0_i}^2} = -\frac{P_f}{\rho_f U_{0_i}^2} + \frac{\mu_f}{R_R\rho_f U_{0_i}}(\nabla^*\overline{u}^* + \nabla^*\overline{u}^{*T} - \frac{2}{3}\nabla^* \cdot \overline{u}^*) \tag{36}$$

$$\overline{E_s}^* = \frac{\overline{E_s}}{\rho_f U_{0_i}^2} = -\frac{P_s}{\rho_f U_{0_i}^2} + \frac{\zeta_s}{R_R\rho_f U_{0_i}}\nabla^* \cdot \overline{v}^* + \frac{\mu_s}{R_R\rho_f U_{0_i}}\ (\nabla^*\overline{v}^* + \nabla^*\overline{v}^{*T} - \frac{2}{3}\nabla^* \cdot \overline{v}^*) \tag{37}$$

The corresponding dimensionless groups that appear from the above equations are

$$Dimensionless\ gas\ pressure = \frac{P_f}{\rho_f U_{0_i}^2} \tag{38}$$

$$Dimensionless\ solids\ pressure = \frac{P_s}{\rho_f U_{0_i}^2} \qquad 39)$$

$$Reactor\ scale\ solids\ bulk\ Reynolds\ number = \frac{R_R\rho_f U_{0_i}}{\zeta_s} \tag{40}$$

$$Reactor\ scale\ gas\ phase\ Reynolds\ number = \frac{R_R\rho_f U_{0_i}}{\mu_f} \tag{41}$$

$$Reactor\ scale\ particle\ Reynolds\ number = \frac{R_R\rho_f U_{0_i}}{\mu_p} \tag{42}$$

The momentum interchange term between the two phases can be expanded as a function of the slip velocity between the two phases

$$\overline{F} = \beta(\overline{u} - \overline{v}) \tag{43}$$

$$\overline{F}^{*} = \frac{R_R}{\rho_f {U_0}_i^2}\overline{F} = (\frac{R_r}{\rho_f {U_0}_i})\beta\left(\overline{u}^{*} - \overline{v}^{*}\right) \tag{44}$$

where β represents the momentum exchange coefficient between the two phases. Non-dimensionalizing the above equation results in

When β is further expanded using a drag correlation suggested in literature, such as the Ergun[2] equation or Wen and Yu[3] formulation, a non-dimensional form of the exchange coefficient can be determined as follows

$$Ergun\ form\colon\ \beta^{*} = \frac{\beta R_R}{\rho_s {U_0}_i} = 150\,\frac{(1-\varepsilon)^2}{\varepsilon}\frac{\mu_f}{\rho_s {U_0}_i d_p}\frac{R_R}{d_p} + 1.75\,\frac{(1-\varepsilon)}{d_p}\frac{R_R\rho_f}{\rho_s} \tag{46}$$

$$Wen\ and\ Yu\ form\colon\ \beta^{*} = \frac{\beta R_R}{\rho_s {U_0}_i} = \frac{3}{4}C_D\left(\overline{u}^{*} - \overline{v}^{*}\right)f(\varepsilon)(\frac{\rho_f}{\rho_s})(\frac{R_R}{d_p}) \tag{47}$$

$$where,\ C_D = f[\frac{\rho_f {U_0}_i d_p}{\mu_f}] \tag{48}$$

It is interesting to note here that in the above equation the reactor scale dimensionless groups interact with the particle scale dimensionless groups such as the particle Reynolds number. These particle-scale groups contain particle-scale information which comes from modeling the drag formulation between the two phases on particle level. The corresponding dimensionless groups that appear from the above equations are

$$Particle\ scale\ gas\ phase\ Reynolds\ number = \frac{d_p \rho_f {U_0}_i}{\mu_g} \tag{48}$$

$$Density\ ratio\ between\ the\ two\ phases = \frac{\rho_f}{\rho_s} \tag{49}$$

$$Reactor\ radius\ to\ particle\ diameter\ ratio = \frac{R_R}{d_p} \tag{50}$$

Combining all the above mentioned characteristic numbers results in the following extensive set of dimensionless groups in the GSVU as follows

$$\left[\frac{{U_0}_i^2 r}{v^2 R_R}, \frac{{U_0}_i^2}{g R_R}, \frac{\rho_s}{\rho_f}, \frac{\beta R_R}{\rho_s {U_0}_i}, \frac{P_g}{\rho_f {U_0}_i^2}, \frac{\rho_s {U_0}_i d_p}{\mu_f}, \frac{R_R}{d_p}, \frac{\rho_f {U_0}_i R_R}{\mu_f}, \frac{P_p}{\rho_f {U_0}_i^2}, \frac{\rho_f {U_0}_i R_R}{\mu_p}\right] \tag{51}$$

These dimensionless groups, along with the characteristic numbers arising from single-phase flow in terms of geometrical parameters, constitute the complete set of dimensionless groups for the GSVU

$$\left[\frac{{U_0}_i^2 r}{v^2 R_R}, \frac{{U_0}_i^2}{g R_R}, \frac{\rho_s}{\rho_f}, \frac{\beta R_R}{\rho_s {U_0}_i}, \frac{P_g}{\rho_f {U_0}_i^2}, \frac{\rho_s {U_0}_i d_p}{\mu_f}, \frac{R_R}{d_p}, \frac{\rho_f {U_0}_i R_R}{\mu_f}, \frac{P_p}{\rho_f {U_0}_i^2}, \frac{\rho_f {U_0}_i R_R}{\mu_p}, \frac{G_s}{\rho_s {U_0}_i}, \frac{R_E}{R_R}, \frac{L_R}{R_R}, \frac{I_0 \times n}{R_R}, \gamma\right] \tag{52}$$

A.3 References

1. Glicksman LR, Hyre M, Woloshun K. Simplified scaling relationships for fluidized beds. Powder Technology. 1993;77(2):177–199.
2. Ergun S, Orning A. Fluid flow through packed columns. Chemical Engineering Progress. 1952;48:89-94.
3. Wen CY, Yu YH. A generalized method for predicting the minimum fluidization velocity. AIChE Journal. 1966;12(3):610-612.